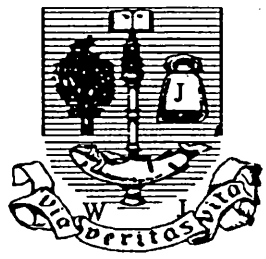

The Application of MALDI and Tandem Reflectron TOF Mass Spectrometry to the Analysis of Biomolecular Ions

Wei Jie Jia

Department of Physics and Astronomy
University of Glasgow

Presented as thesis for the degree of Doctor of Philosophy in the University of Glasgow

ProQuest LLC.
789 East Eisenhower Parkway
P.O. Box 1346
Ann Arbor, MI 48106 – 1346

This thesis is dedicated to my dearest wife,
Yi Shen,
whose love, encouragement and help
during the period of my studies made
this thesis complete

Acknowledgements

A great number of people have provided valuable help and encouragement during my Ph.D. studies. I would like to thank them all, especially to:

♥ my supervisor, Dr. K.W.D.Ledingham for his valuable advice, constant help and encouragement during the period of research and completion of this thesis.

♥ Dr. R.P.Singhal for helping me to overcome many theoretical problems in the thesis.

♥ Dr. C. Kosmidis for his helpful assistance and discussions in some of experiments.

♥ Miss C. McIntyre for her secretarial assistance in my academic life and her friendly and kindly help and hospitality in my daily life.

♥ Dr. C. T. J. Scott for his experimental assistance in some of my work.

♥ Mr. R. Maxwell and T. McCanny for their technical support.

♥ My research colleagues in LIS group: Dr. R. Zhen for her useful advice and assistance during my Ph.D. studies; Dr. R. Jennings, Dr. A Marshall, Dr. A. Clark, Dr. J. Sander for many helpful discussions on very aspects of my work; Ms. W. Peng, Mr. R. M. Deas, Mr. H. S. Kilic and Mr. S. Wang for helpful assistance and friendship.

♥ Sino-British Friendship Scholarship Scheme(SBFSS) for the financial support of my Ph.D. Studies and the British Council for the valuable advice and support.

♥ Finally I would like to thank my family: My father(Mingguang Jia) and mother(Minxian Ye), my father in-law(Zhengxiong Shen) and mother in-law(Weijun Zhao), my sisters and their families for their support and encouragement during my studies in the United Kingdom.

Publications during the Ph.D. studies

A Tandem Reflectron Time-of-flight Mass Spectrometer for the Investigation of Laser Photofragmentation of Molecular Ions
W.J.Jia, K.W.D.Ledingham, C. Kosmidis, and R.P.Singhal
Rapid Communications in Mass Spectrometry. Vol.9, (761)**1995**.

Investigations of Desorbed Species from Matrix Materials Used in MALDI
C.T.J.Scott, C.Kosmidis, **W.J.Jia**, K.W.D.Ledingham, R.P.Singhal;
RIS 94 proceedings, Ed. H-Jurgen Kluge, James E Parks and Klaus Wend, American Institute of Physics (AIP) Conference Proceedings, 329, **1995**.

The characterisation of Laser Ablation of Bulk Super-conducting Material Using Post Ablation Ionisation of the Neutrals
R.Zheng, M.Campbell, **W.J.Jia**, K.W.D.Ledigham, R.P.Singhal.
RIS 94 proceedings, Ed. H-Jurgen Kluge, James E Parks and Klaus Wend, American Institute of Physics (AIP) Conference Proceedings, 329, **1995**.

Formation of Atomic Hydrogen in Matrix-assisted Laser Desorption Ionisation
C.T.J.Scott, C.Kosmidis, **W.J.Jia**, K.W.D.Ledingham, R.P.Singhal.
Rapid Communications in Mass Spectrometry. Vol.8, (829)**1994**.

The Resonant Laser Ablation of Atoms in Solid Samples
W.X.Peng, I.S.Borthwick, A.Clark, **W.J.Jia**, K.W.D.Ledingham, A. Marshall, C.T.Scott, R.P.Singhal, R.E.Zheng, M.Campbell.
Proceedings of 25th E.G.A.S. Conference, Caen, France, July, **1993**.

The Use of a Reflectron Time-of-flight Mass Spectrometer to investigate fragmentation of Molecular Ions in MALDI.
W.J.Jia, C.T.Scott, C.Kosmidis, K.W.D.Ledingham, and R.P.Singhal.
XVIIth International Conference on Photochemistry, London, England, Jul. 30-Aug.4, **1995**.

Studies on Silicon-Nitride(Si_3N_4) Using Laser Ablation Postionization Mass Spectrometer

S.L.Wang, **W.J.Jia**, K.W.D.Ledingham, R.P.Singhal.

XVIIth International Conference on Photochemistry, London, England, Jul. 30-Aug.4, **1995**.

Studies of Silicon-Nitride (Si3N4) Using Laser Ablation Mass Spectrometry

S.L.Wang, **W.J.Jia**, K.W.D.Ledingham, R.P.Singhal.

J.Appl. Surface Science, Vol.93(205) **1996**.

Matrix-assisted Laser Desorption Ionisation

W.J.Jia

accepted and to be published in Scientific Technological Review Encyclopaedia (in Chinese).

Laser Mass Spectrometry of Biological Molecular Ions Produced by Matrix Assisted Laser Desorption Ionisation (MALDI)

W.J.Jia, C.Kosmidis, K.W.D.Ledingham, C.T.Scott, and R.P.Singhal.

accepted and to be published in J.Appl.Surface Science in 1996.

Photofragmentation of Biomolecular ions of Amino Acids by a Tandem Time-of-flight Mass Spectrometer

W.J.Jia, K.W.D.Ledingham, C. Kosmidis, and R.P.Singhal.

To be submitted to Rapid Communications in Mass Spectrometry.

Summary

This thesis describes the application of a reflectron time-of-flight (TOF) mass spectrometer , in particular, with the new laser desorption technique, "matrix-assisted laser desorption/ionisation" (MALDI), to the studies of biological molecular ions. MALDI has opened a new door of production of large intact biomolecular ions for the determination of the masses of large biomolecules. The work presented in this thesis was also carried out with primary objective of developing a tandem reflectron time-of-flight mass spectrometer for the studies of laser photodissociation of molecular ions. Chapter 1 presents a brief review of the techniques involved in my research work, such as resonance ionisation spectroscopy (RIS), Matrix-assisted laser desorption ionisation(MALDI), and tandem reflectron TOF mass spectrometry. The second chapter provides the readers with relevant theories for an understanding of the techniques of RIS, MALDI etc.. A discussion and description of photophysical processes which occur in the excited states of molecules and molecular ions, and probable mechanism of photofragmentation is also described in this chapter.

The purpose of Chapter 3 is to present the experimental apparatus in detail, which include a Nd:YAG laser, N_2 laser, dye laser, high vacuum chamber, reflectron, detector, data acquisition system, pulse delay generation system etc.. Chapter 4 presents the experimental investigations of MALDI, such as matrix selection, sample preparation, MALDI mass spectra, and power dependence etc.. The 1s -› 2s two-photon resonance and one-photon ionisation mass spectra of hydrogen from the matrix of 2,5-DHB have been shown. Two groups of hydrogen ions (one from ablation, another from postionisation) were observed. This work was carried out with Dr. C.J. Scott and the interpretation of the results and analysis was carried out jointly.

The work of Chapter 5 describes the development of a new tandem reflectron TOF mass spectrometer(TRTOF) for the investigations of laser photofragmentation of molecular ions. The computer program called 'SIMION' was used to simulate the ion trajectories in the reflectron and gave theoretical results of fragment trajectories with various fragments and different fragmentation position. Then the experiments were carried out with various parameters of the tandem reflectron TOF mass spectrometer, such as mass calibration, selection of parent ions, fragment ion collection, reflectron field effect, fragmentation mass resolution, and influence of the fragmentation laser parameters. The results show that the new TRTOF has a relatively simple timing

requirement for overlapping the pulsed laser and ion packets, and also has a multichannel fragment ion detection. It has also been shown that a TRTOF of considerable potential can be easily adapted from an ordinary reflectron TOF instrument to carry out tandem MS/MS experiments.

Chapter 6 presents and discusses laser photofragmentation mass spectroscopy of molecular ions using the tandem reflectron TOF mass spectrometer. The "Ladder-switching model" has been introduced and laser photofragmentation mass spectra of matrix molecular ions of 2,5-DHB have been shown. The power dependence of fragments from various molecular ions has been presented and possible fragmentation pathways have been discussed as well. In addition, the distinguishing between the ion isomers in this experiment indicates another advantage of this newly developed TRTOF.

Chapter 7 describes the application of the tandem reflectron TOF mass spectroscopy to the analysis and study of photofragmentation of biomolecular ions. Some biomolecular ions, such as PTH-tryptophan, PTH-valine, PTH-alanine, Cytosine, Guanine, which were produced by the MALDI technique, have been fragmented by a photofragmentation laser and their fragmentation mass spectra have been recorded. These results imply a promising future for this technique in photofragmentation of biological molecular ions.

The last chapter (Chapter 8) gives conclusions and some experiments for the future.

Contents

Chapter 1

Introduction

1.1 Introduction

The laser is one of the most remarkable inventions of the twentieth century and has been developed dramatically and put to use in many fields of application. The application of lasers in spectroscopy not only has greatly improved the characteristics of already known spectroscopic methods but also has introduced many new techniques, such as laser ionisation spectroscopy, which has no analogies in traditional spectroscopy.

Material analysis is one of the most significant tasks of spectroscopy. In principle, there are four methods to detect atoms and molecules. (a) the absorption method which is based on measurements of the attenuation of the exciting laser beam intensity; (b) the fluorescence method which is based on measurement of the intensity of photons re-radiated and scattered in different directions and at different frequencies; (c) the resonant deflection method which is based on the change in the direction of motion of the excited particles; (d) stepwise resonant photoionisation method which is based on the direct detection of the excited particles by way of its ionisation. The schematic diagrams of the four laser spectral methods of detection of atoms and molecules are shown in Fig.1.1

In this thesis I will concentrate on laser mass spectrometry in which lasers are used for the ionisation and fragmentation of molecules(the scheme d in Fig.1.1) and mass spectrometry for the separation of the ions with different m/z ratios.

Laser mass spectrometry is a fast and ultra-sensitive analytical technique. Acronyms in this field abound and are rather complicated. Fig.1.2 shows a general arrangement of laser mass spectrometry which can be used to explain a number of these acronyms.

When the ion beam hits the sample and sputters off ions the procedure is called secondary ionisation mass spectrometry (SIMS). SIMS is a very useful tool in the analysis of semiconductors and polymers. In the sputtering process, the yield of ions is several orders of magnitude lower than the production of neutral species. If the neutral

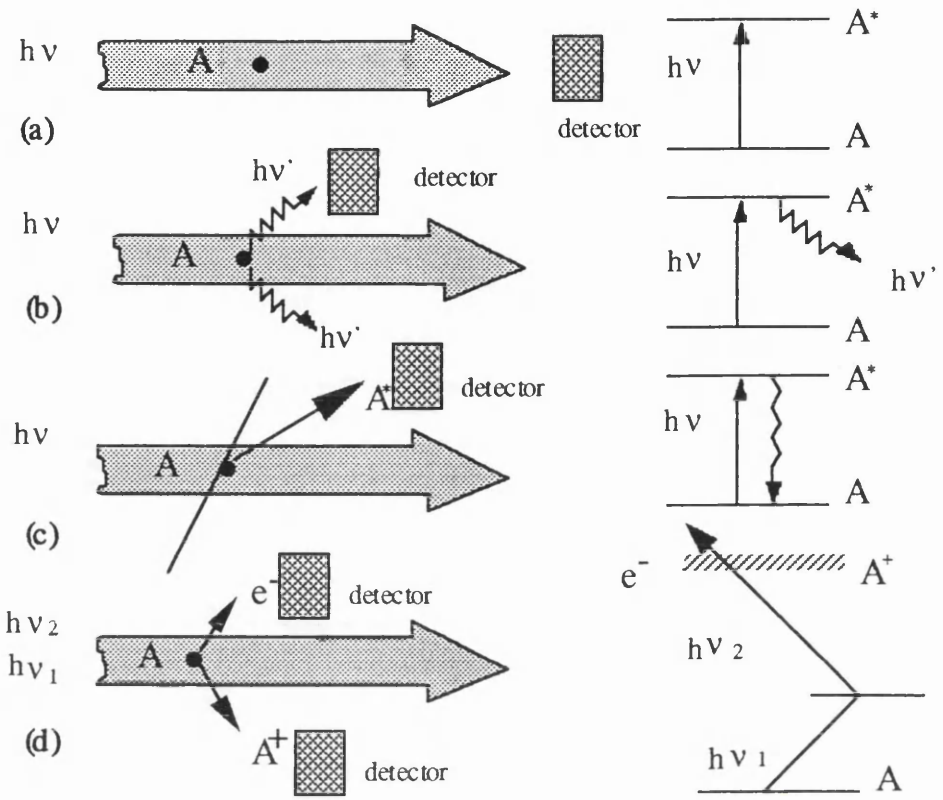

Fig.1.1 Four main schemes of laser spectral detection of atoms and molecules: (a) absorption method; (b) fluorescent method; (c) resonant deflection method:(d) stepwise multiphoton ionisation method.

plume is postionised non-resonantly by a second laser beam this technique is called surface analysis by laser ionisation(SALI). If the lasers are resonant, this process is called resonance ionisation mass spectrometry(RIMS).

When the laser beam hits the sample and ablates or desorbs ions, the process is called laser-microprobe mass analysis (LIMA or LAMMS). If the ablation laser is on resonance, this method is called resonance laser ablation(RLA). If the analytical sample is embedded in a matrix material, the procedure of the production of analytical ions by a desorption laser is called matrix-assisted laser desorption/ionisation(MALDI).

When the second laser is used for resonant postionisation of the neutrals the procedure is called laser ablation resonant ionisation spectrometry (LARIS) or (RIMS). If the plume

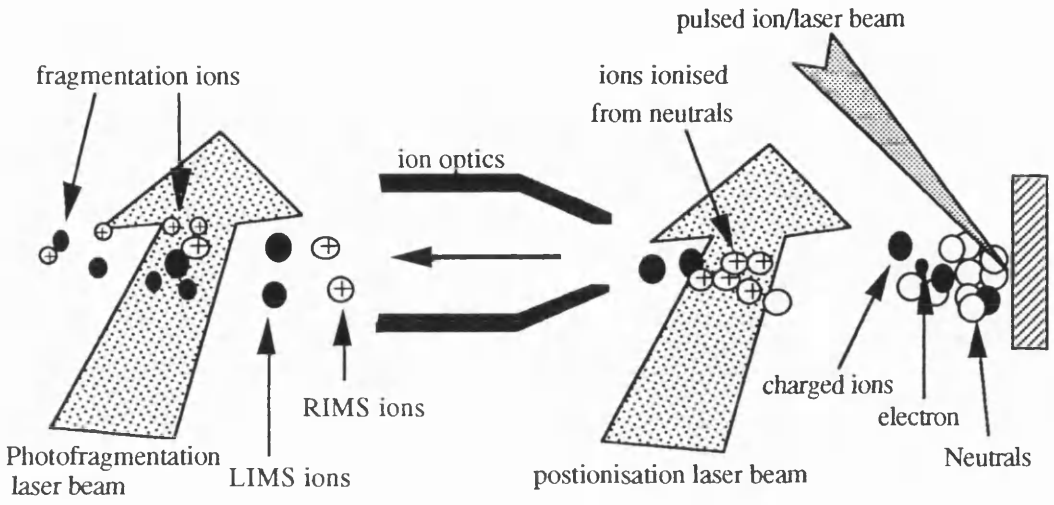

Fig.1.2 The diagram of the arrangement of the laser mass

consists of molecules rather than atoms it is called resonance enhanced multiphoton ionisation(REMPI). More generally, if the lasers are resonant and used to ionise neutrals in the field of spectroscopy this procedure is called resonance ionisation spectroscopy(RIS).

If selected ions in a first mass analysis are fragmented by another laser and their product ions are recorded in second mass spectrometry this procedure is called laser fragmentation mass spectrometry or tandem mass spectrometry(MS/MS).

In the following section of this chapter I would like to present the details of RIS, MALDI and MS/MS which are mainly used in my PhD research experiments.

1.2 Resonance Ionisation Spectroscopy(RIS)

1.2.1 RIS development

Although Resonance Ionisation Spectroscopy has just been introduced for less than three decades, it has made a considerable contribution to the progress in many areas of pure and applied physics, and has become a significant measurement tool for a host of other fields such as microelectronics, analytical chemistry, biological science and earth sciences.

The first demonstration of RIS was carried out in 1971 by V.S.Letokhov and his colleagues in the Institute of Spectroscopy (IOS) of USSR Academy of Sciences(Ambartzumian et al., 1971). A ruby laser pumped dye laser (λ_1=794.8 nm) was used to excite the Rb atoms from its ground state to the $5^2P_{1/2}$ intermediate state, then a second harmonic of the ruby laser (λ_2 = 347 nm) was used to ionise Rb atoms vis its intermediate state to its ionisation continuum. This is a two photon ionisation process. After that, a series of RIS experiments were performed with ground state Na (Duong et al., 1973), U(Tuccio et al., 1974), and Cs(Popesku et al., 1974) atoms in atomic beams using pulsed and cw dye lasers. In 1975, Hurst and his colleagues at Oak Ridge National Laboratory (USA) found that the cross section for resonant absorption of one photon between bound levels was typically of the order of 10^{-12} cm^{-2} and a laser fluence of about 0.1 μJcm^{-2} was sufficient to excite all atoms to that level. They also found that the cross section from the excited state into the ionisation continuum was approximately six orders of magnitude smaller than that of the excitation step and a laser fluence of about 100 mJ was required for its ionisation saturation. Therefore a 100% efficient ionisation of metastable He atoms was achieved by them. This experiment demonstrated that RIS was a highly sensitive technique with the potential of ionising all atoms of interest in the laser beam volume.

After the conditions for effective atom ionisation had been found, single atom detection was carried out by Hurst and his colleagues at ORNL in 1977(Hurst et al., 1977), where Cs atoms were ionised in an argon-methane gas phase, and electrons were detected by a proportional counter.

This technique also has high selectivity, since atoms of each element have a unique set of excited states which may be reached by the absorption of one or more photons from the ground states at the correct laser frequency providing certain optical selection rules are satisfied. The laser linewidth typically used in RIS measurements is between 0.1 and 1.0 cm^{-1}, and all atomic transitions between the ground state and some excited states, with the exception of He and Ne, may be resonantly excited with commercially available tuneable dye lasers. Bushaw et al developed the cw RIMS technique which is based on multi-step excitation of atoms to a Rydberg state by single-frequency cw dye lasers and ionisation by a high power cw CO_2 laser. By being combined with a continuous source

of atoms and mass spectrometer, this method provided extremely low detection limits down to few attograms and selectivity of the order of 10^{10}.

In addition, isotopes of an element can be ionised simultaneously and separated by a mass spectrometer. One of these applications to noble gases was developed by Atom Science, Inc. (USA) in 1984. The noble gas isotopic abundance are of significant importance for such research areas as solar neutrino study, dating in cosmochemistry and earth sciences. At present, the reported detection limit (Thonnard et al., 1992) is about 100 Kr atoms of the 81 or 85 isotopes detected in less than 5 minutes.

1.2.2 Basic RIS schemes

Since every atom has its own unique structure of discrete energy states or levels. The high energy states usually called excited states may be reached by the absorption of one or more photons from the lowest energy level(ground state) at the correct frequency providing certain optical selection rules are satisfied. The lifetime of the excited atom normally is about 10ns and after that the excited atom would de-excite to the ground state. During this lifetime further transitions from low to high excited states may occur by subsequent photon interaction, until sufficient energy is supplied to promote an electron into the ionisation continuum, thereby creating a positive ion and an unbound electron. The term of "resonant" means that the photon chosen for the transition is equal in energy to the difference between the two states of the elements of interest. A typical cross section for resonant absorption of one photon between bound levels is of the order of 10^{-12} cm^{-2}. Resonant multiphoton ionisation can be achieved via real intermediate states or a virtual intermediate state. Fig.1.3 shows the schematic diagram of the resonant multiphoton ionisation.

Normally a laser fluence of about 0.1 μJcm^{-2} is sufficient to cause saturated excitation of the atoms in the laser beam since the transition cross section is high. However the cross section for ionisation is smaller than those of resonant excitation(10^{-17}-10^{-18} cm^{-2}). Therefore a laser fluence of about 100 $mJcm^{-2}$ is required for saturation. Usually there are three ionisation procedures involved in the field of laser ionisation. Fig.1.4 illustrates the schematic diagram of these three ionisation procedures in the two photon ionisation process. In the scheme a, the atom is excited to the ionisation continuum, and becomes the ion by releasing an electron. This ionisation cross section (σ_{ion}) is small

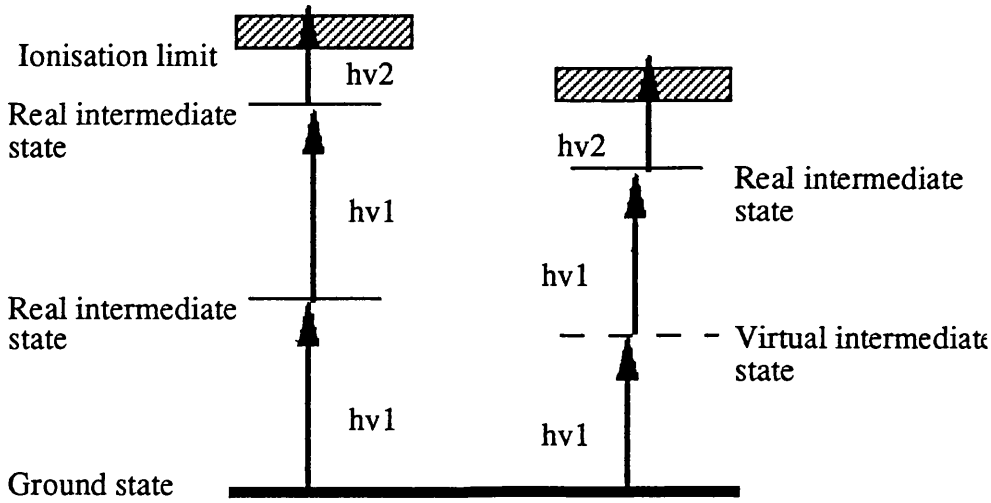

Fig.1.3 Schematic diagram of resonant multiphoton ionisation via real or virtual intermediate states.

(10^{-17}-10^{-18}cm^{-2}). In the scheme b, the atom is excited to a Rydberg state which is slightly lower than the ionisation continuum, and it is ionised by a pulsed electric field. The cross section of this procedure(σ_R) is rather high (about 10^{-14}cm^{-2}). In the final ionisation scheme, the atom is excited to an autoionisation states with a cross section (σ_A) of about 10^{-15}cm^{-2}.

The ionisation of elements can also be achieved by non-resonant transition whose cross section is many orders of magnitude smaller and requires a much higher fluence to reach saturation.

Five basic resonant ionisation schemes (Fig.1.5) have been proposed by Hurst and Payne (Hurst and Payne, 1988) to enable resonant ionisation of all the elements, except He and Ne which have very high ionisation potentials. In the first scheme, a single photon is required to excite the electron into an upper level more than halfway to the continuum and the second photon with the same energy is sufficient to cause ionisation. Hence the atom can be ionised by two photons from the same laser. In the second scheme, the use of a frequency doubled photon is required to excite the atom resonantly,

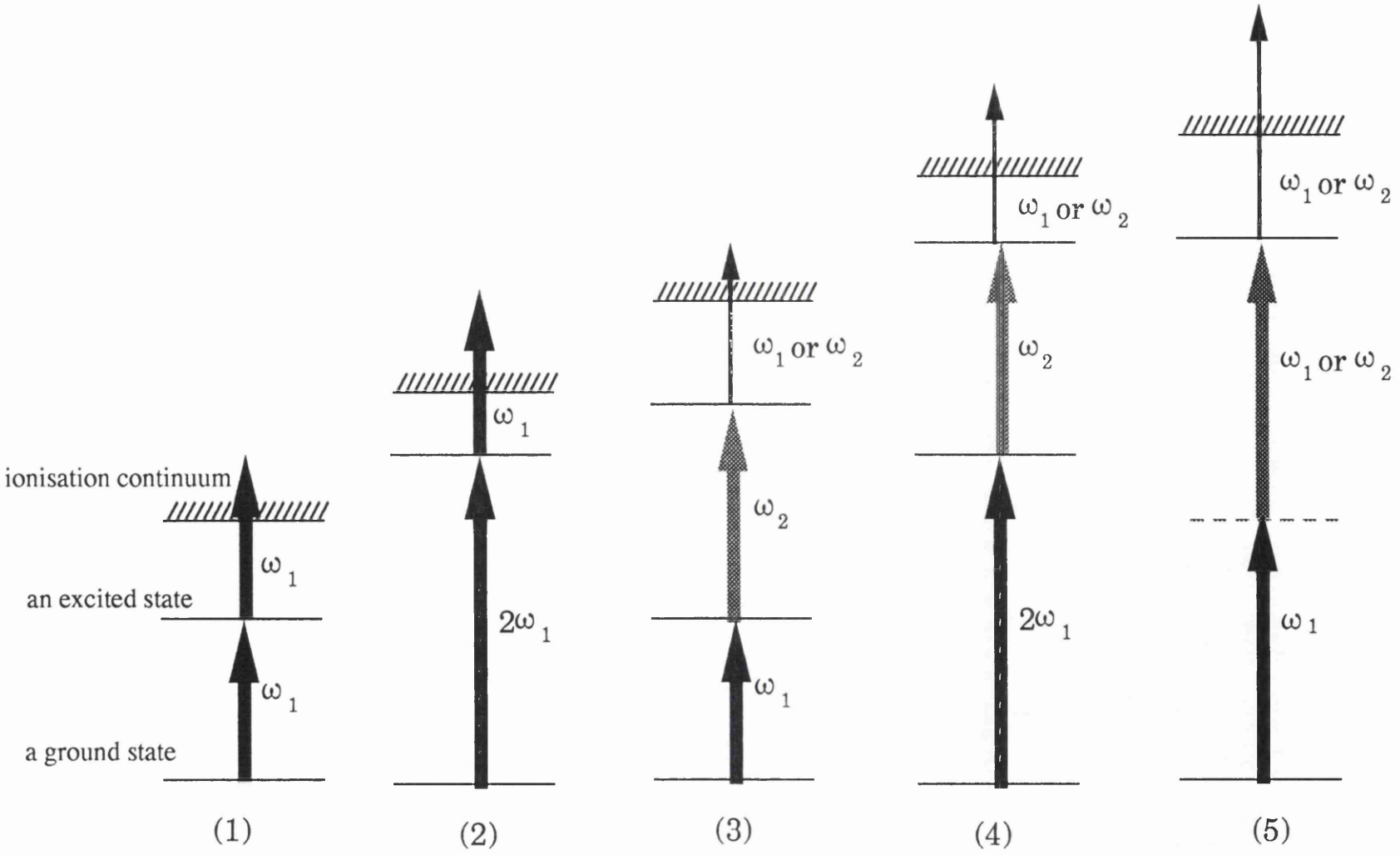

Fig.1.5 The five basic atomic resonant ionisation schemes

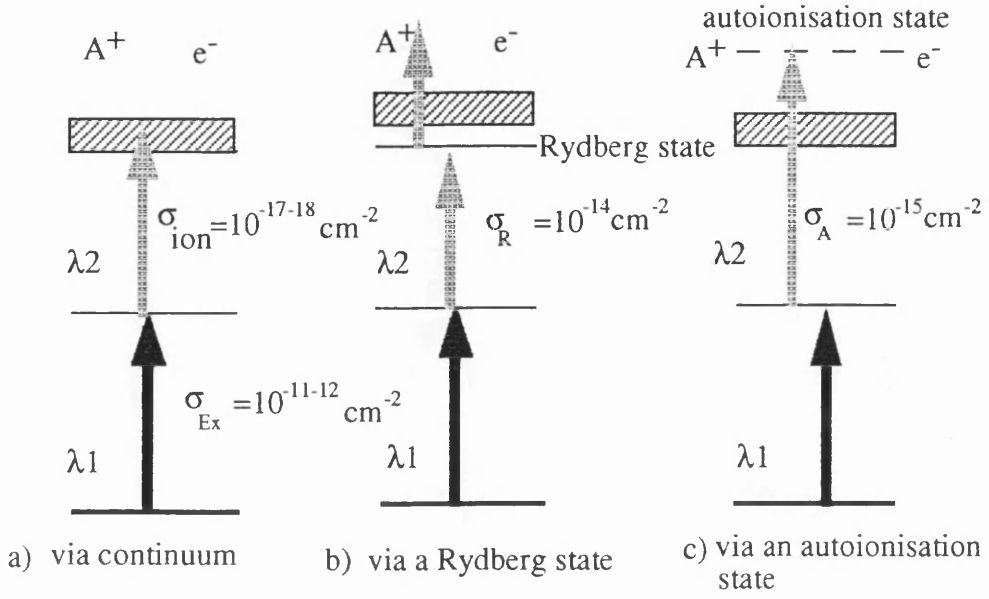

Fig.1.4 The diagram of three ionisation schemes

and the atom is ionised by a photon from the more intense fundamental beam. The only difference between the scheme 2 and scheme 5 is that the intermediate state in scheme 2 is real but is virtual in the scheme 5. The remaining schemes are performed by various combinations of photons with different energy.

Molecules can also be ionised by RIS technique. However molecular structure is considerably more complex. Each electronic level of a molecule has an associated set of vibrational levels, and each vibrational level also has a set of rotational levels. Several basic schemes of multiphoton excitation(Ledingham, 1994) can be used for the photoionisation of molecules (Fig.1.6). The single photon ionisation is the simplest type of photoionisation of molecules(i). However the photon energy should be very large (usually VUV photons) since the ionisation potentials of molecules are above 8 eV. The most common ionisation scheme is two-step photoionisation via intermediate excited electronic vibrational states(iv), commonly referred to as Resonance Two Photon Ionisation (R2PI). The remaining scheme can be achieved by either multi-IR-photon ionisation(ii), multi-VIS-photon ionisation(v) or combination of these two schemes(iii).

In Fig.1.6 each vibrational level also contains a set of rotational levels(not shown in Fig.1.6). Hence the absorption features of some molecules at room temperature are in

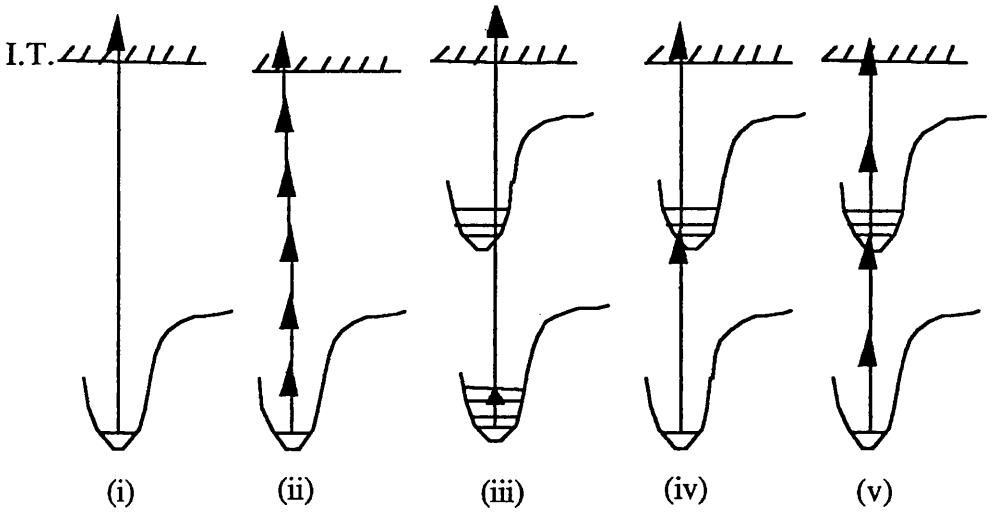

Fig.1.6 Five different molecular ionisation schemes I.T. represents the ionisation threshold of the molecule. (K.W.D.Ledingham, 1994)
(i) Single photon ionisation.
(ii) Non-resonant Multiphoton Ionisation (MPI).
(iii) Resonant two-photon ionisation via ground state-rovibrational levels.
(iv) Resonant two-photon ionisation via excited state rovibrational levels.
(v) Resonant Enhanced Multiphoton Ionisation(REMPI).

general broad and have complicated structure information. In order to obtain better absorption spectroscopy, the molecules can be cooled down to a few sharp peaks by supersonic jet cooling.

1.3 Matrix-assisted Laser Desorption Ionisation (MALDI)

1.3.1 What is MALDI ?

Comparing the detection of molecules with atoms, it can be found that it is much more difficult to detect single molecules than single atoms. A relatively simple task, such as the selective detection of traces of a polyatomic molecule (around 10^6 molecules) has not yet been solved by physical methods. The basic method of identifying trace quantities of molecules is mass spectrometric analysis. For many years scientists have been trying to create ion sources with high ionisation efficiencies and moderate molecular fragmentation. However, the ionisation efficiencies of the transformation from molecules into ions were rather low and one in one hundred thousand was usually obtained at optimal conditions. Moreover, most of the mass spectra contain largely

fragment ions, especially for large biomolecules (molecular weight over 1000 Dalton). Often no parent molecular ions were observed in the mass spectra at all. The main reason is that during irradiation by intense resonant UV laser there is a possibility that the molecule (or its fragments) absorbs more photons than is necessary for simple ionisation and results in a highly fragmented mass spectrum. Despite the fact that an analysis of fragments can obtain valuable information on the molecular structures, it is difficult to analyse multicomponent mixtures because the overlap of fragment mass peaks.

With the development of the life sciences, there is an increasing demand for more accurate, sensitive and fast methods measuring biomolecular masses, such as proteins, peptides etc. Matrix-assisted laser desorption ionisation or MALDI, which was developed in 1987, is a new laser desorption ionisation technique for large organic molecules. MALDI has shown its potential for desorbing ions of biomolecules with molecular weight more than 400,000 Da. In addition, MALDI is very sensitive and only needs about picomole of analytes. MALDI is also suitable for mixture analysis because of the production of molecular ions with few fragments.

The basic principle of MALDI that has been suggested is that: a matrix absorbs the energy from a laser beam and is excited from the ground state to the excited state, which is then responsible for the disintegration of the condensed phase. Meantime, the analyte, which is present in extremely small concentration relative to the matrix, is ejected intact by the matrix(Fig.1.7). Finally, the ions are attracted by the ion optics and directed towards a time-of-flight mass spectrometer or other kinds of mass spectrometers to be separated.

The key of this technique is to choose suitable matrices, which are the small volatile organic molecules with a capacity to absorb the laser beam strongly and are soluble in aqueous solutions. It is also essential that a matrix is present in large excess relative to the analyte because strong intermolecular forces among the analytes need to be reduced (matrix isolation). Usually, the ratio of matrix to analyte is about 1000.

1.3.2 History of MALDI

Before 1987, it was very difficult to measure a large intact biomolecular mass. The

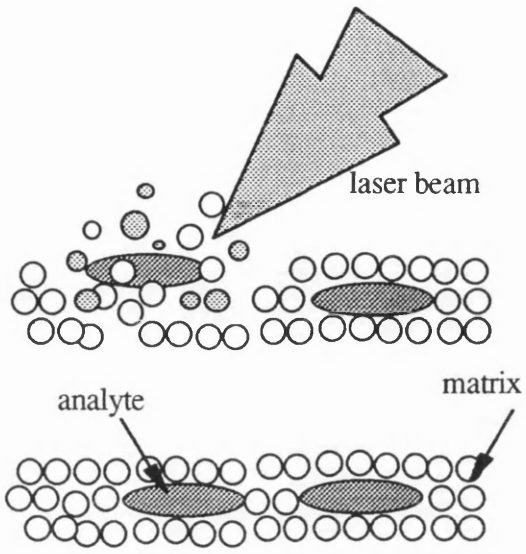

Fig.1.7 Schematic diagram of MALDI. The concentration of matrix molecules is much larger than that of analytes. Hence the strong forces between the analytes are reduced.

range of molecular masses which laser desorption could effectively absorb without fragmentation was about 1500 Da. In September of 1987, Professor A. Benninghoven broke into the proceedings of a conference to announce some results that he had just got from Dr. Koichi Tanaka of Shimadzu in Japan in the Fourth Ion Formation from Organic Solids. In fact, this reprint had just been presented at the 2nd Japan-China Joint Symposium on Mass Spectrometry several days earlier(Tanaka et al., 1987). There were very impressive mass spectra in this paper. The spectra had very intensive mass peaks with high molecular masses, and also had very good signal-to-noise ratios. However, the paper did not tell what kind of ion source was used until later. What was known about the ion source was that a pulsed nitrogen laser was used as an exciting light source, and sample was made up a mixture of a protein with a liquid matrix and a metal powder.

After the conference, Professor F.Hillenkamp and his co-worker M.Karas started to work on this project(Karas, et al. 1987). They announced their exciting results at the International Mass Spectrometry Conference held in France, in August, 1988. They found that nicotinic acid had special properties as a matrix-assisted material, which is solid at room temperature, with a low vapour pressure (but a tendency to sublime) and a

high absorption coefficient at the laser wavelength used. They made aqueous solutions of a nicotinic acid and a protein and mixed them according to a certain ratio (usually 1000), then dropped it on and dried on a sample stub. The sample was transferred into a vacuum system and irradiated by the fourth harmonic of a Q-switched, Nd:YAG laser. Large signals of the protein ions with masses up to 25,000 Da were observed after the ions went through a reflection TOF mass spectrometer. In addition, the sensitivity of this new technique was very impressive, and the total amount of protein loaded into the mass was roughly 1 picomole. The name given to this new technique was "Matrix-assisted Laser Desorption Ionisation" which indicates that this method was different from the old technique of 'ordinary' laser desorption.

In the following years, many people concentrated on finding new matrices. To date, many hundreds of matrix-like materials have been tested, but only about 10 of them are suitable for MALDI. R.C.Beavis and B.T.Chait(Beavis and Chait, 1990) in Rockefeller University have done outstanding work on this project. They used insulin as an analyte, and chose nearly 3 dozen materials as matrices. They developed their own sample preparation method: 0.1 g/L of the analyte was dissolved in a 5-10 g/L solution of matrix in water (or 1:1 water and ethanol) and disposed about 1μL of the solution on a probe tip. The solution was then gently dried with a hot-air gun. Finally four useful matrices were found and two of them, sinapinic acid and ferulic acid, are still very popular. Up to 116,000 Da of protein has been observed using sinapinic acid as a matrix. The mass resolution was improved from dozens to several hundreds. Furthermore negative high-mass pseudomolecular ions produced by this type of desorption are demonstrated for the first time. After that, some new effective matrices has been found, for example, 2,5-Dihydroxybenzoic acid(2,5-DHB). In 1993, 2-(4- Hydroxypheny lazo)benzoic acid or HABA was introduced by K.Biemann in Massachusetts Institute of Technology(Biemann et al., 1993) and shown to be very advantageous as a matrix for MALDI. Comparing with other matrices, such as sinapinic acid, 2,5-DHB etc., it indicates that HABA provides the best temporal and spatial stability and shot-to-shot reproducibility of the ion signals, and comparable sensitivity for peptides and smaller proteins, but results in better sensitivity for larger proteins and glycoproteins in protein mixtures. Up to 250 KDa mass biomolecules has been successfully desorbed from the solid sample. Furthermore many hundreds of single-shot mass spectra could be accumulated from the same spot.

Although the techniques of MALDI has been developed rapidly, its theory is still unclear, and a lot of work need o be done. Several models, including the 'Homogeneous Bottleneck Model' by A.Vertes(Vertes and Gijbels 1990); 'Pressure Pulses Model' by R.E.Johnson(Johnson et al., 1991); 'Jet Expansions Model' by R.C.Beavis, (Beavis, et al., 1991), and 'Photochemical Ionisation Model' by F.Hillenkamp (Hillenkamp, et al. 1992) have been proposed.

MALDI has progressed considerably since its application to proteins in 1987. Nowadays the main work on MALDI has concentrated on the following three aspects:
1), The basic understanding of the underlying desorption mechanism. This is not an easy task, and needs a lot of experiments and improvement of MALDI techniques; 2), The improvement of techniques of MALDI mass spectrometry which means that resolution and sensitivity need to be improved by optimisation of designs of ion optics and detectors; 3), Applications of MALDI on proteins and peptides, especially on oligonucleotides and nucleic acids. DNA molecules with molecular masses up to 400,000 Da have been detected by MALDI. Even larger DNA molecules, up to 1000 nucleotides long, have been vaporised intact. However if MALDI can be a direct replacement for gel electrophoresis for sequencing of DNA or other biomolecules, there are still improvements to be made, such as mass resolution, sensitivity, mass calibration and applicability to biomolecules having the necessary base compositions of range and molecular size produced by the Sanger procedure. In general, with the improvements in time focusing and detection efficiency in spectrometers without mass discrimination, people speculate that developments in other new techniques will take MALDI to new levels.

1.4 Tandem time-of-flight mass spectrometry

In general, where two or more mass analysers have been used in conjunction, they have been referred to as tandem mass instruments(MS/MS). Tandem mass spectrometry selects one (or more) of a mixture of ions in a first mass analysis, and then the selected ion generates product ions whose mass spectrum is characteristic of the ion's structure. A general review of tandem mass spectrometry has been written by Busch et al (Busch, et al. 1988).

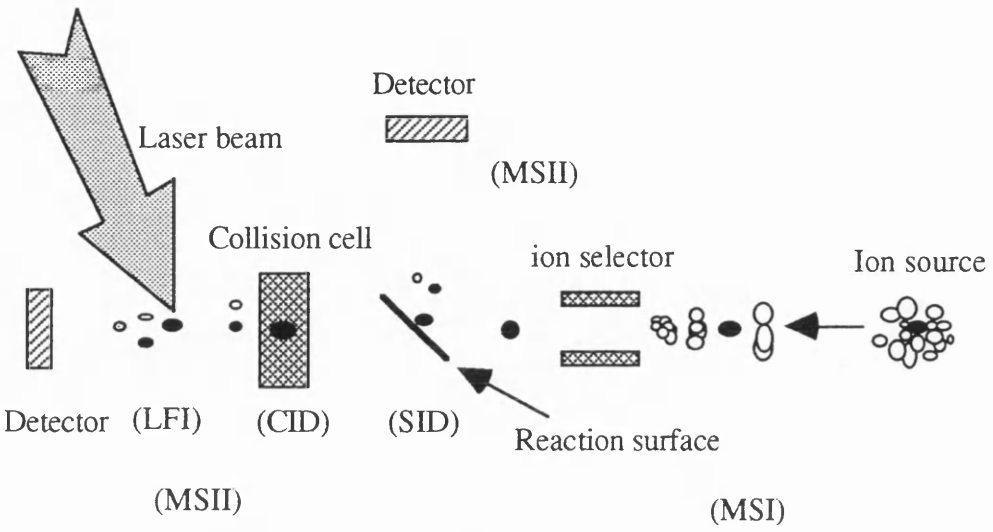

Fig.1.8 Schematic diagram of tandem mass spectrometry. SID represents " Surface-induced Dissociation"; CID is "Collision-induced Dissociation"; LFI represents "Laser fragmentation of Ions".

When the final product ions are generated by collisionally activated dissociation or surface-induced decomposition, the processes are called collision-induced decomposition (CID) and surface-induced decomposition (SID), respectively (see Fig.1.8). When the product ions are produced by a laser, it is called laser fragmentation of ions(LFI).

One major application of tandem mass spectrometry is structural characterisation of parent ions, such as isomeric ions. In recent years an unusually exciting development in mass spectrometry has been the introduction of methods such as MALDI, fast atom bombardment(FAB) and electrospray ionisation(ESI) to produce molecular ions from molecules of over 400 kDa. The fragment ions from peptides, proteins, nucleotides and other biomolecules can provide readily interpretable structural information. Therefore structural characterisation of ions becomes more and more important and tandem mass instruments have proved to be of unique value for amino acid sequencing of components in oligopeptide mixtures.

Chapter 2

Theoretical considerations

2.1 Introduction

This chapter will give an account of the current state of understanding of molecules/atoms interactions with laser light. Such interactions involve the photon absorption/emission with an account of spectral line broadening, rate equations for ionisation conditions, laser power dependence, laser-induced heating and thermal desorption, irradiance threshold for desorbed plume formation and so on. Therefore the background theories of these processes will be discussed. The energy transfer during these processes, especially in MALDI, will be explained by the "Bottleneck model" and the velocity distributions of materials liberated by a laser will be described by the Maxwell-Boltzmann distributions and the Hydrodynamic model. Finally the ion formation in MALDI, dissociation energy, predissociation and fragmentation of molecules and ions will be considered.

2.2 Absorption and emission

The simplest interaction between a laser and particles(atoms or molecules) is the absorption of the laser radiation by the particle or the emission of photons from the excited particles. Let us consider two non-degenerate levels of a particle with respective energies of $E_1(|1>)$ and $E_2(|2>)$. For the resonant absorption ($|1> \rightarrow |2>$) the frequency of a photon (f) absorbed by the particle (atom or molecule) can be written in equation 2.1:

$$f = (E_2 - E_1)/h \qquad \text{(Eq.2.1)}$$

where h is Planck's constant, 6.626×10^{-34} Js. The probability per second of an atom absorbing a photon, dP_{12}/dt, is proportional to the number of photons of energy hf per unit volume, $\rho(f)$, and is usually expressed as equation 2.2:

$$dP_{12}/dt = B_{12}\rho(f) \qquad \text{(Eq.2.2)}$$

where B_{12} is Einstein absorption coefficient. The atom which absorbs a photon is in its excited state and unstable. In the presence of a flux of photon of energy hf it will make the transition ($|2> \rightarrow |1>$) from its higher energy level to its low energy level(usually the

ground state) with simultaneous emission of a photon of frequency f. This process is called the stimulated emission. Its probability per second, dP_{21}/dt, can be written:

$$dP_{21}/dt = B_{21}\rho(f) \qquad \text{(Eq.2.3)}$$

where B_{21}, the Einstein coefficient of stimulated emission, is equal to B_{12} in the case that the levels |1> and |2> have the same degeneracy. Without the presence of the radiation field, an excited atom in state |2> may also lose energy with an emitted photon. This process is referred to as spontaneous emission. For a given atom in a given state its probability per second is a constant, the Einstein coefficient for spontaneous emission, A_{21}(units s^{-1}). The relationship between A_{21} and B_{21} is shown in the equation 2.4:

$$A_{21} = \frac{8\pi hf^3}{c^3} B_{21} = \frac{16\pi^3 f^3}{3\varepsilon_0 hc^3} (\langle 2|\mu|1\rangle)^2 \qquad \text{(Eq.2.4)}$$

where $<2|\mu|1>$ is the transition moment, ε_0 is the permittivity of free space(8.854×10^{-12} Fm^{-1}), and c is the speed of light in vacuum. The natural (or spontaneous) radiative lifetime, τ, of the excited state is just the inverse of A_{21}.

2.3 Spectral linewidths

The absorption peak is referred to the form of a plot of the intensity of the transition against wavelength (or frequency, or wavenumber). Theoretically, a transition between two energy levels needs an exact match between the excitation frequency and the energy difference E_2-E_1. However, in practice, a range of frequencies(spectral linewidth) will be effective in producing a spectral transition. Fig.2.1 shows a characteristic absorption line with its full-width half-maximum(FWHM) which is chosen as the distance between two points when the intensity of line drops by half. Three main factors may contribute to the spectral linewidth and shape.

1) Natural linewidth: the natural linewidth of a transition between two energy levels is determined solely by the radiative lifetime of the excited state. According to the Heisenberg uncertainty principle, the relationship between the lifetime and energy width can be written as :

$$\tau \Delta E \geq h \qquad \text{(Eq.2.5)}$$

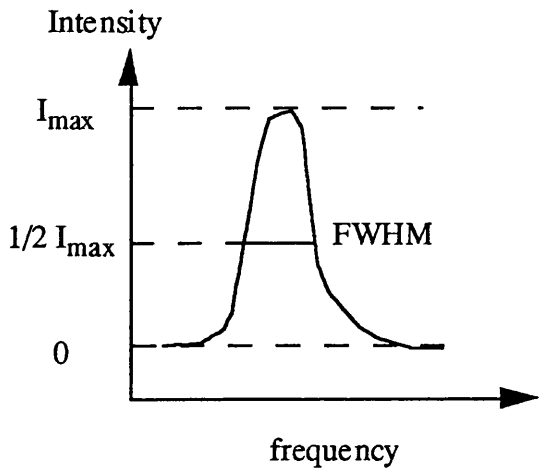

Fig.2.1 A typical spectral peak.

$\Delta E=h\Delta f$, therefore the linewidth can be expressed in Eq.2.6.

$$\Delta f \geq \frac{1}{2\pi\tau} \qquad \text{(Eq.2.6)}$$

It illustrates that all energy levels have finite width with resulting line broadening since τ is finite. 30 MHz is a typical linewidth for an excited electronic state. Therefore the natural line broadening makes a negligible contribution under most experimental conditions.

In more general case of a transition between two excited energy levels, the overall linewidth is given by equation 2.7.

$$\Delta f = \frac{(\tau_1^{-1} + \tau_2^{-1})}{2\pi} \qquad \text{(Eq.2.7)}$$

2) Doppler Broadening: The Doppler shift makes radiation appear of different wavelengths when the atoms or molecules are moving towards or away from the detector. If an atom or molecule is moving towards the detector with a velocity V_z, then the Doppler shifted absorption frequency is given by equation 2.8.

$$f = \frac{f_0}{(1 - V_z / c)} \qquad \text{(Eq.2.8)}$$

where f_0 the absorption frequency of the stationary atom or molecule. For an atom moving away the Doppler shift in Eq.2.8 is positive. Under usual conditions the velocity distribution of a particle at a temperature T is a Maxwell-Boltzmann distribution. Hence a characteristic linewidth Δf_d is given by the equation 2.9.

$$\Delta f_d = \frac{2 f_0}{c}\left[\frac{2RT\ln 2}{M}\right]^{1/2} \qquad \text{(Eq.2.9)}$$

where M is the molar mass, and R is the gas constant(8.314J/mol.K).

3) Pressure Broadening: Collisions between gas phase atoms or molecules have the effect of reducing the lifetime of excited states and thus lead effectively to a broadening of a spectral linewidth. The line broadening is given by the equation 2.10.

$$\Delta f = \frac{1}{2\pi\alpha} \qquad \text{(Eq.2.10)}$$

where α is the mean time between collisions.

2.4 Rate equations

In order to investigate the requirements of the resonant and non-resonant lasers for saturation of the ionisation process, simple population rate equations can be used. Let us consider a simple two photon resonant ionisation process (Fig.2.2).

Let N_0, N_A and N_I be the total number of the ground state atoms, the number of the first excited state atoms and the number of the ionised atoms in the laser beam, respectively. All these number are time dependent during the laser pulse. σ_A, σ_I and σ_E are the cross sections for the absorption, ionisation and stimulated emission, respectively. Γ is the spontaneous decay rate, β is the rate of non-radiative decay to a state not contributing to the photoionisation process, and Φ is the photon flux (number of photons per unit area

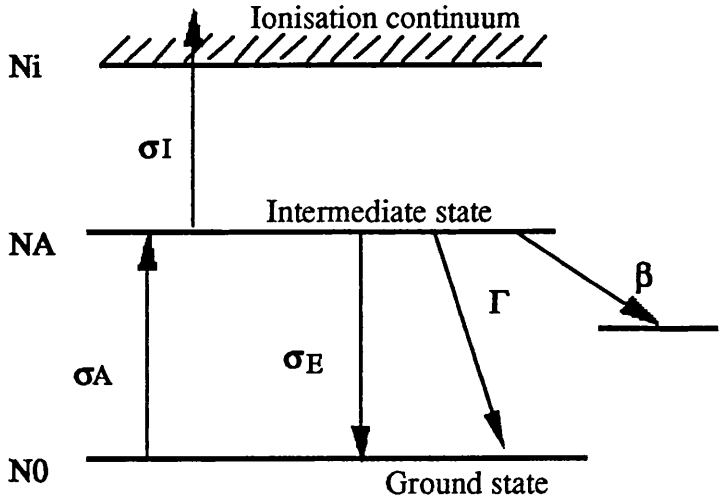

Fig.2.2 A simple two photon resonant ionisation scheme

per unit time). Therefore the rate equations can be written as:

$$dN_0/dt = -N_0\sigma_A\Phi + \Gamma N_A + N_A\sigma_A\Phi \qquad \text{(Eq.2.11)}$$

$$dN_A/dt = N_0\sigma_A\Phi - \Gamma N_A - N_A\sigma_I\Phi - N_A\sigma_E\Phi - \beta N_A \qquad \text{(Eq.2.12)}$$

$$dN_I/dt = N_A\sigma_I\Phi \qquad \text{(Eq.2.13)}$$

By adding (Eq.2.11) and (Eq.2.12) and differentiating (Eq.2.12) with respect to t we get:

$$\frac{d^2N_A}{d^2t} + A\frac{dN_A}{dt} + B^2N_A = 0 \qquad \text{(Eq.2.14)}$$

where:

$$A = \Gamma+\beta+(\sigma_A+\sigma_I+\sigma_E)\Phi \qquad \text{(Eq.2.15)}$$

$$B^2 = (\beta+\Phi\sigma_I)\sigma_A\Phi \qquad \text{(Eq.2.16)}$$

The solution of this second order differential equation(Eq.2.14) is:

$$N_A = \frac{N_0\sigma_A\Phi}{\lambda_2-\lambda_1}\left[\exp(-\lambda_1 t) - \exp(-\lambda_2 t)\right] \qquad \text{(Eq.2.17)}$$

where:

$$\lambda_1 = A/2 + 1/2(A^2-4B^2)^{1/2} \qquad \text{(Eq.2.18)}$$

$$\lambda_2 = A/2 - 1/2(A^2-4B^2)^{1/2} \qquad \text{(Eq.2.19)}$$

For a pulse laser, tuned on resonance, the σ_A and σ_E (10^{-12} cm^{-1}) are much larger than σ_I (10^{-18} cm^{-1}). $\sigma_A\Phi >> \Gamma+\beta$ (typical values: $\Gamma \propto 10^8 s^{-1}$, $\beta \propto 10^6 s^{-1}$). Then $\lambda_2 >> \lambda_1$ the (Eq.2.17) becomes:

$$N_A = \frac{N_0 \sigma_A \Phi}{\lambda_2}[\exp(-\lambda_1 T)] \qquad \text{(Eq.2.20)}$$

Substituting Eq2.20 into Eq.2.13 and integrating the time over the laser pulse and we can get the ionisation yields:

$$N_i = N_0[1-\exp(-\lambda_1 T)] \qquad \text{(Eq.2.21)}$$

where T is laser pulse duration. In order to ionise all atoms i.e. $N_i=N_0$, the saturation conditions are :

$$\sigma_A\Phi >> 1/T \qquad \text{(Eq.2.22)}$$

$$\sigma_I\Phi >> 1 \qquad \text{(Eq.2.23)}$$

Therefore the laser flux for the saturation conditions of bound/bound transition is about $0.1 \mu Jcm^{-2}$ and for the bound /ionisation continuum is about $100mJcm^{-2}$.

2.5 Laser power dependence

In the last section, the requirements of the lasers for the saturation of the transitions between a state and a state or a state and ionisation continuum were described. In this section the power dependence of the transition rate will be discussed before the lasers reach the saturation conditions. The transition rate constant for n-photon process can be given by the following equation:

$$k = \frac{\sigma_{(n)} I^n}{(h\omega)^n} \qquad \text{(Eq.2.24)}$$

where $\sigma_{(n)}$ and ω are the nth order transition cross section and the laser frequency, respectively. I is the laser irradiation in units of $cm^{-2}s^{-1}$. The intensity dependence of the transition probability for the n-photon process is called the formal intensity law which is used to determine the orders of multiphoton processes such as excitation, and ionisation.

2.6 Laser-induced heating and thermal desorption

When the laser radiation (nanosecond) imparts to a solid sample surface(substrate), it transfers photon energy into the sample which heats up on the time scale comparable to the laser pulse length if the substrate absorbs the energy. The resulting temperature rise leads to the detachment of the sample molecules. This process is usually called laser-induced thermal desorption(LITD).

In LITD process, the evolution of temperature rise on the sample surface plays a decisive role. The distribution of the heat in the substrate can be described by the heat conduction equation:

$$c(T)\frac{\partial T(r,t)}{\partial t} = -\nabla \mathbf{J}(r,t) + I(r,t) \qquad \text{(Eq.2.25)}$$

and

$$\mathbf{J}(r,t) = k(T)\cdot T(r,t) \qquad \text{(Eq.2.26)}$$

where T(r,t) is temporal and spatial temperature distribution, I(r,t) is the source term describing the laser heating (the heat production per unit volume per unit time). c(T) and k(T) are the specific heat and the heat conductivity. J(r,t) is the heat flow. If the laser has a uniform spatial energy distribution and has a flat temporal energy profile of duration t, the source term can be expressed by the equation 2.27

$$I(r,t) = \alpha(1-R)I_0(r,t)e^{-\alpha z} \quad \text{Eq.2.27}$$

where α is the light absorption coefficient of the substrate at the laser frequency; R is the reflectance; z is the distance through which the incident light propagates along the z-axis perpendicular to the surface; $I_0(r,t)$ is the laser irradiance.

In metals usually the absorption length is very short (of the order of tens of nanometres)

and can be negligible comparing to the depth to which heat is conducted. For simplicity, one can assume z=0, which means that the heat is produced at the surface. k is the heat conductivity and R is the reflectance (constants and temperature independent). The Eq.2.25 can be deduced as following two equations:

$$T(0,t) = T_0 + \frac{2I(1-R)}{k}\left(\frac{\kappa t}{\pi}\right)^{1/2} \qquad \text{for } t<\tau \qquad \text{(Eq.2.28)}$$

$$T(0,t) = T_0 + \frac{2I(1-R)}{k}\left(\frac{\kappa t}{\pi}\right)^{1/2}\left\{\left(\frac{t}{\tau}\right)^{1/2} - \left(\frac{t}{\tau}-1\right)^{1/2}\right\} \qquad \text{for } t>\tau \quad \text{(Eq.2.29)}$$

where κ is the thermal diffusitivity of the material and τ is the laser pulse duration. From these two equations one can estimate the basic features of the laser induced surface heating. For an example, if a laser pulse duration is 10 ns, R is 50%, and aluminium as the substrate, for the laser with a power of 10^7 W/cm^{-2}, the surface temperature rises about 100K; for a power of 10^8 W/cm^{-2}, temperature raises about 933K, and for 10^9 W/cm^{-2} the temperature is about 10000K.

2.7 The different irradiance thresholds and regimes for plume formation

As laser irradiance increases, the forms of laser-solid interaction change. For a given material there are several different regimes depending on the laser irradiance, which involve the following possibilities(Vertes and Gijbels, 1993 b):

a) Surface heating with thermal desorption
b) Surface melting with surface evaporation
c) Volume evaporation
d) Formation of an optically thick plume
e) Plasma absorption in the plume
f) Optical breakdown (in transparent insulators)

Laser irradiance (I_0) and the solid optical absorption coefficient(α) are the two principal factors for the determination of these regimes. Vertes(Vertes. et al., 1990a) proposed three different thresholds for these processes, volatilisation threshold I_v, plasma ignition threshold I_p, and optical break-down threshold I_b. The different regimes separated by the laser intensity is shown in Fig.2.3.

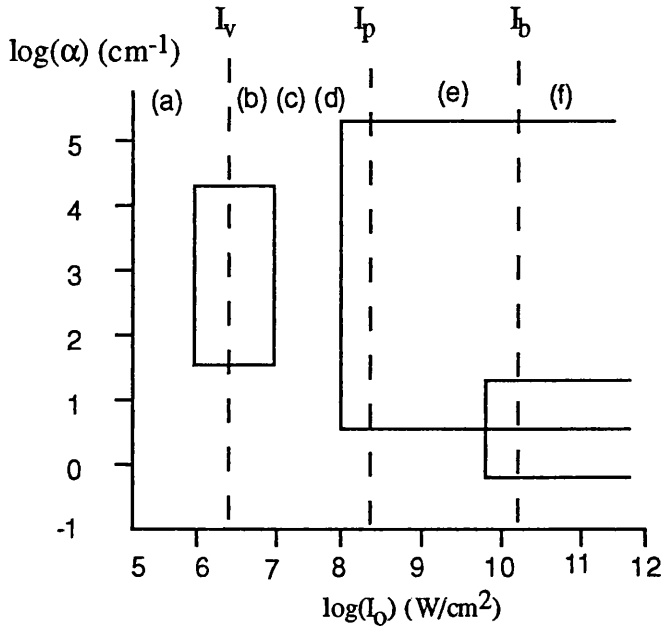

Fig.2.3 Different regimes of laser solid interaction are roughly divided according to laser irradiance and optical absorption coefficient. (a), (b), (c), (d), (e) and (f) represent the different regimes and I_v, I_p and I_b are the thresholds of volatilization, plasma ignition and optical break-down, respectively.(from Vertes et al., 1991).

2.8 Energy redistribution processes (Homogeneous Bottleneck Model)

The UV laser desorption processes are usually described by the following mechanism: the sample molecules absorb the photon energy and are excited to higher electronic excited states. Quick deexcitation of these molecules leads to vibrationally highly excited ground states. Some of vibrationally excited molecules will decompose, and other will transfer its energy to the lattice. Thus the lattice is heated up, the phase transition temperature can be reached and emission plume eventually be formed. In most cases the surface temperature calculated from this mechanism is rather high, and large fragile biomolecules can easily be decomposed at this temperature. However in MALDI experiments, large intact biomolecular ions are produced in the plume with abundant fragments of a matrix. Therefore it needs other models to explain this phenomenon.

Vertes(Vertes. et. al., 1990b) proposed the "Homogeneous Bottleneck Model"(HBM) which is the best model up-to now to explain the energy redistribution processes in

MALDI. HBM suggests that there is an obstacle in the energy transfer from the matrix material (host) towards the embedded large biomolecules (guest). This obstacle is caused by mismatch between the guest-host interaction frequency and the internal vibrational frequencies of the guest molecules. Vertes et al. divided the deposited photon energy by the following way:

$$\rho_e=(1-x)H+L+xG+B \qquad \text{(Eq.2.30)}$$

where ρ_e is the energy density, H, L, G and B denote the energy density content of the host, the lattice, and the guest and energy density used for bond breaking, respectively. x is the volume fraction of the guest molecules. Then they used the kinetic equations, where the energy exchange terms are proportional to the energy differences, to follow the energy redistribution processes. Fig.2.4 shows the time development of host (H) and guest (G) internal temperatures.

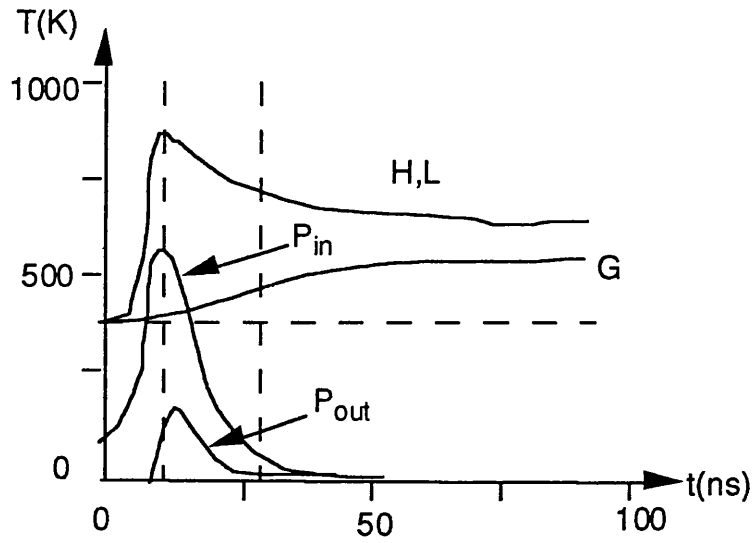

Fig.2.4 The time dependence of host (H), guest (G) and lattice (L) internal temperatues. P_{in} and P_{out} are the laser power input and output carried by sublimation per unit matrix area, respectively. The matrix is nicotinic acid. Guest is a protein with a molecular weight of 10^5 and a volume fraction of 10^{-4} (from Vertes et al,1990.).

According to this model, when a laser input energy into a MALDI sample, it heats up the host(matrix) quickly. The lattice temperature is proved to be identical with the host

temperature. The power output (P_{out}) does not follow the input since some of energy is used by phase transition for sublimation. The guest temperature rises slowly. Near the maximum desorption rate the guest molecules are still close to their initial temperature. This may be the main reason why large biomolecules can exist intact in the MALDI plume. A general form for liberating internally cold molecules from a strongly absorbing matrix can be expressed by the equation 2.31:

$$\tau(T_L=T_{subl}) << \tau\ (T_G \sim T_H) \qquad \text{(Eq.2.31)}$$

where $\tau(T_L=T_{subl})$ is the time required by the lattice temperature(T_L) to reach sublimation temperature(T_{subl}), and $\tau\ (T_G \sim T_H)$ is the approximate time required to reach the equality of T_G and T_H, the guest and host temperatures. In this model, there are two competing energy transition rates. One of them is the energy transition from the matrix to the guest molecules, another is from the matrix to the lattice which results in the desorption by sublimation. Due to the bottleneck effect the energy transfer from the matrix to the guests always lags behind that from the matrix to the lattice if the matrix has a low heat of sublimation, extremely large concentration compared to the guests and short irradiance input time compared to the sublimation induction period. When a sufficiently high rate of sublimation is reached, the guest molecules will desorb internally cold and will not fragment.

2.9 Velocity distribution and Hydrodynamic velocity

When atoms or molecules are desorbed from the solid state to the gas phase, they are moving with characteristic velocity distributions. A common velocity distribution of atoms or molecules liberated from a sample surface can be expressed by the Maxwell-Boltzmann velocity distribution. In the laser time-of-flight mass spectrometry, the duration of material emission is much shorter than the time-of-flight to the secondary technique, e.g. postionisation laser firing. Therefore the MB distribution is derived by the following equation(Eq.2.32)

$$\frac{dn}{n} \propto \left(\frac{m}{2\pi kT}\right)^{3/2} \cdot \exp\left(\frac{-md^2}{2kTt^2}\right) \cdot t^{-i} \qquad \text{(Eq.2.32)}$$

where T, k and m are the characteristic temperature, Boltzmann's constant and the mass

of atoms or molecules, respectively. d is the distance between the sample and the laser beam(for ionisation). The value of i depends on the experimental system and is usually taken as 4 in the time-of-flight system(Kelly and Dreyfus, 1988). By differentiating Eq.2.32 with respect to time, the characteristic temperature can be derived as:

$$T = \frac{mV_m^2}{ik} \qquad \text{(Eq.2.33)}$$

where V_m is the most probable velocity. Therefore the energy of the particles at the peak of the distribution is given by the equation 2.34.

$$E = \frac{mv_m^2}{2} = \frac{ikT}{2} \qquad \text{(Eq.2.34)}$$

However, in these discussions, we have assumed that there were no interaction between the particles in the emerging plume. In fact many cases show that there are lots of collisions in a highly dense plume which cause the energy redistribution in the plume. During the collisions there is a strong tendency for the direction of the velocities of two particles to lie closer to the centre of mass velocity than they were without collisions (or negligible collisions). The resulting velocity distribution is that of a Maxwell-Boltzmann velocity distribution, superimposed on the centre of mass velocity. Peugnet (Peugnet, 1977) proposed the Hydrodynamic velocity model (Eq.2.35) for fitting the velocity distribution measured in experiments.

$$\frac{dn}{n} \propto \left(\frac{m}{2\pi kT}\right)^{3/2} \cdot \exp\left(\frac{-m}{2kT}(v-u)\right) \cdot t^{-i} \qquad \text{(Eq.2.35)}$$

where v=d/t and u is the hydrodynamic velocity (a constant) which represents the centre of mass motion. It can be found that the temperature (calculated from Eq.2.33) will increase when the hydrodynamic velocity (positive) is considered.

2.10 Ion formation in MALDI

Thermal ion formation is not likely in the case of production of molecular ions in MALDI since the required temperatures would certainly destroy these molecules. Photo-processes are very inefficient for IR radiation but are worthy of some interest in UV-LD.

Indeed, two photons of the most often used frequency-quadrupled Nd:YAG laser provide enough energy to ionise many organic molecules. However it is clear from postionisation experiments that the degree of ionisation in the plume is very low, especially for the large biological molecules (MW>1000 Da).

Most MALDI experiments are performed on peptides and proteins. These compounds are amphoteric in character and readily associate in solution. In principle the associates can survive sample preparation and desorb as a single particles. Ion formation mechanism can be classified according to the ion formation site and according to the process involved. Some molecules are built up in the form of organic salts. If the sample has an absorption band of an appropriate energy, electronic excitation can occur. For thin layers of nonabsorbing molecules, the substrate absorbs most of the energy , transferring it back to the molecules as thermal energy. The desorption occurs if the translational energy made available is sufficient to overcome the lattice binding energies. Cation-anion bond breaking (C^+A^-) is the key step and results in C^+ and A^- being liberated as charged particles, making this a very efficient ion formation process. Inspecting MALDI spectra indicates that the most favoured channel of molecular ion formation in MALDI is cationisation which included protonisation and alkalinisation. Kammer (Kammer, 1987.) suggested that the protonated ions are already formed on the surface or even in the solid phase by proton hopping. However, other people (Wang, 1993. Karas et al. 1990) suggested that most of protonisation and alkalinisation occur in the gas phase by molecule-ion reactions(van der Peyl et al., 1982). The possible mechanism is that the original ions, which usually are from small molecules and their fragments or alkali ions, are formed in the solid phase or on the surface. The large biomolecular ions are formed by proton exchange between these photochemically activated matrix and biomolecules or by alkalinisation.

A simple rate constant expression (Gioumousis and Stevenson , 1958) can be derived for the case of cationisation of a very large molecule by a relatively light ion (M2<<M1):

$$k = 2\pi e\left(\frac{\alpha_{pol}}{M_2}\right)^{1/2} \qquad \text{(Eq.2.36)}$$

where α_{pol} and M_2 are the polarizability of the large molecule and the mass of the light

ion, respectively. Evaluation of Eq.2.36 indicates that protonisation(H^+) is six times faster than the reaction with K^+ if the concentration are similar.

There are other types of ions abundant in the high mass region. Adduct ions are formed by the combination of the high-mass molecules with fragment ions of the matrix. from the gas phase ion-molecule reaction process. Multiply charged species in MALDI spectra are formed due to distance independent charge locations in a large molecule.

2.11 Dissociation energy and predissociation

The energy required to separate the stable molecule AB initially in the v=0 level into two unexcited atoms A and B, that is:

$$AB \longrightarrow A + B$$

is called as the dissociation energy (D). The value of the dissociation energy can be found by thermochemical methods. However, its value differs very slightly from the corresponding one (D) obtained from spectroscopic data since the latter is calculated for 298 K while the former is for 0 K. Fig.2.5 shows the potential energy curve and the representation of thermal dissociation (D_e) and spectroscopic dissociation energy (D). Therefore the relationship between the two dissociation energies can be expressed by equation 2.37.

$$D_e = D + G(0) \qquad \text{(Eq.2.37)}$$

where G(0) is the value of the vibrational energy in the v=0 level, and can be calculated by $G(0)=E_{v=0}/hc$ in the unit of cm^{-1}. Infrared spectroscopy can be used to determine D and D_e for the ground state of the molecule, while electronic spectra can be used to determine D and D_e not only for the ground state but also for some of the excited states as well. In order to determine the dissociation energy from spectroscopic data it is necessary either (1) to determine the lowest absorption frequency which will produce dissociation of the molecule, and to identify the electronic state of the dissociation products, or (2) to determine the energy values of as many vibrational levels for the electronic state whose dissociation energy is required.

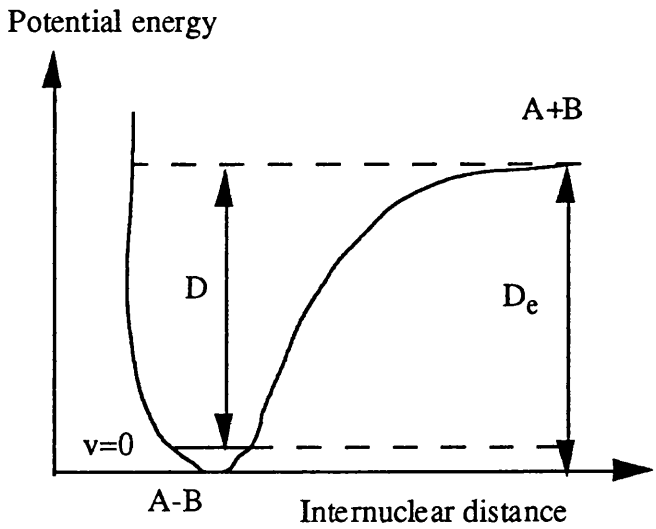

Fig.2.5 Potential energy curve of a diatomic molecule. D is the spectroscopic dissociation energy and D_e is the thermochemical dissociation energy.

Predissociation is the spontaneous dissociation of a molecule through a radiationless transition from a stable electronic excited state to an unstable one having the same energy. Fig.2.6 illustrates the Morse curves of predissociation. The stable ground state (A) is excited to the state (B). The state (B) is stable since it has a minimum in the curve. There is an unstable continuum excited state (C) which cross the state (B) at the intersection X. If a transition takes place below the intersection level, a normal vibrational electronic spectrum is obtained complete with rotational fine structure. If the transition takes place above X, there is a possibility that the molecule will cross over to the unstable state (C) and lead to predissociation. Usually the rotational structure of the molecule will be destroyed, and the vibrational structure is not affected when predissociation occurs since the crossing rate between two excited curves is faster than those of rotation of the molecules, but slower than vibrational rate of the molecule.

2.12 Fragmentation of molecules and ions

For the formation of fragment ions with single-photon ionisation, the primary process is usually detachment of the electron, and then, in the presence of sufficiently high vibrational or electronic excitation of the ions, cascade fragmentation of the ions occurs.

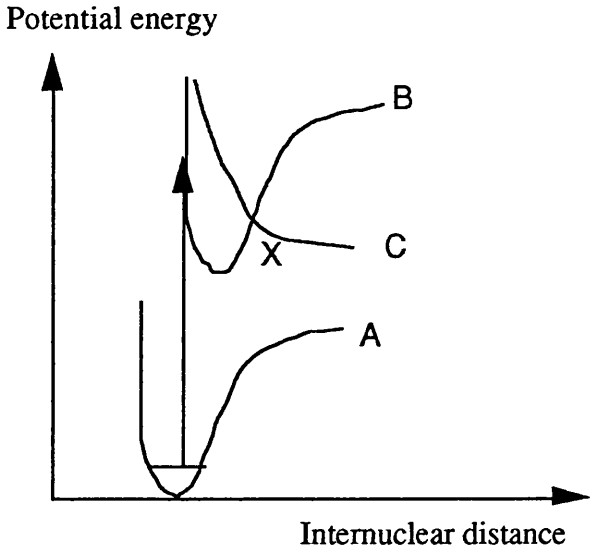

Fig.2.6 Potential energy curves involved in the phenomenon of predissociation. Predissociation occurs during transition into a stable upper state intersected by a continuum state.

In contrast to single-photon ionisation, the method of the two-step or multiphoton ionisation permits an investigation of the fragment ion formation from high-lying vibrational levels of the intermediate electronic state. In addition, absorption of two or more photons by the molecules can lead to the excitation of other states of the ions, which can also change the picture of fragmentation patterns.

The yield of fragment ions by the multiphoton ionisation are much larger compared with single-photon ionisation at the same energy. This is because the energy of the multi-UV photons exceeds not only the ionisation potential of a organic molecule (usually 8-9 eV), but also the appearance potential of the fragment ions. For example, absorption of a photon with energy 3.7 eV by benzaldehyde molecule corresponds to an electronic transition of the type n --> π^*, i.e. a transition of an electron from a nonbonding atomic orbital of oxygen into an antibonding molecular π^* orbital. The restructuring of the electronic configuration occurs primarily in the aldehyde group CHO. Since the antibonding orbital of the molecule is occupied, the parameters of the bonds in the aldehyde group, especially the C=O bond, change considerably. This leads to the fact that in an electronic transition, vibrations are excited primarily in the region of the aldehyde group, After absorption of light with 3.7 eV, the vibrational degrees of freedom of the molecule, after conversion into the triplet state, contain a large amount of

vibrational energy. After absorption of the second photon, ionisation occurs from this molecular state, localised in the aldehyde group, which increases the probability of formation of the fragmentation ion with detachment of the aldehyde hydrogen atom.

Another factor that leads to a large yield of fragment ions in two-step or multi-photon ionisation is that in the case of single-photon ionisation, the nuclear configuration of the neutral molecule differ little from one another. Due to the fact that in the multiphoton ionisation, the intermediate electronic state has a considerably changed nuclear configuration in the region of the chromophore, which can lead to a displacement of the peak in the vibrational energy distribution function of the ions formed. This must likewise facilitate an increase in the fraction of fragment ions, and correspondingly drop in the yield of parent molecular ions.

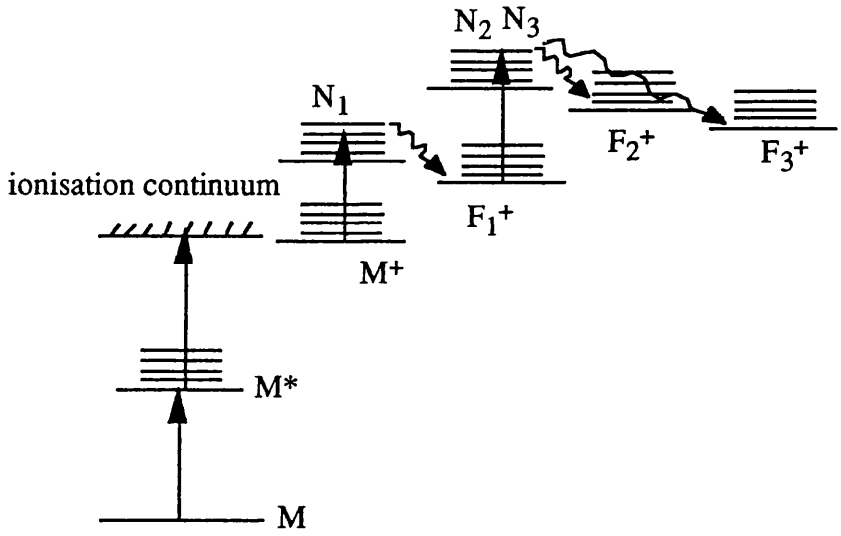

Fig.2.7 The diagram of ionisation of a molecule and fragmentation of the molecular ion and its fragment ions. M, N and F represent the parent molecule, the excited ions and fragment, respectively. Details are shown in the text.

By increasing the laser intensity, photon absorption within the molecular ions will occur. When the energy absorbed by the molecular ion exceeds the lowest ion dissociation threshold, fragments are produced. These fragments can absorb further photons and will continue to induce fragmentation from the fragments to its smaller fragments(see Fig.2.7). The fragmentation of ions can also take place through parallel decay channels.

This process is called a "ladder switching" model which will be discussed in chapter 6. of this thesis.

Chapter 3

Experimental Set-up

3.0 Introduction

The experimental apparatus described in this thesis consists of: a reflectron time-of-flight mass spectrometer, an ablation and ionisation (or photofragmentation) laser system, and a data acquisition and analysis system. In order to explain the details of the instrumentation, each system can be subdivided into several sub-systems.

The reflectron time-of-flight mass spectrometer will be described by its vacuum system, ion optics, reflectron, and ion detector system. Meanwhile, the laser system consists of a nitrogen laser, a Nd:YAG laser, a dye laser, a pulse generation and delay system. Finally a digital storage oscilloscope linked to a PC computer in the data acquisition and analysis system will be presented in detail in this chapter.

3.1 The reflectron time-of-flight mass spectrometer

The principle of the mass separation by time-of-flight mass spectrometers is the dependence of the flight time on the masses of ions starting at the same time and same position within an electrostatic field. The main advantages of such a system in comparison with a magnetic mass spectrometer are: 1), all the ions from the same source can be detected at the same time; 2), in principle, no upper mass limit exists; 3), the construction is rather straight forward and inexpensive. In the simplest time-of-flight mass spectrometers (the Wiley-Mclaren pulsed two electrode ion source, linear drift region)(Wiley and McLaren, 1955) the time-of-flight(TOF) of these ions is proportional to the square root of their m/z ratio:

$$t = \left(\frac{L^2}{2Ve}\right)^{1/2} \cdot \left(\frac{m}{z}\right)^{1/2} \qquad \text{(Eq.3.1.1)}$$

where L is the drift distance of ions, V is a potential difference of a constant acceleration electric field, e is the unit electron charge. m and z are the mass and charge of the ion, respectively. However, a big problem of this linear TOF instrument is the large initial energy spread of the ions produced in the extraction zone, which considerably limits the

theoretically possible mass resolution. The normal mass resolution limit of such instruments is around 200-300. An important advance in the field of time-of-flight mass spectrometers is the reflectron TOF mass spectrometer (Mamyrin, 1966. Karataev, et al. 1971). It increases the ion drift length by two times, furthermore, it also compensates the energy spread of the ions produced during the ion generation. Hence, the mass resolution has been improved to over 1000, some reflectron TOF instruments have the mass resolution up to 35,000 (Bergmenn, et al., 1990).

3.1.1 Vacuum system

The TOF instrument designed at Glasgow University is a typical reflectron time-of-flight mass spectrometer (Towrie et. al, 1990). Figures 3.1a and 3.1b show the system in detail. The entire system is constructed of stainless steel. The TOF instrument consists of a large spherical sample chamber(30 cm in diameter) and a 1.5 m ion drift tube. The spherical sample chamber has as many ports as possible facing the centre of the chamber where the sample stub is held. The sample chamber is pumped by an oil diffusion pump (Edwards Diffstak Mk2 model 160) with a pumping speed of 700 litres per second. The pumping oil used is Santovac 5 with pumping limit $2x10^{-10}$ mbar(Monsanto Company, St Louis, Missouri, USA). The diffusion pump has a liquid nitrogen cold trap, and could be used to reach higher vacuum if needed, but was not used in the experiments described in this thesis. The ion drift tube is also pumped by a titanium sublimation pump (Edwards ETP6), having a base pumping speed of over 200 litres per second. The both pumps keep the system pressure of 10^{-9} torr.

3.1.2 Sample stub and ion optics

Fig.3.2 shows the sample stub and sample holder which were made of stainless steel. The sample stub is held in identical spring loader forks on the transfer probe (Kratos WG-707) and on a sample XYZΘ manipulator (Kratos WG-194) which can precisely control the 3-D movement and rotation of the stub. The sample fork is electrically insulated from the manipulator to allow the use of the stub as the acceleration electrode. The sample usually is in a liquid form and carefully placed on to the surface of a sample stub and dried(detailed description in chapter 4). The sample stub can be inserted and withdrawn from the chamber using a rapid transfer probe. This arrangement allows the fast sample exchanges without disruption of the main chamber vacuum(the system returned to the operating vacuum in about 5 minutes).

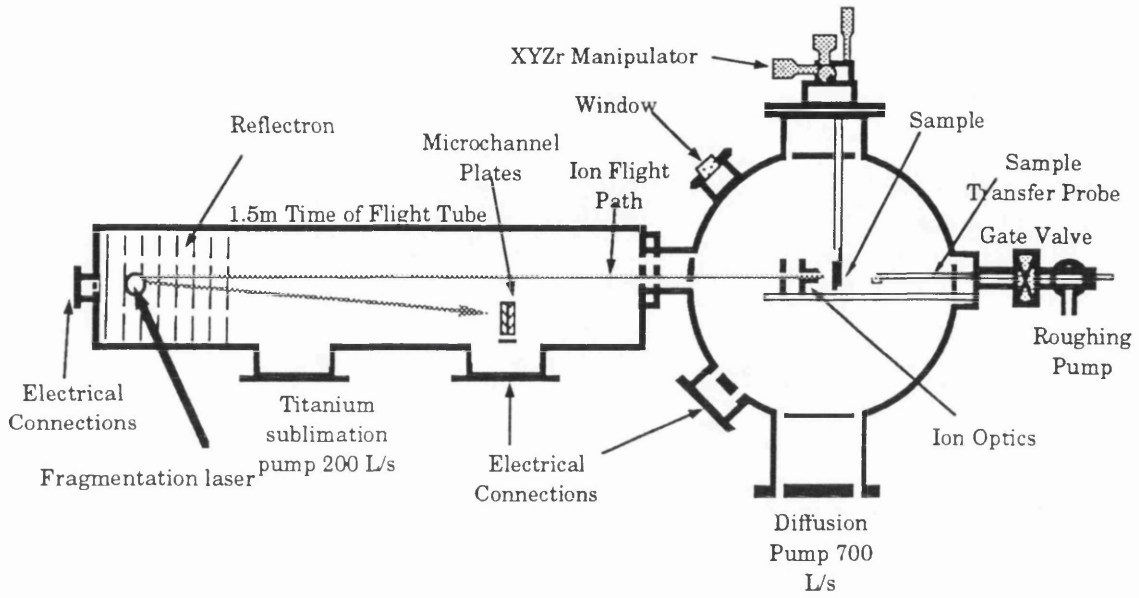

Fig.3.1a. Elevation of the analysis chamber and TRTOF mass spectrometer

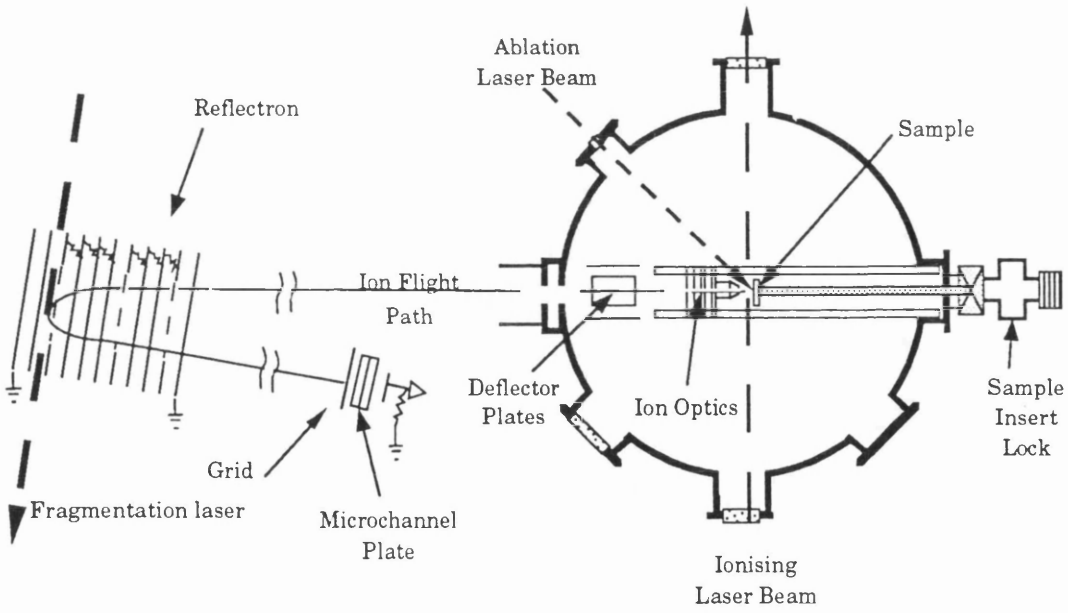

Fig. 3.1b. Plan view of the analysis chamber and TRTOF mass spectrometer

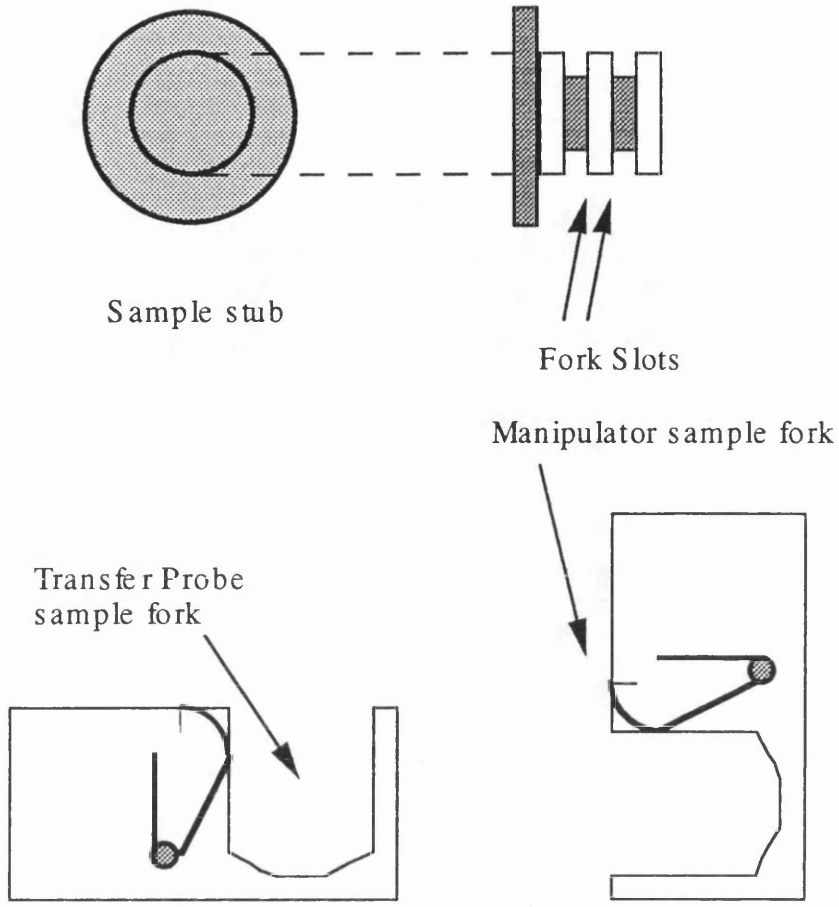

Fig.3.2 Diagrams of the sample stub and the sample forks. The forks are translated perpendicular to each other and each accomodated in a slot in the stub.

The ions produced on the sample surface or above the surface are attracted by ion optics and transmitted efficiently through to the detector, although acceptance volume of ions by ion optics is small, ~1mm^3 (measured by Land, 1990). A schematic arrangement of the sample stub, ion optics, the distribution of electrostatic potentials and ion trajectories are illustrated in Fig.3.3. It shows clearly that a diverging plume of ions generated by a laser or ion gun is attracted by the ion optics and converted to form a parallel ion beam towards the reflectron. Well-designed ion optics with suitable voltages will improve the ion transmission greatly. Behind the ion optics are a set of X and Y deflecting plates with applied voltages in the range of ±50V. The X deflecting plates can be used to deflect the

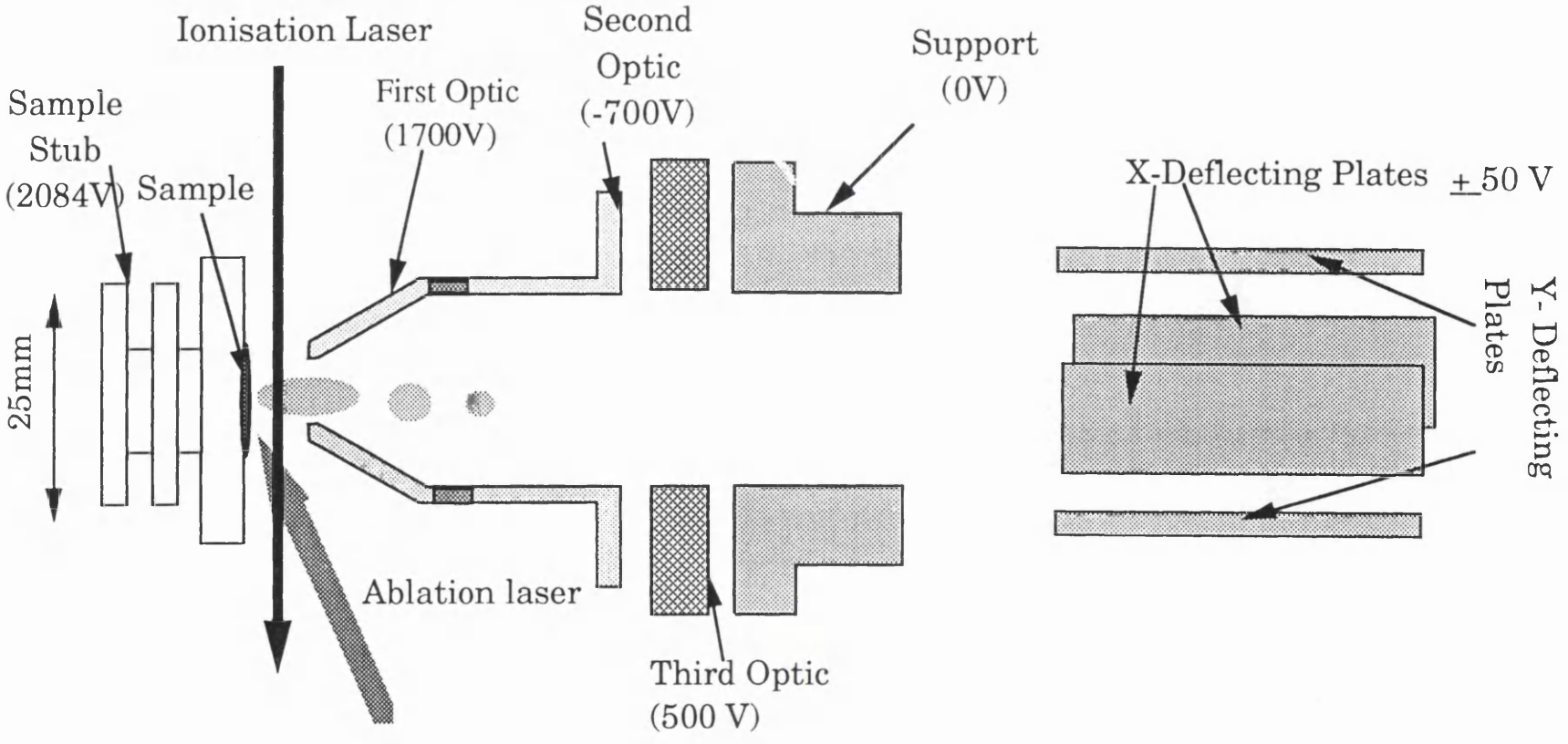

Fig.3.3 A section through the conical ion optics, showing the typically operating voltages.

ion beam in horizontal plane, while the Y deflecting plates deflect ions in the vertical plane. This is important to get optimum transmission of ions or to select the desired ions(detail description will be presented in chapter 5).

When the ions travel into the field-free drift region, they are guided by a fine wire with a small negative voltage (-15 V) strung along the flight path. This increases the transmission efficiency of the TOF mass spectrometer (See reference Oakey and MacFarlane, 1967).

3.1.3 Reflectron

All ions guided by the fine wire move into a commercial 'Reflectron' electrostatic mirror (Cambridge Mass Spectrometers UK). The reflectron consists of 20 rings (138 mm o.d. 90 mm i.d. separated by 7.08 mm). All the rings are connected by precision resistors to generate a smoothly varying static electric field. The equation 3.1.1 describes the simple relationship between the time-of-flight and m/z ratio, which assumes that all the ions have exactly the same energy. However in practical instruments that is not the case. The slightly different kinetic energies cause by the time spread in ionisation and acceleration ranges due to the following reasons :

a) spatial size of the laser beams, such that ions are produced at different positions and hence acquire different energies in the extraction field.

b) time spread due to laser pulse width, so that ions are produced at different time.

c) different initial velocities of atoms and molecules before ionisation (thermal velocity distribution) also causes a reduction of mass resolution in TOF instruments.

In practice, since L and V in equation(3.1.1) are rarely known sufficiently accurate, a mass spectrometer has to be calibrated by a series known element masses, and the following equation can be used to determine unknown masses:

$$m = kt^2 + c \qquad \text{(Eq.3.1.2)}$$

where m and t are the mass and time-of-flight of the ion, respectively. This equation can

be obtained by fitting a linear equation of the known masses(m) with respect to t^2 to get k and c(constants). Hence the exact mass can be received by measuring its time and calculating using equation(3.1.2).

The mass resolution is defined as $m/\Delta m$, where Δm is the full-width at half maximum (FWHM). In a time-of-flight mass spectrometer, this resolution can be related to the temporal resolution:

$$\frac{m}{\Delta m} = \frac{t}{2\Delta t} \qquad \text{(Eq.3.1.3)}$$

There are three grids in the most commonly used reflectron. The ions penetrate the first grid, whose potential is the same as that of the flight tube (generally ground potential). The second grid, located at about 20% of the depth of the reflectron, is applied at about two thirds of the potential of the ion acceleration voltage. In this short distance the ions lose about two thirds of their kinetic energy. The voltage on the third grid is adjusted slightly above the accelerating voltage to provide different penetration depths over the longer stage.

To understand the operation of the reflectron, let us take a look at a space focus of an ion source as a starting point for ions of one distinct mass with different initial kinetic energies. The ions with higher kinetic energy penetrate deeper into a reflectron and hence experience a longer flight time than the ions with low energy. If the electrostatic fields in the reflectron are well-adjusted, it is possible to arrange all the ions with different kinetic energies arriving at the detector at the same time. Now the question is how to choose the appropriate potentials of a reflectron. Fig.3.4 shows the basic scheme of a reflectron TOF mass spectrometer with geometric dimension and electric potentials. Let us assume k_0 is initial energy, q and m_o are the ion charge and mass, respectively. δ is energy spread. t_d, t_{12}, and t_{23} are the time-of-flight of the ion in field-free drift, retarding and reflecting regions, respectively. U_0, U_{12} and U_{23} are the potentials on the sample stub, the retarding plate and the reflecting plate, respectively. It can be deduced to the following equations:

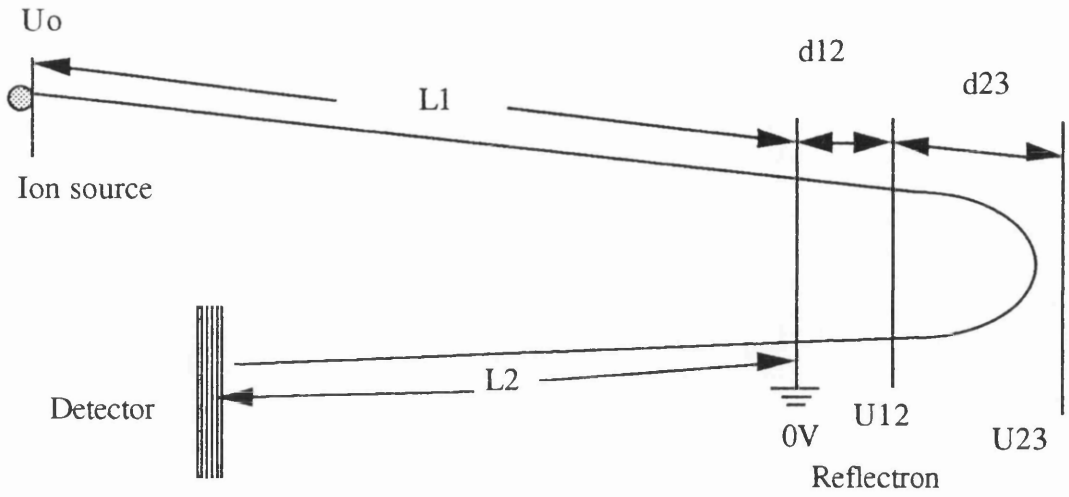

Fig.3.4 Basic scheme of a reflectron time-of-flight mass spectrometer with geometric dimension.

$$t_d = (L_1 + L_2) \cdot \left(\frac{m_0}{2k_0}\right)^{1/2} \div (1+\delta)^{1/2} \qquad \text{(Eq.3.2)}$$

$$t_{12} = \frac{4d_{12}U_0}{U_{12}} \left(\frac{m_0}{2k_0}\right)^{1/2} \left[(1+\delta)^{1/2} - \left(1+\delta - \frac{U_{12}}{U_0}\right)^{1/2} \right] \qquad \text{(Eq.3.3)}$$

$$t_{23} = \frac{4d_{23}U_0}{U_{23}} \left(\frac{m_0}{2k_0}\right)^{1/2} \left(1+\delta - \frac{U_{12}}{U_0}\right)^{1/2} \qquad \text{(Eq.3.4)}$$

$$\text{Total time-of-flight} = t_d + t_{12} + t_{23} \qquad \text{(Eq.3.5)}$$

To obtain high mass resolution, both the first and second derivatives of the time-of-flight have to be zero with respect to energy spread (δ), i.e.

$$\frac{\partial t}{\partial \delta} = 0$$

$$\frac{\partial^2 t}{\partial \delta^2} = 0$$

From these conditions, the relationships between the lengths of retarding and reflecting regions and the potentials on them can be deduced. The final results show in the following equations:

$$d_{12} = 1/2(L_1 + L_2)\left(\frac{3U_{12}}{2U_0} - 1\right) \qquad \text{(Eq.3.6)}$$

$$d_{23} = \frac{(L_1 + L_2)}{2}\left(\frac{3U_{12}}{2U_0} - \frac{U_{23}}{U_{12}}\left(1 - \left(1 - \frac{U_{12}}{U_0}\right)^{3/2}\right)\right) \qquad \text{(Eq.3.7)}$$

Usually, d_{12} and d_{23} are fixed when a reflectron is made, and so the optimised potentials of retarding and reflecting fields can be calculated through the Eq.(3.6) and (3.7).

Another important feature of the reflectron is that all the ions on entering the reflectron, reaching zero velocity in the vicinity of the turn-around point of the ion trajectories. The slowly moving ion packets spend about 3 to 4 μs in the turn-around region where they can be easily selected and fragmented by a laser beam. This characteristic of the reflectron led to a new tandem TOF mass spectrometer "Tandem Reflectron Time-of-Flight Mass Spectrometer" (TRTOF) being introduced. This will be described in detail in Chapter 5.

The reflectron can also act as a ion filter to discard the ions with kinetic energies greater than the voltage on the reflecting plates. This is especially useful when the ions from ablation processes and postionisation processes require to be distinguished.

3.1.4 Detector

After the ions exit from the reflectron, they move into the detector. The ion detector used in these experiments is a dual microchannel plates with an aperture of 2.5 cm in diameter (TOF-2003 Galileo Electro-optics Corp. Strubridge, MA, USA).

Fig.3.5 shows the biasing of the detector. The grid in front of the detector, with a potential just below those of the signal ions, is used to prevent any secondary ions, formed by the scattering of the signal ions on the plates and grids of the reflectron, from

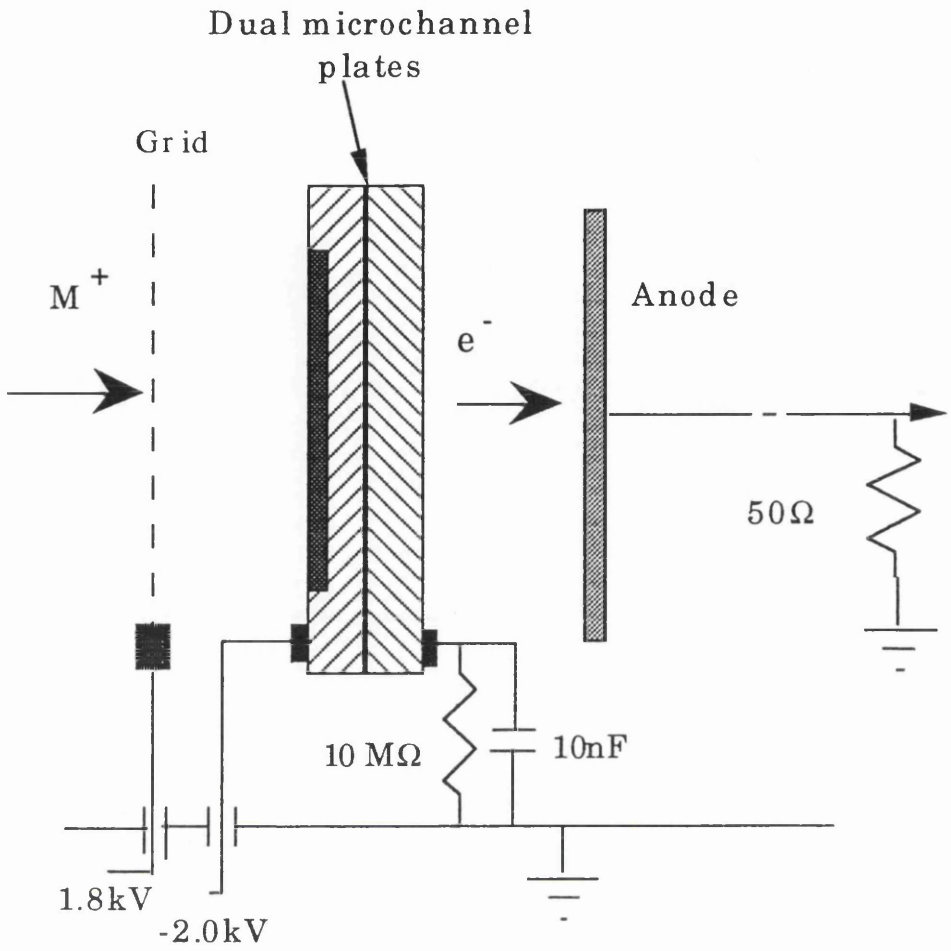

Fig.3.5 Biasing of the dual microchannel detector. A grid in front of the detector was used to prevent secondary ions from being transmitted to the detector.

being detected.

The voltages applied to the detector are usually adjusted such that the pulse output from the detector does not exceed 10 V. The dependence of the detector signal on the applied voltage was determined by the following equation.

$$S_1 = S_2 \cdot 10^{k(V_1 - V_2)} \qquad \text{(Eq.3.8)}$$

where S_1 and S_2 are the ion signals when the detector volts are V_1 and V_2, respectively. k is a constant for the detector ($k=5.58\times10^{-3}$ in our experimental conditions).

3.2 Laser system

A nitrogen laser and a Nd:YAG pumped dye laser were used in the MALDI experiments. The nitrogen laser with pulse energy of 100 μJ acted as a desorption/ionisation laser. The laser beam was incident at 45° on the sample and was focused by 25 cm quartz lens to give a spot size of approximately 80μm by 40 μm. Meanwhile a tunable dye laser was used as a postionisation laser in the experiment of MALDI in probing neutral hydrogen in the ablation plume. The ionising laser is focused by a 30 cm quartz lens and introduced into the sample chamber parallel and as close to the sample stub as possible (0.4 mm in this work) to maximise the overlap with the ablation plume. Both the lasers operate at repetition rates of 10 Hz and with pulse duration of about 5 ns. The tunable laser pulse energy depends on the dyes used, but normally is at 100 μJ around the 243 nm region. The time delay between the ablation and postionisation lasers was generated using a custom-built delay generator accurate to 10 ns. The detail arrangement of this work is shown in Fig.3.6.

In TRTOF experiments, the parent ions were generated by the nitrogen laser with the same arrangement as in the MALDI experiments, while all the harmonics (1064, 532, 355, 266 nm) of a Nd:YAG laser were used for photofragmentation of the molecular ions, 355 and 266 nm were the preferred. The delay time between the two lasers was controlled by the same delay box. The main difference between these two experiments was that the fragmentation laser beam in TRTOF was at the end of the reflectron where the photofragmentation of the selected molecular ions was taking place(see Fig.3.7), while the postionisation of neutrals took place in front of the sample stub.

The nitrogen laser, the Nd:YAG laser, and the dye laser will be discussed in the following sections in greater detail.

3.2.1 Nitrogen Laser

The nitrogen laser used in this work is a compact, high peak power device, producing ultraviolet light at 337.1 nm. Table(3.2.1) presents some main characteristics of the nitrogen laser:

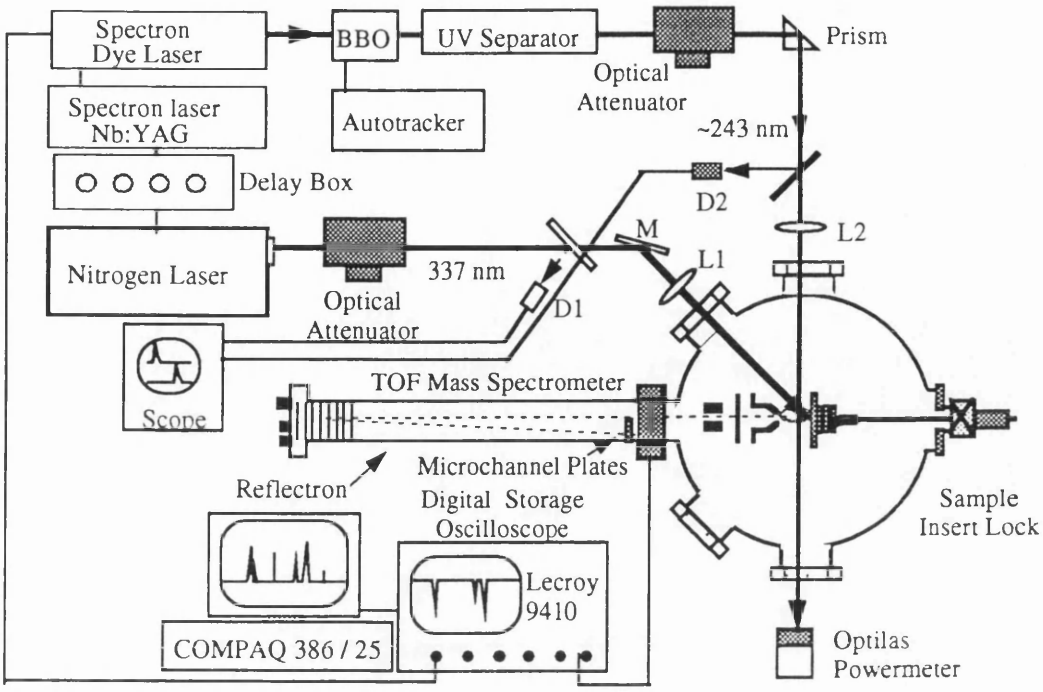

Fig. 3.6 Experimental set-up for the postionisation of the neutrals in MALDI

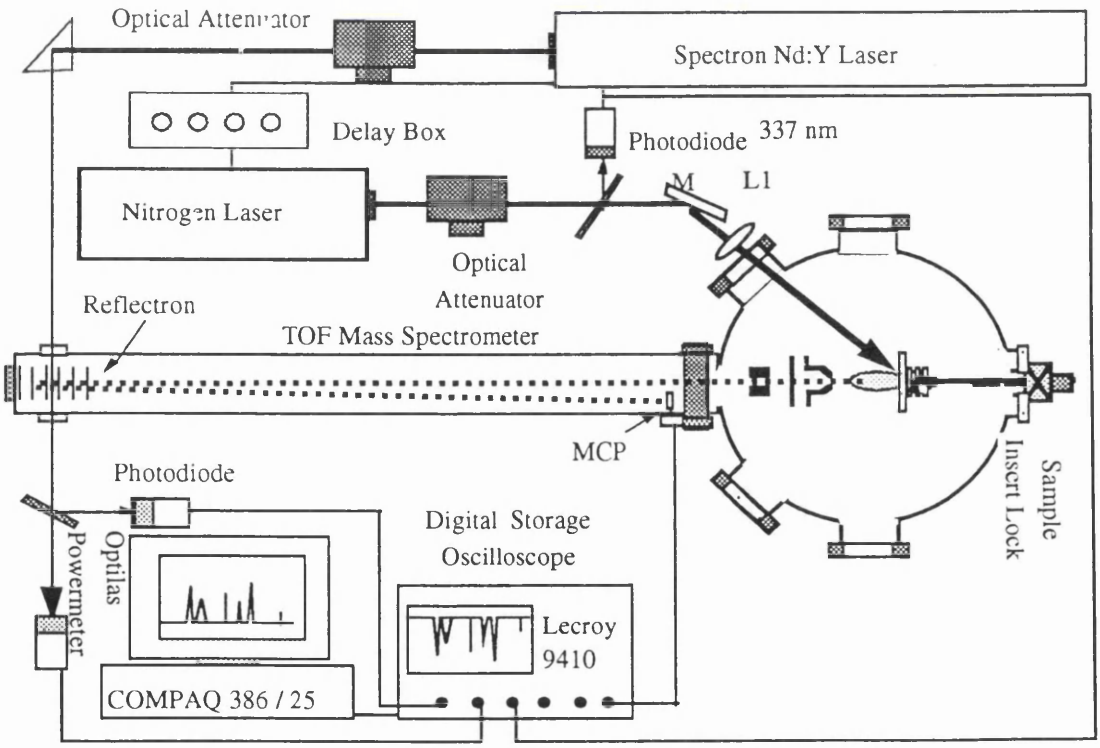

Fig. 3.7 Experimental set-up for laser photodissociation in TRTOF

The LN300 Nitrogen Laser System Specifications

Item	Description
Spectral Output (nm)	337
Spectral Bandwidth (nm)	0.1
Pulsewidth (ns)	5
Energy/Pulse (uJ)	250
Stability(@10Hz)	3%
Peak Power (kW)	50
Repetition (Max.)(Hz)	40
Maximum Average Power (mW)	7
Beam Dimension (hor. x ver.) (mm)	9x4
Beam Divergence (hor. x ver) (mrad)	1.6x0.7
Trigger In	TTL
Trigger Out	TTL

Fig.3.8 shows the nitrogen laser mechanism. The electrons are excited from the ground state ($X^1\Sigma g$) to the excited state ($C^3\Pi u$) by collisional excitation from discharge electrons. Then the high gain population inversion is established between these two upper levels of the nitrogen molecules($C^3\Pi u$ and $B^3\Pi g$). The electrons deexcite from the high excited state ($C^3\Pi u$) to the lower excited state ($B^3\Pi g$) and a laser with wavelength of 337.1 nm is produced.

3.2.2 Nd:YAG Laser

The Nd:YAG laser used in this work is a Spectron SL2Q & SL3A Q-Switched Nd:YAG laser. A schematic arrangement of this laser is shown in Fig.3.9. This laser consists of three main parts. The first part of the laser is the oscillating region in which laser light is generated by flashlamps through the laser rod, two reflecting mirror (100 % reflective of a rear mirror and 17 % of the output etalon) and a pockels cell. The pockels cell is an electron-optical crystal used to achieve a Q-switch. The telescope used in the laser is to optimise the laser beam quality. The second part is the laser amplification region. The low intensity of the laser generated in the oscillator is greatly increased by the laser amplifier which also consists of a laser rod and pumping flashlamps. The fundamental laser wavelength is 1064 nm with an output power of ~800 mJ at the normal operating frequency of 10Hz. The rest of the laser system is used to generate the harmonics of the fundamental wavelengths such as the second harmonics (532 nm), the third (355 nm)

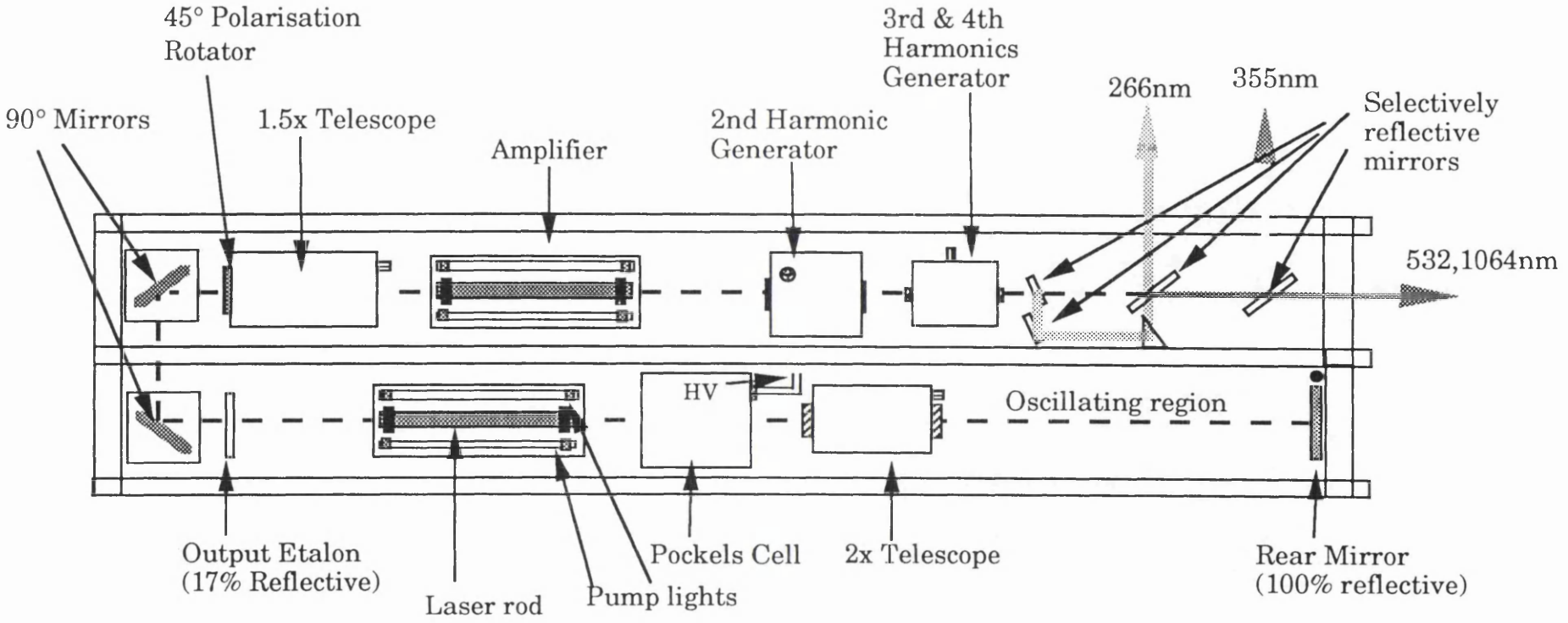

Fig.3.9 Diagram of the layout of the Spectron Nd:YAG laser

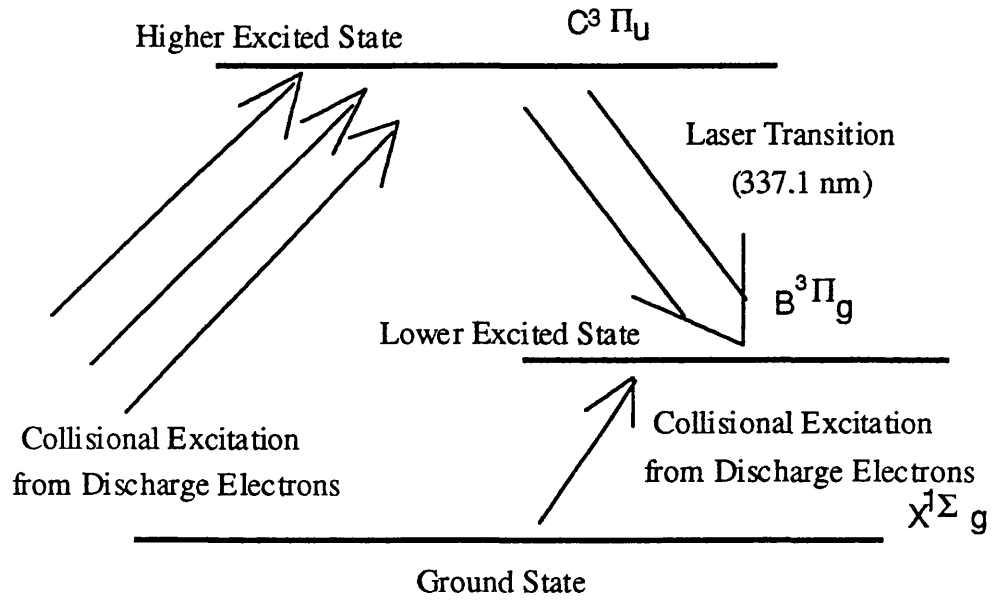

Fig.3.8 The Nitrogen Laser Mechanism

and the fourth (266nm) by incorporation of Potassium di-deuterium phosphate (KD*P) crystals. These crystals are maintained at 55 °C in order to give a good power stability (about 10 %). All the harmonics are available at any one time.

3.2.3 Dye Laser

The tunable dye laser used in this work was the Spectralase 4000 dye laser (Spectron Laser System, Rugby, UK). The dye is pumped through oscillator and amplifier cells. The wavelength of light may be tuned by adjusting optical tuning elements, such as diffraction grating, rear mirror or changing the dye used. Fig.3.10 illustrates the layout of the Spectron dye laser. The dye laser is transversely pumped by the third harmonic(355 nm) of the Nd:YAG laser. The laser can pump dyes from 400 nm to 750 nm. The laser is generated in the oscillator region and amplified in the amplifying region. The wavelength of the output of the dye laser is selected by rotating the rear mirror which is on a sine drive controlled by a manually programmed unit to allows a desired wavelength and a scan speed to be specified. This dye laser has a specified resetability of 0.001 nm and an accuracy of 0.005 nm. Wavelength calibration is usually achieved by employing a monochrometer or the optogalvanic effect in a hollow cathode discharge lamp(Duncan and Devonshire, 1991).

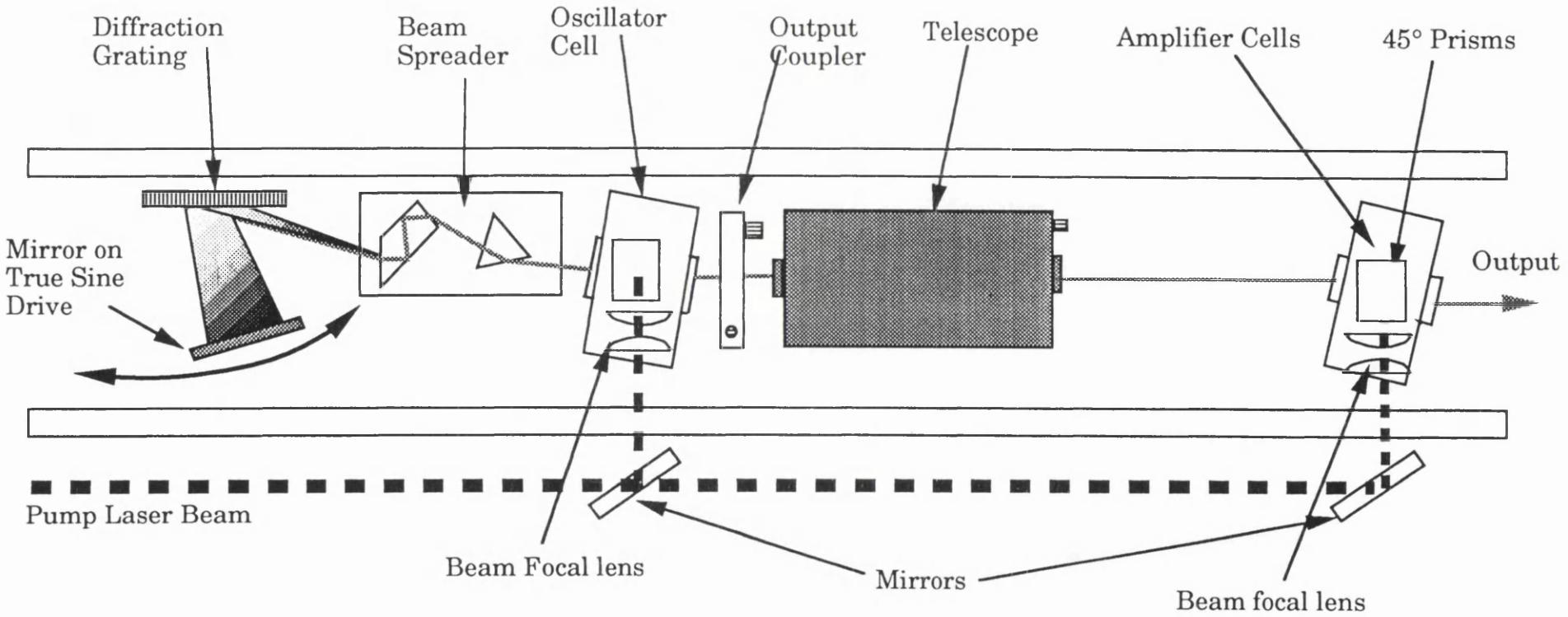

Fig.3.10 Diagram of the layout of the Spectron dye lasers

3.2.4 Laser triggering and delay system

Firing the lasers and controlling a desirable delay were achieved by a Stanford DG535 digital gate and delay generator (SRS, Sunnyvale, USA), and a custom-built delay unit. The timing sequence used with the Spectron Nd:YAG laser and the N_2 laser is shown in Fig.3.11. The start pulse from the Stanford digital generator triggered the delay unit. The unit produces three triggering electric pulses with different timing sequence. The first pulse(B) triggered the nitrogen laser which acted as an ablation laser. The second(C) fired the flashlamps of the Nd:YAG laser. Finally the third pulse (D) fired the Q-switch of the Nd:YAG laser. The timing sequence of the third pulse could be adjusted, so that it gave a desired delay time (0-15μs) between the N_2 laser and the Nd:YAG laser. The longer delay time (over 15 μs) between the two lasers could be achieved by changing both (C) and (D) timing sequence with the delay of 193μs between them. For example, if a delay of 100μs between the nitrogen laser and the Nd:YAG laser is required, this can be done by changing (C) from 182 μs to 282μs, and (D) from 375μs to 475μs. Therefore the delay between the two lasers can be varied from 100μs to 115μs. The delay between the two lasers was measured by an oscilloscope from two fast photodiodes responding to the outputs of the ablation and ionisation (or fragmentation) lasers, respectively.

3.2.5 Autotracker and attenuator

The wavelengths around 243 nm was used in investigation of formation of atomic hydrogen in MALDI by post-ablation ionisation (PAI). So the frequency doubling of the output of the dye laser was required. The Inred Model 5-12 SHG Autotracking system was used to achieve frequency doubling. The basic operational principle of the auto-trackor is that the incoming laser beam is directed through either the compensation block and a doubling crystal(here BBO). The compensation block monitors the ultra-violet power and adjusts the angle of the doubling crystal to ensure that the crystal is constantly at the optimal angle for second harmonic generation as the incident wavelength varies(see Fig.3.12).

The variety of the power of the beam was achieved by a precision attenuator (Newport 935-10 Model). The laser beam passes through a series of quartz plates, and its power decreases by reflection on the plates. The degree of attenuation depends on the angle of

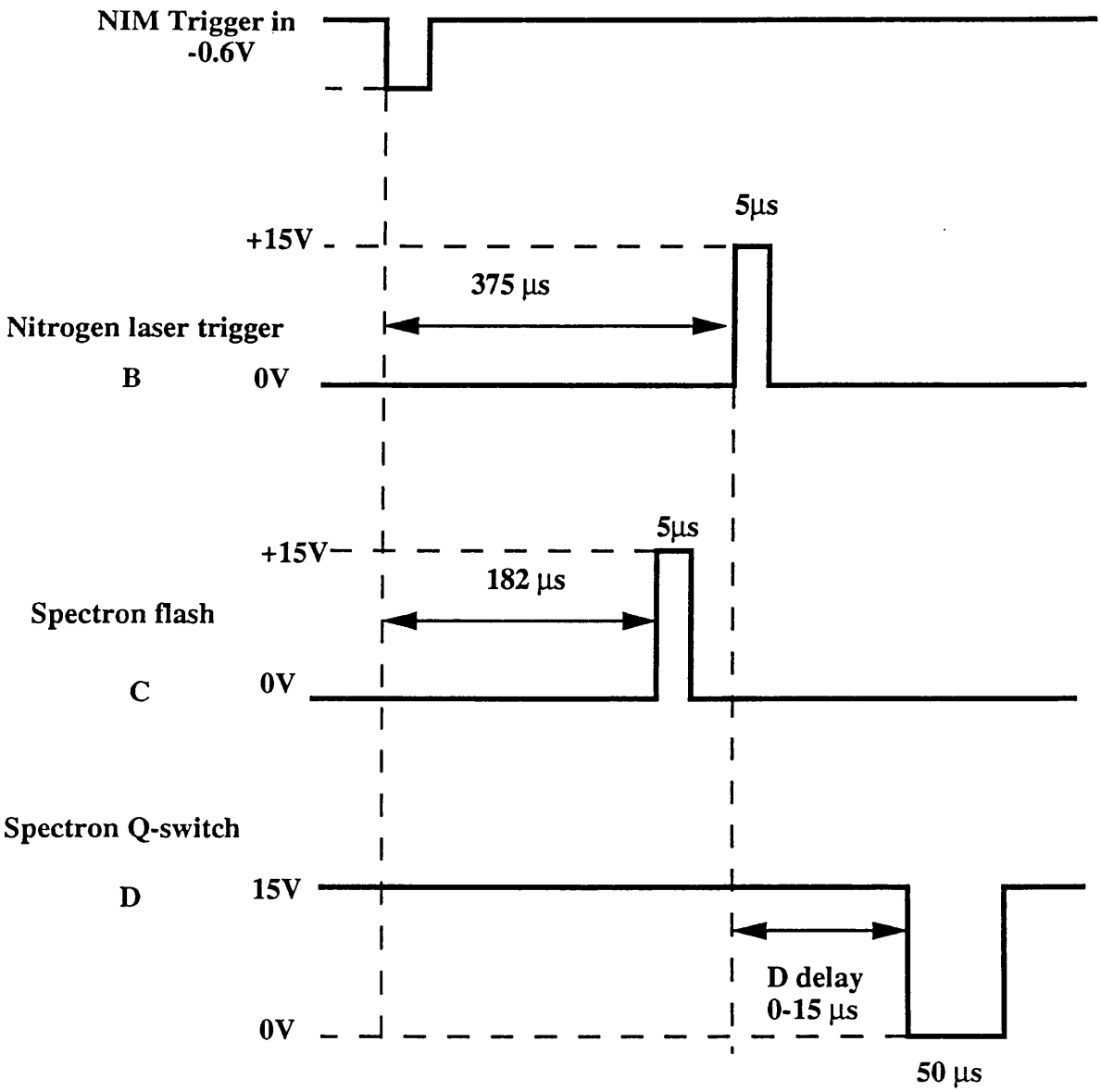

Fig.3.11 Timing sequence of custom pulse generator for both the nitrogen laser and the Spectron Nd:YAG laser. A desirable delay time between the nitrogen laser and the Nd:YAG laser can be adjusted by D-delay.

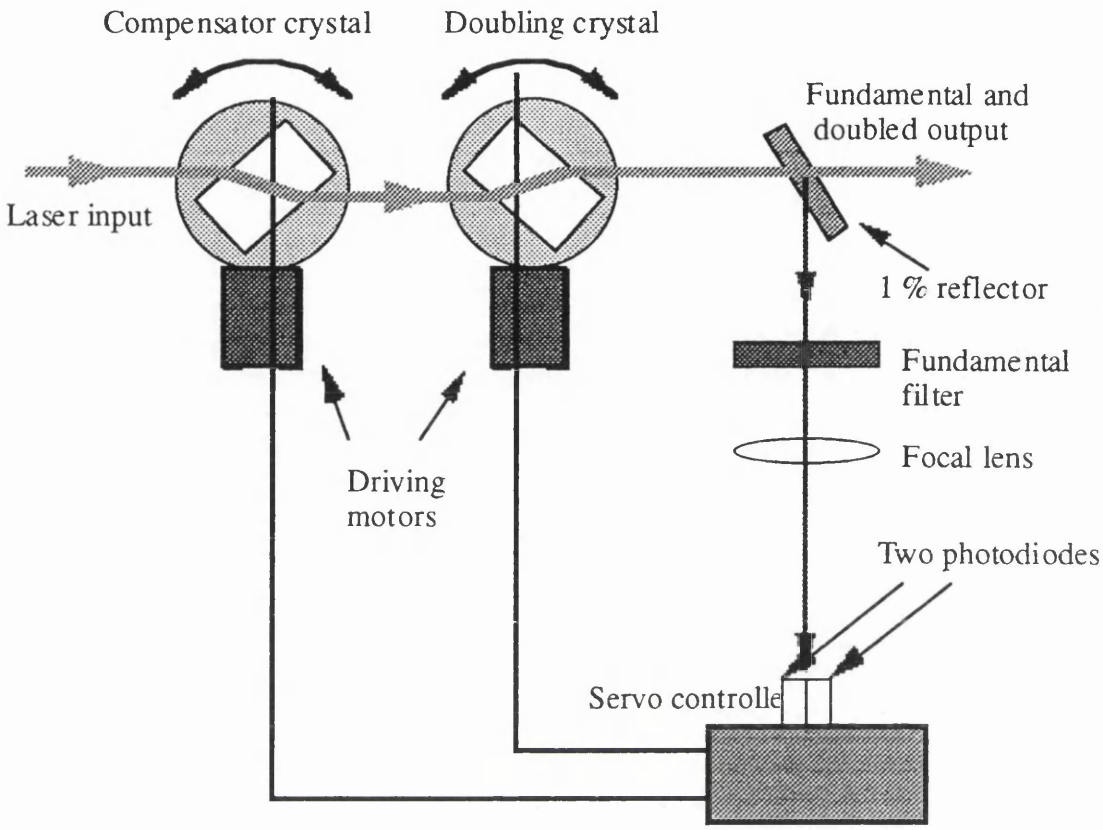

Fig.3.12 Schematic layout of Inrad Auto-tracker

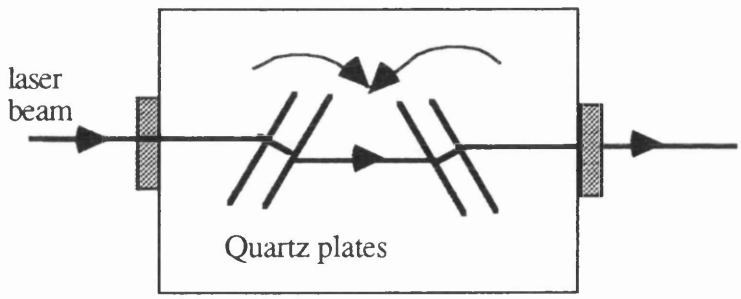

Fig.3.13 Plan view of the attenuator. The arrows show the direction of the movement of the quartz plates which keeps the net displacement of the laser beam is zero

incidence upon the plates and the number of plates used. Fig.3.13 shows the plan view of the attenuator.

3.2.6 Joulemeter

The pulse energy of the laser beam was recorded by two kinds of joulemeters. Molectron joulemeter(Model J3-09,USA) and Optilas joulemeter (Model 03A-P-Cal. UK). The calibrated Molectron joulemeter was used to measure the UV and visible beam with pulse energy lower than 1 mJ. This joulemeter is designed to record the laser beam with pulse widths ranging from picoseconds to 250 ms, and its peak height gives the value of the pulse energy. The operation of the joulemeter is based on its detecting lithium tantalite crystal which absorbs the photon energy, then rapidly heats up and becomes electrically polarised. This polarisation generates a surface charge whose integrated value gives an indication of the pulse energy.

The Optilas joulemeter relies on that the absorbed photons is transformed into the heat and then the heat generates a voltage, which is proportional to the pulse energy. This kind of joulemeter is used to measure the fundamental and visible light with high pulse energy.

3.3 Data acquisition and analysis system.

3.3.1 The Oscilloscope

The main instrument for recording mass spectra in the data acquisition system reported in this thesis is the digital LeCroy 9410 oscilloscope. The LeCroy 9410 is a dual 150 MHz oscilloscope (LeCroy Corp., Chestnut Ridge, NY, USA). It features two 100 megasample/second 8-bit Flash ADC systems, two 10K memories for waveform acquisition and storage, and four 10K memories for waveform processing, expansion and temporary storage. High-speed internal data transfer and processing are performed using a multi-processor system. The powerful Motorola 68020 microprocessor performs computations and controls the oscilloscope's operation and the unit's GPIB(General Purpose Interface Bus, IEEE-488).

The Lecroy 9410 oscilloscope has three main standard waveform processing functions, which can be selected by its front-panel knobs. 1) Summed average which includes the

repeated addition with equal weight, or successive source waveform records; 2) Arithmetic which consists of the functions of identity, negation, reciprocal, addition, subtraction and ratio; 3) Mathematical functions which contain functions of integral, derivative, square, square root, logarithm e, logarithm 10, exponential e, exponential 10 and absolute value.

The instrument can be operated either manually by using the front-panel controls, or remotely by means of an external controller (which is usually a computer). The mass spectra can be dumped directly into a plotter via the RS-232-C communication port or transferred to a PC computer via the GPIB. The data format of the mass spectra obtained from the oscilloscope has to be transferred in order to analyse and print using Apple Mackintosh computers. This was achieved by using a computer program" 94tran ", then using the " Apple File Exchange " program to transfer the data from PC format to Apple Mackintosh format. Finally " Cricket Graph " and "MacDraw" were used to analyse and print the mass spectra.

3.3.2 SIMION

In TRTOF experiments, one of the key problems which should be solved before the experiments could be carried out was the determination of the position and time of the ions at the turn-around point in the reflectron. This can be done by using a computer program "SIMION"(Dahl et. al, 1990). SIMION PC/PS2 4.0 is a personal computer program for designing and analysing charged particle (ions and electrons) lenses, ion transport systems and various types of mass spectrometers and surface probes that utilise charged particles. It was originally developed by D.C.McGilvery at Latrobe University, Australia, 1977. The current version which have dramatically improved its computational speed and accuracy with new features of 3D modelling, potential energy surface displays, arbitrary direction magnetic fields, ability to incorporate user written programs, compatibility with IBM PC, has been developed by Idaho National Engineering Laboratory.

In SIMION an electrostatic lens is defined as a 2-dimensional electrostatic array containing both electrode and non-electrode points. The planar and cylindrical symmetry assumptions allow the 2-dimensional fields to permit modelling a wide variety of 3-dimentional electrostatic devices. A potential array consists of a collection of equally

spaced points (up to 16,000 points) forming a rectangular grid. Trajectory computations employ self-adjusting integration intervals to reduce trajectory errors, and the contouring option can automatically pick voltage contours for display by examining the electrodes. Up to 30 adjustable electrodes may be defined by using specific voltage values. Furthermore, the trajectories of fragmentation and neutralisation at specific time and distance can be simulated.

Chapter 4

Experimental Investigation of MALDI

4.1 Introduction

Matrix-assisted laser desorption/ionisation(MALDI) represents a landmark in mass spectrometry and has shown its potential for desorbing intact ions of biomolecules with molecular weight up to 400,000 Dalton. In addition, MALDI is very sensitive, it needs only a few picomoles of the analyte (usually large biomolecules), and also is suitable for mixture analysis because of the production of molecular ions with few fragments. Although the practical aspects of MALDI are well known, the detailed its mechanisms are still uncertain.

This chapter will initially discuss the practical aspects of MALDI, such as how to select good matrices, how to prepare samples, and application of MALDI to some large biological molecules. Then its mechanisms, especially, the processes involved in ion formation will be discussed. The existence of neutral hydrogen atoms in the ablated plume which was first investigated and reported by our group using RIMS will also be presented in this chapter.

4.2 Matrix Selection

The key to MALDI is to choose suitable matrices, which are small volatile organic molecules. The following properties permitting the desorption and ionisation of large biomolecules can be attributed to a good matrix.

a) The matrix absorbs the photon energy from a laser pulse and results in the rapid deposition of large amounts of energy into the solid matrix-analyte solution. Thereby an instantaneous phase change of a micro volume of the sample is induced. As a result of the volume excitation, a dense gas is formed, expanding supersonically into the vacuum and analytes are also released into the vapour phase with little internal excitation(Beavis and Chait, 1990). Therefore one of the criterion for a good matrix is that the matrix has to be easily sublimable and strongly absorbent to the photons.

b) The matrix serves as a "solid solvent" for analytical molecules. It is present in large excess relative to the analyte, so that the strong intermolecular forces are reduced (matrix isolation effect). Usually the molar ratio of an matrix to a analyte is about

1000. Additional prerequisites for a matrix are vacuum stability and water solubility, at least for biomolecules that are normally water soluble.

c) The matrix is thought to perform an active role in the ionisation of analytes by photoexcitation or photoionisation of the matrix molecules followed by proton transfer to the analyte molecules. Thus the final criterion for a suitable matrix is that the intermediates of radical molecular ions of a matrix can be easily formed by photoionisation.

From the discussion mentioned above, it indicates clearly that it is not so easy to find a good matrix. Several hundred matrix-like materials have been tested since MALDI introduced, unfortunately, only about 10 of them are suitable for MALDI as a matrix. 2,5-dihydroxybenzoic acid (2,5-DHB)(Karas et. al 1990), Nicotinic acid (Karas and Hillenkamp, 1989), Sinapinic acid (Beavis and Chait 1990) and some other cinamic acid derivatives(Beavis and Chait 1989) have been proven to give the best results as matrices in MALDI.

The most commonly used matrix in this work is 2,5-DHB because it is cheap, insensitive to contamination by inorganic salts, buffers and detergents, even to a 10% sodium dodecylsulfate mixture. It is also easy to be made as crystal samples which contain analytes in an apparently homogeneous distribution. Fig.4.1 shows the UV absorption spectrum of 2,5-DHB in a water/ethanol (9:1 v/v) solvent which was typically used in MALDI experiments for the wavelength range of 220-369nm. This absorption spectrum does not exactly reflect the experimental situation as the absorption characteristics of the molecule in the solid state can be different from that in the solution, nevertheless, it serves as a general quality indicator. It can be seen from the absorption spectrum that the absorption peak of 2,5-DHB is around 325 nm. There is a large molar extinction coefficient of this matrix(about $4x10^3$ $lmol^{-1}cm^{-1}$) at wavelength of 337nm, which is main reason why the N_2 laser(wavelength 337.1 nm) is used in MALDI experiments when 2,5-DHB serves as a matrix. The large molar extinction coefficient increases the efficiency of the photon energy transferring into the sample. Fortunately, most of large biomolecules absorbs the photon wavelength below 240 nm, so they are not be excited and fragmented by the N_2 laser and stay cool. Substance P is the typical and commonly used biomolecule and its absorption spectrum is shown in Fig.4.2. It is clearly shown from Fig.4.1 and 4.2 that the two absorption peaks are separated.

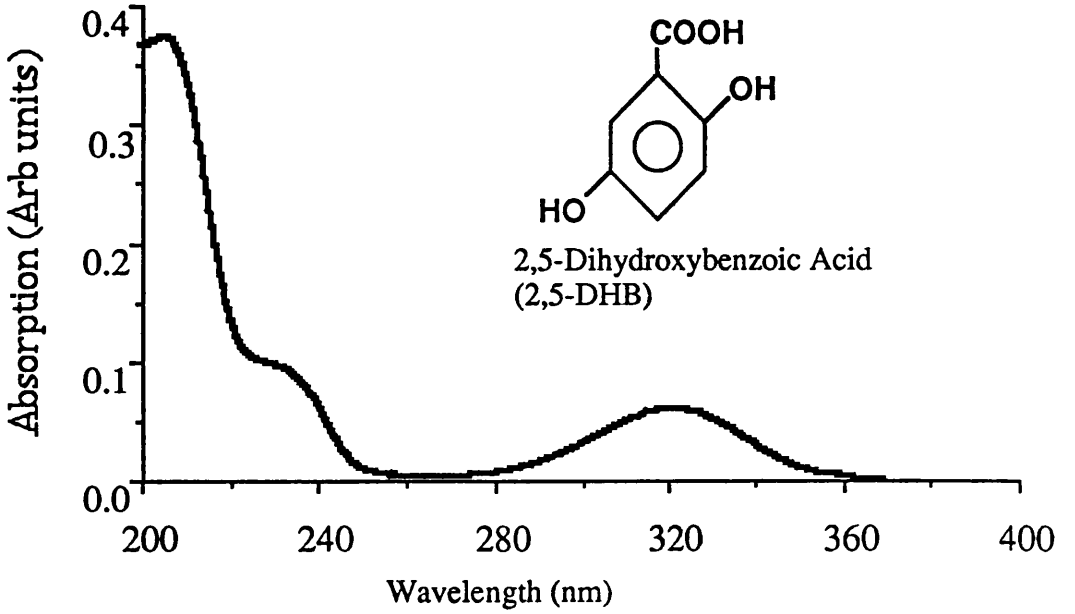

Fig. 4.1 The absorption spectrum of 2,5-DHB in water/ethanol (9:1, V/V) solvent.

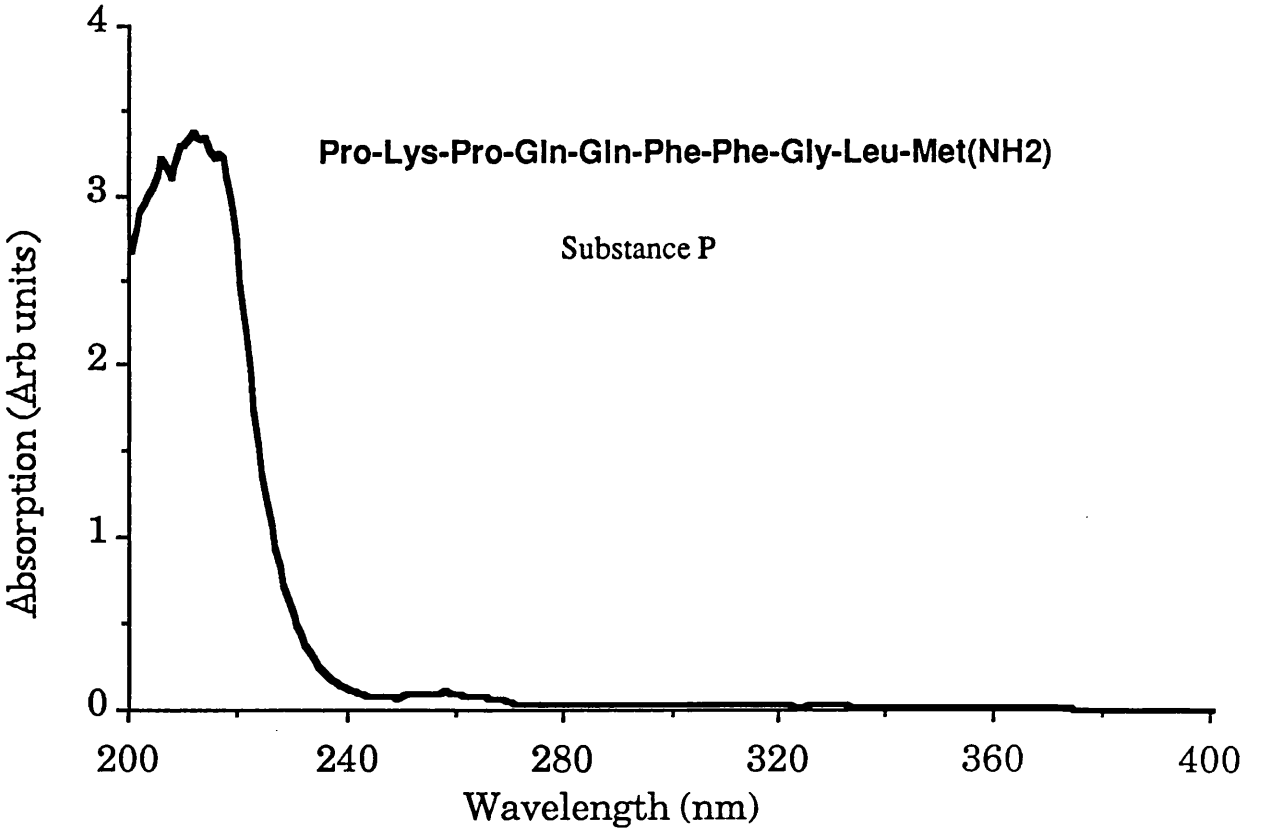

Fig.4.2 The absorption spectrum of Substance P in water/ethanol (9:1,V/V) solvent

Fig.4.3 shows a MALDI mass spectrum of Substance P with 2,5-DHB as a matrix ablated by a nitrogen laser with a power of $2.5x10^6$ Wcm^{-2}. Obviously there are three main groups of 2,5-DHB mass peaks which are far away from the Substance P . After mass calibration, it was found that the first group of the peaks contained the ions of ($M-OH_2$)(136 Da), (M-OH)(137 Da), and (M-O)(138 Da)(here M represents the parent molecule, i.e. 2,5-DHB). Among these peaks, $(M-OH)^+$ is much larger than the two other peaks, and probably it comes directly from photodissociation of 2,5-DHB(M), by its losing or receiving a hydrogen atom to form $(M-OH_2)^+$ and $(M-O)^+$. The second group of the peaks contained M^+(154 Da), $(M+H)^+$(155 Da) and $(M+H_2)^+$ (156 Da). The peak of M^+ is the largest in this group. Therefore it is reasonable to assume that $M^{+\cdot}$ was formed by the ablation laser directly and $(M+H)^+$ and $(M+H_2)^{+\cdot}$ were produced by adding one or two H atoms. Finally the last group of peaks was assigned to be a protonated dimer with loss of two water molecules $(2M-2(H_2O)+H)^+$. This ion was probably formed by association of two $(M-OH)^+$ and hydrogen atoms.

A large intact molecular ion of Substance P along with its adduct $(Subp+Na)^+$ and fragment $(Subp-NH_3)^+$ appears (see Fig.4.3). It was impossible to obtain such an impressive mass spectrum by laser desorption mass spectrometry technology a few years ago. A mass spectrum of Substance P without the matrix of 2,5-DHB is shown in Fig.4.4. In Fig.4.4 the mass spectrum contains some large mass peaks which are the fragments of Substance P, and very small intact parent mass peak. Obviously, most of the parent molecules were dissociated by the ablation laser.

It has been confirmed that the 2,5-DHB mass spectrum contains the radical parent molecular ion ($M^{+\cdot}$) . The other dominant ions, such as $(M-OH_2)^{+\cdot}$ and $(M+H_2)^{+\cdot}$, can be assigned as fragment ions and production ions related to photochemical reactions during the ablation processes. These radical ions have also been observed in UV laser desorption ionisation (UV-LDI) spectra of other groups of molecules and in particular for materials found suitable as matrices (Karas and Hillenkamp, 1989). These observation hints that these radical ions maybe play an important role for ionisation of macromolecules in MALDI. However, this does not means that all the molecules which can produced plenty of radical ions are good matrices. For example, 2,3-DHB is an isomer of 2,5-DHB which has a very similar structure to 2,5-DHB except the group of (-OH) connects benzene's 3rd carbon. They have very similar chemical and physical properties. The mass spectrum of 2,3-DHB ablated by the same laser(Fig.4.5) shows that the dominant ions peaks are the same as that appears in 2,5-DHB ablation mass spectrum. Unfortunately, it was found very strangely that 2,3-DHB

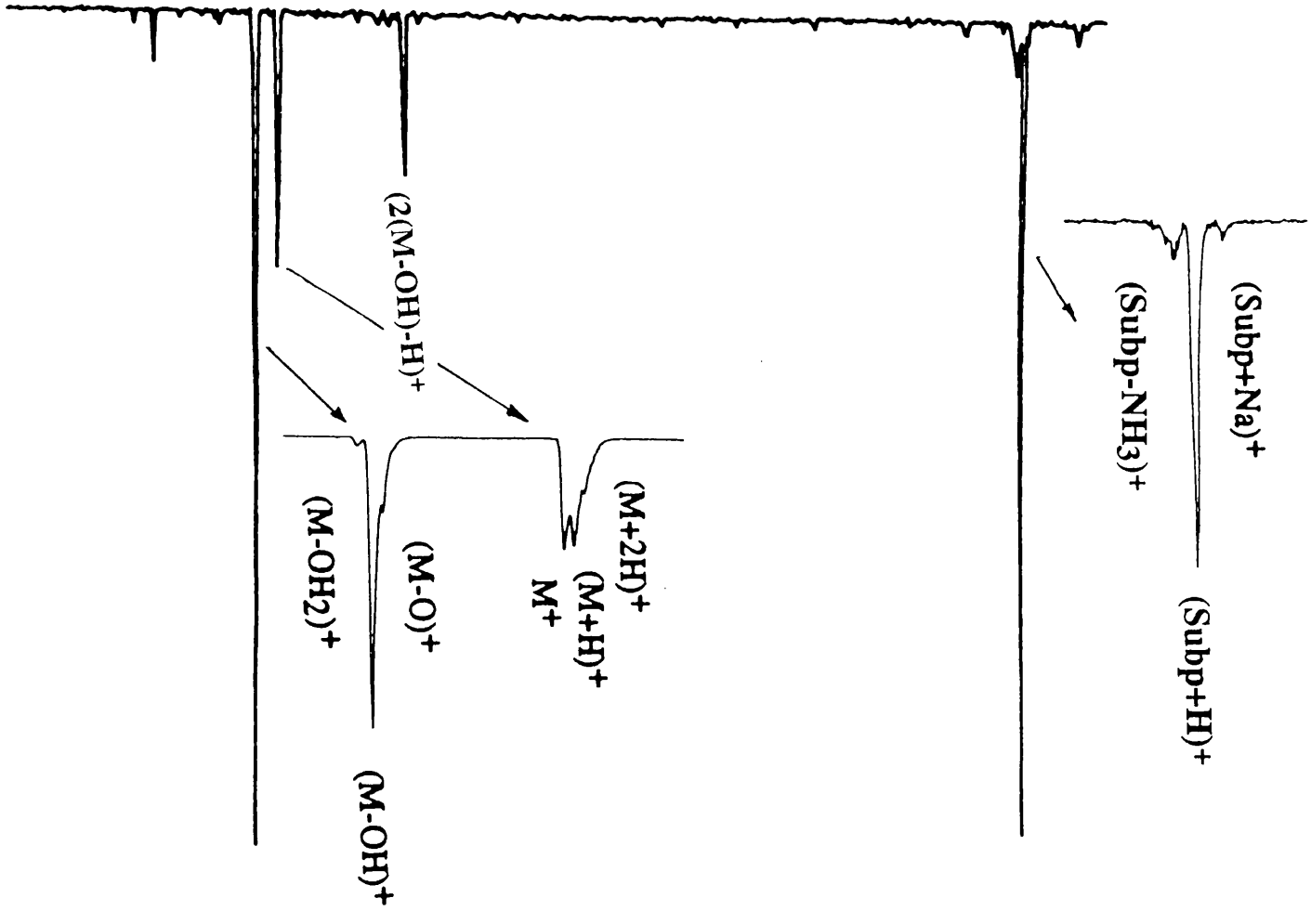

Fig.4.3 A typical MALDI mass spectrum of Substance P in 2,5-DHB as a matrix, ablated by a nitrogen laser with a power of $2.5 \times 10^6 Wcm^{-2}$.

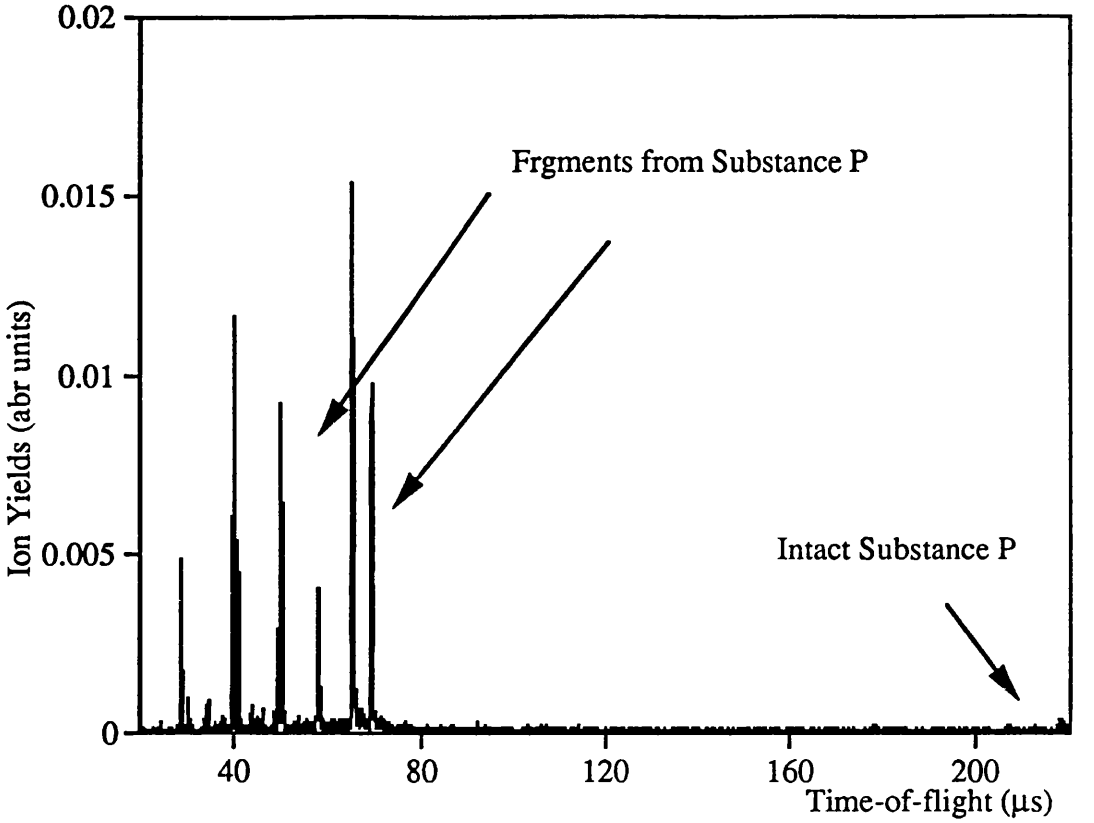

Fig.4.4 The mass spectrum of the pure Substance P ablated by a nitrogen laser with a power of 8.6×10^6 W/cm^2.

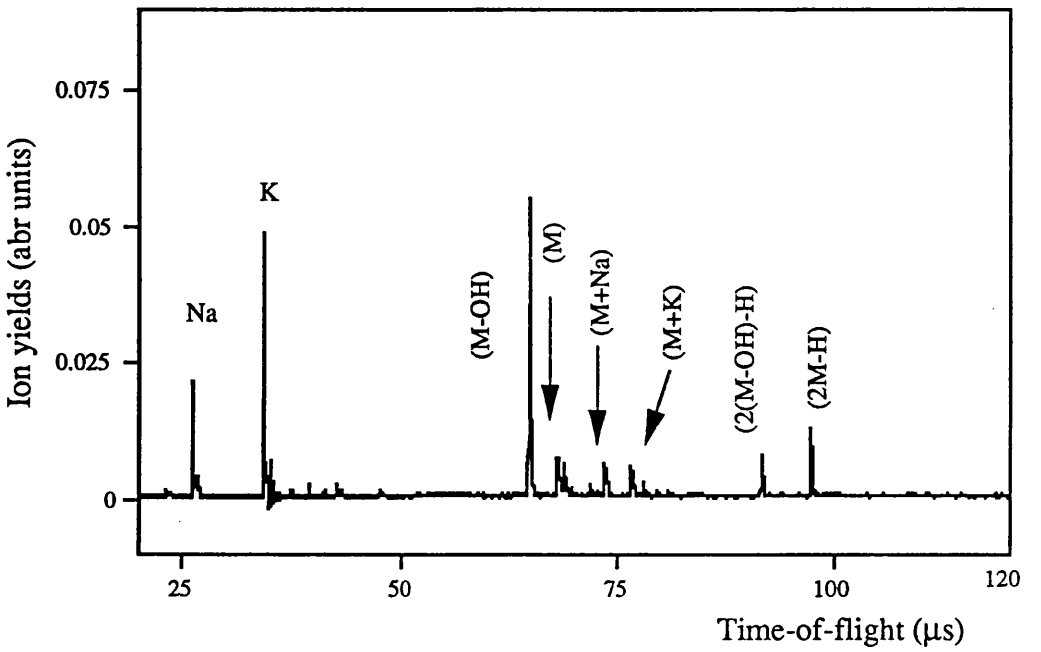

Fig.4.5 The mass spectrum of 2,3-DHB ablated by a nitrogen laser.

was not a good matrix and couldn't produce large intact analyte ions as its isomer 2,5-DHB did, although it can produce the same radical ions. This further demonstrates the difficulty of finding a good matrix. The reasons why 2,3-DHB is not as good a matrix as 2,5-DHB are still not clear. It has been found that the 2,3-DHB crystals formed in a solid sample are not good as those of 2,5-DHB, which prevents forming a sample with homogeneous distribution of analytes, and also resists photons penetrating into the sample. This effect reduces the release of the analyte molecules into the vapour phase. The ideal that a good matrix can be easily ablated into the vapour phase and produce plenty of its radical ions lead us to attempt to find a new matrix. TNT is an explosive, and can be easily and explosively ablated by a laser into the vapour phase and produce plenty of its neutrals and radical ions. Fig.4.6 shows the mass spectrum of Substance P with TNT as a matrix. It can be found that there is no Substance P ion signals, but with huge fragment ions of TNT and Substance P. Another explosive RDX has also been tried as a matrix, but unsuccessfully as well. These experiments demonstrate that a material which can produce plenty of radical ions is not necessarily a good matrix in MALDI.

Another possible important reason why 2,3-DHB is not good matrix may be that the radical ions of 2,3-DHB produced by the ablation laser are not as active as those of 2,5-DHB. It has been proven that the photofragmentation patterns of molecular ions from 2,3-DHB and 2,5-DHB are not same (This will be discussed in Chapter 6). Hence the active role in the ionisation of analyte molecules by these radical ions from the matrix is reduced.

The present results illustrate the uncertainty of the mechanism of the matrix role in MALDI and the difficulties of finding a good matrix in recent MALDI research.

4.3 Sample Preparations

Standard sample preparations appear to be very simple. Nevertheless it is a critical step for successful matrix desorption. Depending on their solubility, matrix compounds are dissolved in water, water-ethanol or water-acetonitrile matrix solutions of 5-10 g/l. For 2,5-DHB, which was the most widely used by the author, water-ethanol (9:1,V/V) was found to be optimal in forming homogeneous matrix-sample compounds after solvent evaporation. Analytes were dissolved in this solution to a final concentration of 1-5 µM. 0.1% trifluoroacetic acid (TFA) is sometimes used for dissolving protein samples, but not systematically necessary. TFA was not used in this work in order to simplify the interpretation of mass spectra. About 0.5 µl of aqueous analyte solution was

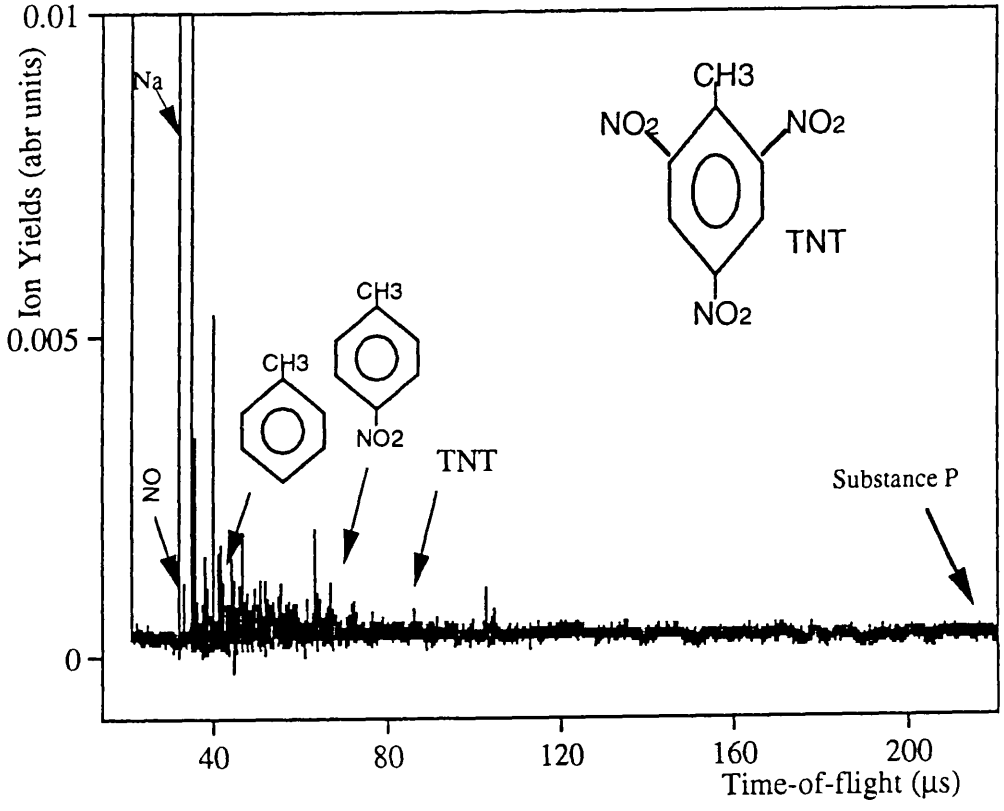

Fig.4.6 The mass spectrum of Substance P with TNT as a matrix, ablated by a nitrogen laser. No ion signals of the intact Substance P expect its fragments were observed. The fragments from TNT appears in this spectrum.

applied to a flat metal sample stub. The solvents were evaporated by gentle heating in a stream of warm air . Then the dried samples were transferred directly into the vacuum chamber.

In the initial experiments, we found that different sample preparations influenced greatly their mass spectra. Consequently different ways of drying the samples and various concentration ratios of the matrix (2,5-DHB) to analyte (Substance P) were studied. The sample which was dried by vacuum appears to be a thin fine homogeneous layer, and its mass spectrum (in Fig.4.7) shows the presence of other dominant contaminant peaks (e.g. Na^+, K^+). In addition the thin layer could be easily evaporated completely by few shots of the UV laser. When a saturated sample solution was dried slowly (more than 24 hours) in a refrigerator (4^oC), large single crystals of 2,5-DHB (about 1x0.2x0.2 mm in size) were obtained. From these crystals the excellent analyte peaks with respect to signal-to-noise ratio and reproducibility from shot to shot were observed with few small contaminant peaks. Crystallisation of the matrix and the embedment of analytes without water-soluble contaminants results its high tolerance to contaminants.

The concentrations of analytes in the matrices also affect the production of intact analyte ions. The ions signals of Substance P taken at different ratios of concentration with respect to the matrix (2,5-DHB) are shown in Fig.4.8. The figure indicates that the ratio of about 1000 is optimum for obtaining the largest substance P signals. The ion signal of the analyte was becoming smaller if the ratio of the matrix to Substance P increased over 1000 because of fewer Substance P molecules. The analyte signal was also became smaller if the ratio decreased less than 1000 when the matrix effect was disappearing and analytes began to be fragmented by the ablation laser.

4.4 General Characteristics of MALDI mass spectra

The mass spectrometry system was calibrated before MALDI experiments were carried out. CsI salt was used as a standard sample for mass calibration because it can easily produce several of its clusters(see Fig.4.9). A mass determination accuracy was about 0.1% and mass resolution was nearly 500 at m/z of 133.

A major drawback of MALDI TOF mass spectrometry has been the relatively low mass resolution, which reduces the accuracy of mass determination. There are a number of quite diverse factors limiting the mass resolution, such as cationisation of the formation

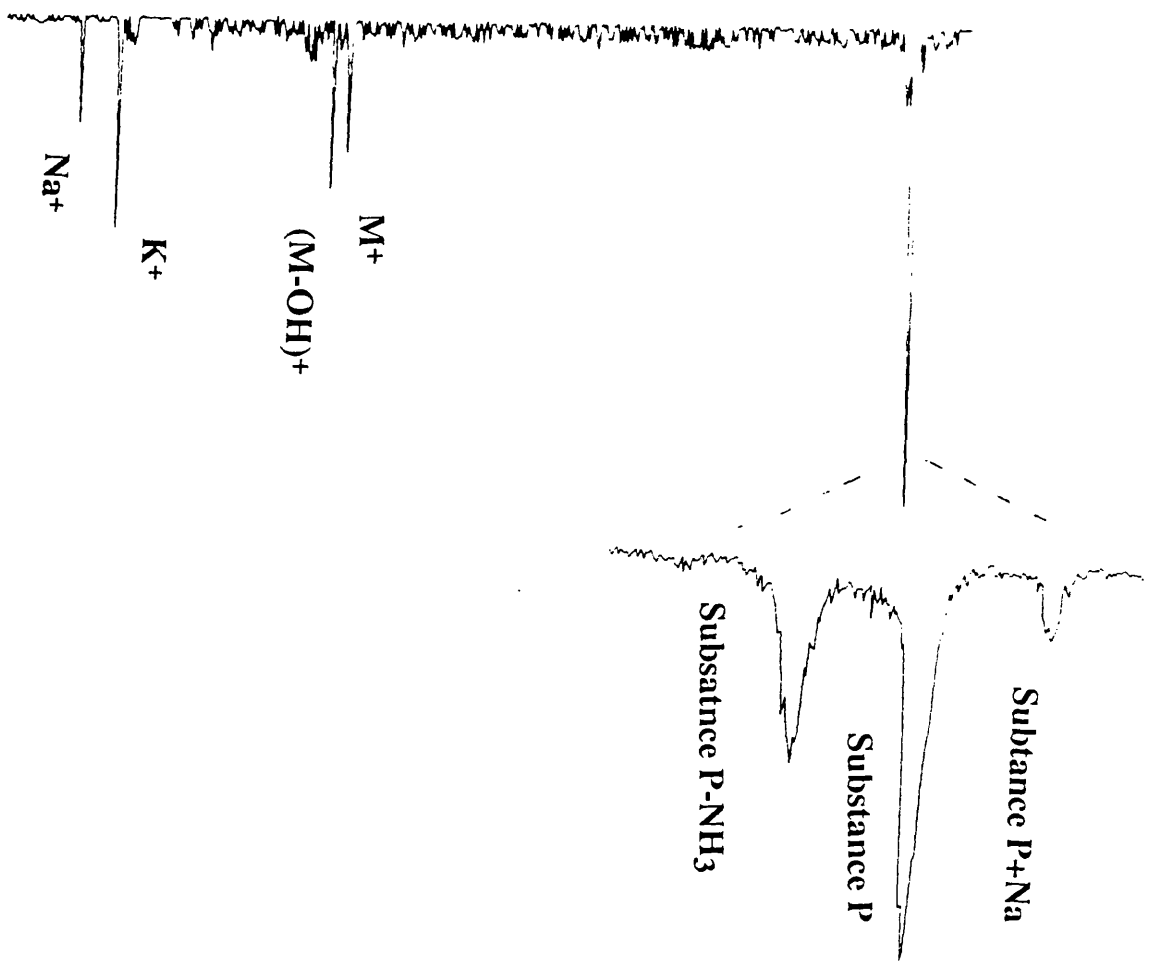

Fig.4.7 Mass spectrum of Substance P with 2,5-DHB as a matrix. The sample was dried in the vacuum. There was the presence of other dominant contaminant peaks(Na^+, and K^+). The sample can be easily vanished by an ablation laser.

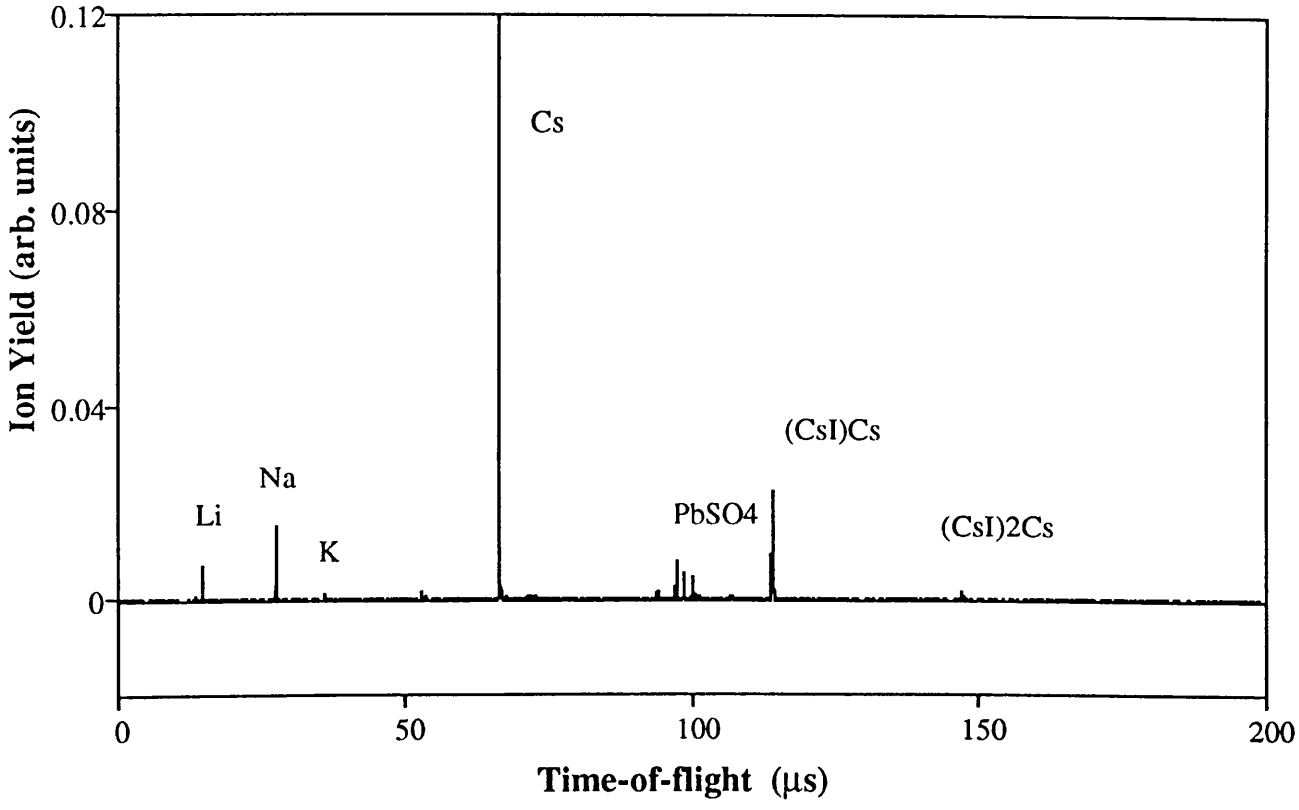

Fig.4.9 The mass spectrum of CsI ablated by a 337 nm laser. (CsI)I was used to calibrate the TOF mass spectrometer.

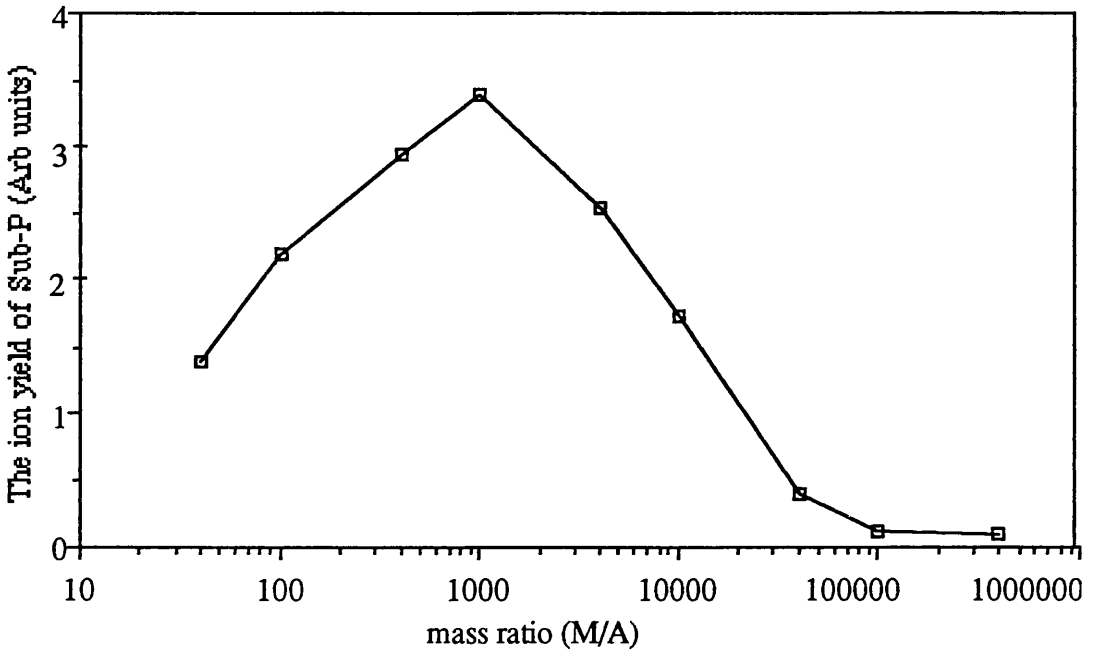

Fig. 4.8 The ion yields of Sub P against the ratios of the matrix(2,5-DHB) with respect to the concentration of Substance P

of adducts between analyte and matrix molecules or fragments, metastable decay of the analyte, the initial spread from either the finite laser spatial width of the pulse or the ion formation process, and fragmentation of analyte ions by cleavage of small neutral components (H_2O, HCOOH ect.). Considerable improvements have been achieved by using a new sample preparation procedure in which matrix and analyte handing were completely decoupled, and salts and impurities were washed off. A mass resolution of up to 5700 (fwhm) was achieved for peptides using this technique(Vorm et. al., 1994).

The best MALDI results obtained in the present work came from the sample in the form of the single crystals due to the homogeneity of the protein or peptide concentration within the 2,5-DHB single crystals. Another advantage of the single crystal matrix is its reproducibility. Fig.4.10 shows the relationship between the ion signals and laser shots from the same spot on the 2,5-DHB crystal surface. The ion signals still exist after several hundred laser shots. There are no significant changes of the spectra during the first 100 laser shots.

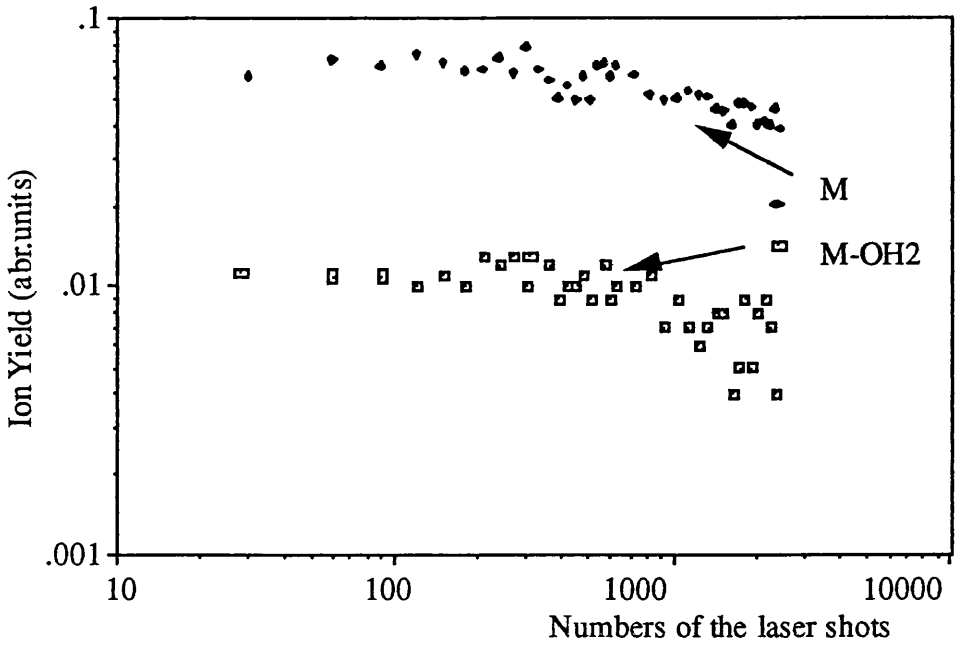

Fig.4.10 The ion yields of 2,5-DHB (M) and its fragment (M-OH2) against the laser shots from the same spot on the 2,5-DHB crystal surface.

In some of MALDI mass spectra (see Fig.4.11), the matrix ions became very small and sometimes were nearly absent. This observation has been also reported by the group of Karas and Derrick (Strupat et al., 1991, Chan et. al., 1991). These spectra can be only obtained in the optimal concentration range of the analyte and near the threshold flux. The finding not only simplifies the MALDI mass spectra for analysing low molecular mass analytes, but it may contain the key information about ion formation processes which implies that an intimate mixture between the matrix and the analyte is essential for the MALDI effect.

The quality of MALDI mass spectra depends on the intensity of the ablation laser dramatically. The power dependence of the ion signals of Substance P and its sodium adduct is shown in Fig.4.12. It is apparent that there is a laser irradiance threshold ($2x10^7$ W/cm^2) in ion generation. This phenomena has been reported many times earlier in the laser desorption mechanism. Although the absolute threshold varies from situation to situation depending mainly on the sample morphology and laser power measurements, the values generally lie from 10^6 to 10^7 W/cm^2. Fig.4.12 also shows that there is a maximum peak of the ion signal of Substance P. The ion yield rises with increase of the laser intensity because more species were released by the laser. As a power density of the laser was increased continuously, however, the ion signals were

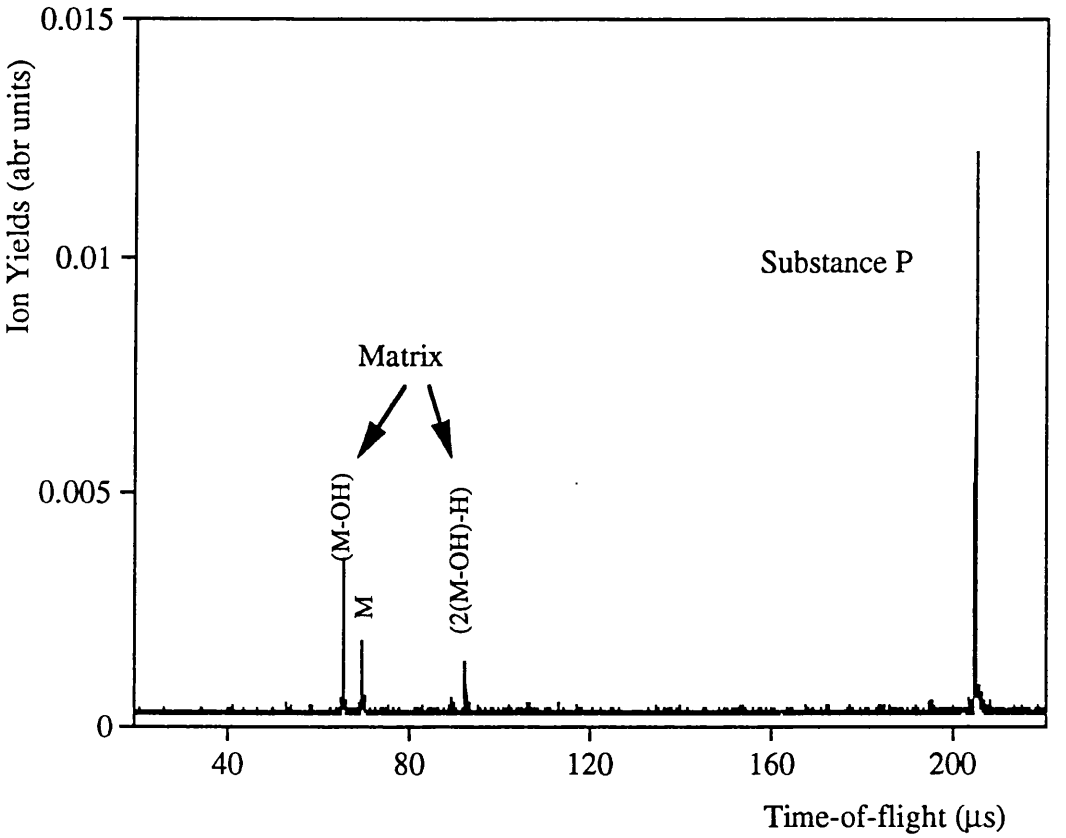

Fig.4.11 The MALDI mass spectrum of Substance P with 2,5-DHB as a matrix. It shows that the ion signals of the analyte molecule (Substance P) is much larger than that of its matrix although the concentration of the analyte is much smaller than its matrix's.

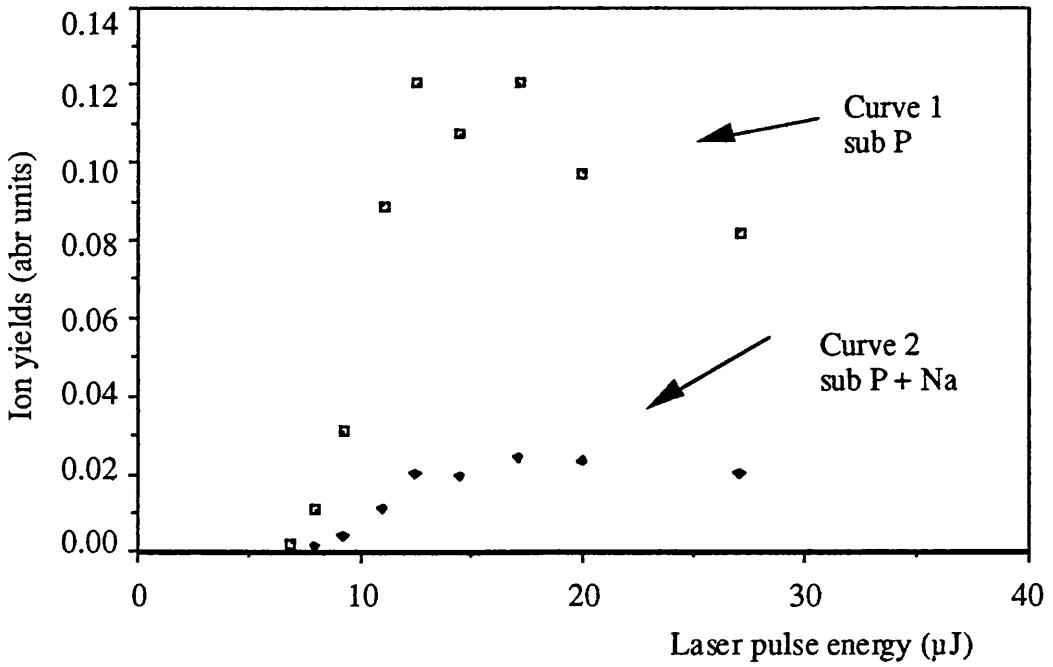

Fig. 4.12 The laser power dependence of the ion signals of Substance P and its sodium adduct.

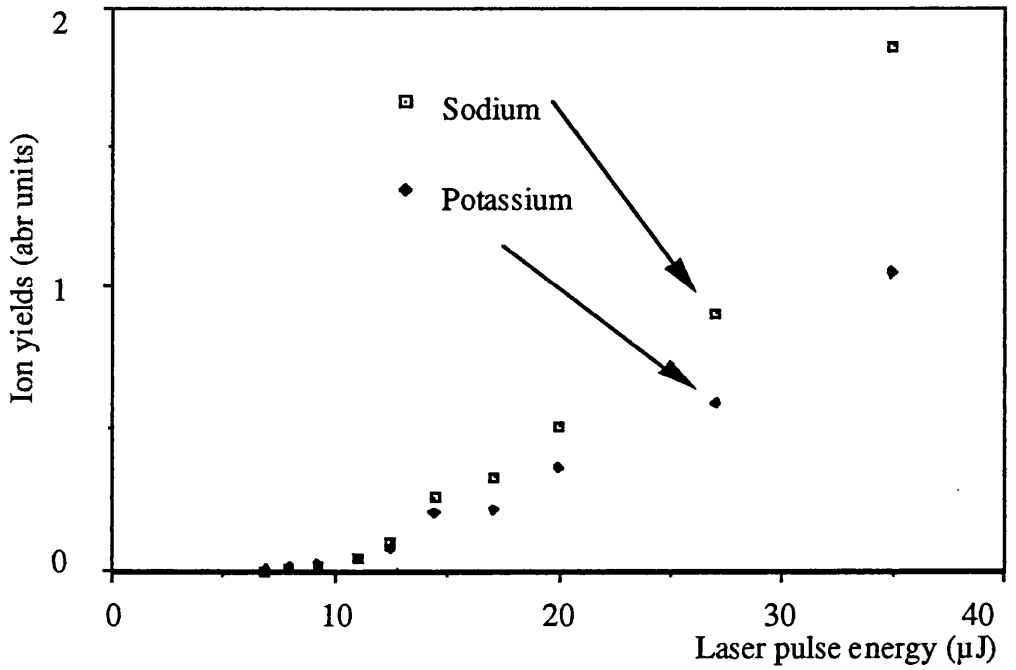

Fig.4.13 The power dependence of the ion signals of sodium and potassium.

reduced because of increasing probability of photofragmentation of Substance P and formation of its adducts under high laser irradiance. The curve 2 in Fig.4.12 illustrates the rise of formation of sodium adduct of Substance P (Subp+Na). Furthermore, with the increase of laser power, contaminant ions on the sample stub surface such as sodium and potassium increase rapidly.(see Fig.4.13) because the laser beam was deeper into the sample and closer to the sample stub surface. Therefore the opportunity of formation of adducts of Substance P becomes larger.

The power dependence of the matrix ions seems different from Substance P mentioned above. There were three main ion groups of 2,5-DHB in the spectrum of Fig.4.3. The prominent fragment ion in first group was formed by a loss of OH radical from the parent matrix (M) and the other two peaks were formed by H atom transferring. The second group of ions were formed by photochemical ionisation and protonisation processes. The last group of ions were the dimers of the matrix fragments. Fig.4.14 shows that the ion signals of the first group peak were much larger than the others and increased with the rise of laser intensity. The ions in the second group decreased with the increase of the laser power. These data support the assumption that $(M)^+$ can be easily fragmented by loss of an water(H_2O) with the increase of the laser fluence to produce its fragment of $[(M+H)-H_2O)^+$ (usually we write it in the form of $(M-OH)^+$, the reaction pathway will be explained in Fig.6.1). As a result of the $(M-OH)^+$ increase with the higher laser intensity leads to a continuing rise in the ion yields of its dimer.

4.5 Mechanism of MALDI

The MALDI technique has developed dramatically since its discovery. However, the underlying mechanism is still obscure. Several models have been proposed to explain different aspects of the processes with varying degrees of success. Vertes and Gijbels (Vertes and Gijbels 1990) have proposed a "Bottleneck Model", in which they suggested a poor coupling with respect to the energy flow between the lattice and analyte molecules in the solid state to explain the existence of large intact biomolecules in the ablation plume. Three years later, they gave another model " The Hydrodynamic Model" (Vertes et. al., 1993) to explain the plume expansion in MALDI. Recently Karas's work (Ehring et. al., 1992) has shown that the ionisation processes occur by gas-phase reactions between matrix species(M) and analytes(A) in the dense plume. In the positive-ion mode, the analyte ion is predominantly seen as $(A+H)^+$. The production of $(A+H)^+$ is due to the proton transferring reaction between a matrix ion and an analyte molecule.

$$(M+H)^+ + A \rightarrow M + (A+H)^+$$

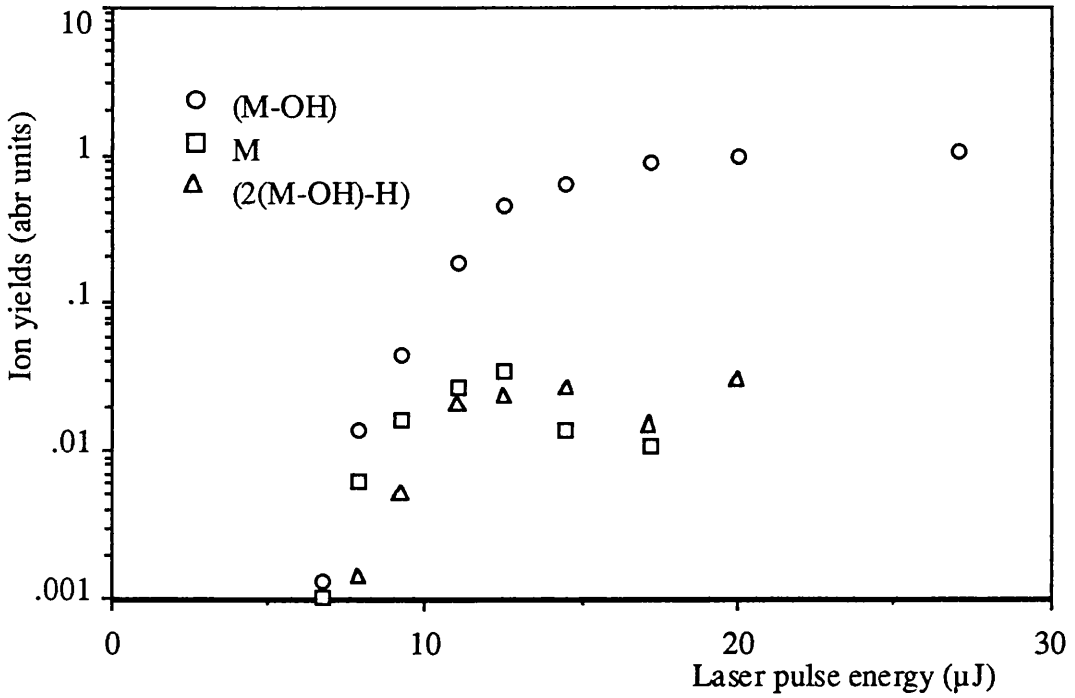

Fig.4.14 The laser power dependence of the ion signals of 2,5-DHB and its fragments.

They have also suggested that many ion peaks in MALDI mass spectra can be rationalised assuming radical precursor ions and subsequent protons or hydrogen atom transfer processes. Typical reactions for production of such ions are shown below:

$$(M)^{+\cdot} + H \rightarrow (M+H)^+$$
$$(M+H)^+ + H \rightarrow (M+2H)^{+\cdot}$$
$$(M\text{-}OH)^+ + H \rightarrow (M\text{-}O)^{+\cdot}$$
$$(M\text{-}OH)^+ - H \rightarrow (M\text{-}OH_2)^{+\cdot}$$

All these ions have been observed in the typical MALDI mass spectra. Therefore the existence of atomic hydrogen in the ejected materials is very important for understanding of the ion formation in MALDI. The key question in this model is whether the hydrogen atoms exist in the ablated plume or not? To our knowledge, the experimental evidence for the existence of atomic hydrogen in the ejected matrix species has not been previously reported. In order to prove the existence of large numbers of atomic hydrogen in the ejected plume, a frequency doubled dye laser in the

wavelength range of 240-250 nm was used to probe the neutral species in the plume using the post-ablation ionisation (PAI) technique.

The ionisation potential of atomic hydrogen is 13.6 eV. At 243.13 nm, ionisation of atomic hydrogen can be achieved with high efficiency via a two photon resonant excitation step followed by the absorption of a further photon to ionise (usually called (2+1) multiphoton resonant excitation/ionisation scheme). Fig.4.15 compares the on-resonance PAI mass spectrum of 2,5-DHB at 243.13 nm with off-resonance mass spectrum at 243.03 nm. A very large resonant enhancement in the hydrogen ion signal is clearly seen in the on-resonance spectrum. The observed atomic hydrogen in this mass spectrum must be attributed, at least partly, to the fragmentation processes of the ejected species induced by the postionisation laser beam. A number of carbon fragment groups (CH_x, C_2H_x, C_3H_x, C_4H_x, x=0,1,2,3...) along with the ions of $(M\text{-}OH)^+$ and $(M)^+$ have been simultaneously recorded. This phenomenon has been reported by this lab (Clark et. al., 1993). From the power dependence of hydrogen ions on the postionisation laser flux at the resonant wavelength, a value around 4.3 was obtained. This fact further supports a strong contribution to the hydrogen ion signal from the fragmentation of the ejected materials. If the detected hydrogen ions had been entirely produced during the ablation process, the above value was expected to be less than 3 (two photons for excitation and one for ionisation).

To distinguish the atomic hydrogen produced by the ablation process from that produced by the fragmentation of matrix species using PAI at 243.13 nm, the mass spectra have been recorded with different delay times between the ablation laser and the postionisation laser. This experiments were based on the assumption that the velocity of hydrogen atoms generated directly from ablation processes would be different from that of fragmentation of the matrix species. The study has been carried out with the N_2 laser intensities below and above the threshold for ion production. It was found that only the hydrogen ions existed in the mass spectrum of a short delay (140 ns)(Fig.4.16 a). This was clear evidence for atomic hydrogen production during the ablation processes, since there was no other neutral species arriving in this ionisation area in such short delay and the fragmentation could not occur. By increasing the delay time (Fig.4.16b, c), the hydrogen ion signal increased due to the hydrogen contribution from fragmentation processes of the higher mass hydrocarbons. It is much clearer to distinguish the two kinds of hydrogen contributions by their velocity distributions. Fig.4.17 demonstrates the velocity distributions of various ions obtained with the N_2 laser fluence under the threshold. It is obvious that there were

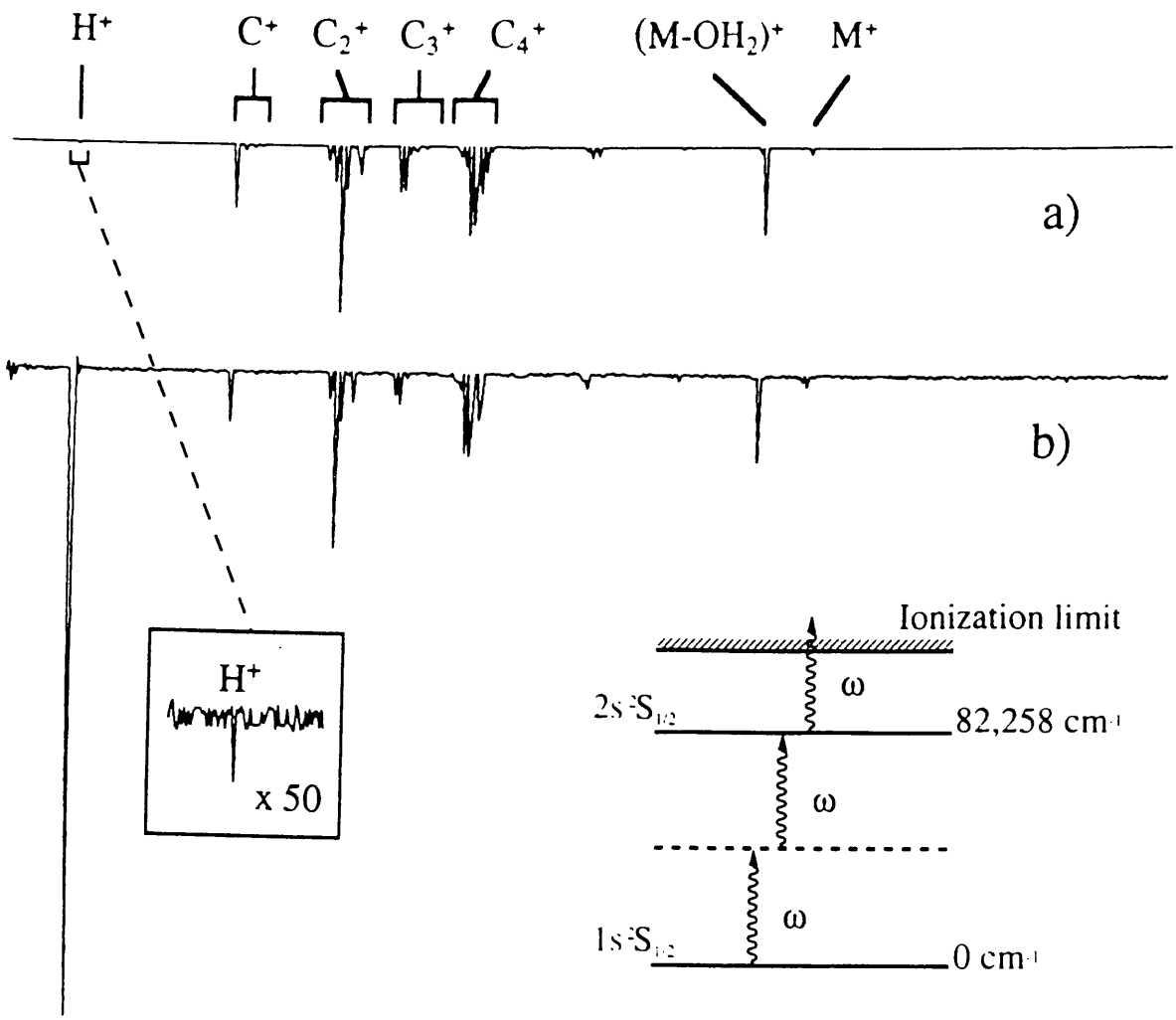

Fig.4.15 Postionisation mass spectra of 2,5-DHB. a) off resonance at 243.03 nm; b) and on-resonance at 243.13nm. (The fluence of the nitrogen laser and dye laser were 100 mJcm^{-2} and 180 mJcm^{-2}, respectively. The delay between the two lasers was 900 ns.) The inset shows the (2+1) multiphoton resonant excitation/ionisation scheme used to ionize atomic hydrogen.

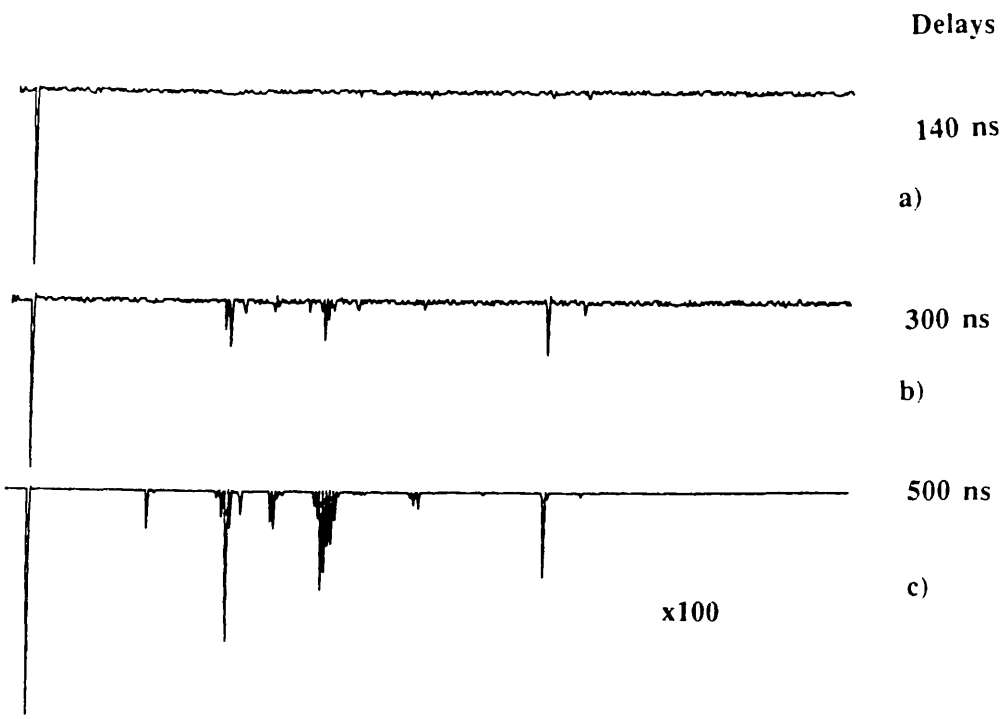

Fig.4.16 Mass spectra of 2,5-DHB as a function of the delay between the nitrogen laser and dye laser (the distance between sample surface and dye laser was 400 μm, and the power of the nitrogen laser was below the ionisation threshold.).

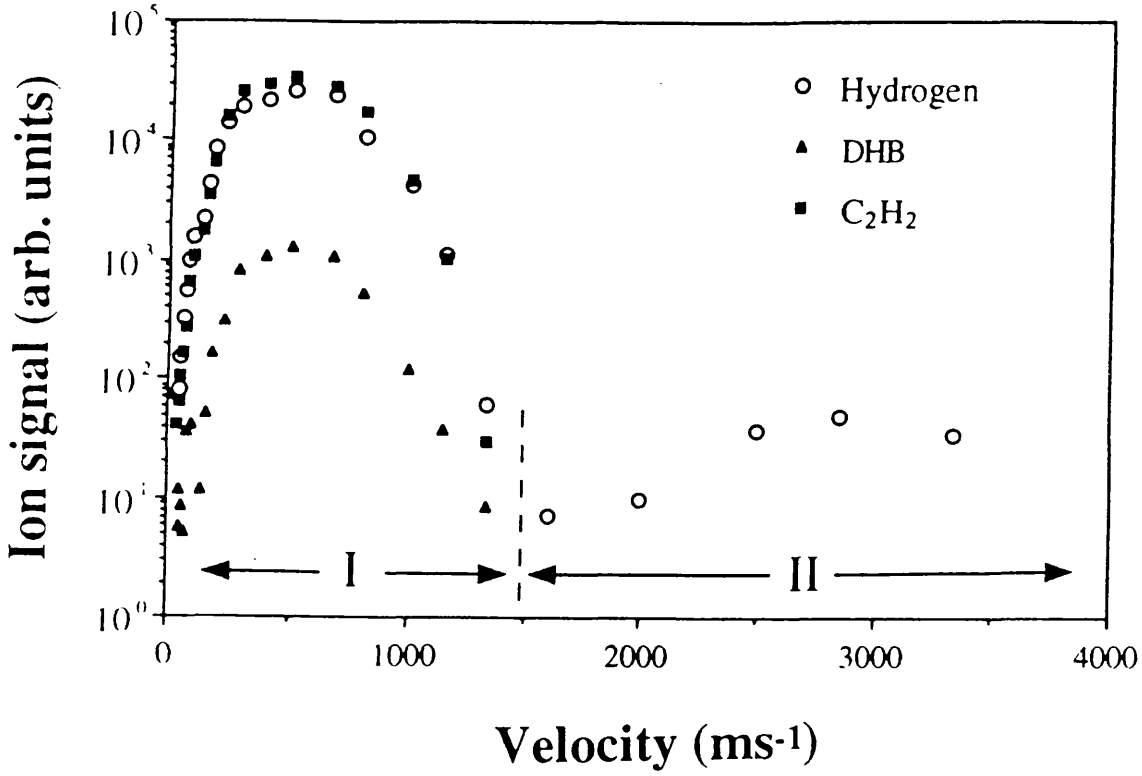

Fig.4.17 The velocity distributions of various ions obtained with the nitrogen laser fluence below the ionisation threshold(the N2 laser fluence was 50mJ cm^{-2}, PAI laser on-resonance with a fluence of 370 $mJcm^{-2}$).. There were two kinds of hydrogens. In the region I , the atomic hydrogen comes from the matrix parent molecules and its fragments (with the same velocity distributions). In the region II, the atomic hydrogen comes from the ablation processes which velocity distribution is totally different from the matrix and its fragments.

two hydrogen distributions. The hydrogen whose velocity distribution is same as that of the matrix parent molecule and its fragment C_2H_2 (the fragment of C_2H_2 is typical of all the carbon fragments seen) comes from the UV fragmentation by the PAI laser. Another velocity distribution of hydrogen with considerable larger velocities is clear evidence for the existence of atomic hydrogen produced during the ablation processes.

Similar results were obtained with the ablation laser above the threshold. Fig.4.18 and Fig.4.19 show a typical mass spectrum with the ablation laser fluence above the ionisation threshold and the normalised PAI velocity distribution of hydrogen taken above the ionisation threshold. In the short delay time (Fig.4.19) the hydrogen ion peak is not evident as it was in the below threshold case, since the characteristic MALDI features (ablation ion signals of the parent molecular ion and its fragment ions) also appeared. The velocity distribution in Fig.4.19 was drawn with concentrating on the atomic hydrogen is approximately 5000 ms^{-1}. To our knowledge this is the largest velocity reported for ejected neutrals during MALDI processes. The parent ion species from PAI are not shown in Fig.4.19 since they are indistinguishable from the parent ions due to ablation.

The most probable velocities of the other neutral species have been measured. The velocity of the parent molecule (2,5-DHB) is approximately 430 ms^{-1} in consistent with the measured neutral particle velocity in MALDI for sinapinic acid (Huth-Fehre and Becker, 1991). The neutral fragments of the parent molecule have the same velocity of their parent's. Initial velocities of the ions are larger than those of the neutral species. This difference may be attributed to the presence of a large extraction field in the experiments (Vertes el. at., 1993). Another feature of the velocity distributions shown in Fig.4.17 and Fig.4.19 is that the most probable velocity (2800 ms^{-1}) of hydrogen with the N_2 laser intensity below the ionisation threshold is smaller than that obtained with the N_2 laser intensity above the ionisation threshold. The hydrogen from above the ionisation threshold receives more kinetic energy due to the higher temperature than that below the ionisation threshold in the sample spot. The ejection of a large amount of the parent and its fragment ions maybe gives the neutral hydrogen an additional kinetic energy from collisions with it.

This finding of the existence of neutral hydrogen atom allows an increased insight into the underlying photochemical reaction principles for ion formation in MALDI. The production of matrix ions can be explained by an atomic-hydrogen-transfer reaction among the matrix radical ions(see Fig.4.20).

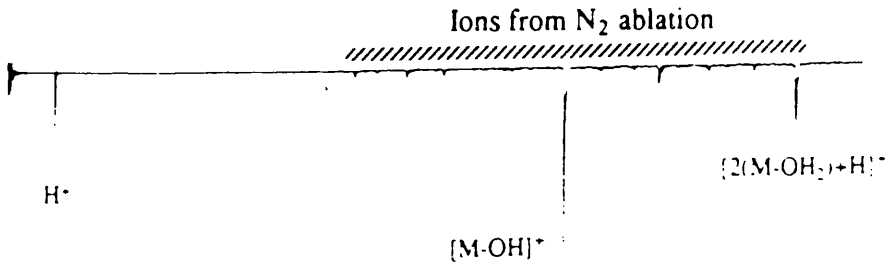

Fig. 4.18 A typical mass spectrum with the nitrogen laser fluence above the ionisation threshold.

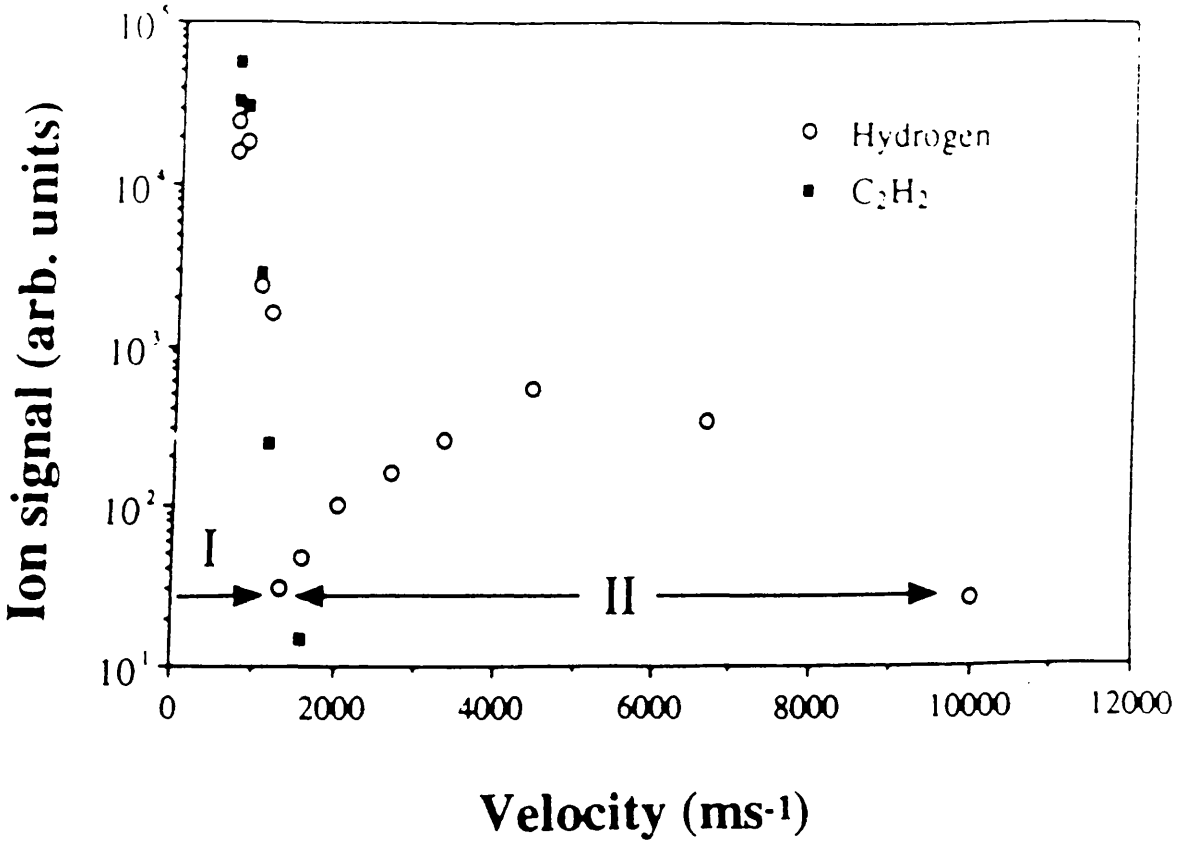

Fig.4.19 The velocity distributions of various ions obtained with the nitrogen laser fluence above the ionisation threshold(the N2 laser fluence was 140 mJcm^{-2}, PAI laser on-resonance with a fluence of 370 mJcm^{-2}). There were also two kinds of hydrogens. In the region I , the atomic hydrogen comes from the matrix parent molecules and its fragments. In the region II, the atomic hydrogen comes from the ablation processes which velocity distribution is totally different from the matrix and its fragments.

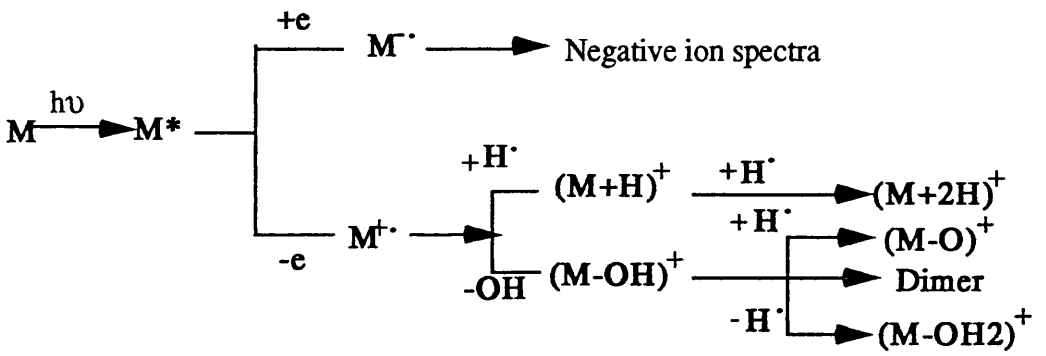

Fig.4.20 Schematic diagram of photochemical reaction pathways for the matrix and its fragment ions.

where M represents the matrix molecule. The parent matrix molecule absorbs photons from a laser to reach its excited states (M*). M* receives an electron and becomes a negative molecular ion, finally it forms negative ion spectra (will not be discussed in this work). M* can continue absorbing photons, and form $M^{+\cdot}$ by ionisation. When $M^{+\cdot}$ is produced, it can receive one or two hydrogen atoms and become $(M+H)^+$ and $(M+2H)^{+\cdot}$, which both appeared in the mass spectra. $M^{+\cdot}$ can also be fragmented by loss of a (-OH) radical and then $(M-OH)^+$ can be produced. $(M-O)^{+\cdot}$ and $(M-OH2)^{+\cdot}$ will be generated through $(M-OH)^+$ by gain or loss of a hydrogen atom, respectively. In addition, $(M-OH)^+$ can associate in pairs to form its dimer. All these products have been observed in the typical MALDI mass spectra.

The analyte molecular ions are produced mainly by various reactions between the analyte molecules and the radical matrix ion, its fragment ions or others. The Fig.4.21 gives a brief summary of photochemical ionisation processes for the production of analyte ions in MALDI.

Most of MALDI experiments show that the majority of analyte ions are produced by the protonisation, but ion adduction and atom-transfer processes can also be found in the MALDI mass spectra. In addition, interestingly, the analyte ions in MALDI can be produced by a charge-transfer mechanism having no transferable proton (Juhasz and Costello, 1993).

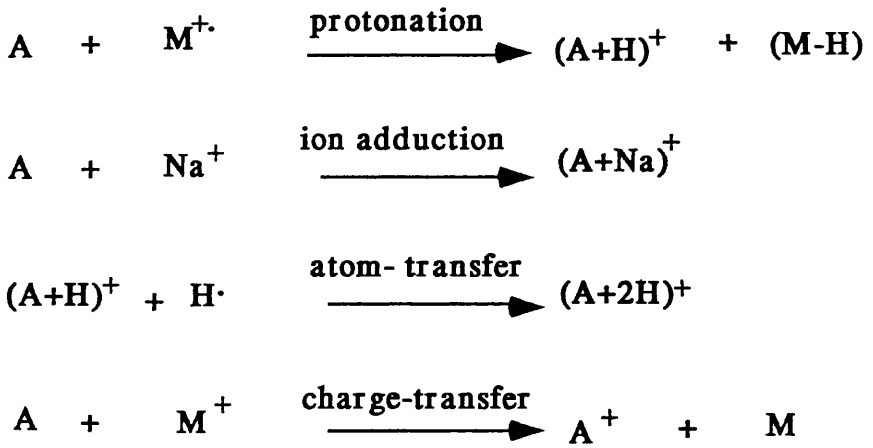

Fig.4.21 Schematic diagram of photochemical ionisation processes for analyte ions in MALDI. M=Matrix, or its fragments, A=Analyte molecule, Na= Alkaline ions or other contaminant ions

4.6 Application of MALDI

The potential of MALDI in the life science field is considerable and it is already considered to be a state of the art to meet the needs in the fast development of peptide synthesis and genetic engineering(e.g. fast DNA sequencing and Human Genome programme). The application of MALDI mass spectrometry is just beginning to develop. The most important achievements are expected on the areas where the unique features of MALDI can be utilised. The accuracy of mass determination in high mass ranges made it possible to revise the calibration curves of molecular weight marker kits of certain commercial gel electrophoresis (Kratzin et. al., 1989). The upper mass detection limit is rather determined by an increasingly inefficient ion detection than by the ion of MALDI process.

The goal of the Human Genome Project is to sequence at least 500 megabases of DNA per year. It will be difficult to achieve this goal simply by improving the current gel electrophoresis process(normal DNA sequencing approach). MALDI mass spectrometry makes these high molecular mass determination possible with unprecedented speed, sensitivity and accuracy. In order to apply the MALDI technique into DNA sequencing, the mixture biomolecular analysis by this technique should be done.

The biomolecules of PTH-alanine(206.3Da), PTH-tryptophan(321.4 Da), Substance P(1348 Da), Gramincidin D (1881 Da) and Insulin (5733.5 Da) were mixed and then

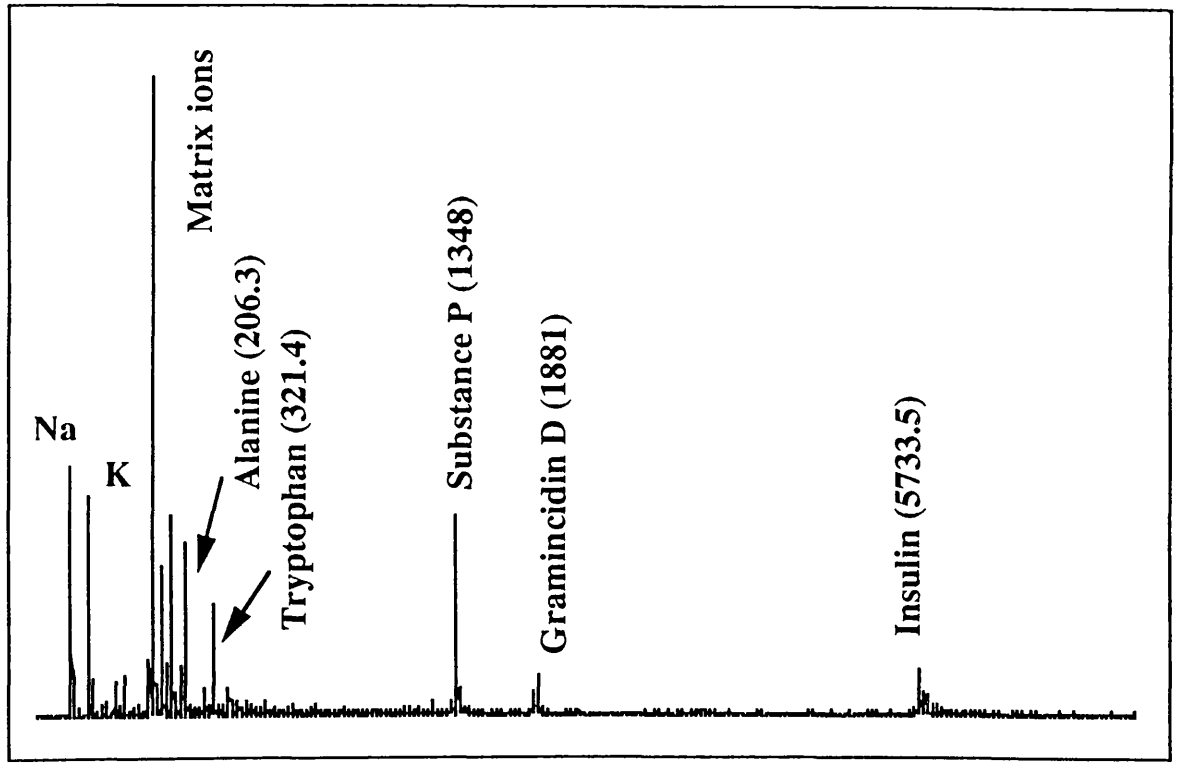

Fig.4.22 MALDI mass spectrum with various biomolecules. The ablation laser energy: 20 uJ; Matrix: 2,5-DHB

added into 2,5-DHB saturated solution. 3 drops (about 0.5 µl) of this mixture were applied on a sample stub and dried by a gentle warm air. The mass spectrum of 5 different biomolecules is shown in Fig.4.22. It can be seen in this Figure that all the analyte ions are with a singly positive charge without significant fragments, which makes MALDI mass spectrum easy to be identify. An additional advantage of MALDI is that the ions of the matrix parent and its fragments appearing in the mass spectrum can be easily distinguished from analytes which arrive later in TOF mass spectrometry. Furthermore the insensitivity to contamination by inorganic salts such as Na^+ and K^+ is another feature of MALDI. All the inorganic ions emerge at the beginning of the mass spectrum. Therefore these features make MALDI ideally suited for mixture analysis of biomolecules.

4.7 Conclusions

In this chapter, I have shown that the proper choice of the matrix and the preparation of a sample greatly influence the results in MALDI. A good matrix has the following main criterion:

* The ability of forming a solid solution for analyte molecules.
*A high photochemical activity (photoionisation and successive photochemical reactions).
* A high volatility.
* A high tolerance towards different solvents and contaminants.
* A good reproducibility of sample preparation.
* A low tendency for adduct ion formation.
* Photostability.

The existence of neutral atomic hydrogen in the MALDI plume with considerable larger velocities than the matrix species has been demonstrated by the RIMS technique for the first time. This finding gives us a more detailed picture of the photochemical reaction pathways for ion formation in MALDI.

Although MALDI is new and evolving technique, its present development shows the high potential for the determination of the relative molecular masses of large biomolecules. One of the important features for future applications may be the fast DNA sequencing with the improvements in mass resolution, sensitivity and sample preparation techniques.

Chapter 5

A Tandem Reflectron TOF Mass Spectrometer for Laser Photofragmentation of Molecular Ions

5.1 Introduction and experimental arrangement

Tandem mass spectrometry (MS/MS) is expected to become increasingly more important in the characterisation of molecular structure particularly for the analysis of large biomolecules. Reflectron time-of-flight (TOF) mass spectrometers are ideally suited for experiments using pulsed laser desorption and postionisation of neutral species with the simultaneous acquisition of masses with reasonable mass resolution(Mamyrin, 1994). Although TOF mass spectrometers are difficult to adapt to tandem mass spectrometry experiments a few designs for the tandem TOF/TOF spectrometer incorporating pulse laser excitation have been published. In the configuration used by Alexander and co-workers(Alexander, et. al, 1988), the laser excitation of a spatially focused ion beam occurs in the field-free drift region before the entrance to the reflectron. Unfortunately, only one fragment ion at a time can be focused onto the detector. In the Boesl's configuration(Buesl et. al, 1990), nanosecond precision timing is required to intersect the fast focused pulsed ion packet with a short laser pulse (5ns). An alternate configuration for a tandem reflectron TOF instrument has been developed by Duncan's group(Cornett, et. al, 1992). The main advantages of this design are that it includes a simple laser timing scheme (microseconds) and preserves the multichannel aspect of fragment ion detection.

In this chapter, a simpler new TRTOF configuration developed recently by the Glasgow group is described, which is similar to the approach of Duncan and co-workers(Cornett, et. al, 1992). The main point of this technique is that the sample molecules are ablated and ionised by an ablation laser, then accelerated and extracted by an ion optics. The ions travel into the field-free flight region and move into the reflectron. The ions decelerate and turn around in the reflectron. Laser photodissociation of the selected ions takes place at the turn-around point of the ion trajectories in the reflectron. In order to provide laser access to the ion packet at the turn-around point in the reflectron, two quartz laser windows were added to the opposite sides of the flight tube containing the reflectron and a laser beam allow to pass through the gap between the electric ring 20 and 21. Fig.5.1 schematically shows the end of the TOF tube.

The outstanding advantage of this TOF/TOF technique is that it includes a simple laser timing scheme (microseconds) and preserves the multichannel aspect of fragment ion detection. The main differences comparing with Cornett's TRTOF configuration are: a) the laser ablation is used as an ion source which is simpler and is available in most TOF instruments; b) no electric field changes in the reflectron are required for tandem mass spectrometry experiments. It is more convenient for a normal two stage reflectron TOF instrument to be adapted to tandem mass spectrometry experiments. c) the fragmentation laser beam at the turn-around point is perpendicular to the plane of the parent ion trajectories. This avoids different fragmentation patterns from the same parent ion due to early or late excitations.

The first goal of the experiment was to generate sufficient molecular ions in the gas phase. This was achieved by ablation using a nitrogen laser delivering 60 μJ in a 5 ns pulse. The laser beam was incident at 45° on the sample and was focused to give a spot size of approximately 80 μm by 40 μm. The harmonics (1064, 532, 355, 266nm) of a Nd:YAG laser can be used for the fragmentation of the molecular ions. The triggers for the ablation and fragmentation lasers were generated by a digital pulse generator. The time delays between the ablation and fragmentation lasers were generated using a custom-built delay unit accurate to 10 ns. The ablated ions were directed by an ion optics into a field-free flight region. The laser fragmentation of selected ions occurs at the turn-around point of the ion trajectories near the end of the reflectron. The ions fragmented were detected by a dual microchannel plate detector with an aperture of 2.5 cm diameter . The signals were recorded by a digital storage linked to a Compaq 386 personal computer.

This new TRTOF will be described in detail in seven parts: fragmentation trajectories of ions in the reflectron, mass calibration of fragmentation ions, selection of parent ions to be fragmented, fragment ion collection, reflectron field effect, fragmentation mass resolution, and influence of the fragmentation laser parameters.

5.2 Theoretical considerations of the trajectories of fragment ions in the reflectron

From the ion trajectories(Fig.5.2) simulated by SIMION, ions with greater kinetic energy penetrate deeper into the reflectron than those with lower energy. If the reflectron is well adjusted, all ions with the same m/z but with different initial kinetic energies will arrive at the detector at the same time. This compensation of energy spread is the main advantage of a reflectron TOF instrument. On entering the

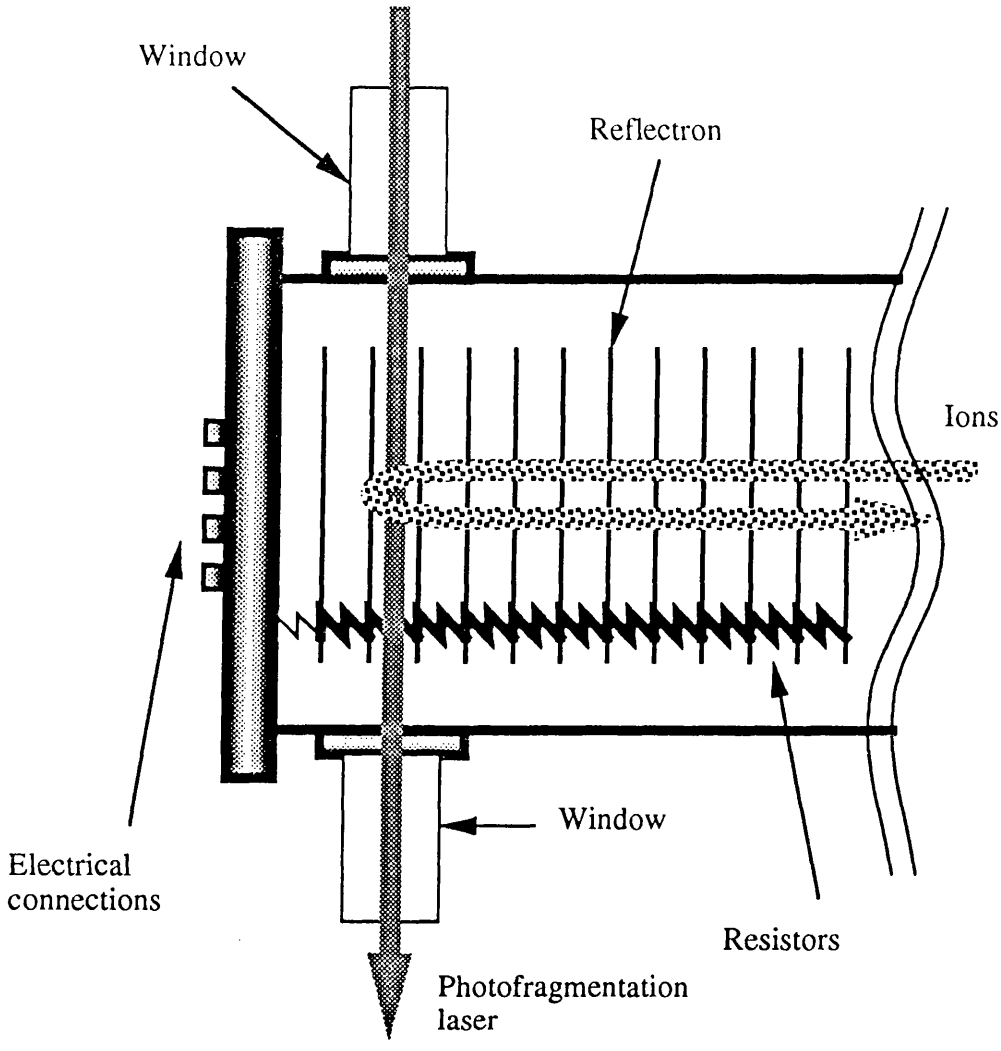

Fig.5.1 Plan view of the end of the TOF tube in TRTOF mass spectrometer

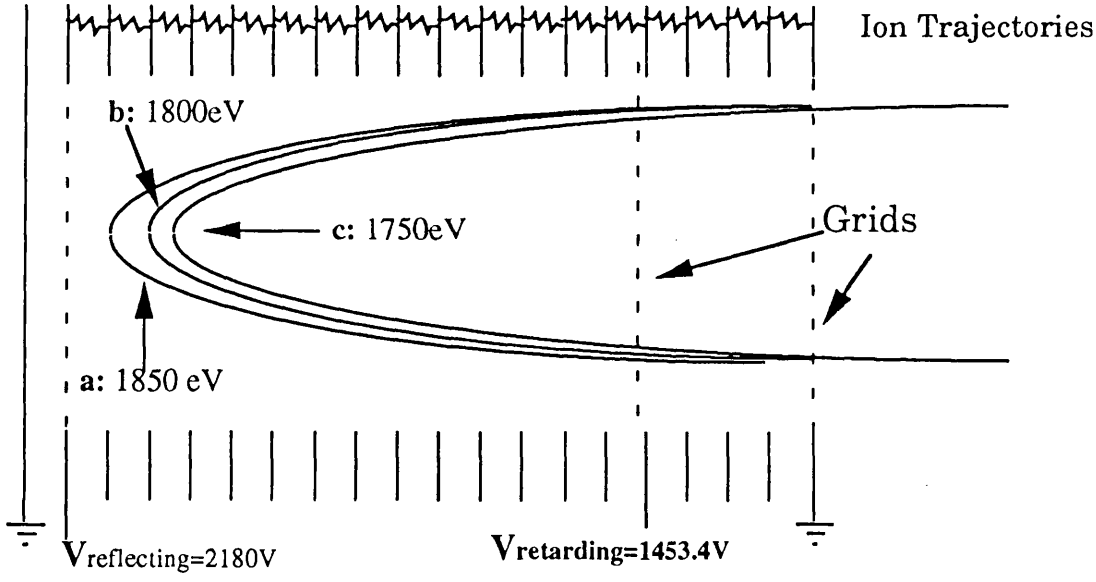

Fig. 5.2 Diagram showing the trajectories of ions with different kinetic energies. Higher energy ions penetrate deeper into the field than lower energy ions, resulting in a reduction in the spread of arrival times at the detector.

reflectron, the ions decelerate, almost reaching zero velocity in the vicinity of the turn-around point and then accelerate again towards the detector. The slowly moving ion packets spend about 3 to 4 μs in the turn-around region where they can be irradiated by a laser beam and fragmented. Consequently, it is necessary to predict where the turn-around point of ions in the reflectron is before the experiments could be carried out.

The position of the turn-around point of ions can be adjusted by changing the voltages on the reflecting fields. The maximum voltage on the reflecting field should not be lower than that on the sample stub in case the ions directly pass through the reflectron. But if the kinetic energy of ions is too small, the ions can't reach the photofragmentation area, therefore they can't be radiated and fragmented by a fragmentation laser. The voltage on the retarding field usually is adjusted to approximately 2/3 $V_{reflecting}$ in order to get better mass resolution. The expected position of turn-around point of ions in the reflectron was calculated by SIMION. Fig.5.2 also shows the grid configuration, the voltages on the retarding and reflecting fields. In this configuration, ions could reach the photofragmentation area, and tandem TOF-TOF experiments can be carried out. The field uniformity in this design is the reason why it has a high mass resolution. Given the general picture of the field design, one can consider ion motion through this reflectron. Fig.5.2 demonstrates how the reflectron transmits ions of the same mass and different kinetic energies. The ion (154 m/z) with energy of 1850 eV(see trajectory a) penetrates deeper into the reflecting field than those with lower energies 1800eV, and 1750eV (see trajectories b, c). Therefore the ions with slightly different kinetic energies spread spatially at the turn-around region. It has been estimated by SIMION that this region is about 0.5-1.5 cm varying according to the intensity of the ablation laser and sample characteristics. Hence an unfocused fragmentation laser beam was used to cover this region in order to get fragmentation mass spectra more efficient.

The delay time between the ablation laser and the fragmentation laser can be calculated from the known TOF tube length (3m), acceleration voltages and the time spending in the reflectron by SIMION if the fragmentation position is fixed. For the parent ion ((M-OH), M=2,5-DHB, m/z=137), the calculated delay time was 37.17 μs, which was in consistent with the actual delay time in the experiment (36.40 μs).

According to the Cornett's TRTOF configuration(Cornett et. al., 1992), the different fragmentation patterns from the same parent ions were observed due to early or late

excitation by changing the delay between the two lasers. It was found by using SIMION that the trajectories of the various fragment ions are different before or after excitation. To avoid this phenomenon, the fragmentation laser was arranged to access perpendicularly to the plane of the parent ion trajectories at the turn-around region. The detail discussion will be presented in the section 5.5.

5.3 Mass calibration

The mass calculation of the fragment ions from fragmentation mass spectra is slightly different from that of ordinary mass spectrometers. If the fragmentation laser is fired a time t_d after the ablation laser, then the fragment ion mass M_f is given in terms of the parent ion mass M_p by the following equation:

$$M_f = \frac{M_p(t_f - t_d)^2}{(t_p - t_d)^2} \qquad \text{(Eq.5.3.1)}$$

where t_f and t_p are the arrival times of the fragment and the parent ions respectively, measured with respect to the ablation laser. The delay time t_d can be calculated from the known TOF parameters mentioned above. However, t_d also depends on the precise position in the turn-around region where the fragmentation happens and may be uncertain by 2 to 3 μs. Therefore, in order to obtain an exact mass of the fragment ions, TRTOF was first calibrated by fragmenting an ion with a known fragment pattern. CsI was chosen for this purpose not only because it has been used as a calibration sample for ordinary TOF mass spectrometers, but also because it has simple fragmentation pattern of its plasma ions. Fig.5.3 shows the ablation mass spectrum of CsI by a nitrogen laser (337 nm). A large Cs^+ ion peak and some clusters of CsI, such as $(CsI)Cs^+$, $(CsI)_2Cs^+$ have been identified. The peaks of $Pb(SO_4)^+$ and its isotope compounds were impurities in the CsI sample (British Drugs Houses Ltd, Poole, Dorset, UK). The spectrum also indicates that there was no CsI^+ peak.

$(CsI)Cs^+$ was selected for calibration of fragmentation of molecular because of its relatively high intensity of the ion peak comparing to that $(CsI)_2Cs^+$ and simple fragmentation pattern. The fragmentation mass spectrum of $(CsI)Cs^+$ by a 266 nm laser(2.5 mJ, unfocused, 5 mm in diameter) is presented in Fig.5.4a. The spectrum b in Fig.5.4 is the ablation only spectrum with the fragmentation laser switched off. It can been seen in Fig.5.4 that the peaks of CsI^+, Cs^+ and $(Cs)_2^+$ are apparent. In the experiment it was also found that $(CsI)Cs^+$ could not be fragmented by a 355 nm

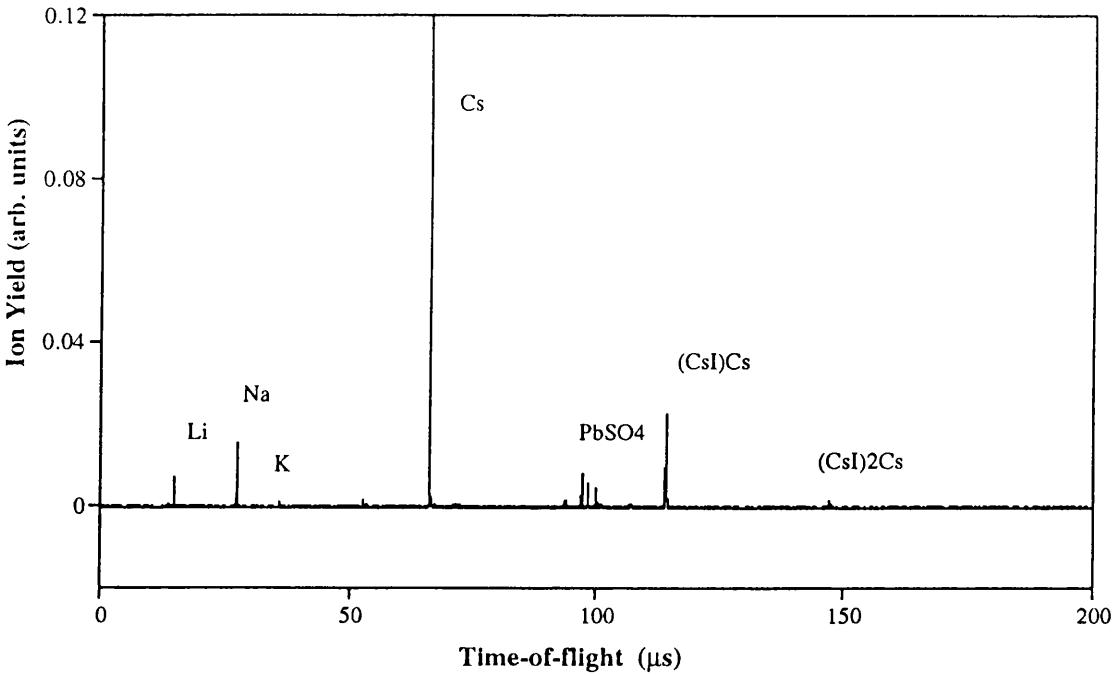

Fig.5.3 The mass spectrum of CsI ablated by a 337 nm laser. (CsI)I was selected as a parent ion.

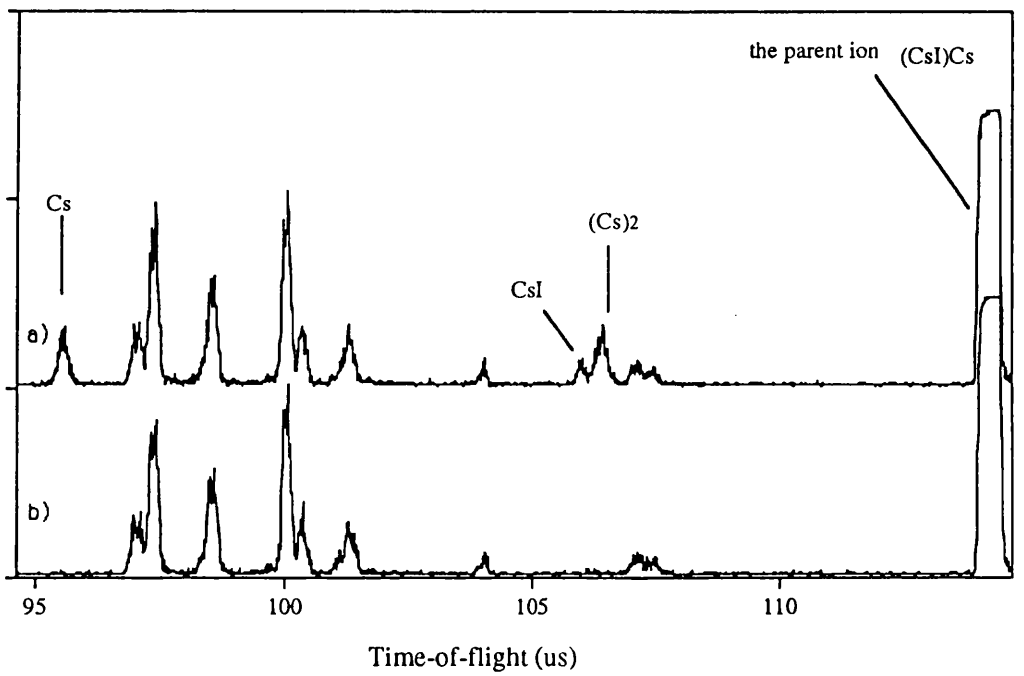

Fig.5.4 The fragmentation mass spectra of $(CsI)Cs^+$. The ion of $(CsI)Cs^+$ was fragmented by a laser (266nm, 2.5 mJ, unfocused), a) the fragmentation mass spectrum of $(CsI)Cs^+$. The fragments of Cs^+, CsI^+, and $(Cs)_2^+$ from $(CsI)Cs^+$ are obtained. b) the background mass spectrum with the fragmentation laser off.

laser (30 mJ, unfocused, 5 mm in diameter). These phenomena indicate that the mechanism of ion formation during the ablation process is considerably different from that in the photofragmentation process. The exact agreement with the expected known masses of Cs^+, CsI^+, and $(Cs)_2^+$ was obtained by varying t_d and using equation (5.3.1). Subsequently, the reflectron voltages were optimised for the maximum ion signals since there is a density distribution in the parent ion packet. These conditions were kept constant in the subsequent fragmentation experiments. The delay times for the other parent ions can now be calculated from the following equation:

$$t_d = \frac{t_r M_p^{1/2}}{M_r^{1/2}} \qquad \text{(Eq.5.3.2)}$$

where t_r and M_r are the delay time and mass of the reference parent ion which has already been fragmented.

5.4 Selection of parent ions to be fragmented

A particular parent ion can be fragmented by selecting the delay of firing of the fragmentation laser with respect to the ablation laser. Fig.5.5 demonstrates the various fragmentation patterns of the molecular ions from 2,5 dihydroxybenzoic acid (2,5-DHB) using a 355 nm fragmentation laser. At a delay of 34.25 μs, none of the molecular ions have reached the turn-around region in the reflectron, and hence no fragment ions were observed. This mass spectrum indicates that there were three main mass peaks from 2,5-DHB: (M-OH)(m/z: 137), M(m/z: 154), and a peak associated with the dimer of (M-OH), (2(M-OH)-H)(m/z: 273). The ion peak of (M-OH) was the largest among these peaks. This is typical ablation mass spectrum of a single crystal of 2,5-DHB.

On increasing the delay time to 35.25 μs, $(M\text{-}OH)^+$ was irradiated by the fragmentation laser, and 6 fragment ions were recorded. These daughter ions are $C_2H_x^+$, $C_3H_x^+$, $C_4H_x^+$, $C_5H_x^+$, m/z 80 and $(M\text{-}CO_2H)^+$. The peaks ratios and shapes are obviously different, but one can gain some insight into the mechanism of photofragmentation of molecular ions. Both $(M\text{-}OH)^+$ and M^+ were fragmented at a delay of 37.25 μs, and a number of fragments from both $(M\text{-}OH)^+$ and M^+ were observed. At that time, both $(M\text{-}OH)^+$ and M^+ were in the fragmentation region. For the longer delay (39.25 μs), $(M\text{-}OH)^+$ had already passed through the fragmentation region and was not fragmented. Only fragment ions from $M^{+\cdot}$ were

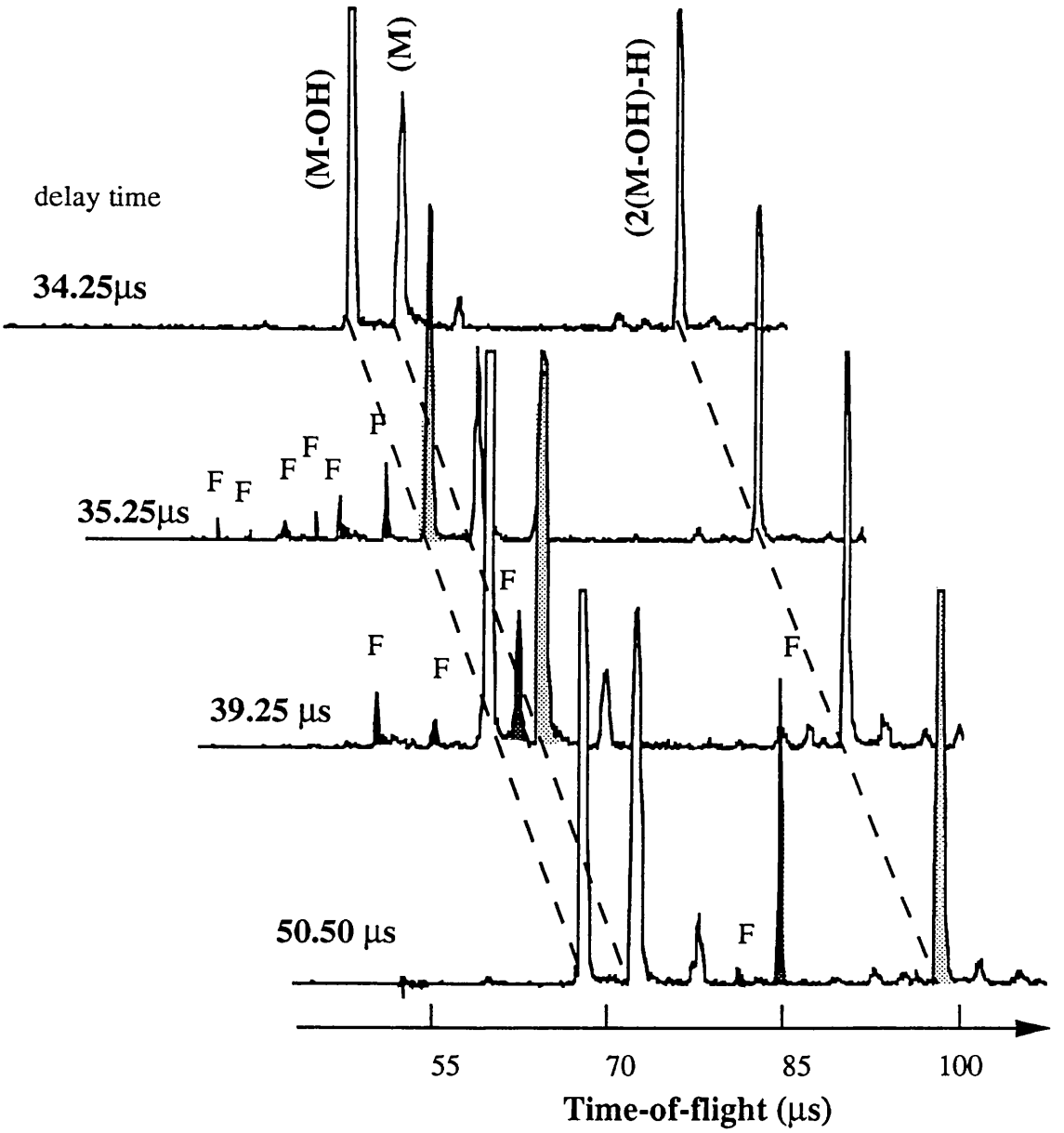

Fig.5.5 The various fragmentation patterns of the molecular ions from 2,5-DHB produced by a 355nm fragmentation laser. At the delay of 34.25 μs, no molecular ions was fragmented because no parent ions arrived at the turn-around region in the reflectron. At the delay of 35.25 μs, $(M\text{-}OH)^+$ was fragmented, and six fragments were observed: At the delay of 39.25 μs. $(M)^+$ was fragmented and three fragments were found. Finally at 50.50 μs delay, $(2(M\text{-}OH)\text{-}H)^+$ was fragmented and another fragmentation pattern was observed. ("F" represents a fragment ion).

obtained. This fragmentation pattern is totally different from that of $(M\text{-}OH)^+$. The daughter ions are $(M\text{-}OH)^+$, $C_4H_x^+$, and m/z 80. The largest fragment ion from $M^{+\cdot}$ is $(M\text{-}OH)^+$ which is reasonable because the intact parent ion of 2,5-DHB is easily fragmented to $(M\text{-}OH)^+$(see its ablation mass spectrum in Chapter 4). A question rose why there were no fragments of $C_2H_x^+$, $C_3H_x^+$, and $C_5H_x^+$? It is very difficult to answer until the underlying mechanism of this fragmentation could be understood. Finally, when the delay was increased to 50.50 μs, the dimer of (M-OH), $(2(M\text{-}OH)\text{-}H)^+$ was dissociated and fragment ions of $C_2H_x^+$, $C_3H_x^+$, $C_4H_x^+$, $C_5H_x^+$, m/z 80, $(M\text{-}CO_2H)^+$, and $(M\text{-}OH)^+$ were found(the ions of $C_2H_x^+$, $C_3H_x^+$, $C_4H_x^+$, $C_5H_x^+$, m/z 80 can only be seen in amplification, see Chapter 6 in details). A large (M-OH) fragment ion appears due to the weak bond between (M-OH) and (M-OH). All the smaller fragment ions probably came from further laser photofragmentation of $(M\text{-}OH)^+$.

A detailed investigation of fragmentation patterns and mechanisms will be described in the chapter 6. The data presented here show that it is possible to fragment a given molecular ion at the turn-around point with good selectivity.

5.5 Fragment ion collection

After fragmentation, the daughter ions follow different trajectories relative to the parent ion according to their m/z ratio. Assuming that the parent ion, $(M\text{-}OH)^+$, was fragmented at the turn-around point in the reflectron, Fig.5.6 presents the trajectories of the various fragments simulated by SIMION. From this simulation, it can be seen that the smaller fragment ions move closer to the reflectron central axis, and the heavier fragments lie closer to the parent ion trajectory. This explains the diverging trajectories: when moving into the reflectron, the parent ion reduces its velocity(V_x) in the X-direction, but keeps a constant velocity in the Y-direction (V_y)(the directions of X and Y are shown in Fig.5.6). At the turn-around point, the parent ion moves only in the Y direction. After fragmentation, the daughter ions are produced and almost have the same velocity as their parent (V_y). When they are moving away from the fragmentation point, their V_x are increasing again. The distance where they cover from the fragmentation point to the detector in the Y direction can be calculated by the following equation:

$$D_y = t \cdot V_y \qquad \text{(Eq.5.5)}$$

where t is the travelling time of the fragment ion from their generation to the arrival at

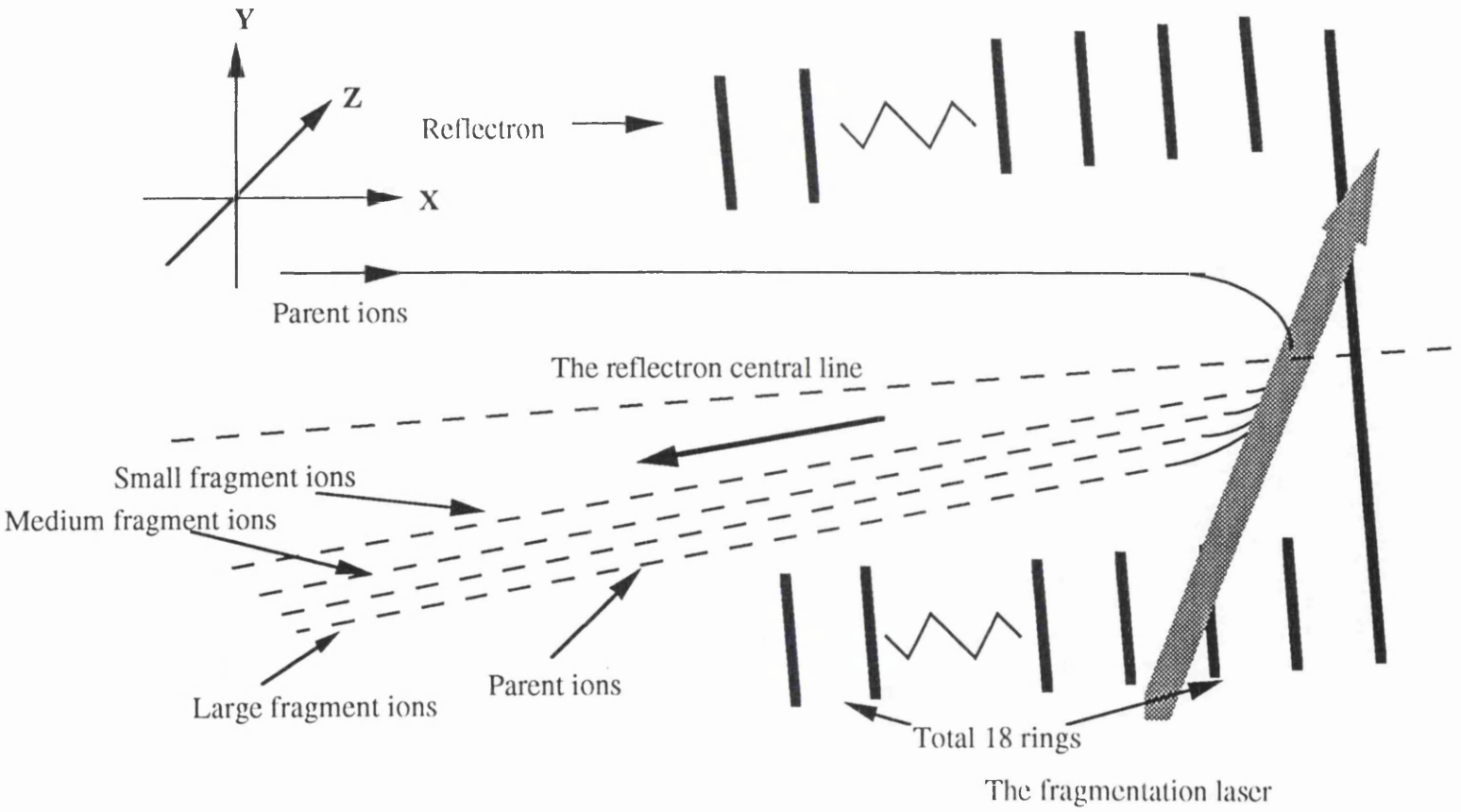

Fig.5.6 The ion trajectories fragmented at the turn-around point in the reflectron. The smaller fragment ions move closer to the reflectron centre axis and the heavier fragments will be closer to the parent ion trajectory. The laser beam is at right angles to the plane of the page.

the detector. The small daughter ions spend less time travelling into the detector than those of large ones. Therefore the distance of the smaller fragment ions is less than those of large ones and they move closer to the reflectron central axis. The spatially spreading of these daughter ions after fragmentation at the turn-around point causes mass discrimination and erroneous branching ratios in the product channels if the detector is not large enough to receive all the fragment ions. The trajectories of the daughter and parent ions can be changed by varying the voltages on the Y-deflecting plates. Fig.5.7 schematically demonstrates the change of ion trajectories by Y-deflecting plates. In the trajectory 1(the bold line) , the small daughter ion arrives at the detector, but the large fragment ion can't move into the detector. By increasing the voltage on the Y-deflecting plates, the parent ion is forced to change its trajectory away from the reflectron central axis, hence its large daughter ion moves closer to the central axis, and can reach to the detector(see trajectory 2 in Fig.5.7).

Fig.5.8 is the fragmentation mass spectra of 2,5-DHB obtained by varying the voltages on the Y-deflecting plates and the diverging trajectories of fragments in this photofragmentation configuration are clearly observed. The mass spectrum in Fig.5.8a shows that the parent ion peak is relatively small. This is because most of the parent ions are not in the aperture of the detector and the collection efficiency is small. By applying the higher voltage on the deflecting plates, daughter ions move closer to the reflectron central axis, hence more fragment and parent ions arrive at the detector and the efficiency of ion collection is increased(see Fig.5.8b). On further increasing the voltage, the fragment ions (Fig.5.8c) move out of the detector and only the large ablation parent ion signals remain. This experiment proves the existence of diverging trajectories of fragment and parent ions. From the sign of the deflecting voltages it can be deduced that the trajectories of the fragment ions are closer to the reflectron central axis. This geometric effect can be reduced by using a large aperture detector or by introducing an einzel lens after exiting the reflectron.

5.6 Reflectron field effect

One of the advantages of a reflectron TOF mass spectrometer which was mentioned above is the compensation of the initial kinetic energy spread of the ions. The ions with different energies are separated spatially at the end of the reflectron. If the position of photofragmentation is fixed, the apparent kinetic energy spread of the parent ions produced by an ablation laser can be deduced. This interesting finding gave us a new method to measure kinetic energy spreads of ablated ions. However this adversely affects the laser excitation efficiency of the parent ions. Increasing the

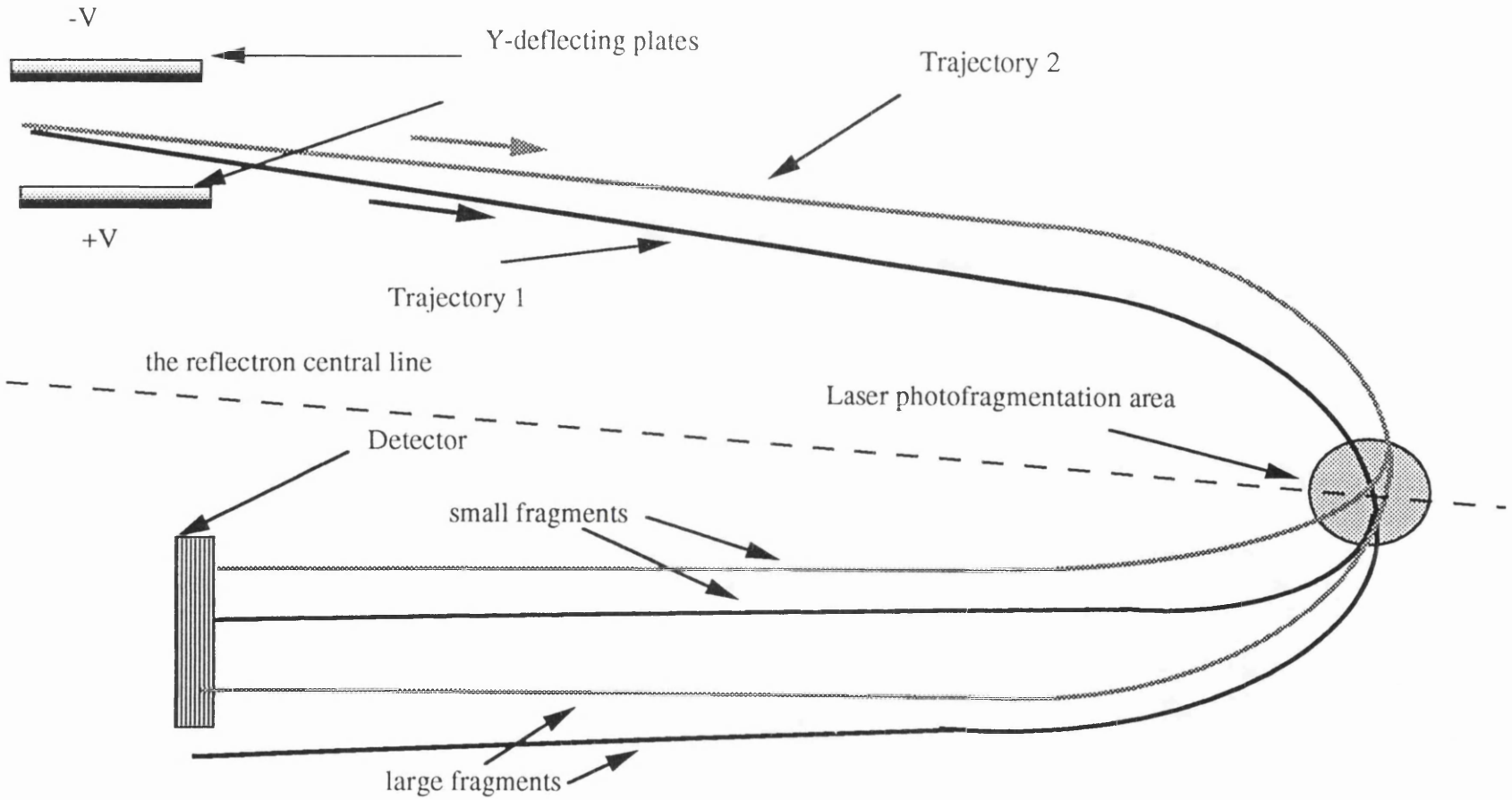

Fig.5.7 The schematical diagram of the change of ion trajectories by the voltage on the Y-deflecting plates. In the trajectory 1, only small daughter ions can arrive at the detector. By increasing the voltage on the Y-plates (negative), the parent ion is forced to change its tragectory away from the reflectron central axis, hence its larger daughter ions or itself can reach the detector.

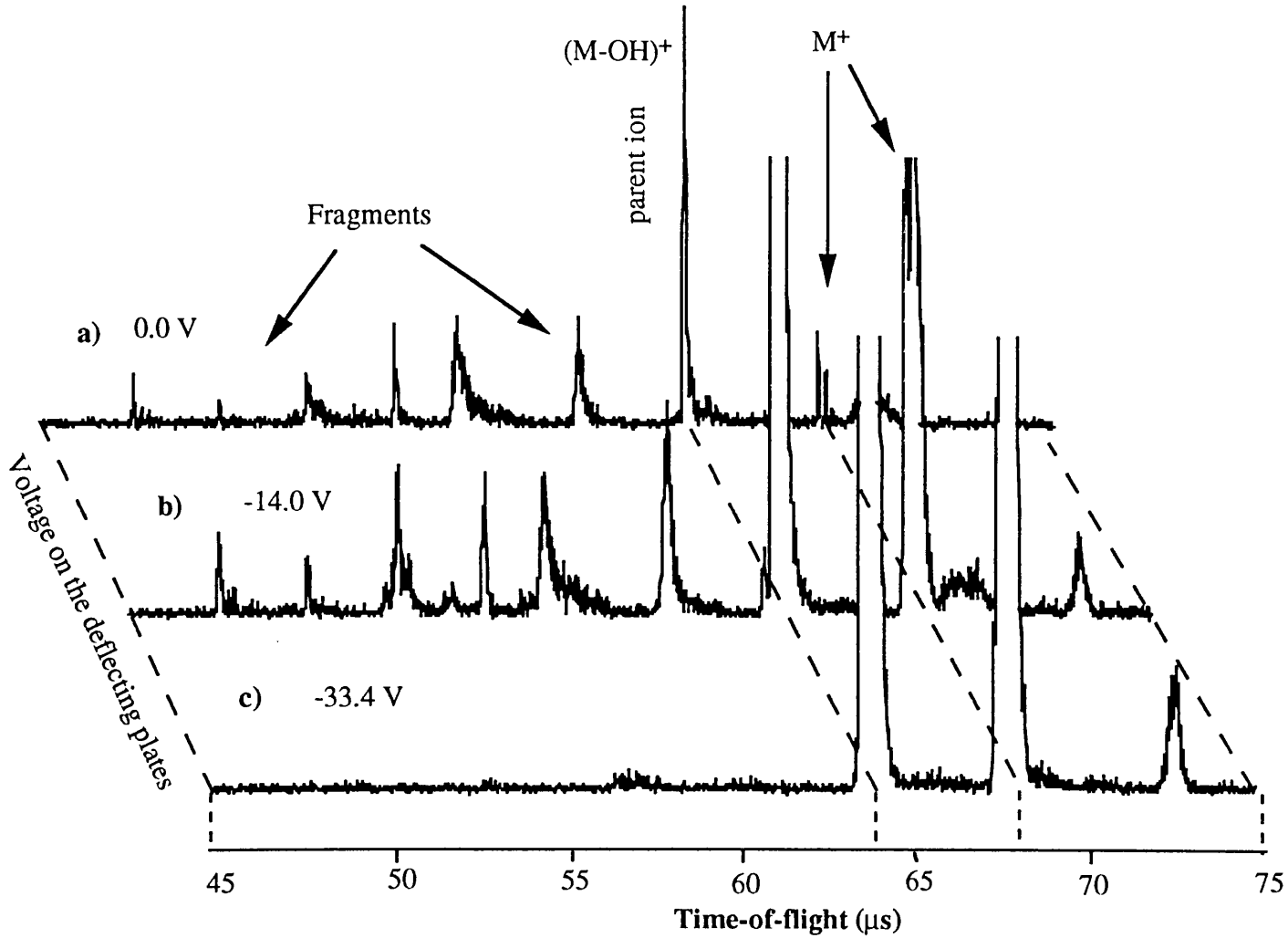

Fig.5.8 The fragmentation mass spectra of (M-OH) from 2,5-DHB by varying the voltages on the deflecting plates. Some of the peaks are missing since their trajectories fall out with the demensions of the detector.

fragmentation laser intensity by focusing the laser beam reduces the interaction volume and does not necessarily provide a greater yield of fragmented ions. The spot size of the fragmentation laser used was about 5 mm in diameter which gave reasonable fragment ion signals.

By changing the reflecting voltage, the turn-around region of the parent ion packet in the reflectron can be moved forwards and backwards. Fig.5.9 shows the fragmentation mass spectra of $(M\text{-}OH)^+$ against reflecting voltage. In these mass spectra, the fragment ion signals increased and then decreased with the increase of reflecting voltage as the ion beam moved through the fragmentation laser beam. At 2168 V, the fragmentation efficiency was highest. However, at 2215 V, the parent ions could not reach the fragmentation area, and no fragment ions were observed. The ion yields of the three fragment ions from $(M\text{-}OH)^+$ against the reflecting voltage have been plotted in Fig.5.10. It can be deduced that the parent ions have an energy spread of around 50eV (FWHM). The distribution of the kinetic energy of the parent ions occurs probably due to the ablation processes. To maximise the fragment ion signals, the reflecting voltage must be adjusted to move the maximum of the ion distribution to coincide with the laser position. It can also be seen from Fig.5.10 that the fragmentation pattern is largely unaffected by the kinetic energy spread of the parent ion. A variation of the parent ion kinetic energy might imply a variation in the molecular internal energy in the ablation process which could lead to different fragmentation patterns.

5.7 Fragmentation mass resolution

The mass resolution of fragment ions can be deduced to

$$\frac{M}{\Delta M} = \frac{(t_f - t_d)}{2\Delta t_f} \qquad \text{(Eq.5.7.1)}$$

here t_f and t_d are as defined earlier, $(t_f\text{-}t_d)$ is the flight time of the fragment ion since its production. Δt_f is the FWHM of the fragment ion peaks. Fig.5.11 shows the typical fragmentation mass spectrum of $(M\text{-}OH)^+$ from 2,5-DHB induced by the laser operating at 355 nm. A typical mass resolution of 64 at m/z 68 was obtained. The mass resolution was poorer than that obtained by a normal reflectron TOF mass spectrometer. Let us look the following diagram (Fig.5.12) of fragmentation of a parent ion at its turn-around point.

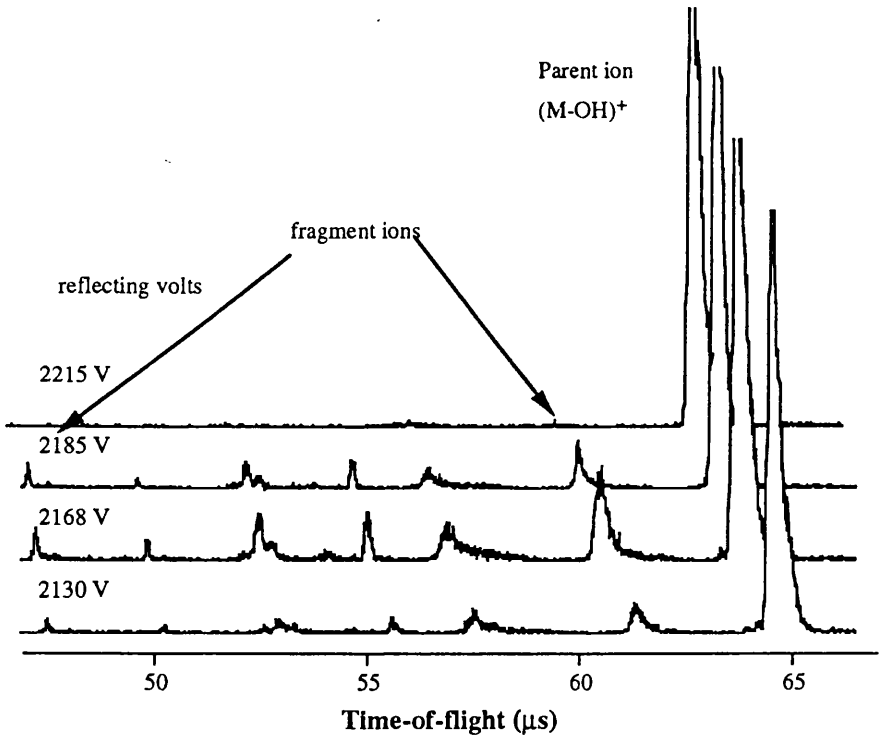

Fig.5.9 The fragmentation mass spectra of $(M-OH)^+$ from 2,5-DHB by a 355nm laser for various reflecting voltages. The fragment ion signals increased and decreased with the increase of the reflecting voltages.

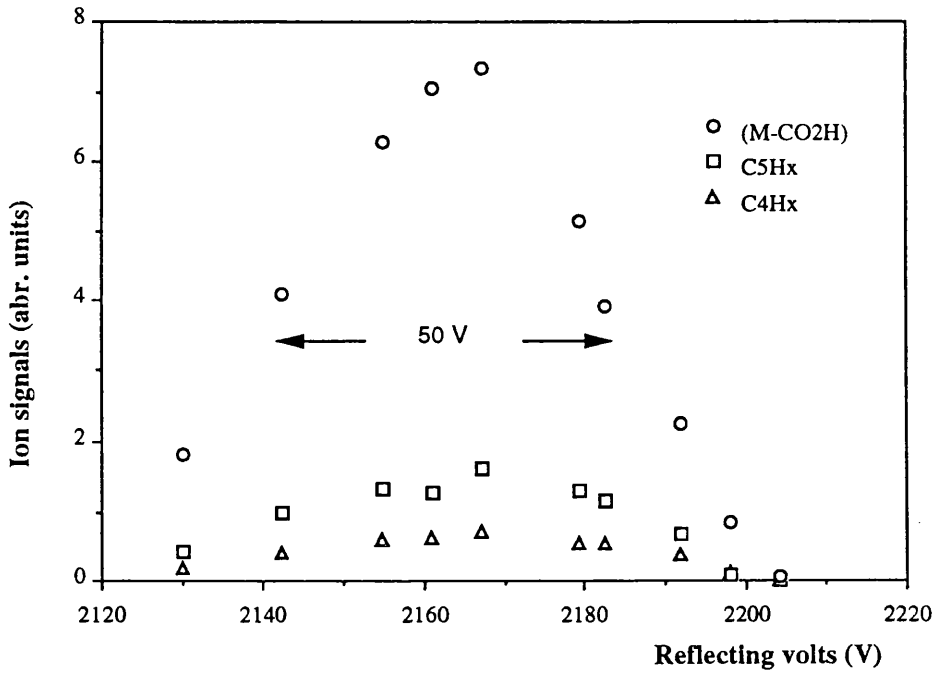

Fig.5.10 The ion signals of the three fragments from $(M-OH)^+$ against the reflecting volts. The pulse energies of the nitrogen ablation laser and the 355nm fragmentation laser are 70 μJ and 25 mJ respectively. The kinetic energy spread of the parent ion is deduced to be 50 eV.

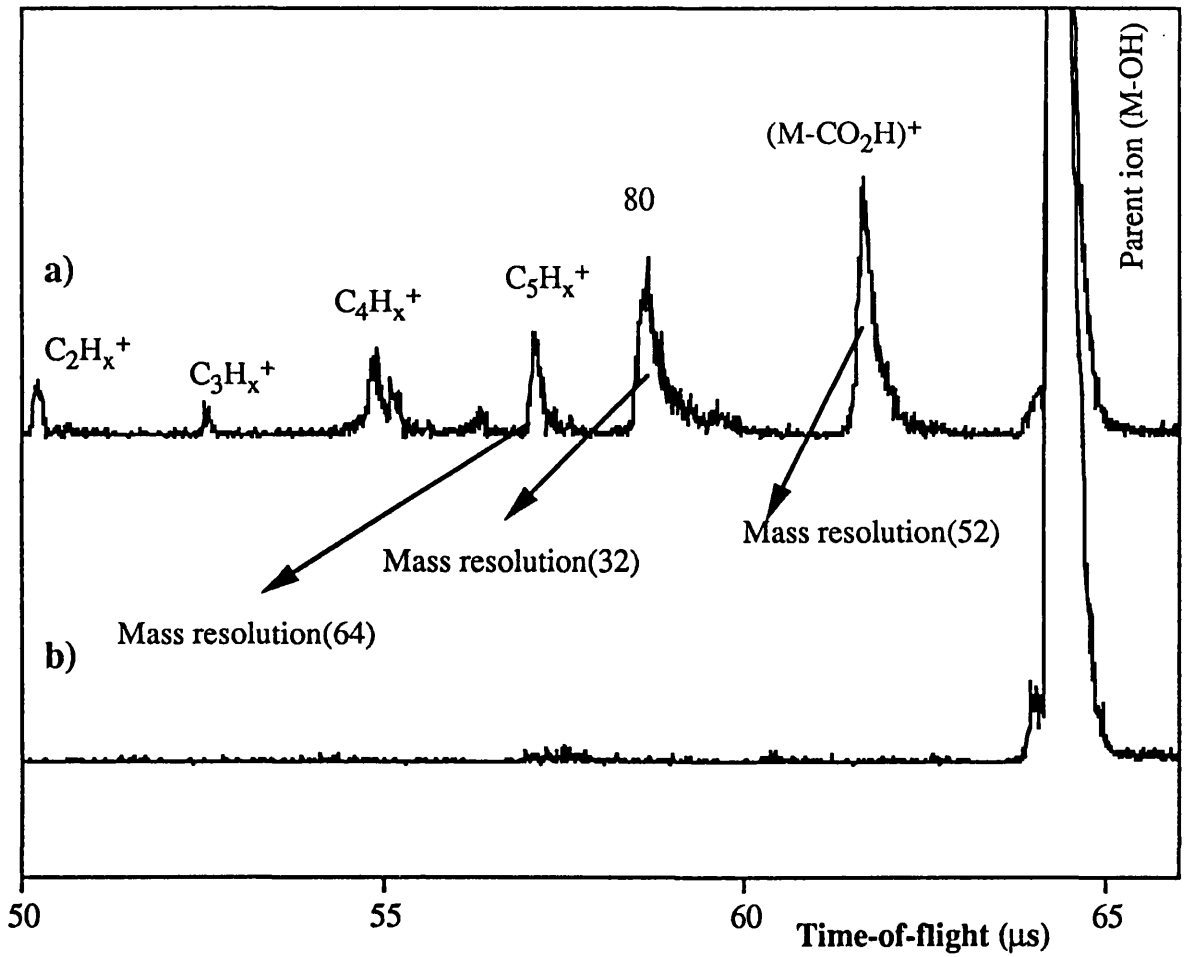

Fig.5.11 A typical fragmentation mass spectrum. a) with the photofragmentation laser(355nm) on. b) with the photofragmentation laser off.

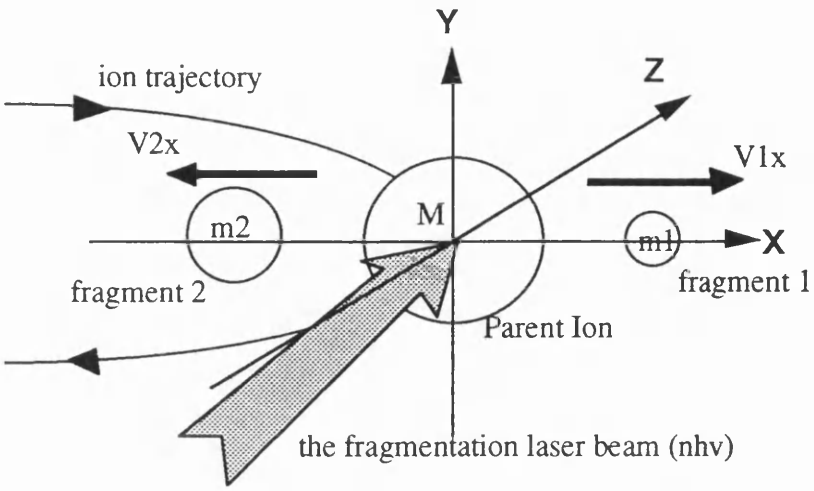

Fig.5.12 The schematic diagram of a parent ion(M) fragmented by a laser into its two daughter ions(m1 and m2).

For simplicity, assuming that the parent ion (M) was fragmented by a fragmentation laser into two daughter ions(m_1 and m_2). The fragment ions moving only in the direction of X axis will affect the fragmentation mass resolution. The ions moving in other direction (Y and Z directions) only cause the spatial divergence. In order to estimate the worst mass solution in this photofragmentation configuration, let us consider the two extreme conditions in which the daughter ion (m_1) moves directly towards the X axis direction or its opposite direction. The velocity of the daughter ion (m_1) at its turn-around point can be calculated by using the following two equations if the photon energy (E) was transferred to their kinetic energy and internal excited energy(E_{in}):

$$E = \frac{m_1 V_{1x}^2}{2} + \frac{m_2 V_{2x}^2}{2} + E_{in} \qquad \text{(Eq.5.7.2)(energy conservation)}$$

$$m_1 V_{1x} + m_2 V_{2x} = 0 \qquad \text{(Eq.5.7.3)(momentum conservation)}$$

All the other symbols are defined in Fig.5.12. Usually the fragmentation of molecular ions under these experimental conditions, e.g. the pulse energy of a photofragmentation laser was 30 mJ, unfocused, is about two-photon process(the details in Chapter 6). Most of the photon energy is used for the fragmentation and internal excitation of the fragment ions. Therefore less than 1 eV of the kinetic energy was estimated. From the equations of (5.7.2) and (5.7.3), the V1x can be deduced:

$$V_{1x} = \pm\sqrt{\frac{2(E-E_{in})}{m_1(1+m_1/m_2)}} \quad \text{(Eq.5.7.4)}$$

The signs of ± represent the two direction in the X axis. Let us estimate the normal mass resolution of this TOF/TOF instrument in the normal operation conditions. Assuming that there are two fragments from $(M\text{-}OH)^+$ (137 m/z)), m_1 =68 (m/z) and m_2=69 (m/z), the initial potential on the stub is 2205 eV, reflecting voltage is 2237 V, $(E\text{-}E_{in})$ is 1 eV, the mass resolution can be calculated by using an computer program " TRTOF " written by the author (see appendix). The results show that the time-of-flight of m_1 with $+V_{1x}$ fragmented at its turn-around point is 55.564 μs, while the time-of-flight of m_1 with $-V_{1x}$ is 55.900 μs, Δt=0.336 μs, hence the mass resolution is $83(t/2\Delta t)$. It is nearly consistent with the mass resolution (64 at m/z 68) obtained from the experiments. Therefore the TRTOF still has a comparable mass resolution to other tandem TOF mass instruments such as CID, SID(Jardine, et al 1992. Williams, et al. 1993).

From the theoretical analyses described above it can be predicted that the more similar the daughter's ions are, the worse the mass resolution is. Fig.5.13 theoretically displays the relationship between the masses of fragments and the fragmentation mass resolution. It demonstrates that the mass resolution of the fragments is poorest when the daughter's masses are the same, and the mass resolution increases as the mass difference between the two fragment ions increases. Moreover $(E\text{-}E_{in})$ has also a significant influence on the mass resolution. Fig.5.14 shows the relationship between $(E\text{-}E_{in})$ and the mass resolution assuming two same mass daughters (70 m/z) produced from their parent ion(140 m/z) by laser photofragmentation. The mass resolution falls sharply with an increase of $(E\text{-}E_{in})$ and tends to be limited to the mass resolution of 50. The limitation of the mass resolution does not depend on the fragmentation mechanism of the molecular ions, but the parameters of the reflectron.

Other factors, such as the size and intensity of the fragmentation laser beam, reflecting voltage settings also affect the fragmentation mass resolution. In the inset of Fig.5.15 it demonstrates the relationship between the signal intensity and the fragment ion peak width (FWHM) of $(M\text{-}CO_2H)^+$ with respect to laser spot diameters. It can be seen that although the signal intensity decreases with decrease of

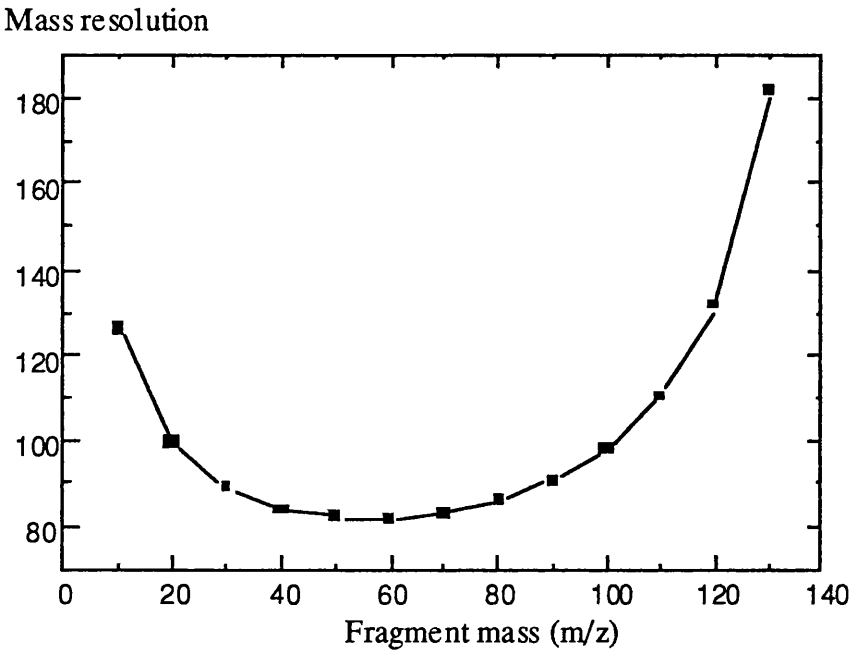

Fig.5.13 The theoretical relationship between TRTOF mass resolution and fragment mass (m/z). Assuming Uo =2205eV, Uc =2237 V, parent ion (m)=140, (E-Ein)=1 eV.

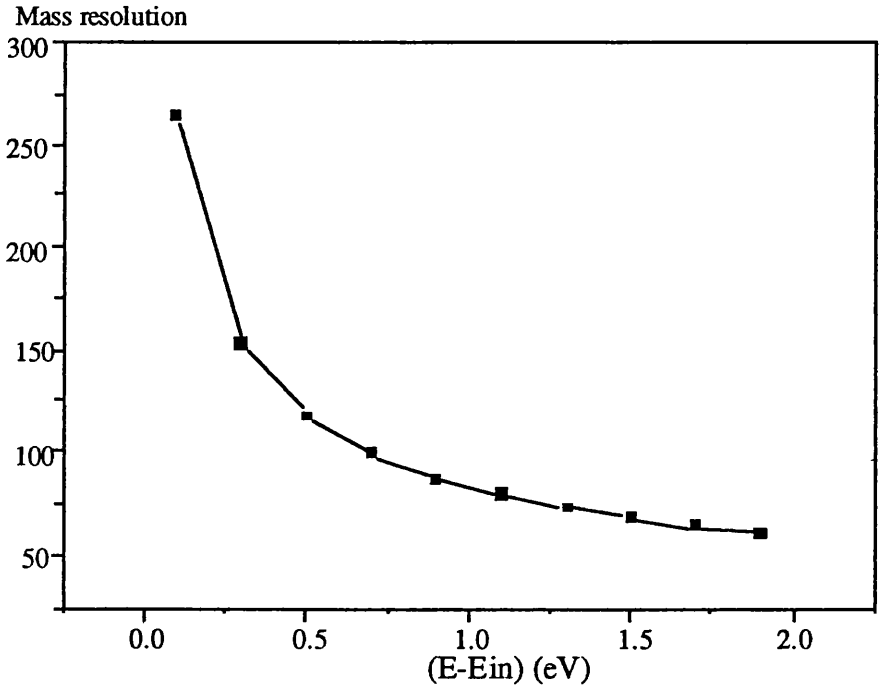

Fig.5.14 The relationship between Ek and fragmentation mass resolution. Assuming Uo=2205 eV, Ub=1491 V, Uc=2237 V, the parent ion (m, m/z)=140, the two fragments (m1, m2, m/z)=70.

the laser spot, the mass resolution increased slightly at the same mass peak because the excitation area was reduced. In our case, these effects do not lead to significant

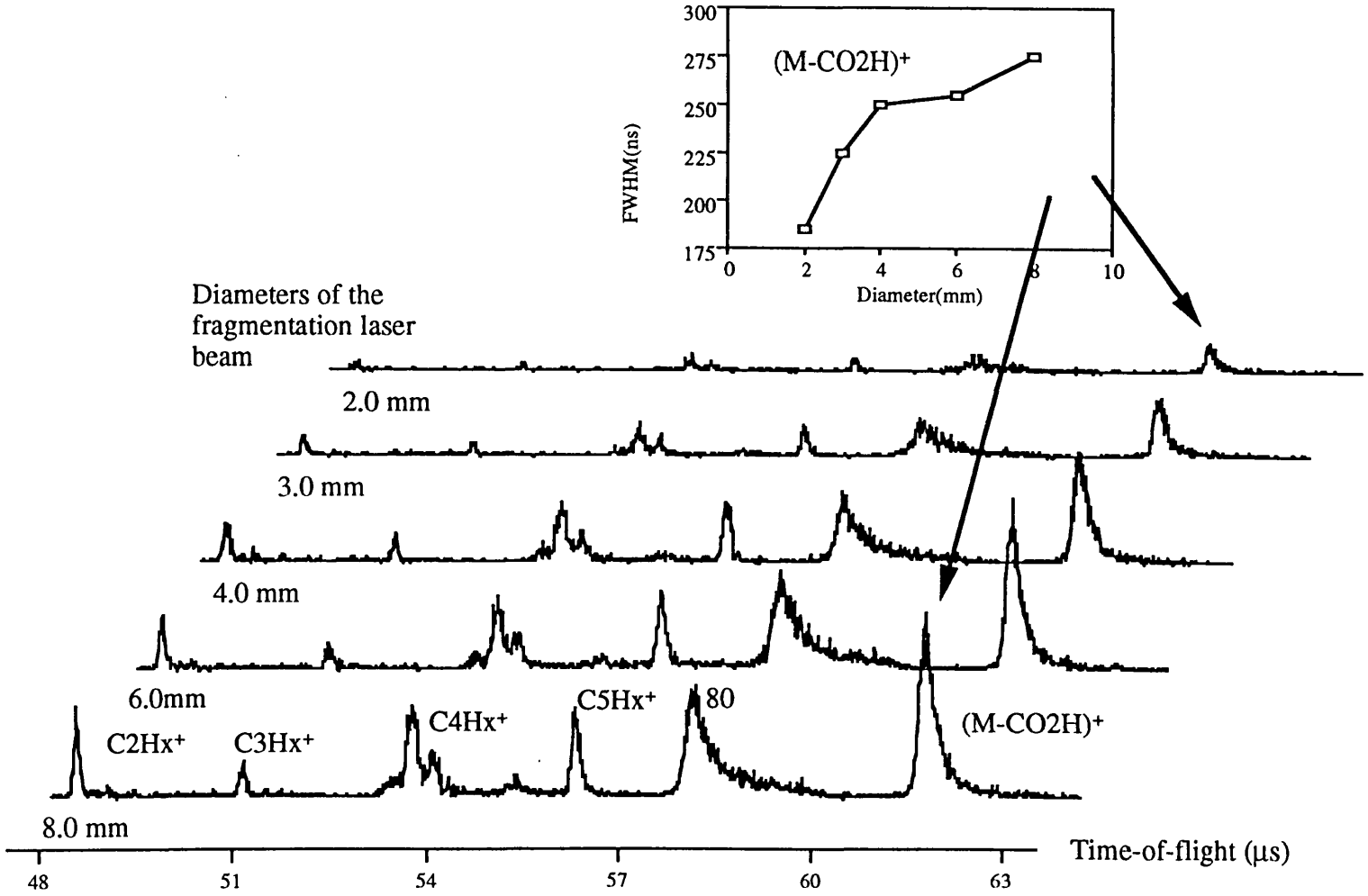

Fig.5.15 The influence of fragmentation laser spots on the fragmentation mass spectra of $(M\text{-}OH)^+$ from 2,5-DHB. The fragment peak intensity decreases with the decreasing of the laser spot size, but the mass resolution slightly increases. The inset graph shows the relationship between the laser spot diameters and FWHM of the fragment of $(M\text{-}CO2H)^+$.

changes in the mass resolution.

From Fig.5.11 it can also be seen that the mass resolution for some fragment ion peaks is different. One possible explanation is that different dissociation mechanisms are involved, for example, the poor mass resolution of the fragment ion of m/z 80 was caused by metastable decay of the ion(details can be seen in Chapter 6).

5.8 Influence of the fragmentation laser parameters

There is a significant influence of the fragmentation laser parameters (wavelength and laser flux) on the fragmentation mass spectra. Laser wavelength determines the photon energy and leads to changes in photofragmentation patterns. The laser flux affects the absorption processes of molecular ions which also leads to changes in patterns of mass spectra. Fig.5.16 shows the influence of the laser wavelength on the fragmentation pattern of 2,5-DHB at 266 nm. This is substantially different from the fragmentation pattern at 355 nm shown in Fig.5.11. The largest fragment of $(M-CO_2H)^+$ in the mass spectrum of Fig.5.11 is absent. In addition, the mass resolution in Fig.5.16 was slightly better than that in Fig.5.11. This phenomenon implies that the different dissociation pathway involved in the photofragmentation. The influence of laser flux is clearly visible with the low mass fragment intensities becoming more prominent as the laser flux increases. The details will be discussed in the following chapter. It is expected that by varying the laser parameters, a greater insight and control of the fragmentation mechanisms of ions will occur.

5.9 Conclusions

It has been shown that a TRTOF of considerable potential can be adapted from an ordinary reflectron TOF instrument to carry out tandem MS/MS experiments. The instrument has a relatively simple timing requirement for overlapping the pulsed laser and ion packets, and also has a multichannel detection capability of fragment ions. Furthermore, different fragmentation patterns can be obtained by changing the fragmentation laser intensity and wavelengths. This is of considerable potential for increasing our understanding of photofragmentation of molecular ions and our ability to determine the structure of large biomolecules. Although the TRTOF described here has a somewhat limited mass resolution and mass discrimination, already in its present form it is likely to be of great importance in the many experiments where high resolution is not required e.g. gas phase biomolecular sequencing and cluster analysis. One modification to the system which will be implemented as soon as

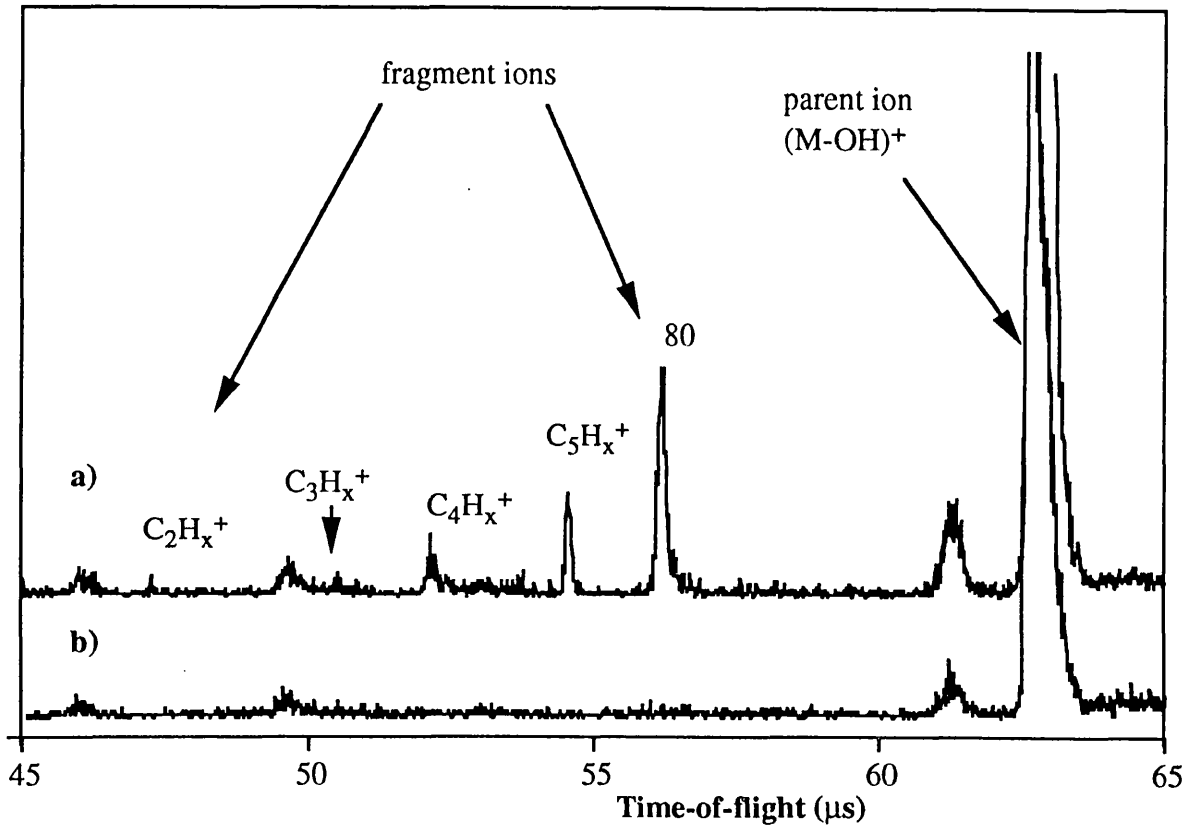

Fig.5.16 The influence of laser wavelength on the fragmentation mass spectra of $(M\text{-}OH)^+$ from 2,5-DHB. a) with a 266 nm fragmentation laser on. b) with the laser off. The fragmentation mass spectrum of (M-OH) is different from that fragmented by a 355 nm laser. There is no large fragment ion peak of $(M\text{-}CO_2H)^+$ in the mass spectrum (see Fig.5.13)

possible is to include a pulsed voltage on the deflecting plates which will permit only one ion to be passed through the reflectron rendering the mass spectra easier to interpret.

Chapter 6

Laser Photofragmentation Mass Spectra of 2,5-DHB Ions

6.1 General description of ions

In general terms, a positive ion is usually generated by simply removing one electrons from the original molecule.

$$M \rightarrow M^+ + e^-$$

The ion M^+ is known as the molecular ion. Its charge (z) and mass (m) are the most important features of this ion. The mass spectrometer measures the mass to charge ratio (m/z) for ions.

Virtually all stable organic molecules have an even number of electrons. Here we write it in the way of M: . These even electrons occupy either bonding or non-bonding electron orbital. If one electron is removed, the resultant molecular ion will have an odd electron configuration, namely it will be left with one unpaired electron. These molecular ions are very unstable and are called radical cations ($M^{+\cdot}$). ($M^{+\cdot}$) gives the proper designation of the electron configuration of the positive ion.

Each molecule has its own ionisation potential which is determined by the nature of the highest occupied molecular orbital since an electron is usually removed from this orbital. Most organic molecules have first ionisation potential in the range of 8~15 eV. The ionisation can be achieved in a number of ways. The most common method used in mass spectrometry is electron impact ionisation in which electrons with the energy greater than the ionisation potentials of molecules are used to form molecular ions. Some of the electron energy is used to remove the electron from a neutral molecule, but some of the extra energy of the ionising electrons is transferred to the ions resulting in excess internal energy as it is formed. The energy used for the ion internal excitation will lead to the ion existing in the electronically excited state, having excess rotational and /or vibrational energy. It may alternatively appear as translational energy.

Ions with electronically excited states are often unstable and prone to dissociation or

fragmentation. In addition, if the excess vibrational energy is sufficiently large, it will lead to the breaking of bonds resulting in fragmentation. The distributions of the products by fragmentation are commonly called fragmentation patterns. Usually there are four factors which determine fragmentation patterns.

1) The strengths of the bonds which are to be broken. Fragmentation involves the breaking of bonds. The bonds can be broken when sufficient vibrational energy is concentrated in them to cause the vibrating atoms to move apart beyond certain distances. As mentioned in the Chapter 2, usually the frequencies of vibration(10^{10} ~ 10^{12} Hz) is much faster that the rates of fragmentation of molecular ions($1x10^6$ ~ $1x10^7$ s^{-1})(not in the case of fragmentation by a laser with high intensity). Nearly thousands of vibrations take place before the molecular ion fragments. During these vibrations, the initial input of the energy to the molecular ion is redistributed. As soon as the redistribution of energy takes place the bond energy of a weak bond in the molecular ion is exceeded, and that bond breaks. Therefore the weaker the bond is, the easier it is to be broken. The single bond is easier to be dissociated than that of a double bond. For example "-C-C-" is much easier to be broken than the bond of "-C=C-".

2) The stability of the products (both ions and neutral) of fragmentation; The stable products of ions or neutrals have a greater opportunity of being formed during fragmentation. Stable positive ions can be formed when a neighbouring group is electron-donating, so as to counteract the positive charge and try to neutralise it. Stable neutral species are usually small molecules with multiple bonds. The multiple bonds can remove large amounts of energy from the parent ions if they are formed in a high vibrational state.

3) The internal energy of the fragmentation ions; The products of fragmentation with high internal energy are not stable and will lead to further fragmentation.

4) The time interval between ion formation and ion detection; Some fragmentation proceed very rapidly whereas others are relatively slow. Whether the slow fragmentation are actually observed or not will depend on the time interval between ion formation and detection. If the ion has not dissociated before it arrives at detector, the products of its fragmentation can't be detected.

In general, in single bond cleavage, molecules only have to achieve the correct energy, whereas in the double bond cleavage or new bond formation, molecules require the correct geometry and the correct energy for the reaction. Thus, the processes will be more difficult and the number of reactions per second will be relatively low compared with simple bond cleavage.

6.2 Fragmentation mass spectra of $(M\text{-}OH)^+$

In the ablation mass spectra of 2,5-DHB, the dominant ion peak was assigned to be $(M\text{-}OH)^+$. It is formed mainly in the following way(see Fig.6.1): the molecule of 2,5-DHB is ionised by removing an electron from the oxygen in the $-HCO_2$ group since there is a strong absorption peak at 337 nm and low first ionisation potential in the carbonyl group, therefore the molecular radical ion $(M)^{+\cdot}$ with an unpaired electron is formed . It has been proven in Chapter 4 that there is abundance of hydrogen in the ablated plume and hence the ion receives a hydrogen atom and forms a stable neutral fragment (H_2O).

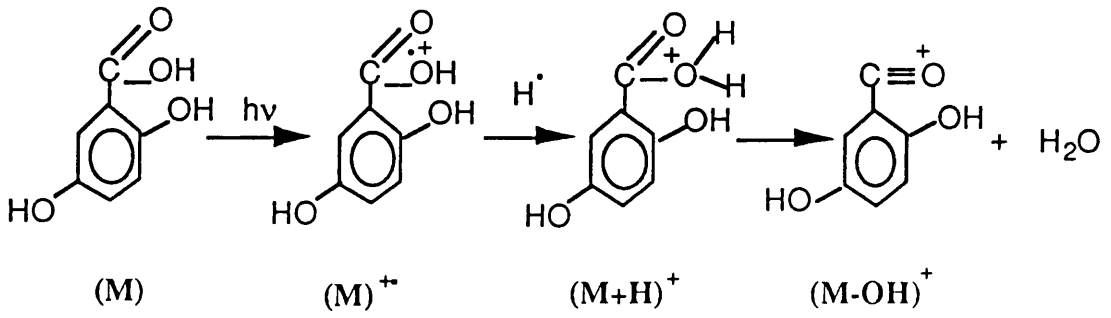

Fig.6.1 Fragmentation of 2,5-DHB by a nitrogen ablation laser

$(M\text{-}OH)^+$ is a kind of carbonyl ions. The ion charge can be delocalised using its π electrons of the benzene ring to give some resonance forms to stabilise it. This explains why the ion of $(M\text{-}OH)^+$ is a basic ion peak in the ablation mass spectra of 2,5-DHB.

Unlike electron-impact ionisation, the fragmentation mass spectra of molecular ions by multiphoton ionisation have their own characteristics: high metastable yield and extreme fragmentation. These features are determined by the internal energy distributions within

these ions. The Fig.6.2 illustrates the internal energy distribution within molecular ions after electron impact ionisation and after multiphoton ionisation with absorption of one additional photon described by U. Boesl (Boesl et. al, 1990). Ions produced by soft multiphoton ionisation (no fragmentation) have very narrow internal energy distributions in contrast to most other ionisation techniques, such as electron impact. By further absorption of additional photon, this narrow energy distribution is shifted to higher energies. A large number of the excited molecular ions are subject to metastable delay if these new energy levels are located near dissociation thresholds of F^+, in which the overlap of internal energy distribution and metastable energy region(in Fig.6.2) is much larger than for the case of electron impact ionisation. Hence a high metastable yield appears in these mass spectra.

Here the metastable yield which we mentioned is the output of metastable ions. Generally speaking, there are only three types of molecular ions in mass spectra: a) the ions with sufficient energy to fragment very quickly before leaving the ion source; b) the ions with insufficient energy to decompose before reaching the detector; c) The ions with an energy which is intermediate between these two extremes. Usually, the ions spend 10^{-6} s in the ion source and 10^{-5} s to travel from the source to the detector. If the ions decompose

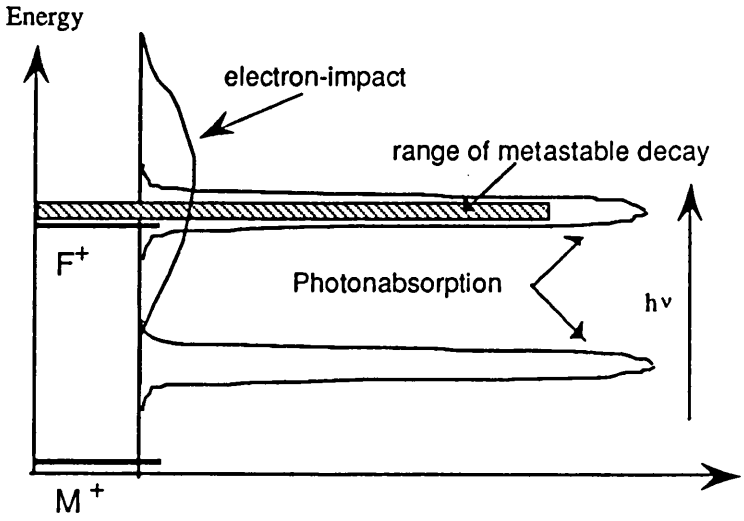

Fig.6.2 Illustration of the internal energy distribution within molecular ions by electron-impact ionsation and by multiphoton ionisation. Ionisation threshold (M^+), fragmentation threshold (F^+), and energy range of metastable decay are indicated. (reproduced from U Boesl el at 1990).

during its flight time out of the ion source region, these ions are called metastable ions. The fragments from the metastable ions fly off in all directions, those projected forwards will get a little ahead (having more kinetic energy), and those backwards a little behind the average metastable ion speed (having less kinetic energy). As the metastable ions are produced with a range of energies, these ion peaks are broad compared with the normal ion peaks.

Another feature of multiphoton ionisation is the extreme fragmentation which can be described by using Boesl's "Ladder-switching model" (Dietz et. al, 1982, Boesl et. al, 1990). This model describes that the maximum excess energy above a dissociation threshold is the energy of one photon (Visible or UV photon). Unlike electron-impact ionisation, the photodissociation rate($\sim 10^{-12}$ seconds) at high laser intensity is considerably faster than the absorption rate of photons ($\sim 10^{-9}$ seconds for nanosecond laser). Therefore the dissociation takes place first, and further absorption will occur within the fragment ions(switching of the ladder of absorbing states). Furthermore, the average excess energy above a dissociation threshold is considerably smaller than the maximal energy(one photon). These narrow internal energy distributions are shifted up by the absorption further photons within the fragment ions, similar to the previous procedure. As a result, the whole mass spectrum contains the molecular and fragment ions with either small internal energy (no photons absorbed after ladder-switching) or a narrow internal energy distribution near the dissociation threshold(one or more photon absorbed after ladder-switching). Therefore, a large fraction of the total energy is deposited in the molecular and fragment ions, and is used for fragmentation and not for increasing the internal and kinetic energy of neutral and ion fragments. These explain the extreme fragmentation in the fragmentation mass spectra.

The mass spectra in Fig.6.3 and Fig.6.4 have been measured under identical conditions expect for the wavelength and intensity of the fragmentation laser. The laser wavelengths of 355nm and 266nm were selected. To achieve considerable photofragmentation for longer wavelength (355nm), higher intensities of the laser have to be applied than that for the shorter wavelength (266nm). The laser pulse energies of 30 mJ for 355nm and 2mJ for 266nm were used in the experiments.

From Fig.6.3 and 6.4, it can be seen that there are the large differences between the

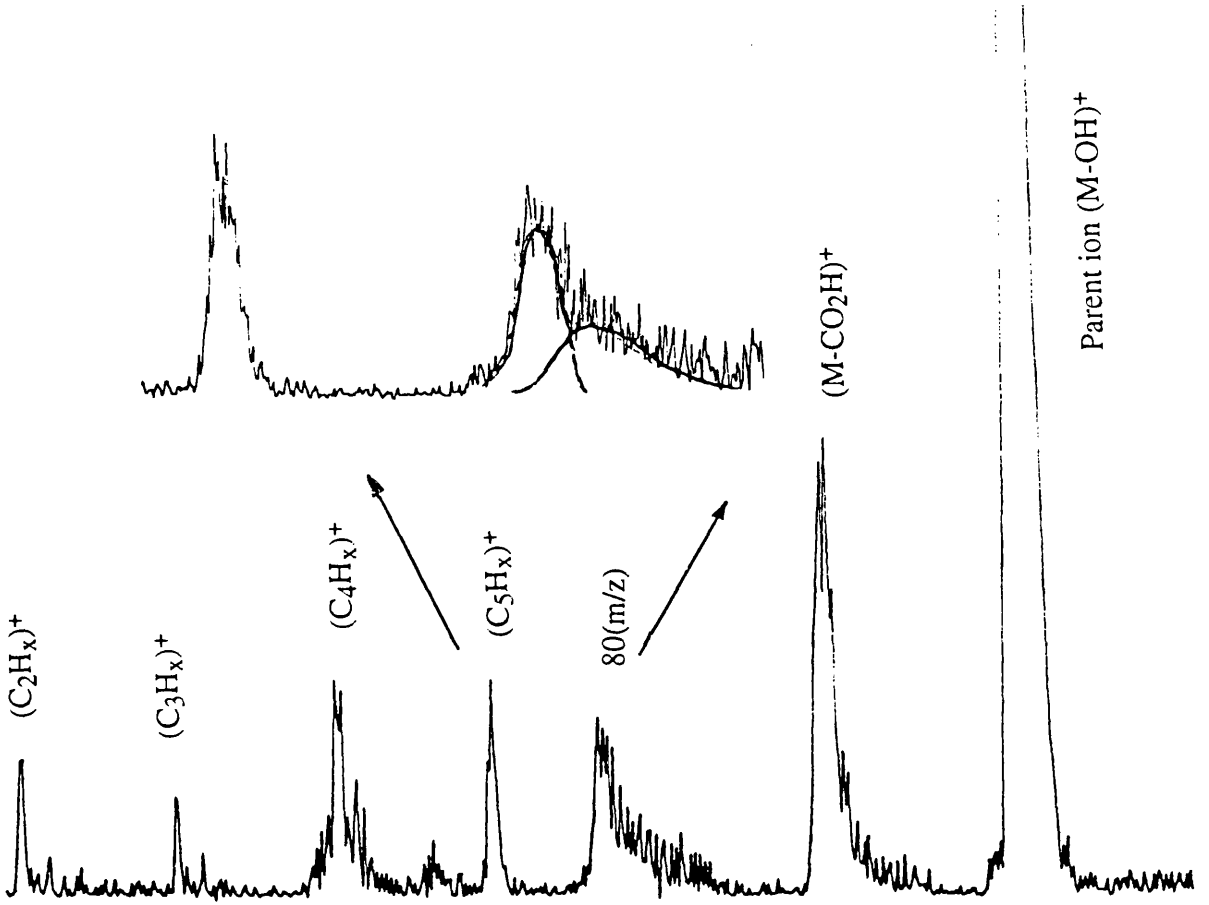

Fig.6.3 A typical fragmentation mass spectrum of $(M-OH)^+$ by a 355nm photo-fragmentation laser with a pulse energy of 30mJ. The inset shows the amplified mass peaks of 80 and $(C_5H_x)^+$. Obviously there is another broad peak mixing with 80. This is assigned to be the metastable ion of $(M-OH)^+$.

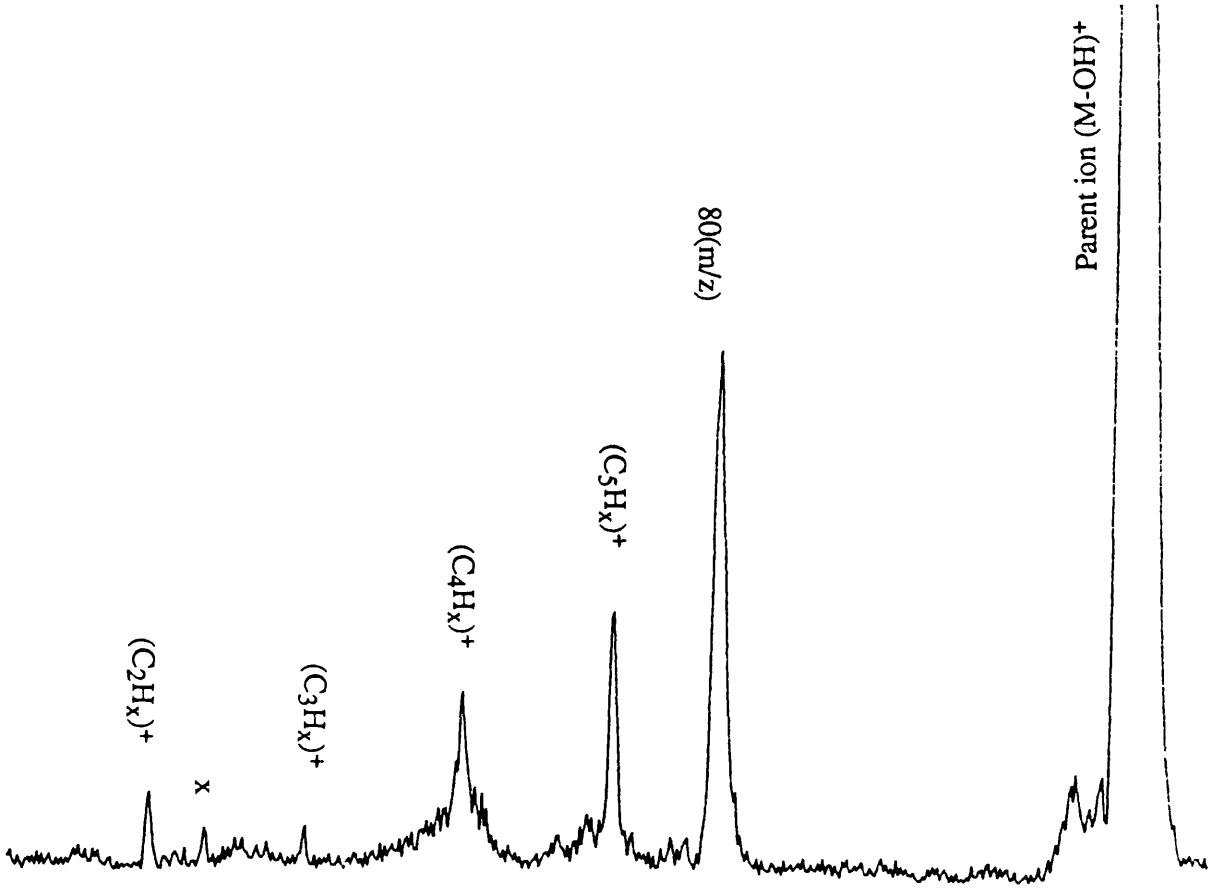

Fig.6.4 A typical fragmentation mass spectrum of $(M\text{-}OH)^+$ from 2,5-DHB by a 266nm photofragmentation laser with a pulse energy of 2 mJ. "x" is from the backgroud

fragmentation mass spectra at 355nm and the fragmentation mass spectra at 266nm, particularly the fragmentation mass peak of (M-CO_2H) in Fig.6.3 is absent in the mass spectrum of Fig.6.4. The other peaks in the both mass spectra are almost same. Both mass spectra contain the mass peaks of 80 , C_5H_x, C_4H_x C_3H_x and C_2H_x.

When the molecular ion of $(M\text{-}OH)^+$ is fragmented by the 355nm fragmentation laser, it loses a small stable neutral molecule CO and forms a relatively stable molecular ion $(M\text{-}CO_2H)^+$ (m/z 109). The other peaks are the further fragmentation products of $(M\text{-}CO_2H)^+$, namely the mass of 80 is from $(M\text{-}CO_2H)^+$, and C_5H_x, C_4H_x, C_3H_x, and C_2H_x are from the mass 80 There is a question: what kind of fragment of mass 80 in this fragmentation mass spectrum is? If the mass 80 was $C_6H_8^+$ (a kind of benzene molecular ion), the further fragments from it observed in this mass spectrum are considerably different from normal mass spectra of benzene ionised by the electron-impact method or by the multiphoton ionisation (Boesl et. al, 1990). It is found commonly that there is no or very small $C_5H_x^+$ in mass spectra of benzene since the benzene ion always tend to lose a HC≡CH units which contains three bonds and easily takes away the internal energy within benzene. However in our mass spectra since there is a relatively large C_5H_x signal, the mass 80 is unlikely to be $C_6H_8^+$.

$(M\text{-}CO_2H)^+$ is a kind of hydroxybenzene (phenol) ion and its mass spectra ionised by electron-impact method has an odd feature which is that $C_6H_x^+$ is very weak and the process

$$C_6H_5\text{-}OH^+ \rightarrow C_6H_5^+ + OH$$

does not occur to any great extent (<1%). The most common fragment ion from $C_6H_5OH^+$ is C_5H_x formed by the loss of CO or HCO. So it is reasonable to assume that the mass peak 80 is $(C_5H_3{+}OH)^+$.

$$(M\text{-}CO_2H)^+ \rightarrow (C_5H_3{+}OH)^+ + CO$$

In the mass spectrum Fig.6.4, the peak of $(C_5H_3{+}OH)^+$ is obviously broader than the other peaks. If we take a closer look at this peak, we can see there are two peaks mixed together, the ion $(C_5H_3{+}OH)^+$ with a normal peak width, and the ion with a broad

peak(see the inset of Fig.6.4). The broad peak is a metastable ion.

Fig.6.5 presents the fragmentation mass spectra of $(M\text{-}OH)^+$ by different intensities of a 355nm photofragmentation laser and Fig.6.6 shows the power dependence of the fragmentation laser at 355nm on the ion yields of the fragments. For all product ions except $(M\text{-}CO_2H)^+$, more than one photon is necessary. The value for the power dependence of the laser on the ion yield of $(M\text{-}CO_2H)$ measured was about 0.5. As the laser power increases, more $(M\text{-}CO_2H)^+$ ions are produced, however, at the same time, the ion is also decomposing more into the small fragments. Hence the value was not an integer. The values for the power dependence of the 355nm laser on the other fragments are: 1.0 for $(C_5H_3\text{+}OH)^+$, 1.5 for both $C_5H_x^+$ and $C_4H_x^+$, 2.0 for both $C_3H_x^+$ and $C_2H_x^+$. According to the power dependence values and the "Ladder-switching model", the following fragmentation pathways can be proposed(Fig.6.7)

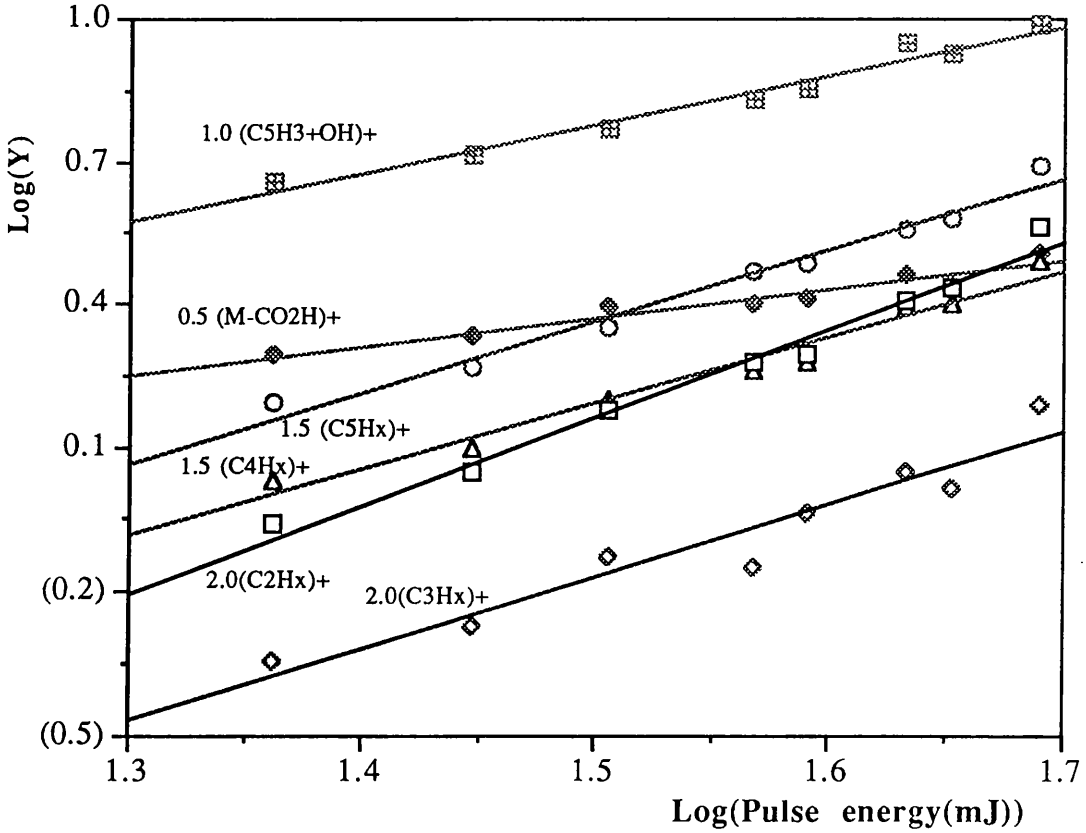

Fig.6.6 Power dependence of a 355nm photodissociation laser on fragments from (M-OH) ion

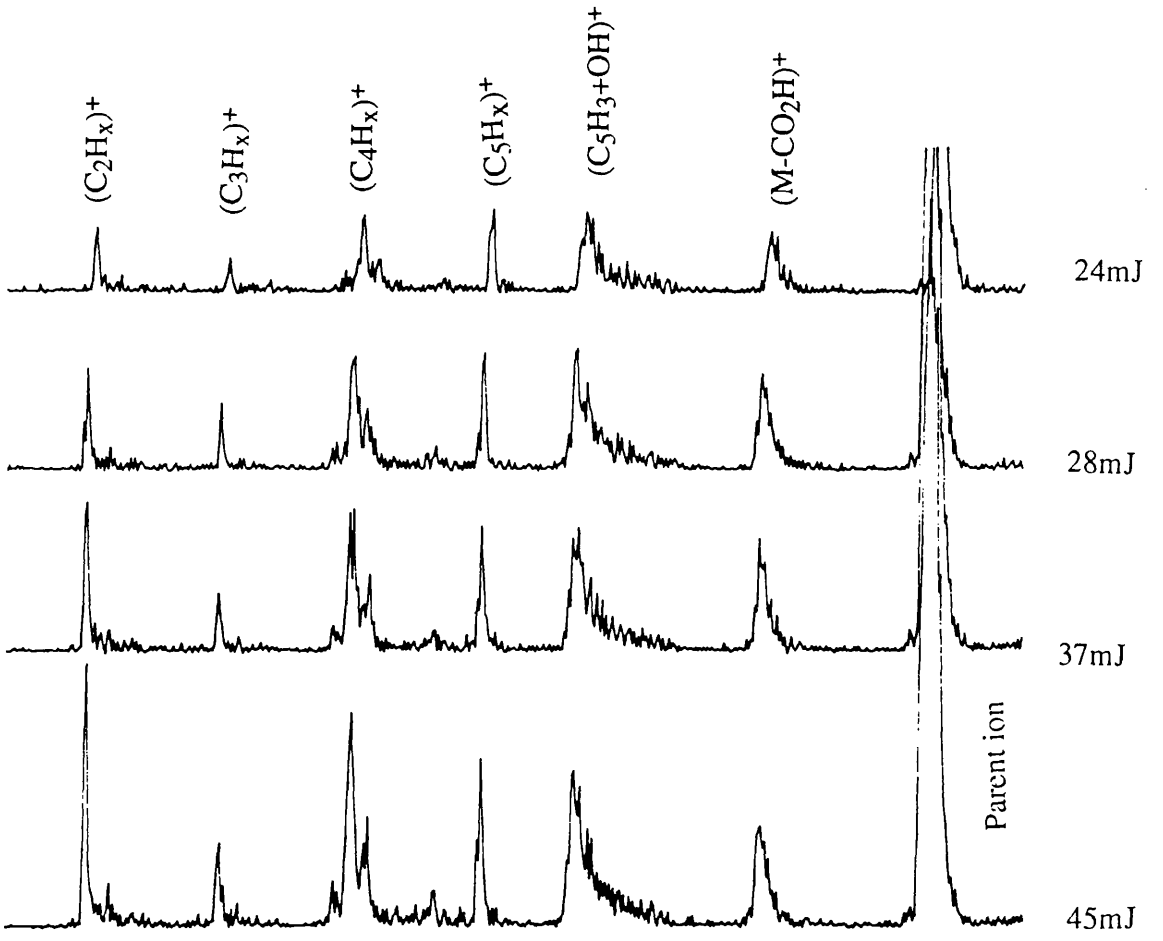

Fig.6.5 Fragmentation mass spectra of $(M-OH)^+$ with different photofragmentation laser intensities at 355nm.

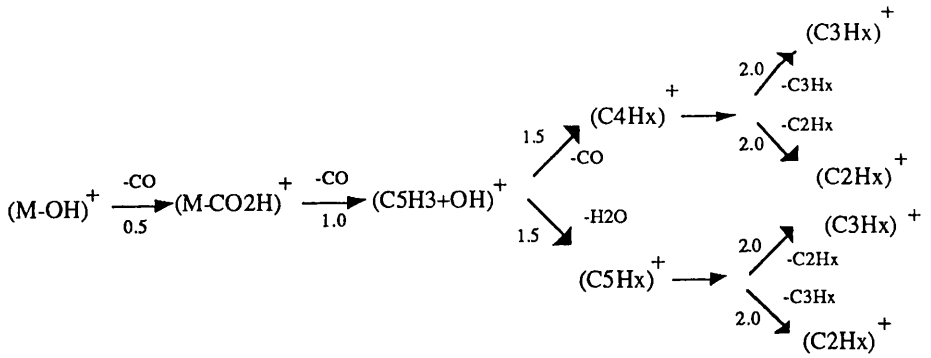

Fig. 6.7 The fragmentation pathways of the molecular ion of (M-OH) and its power dependence values fragmented by a 355nm laser.

All of The fragmentation pathways in Fig.6.7 can be explained by the following descriptions. $(M\text{-}OH)^+$ is directly dissociated by loss of a stable neutral molecule CO which has been proven by observation of the metastable ion of $(M\text{-}CO_2H)^+$. The ion of $(M\text{-}CO_2H)^+$ absorbs another photon during the same laser pulse and fragments to $(C_5H_3\text{+}OH)^+$ by further loss of a CO molecule. Then $(C_5H_3\text{+}OH)^+$ can absorbs 2 photons and decomposes to either $C_5H_x^+$ or $C_4H_x^+$ by loss of the small stable molecules H_2O and CO, respectively. The $C_5H_x^+$ and $C_4H_x^+$ ions can be further dissociated into $C_3H_x^+$ and $C_2H_x^+$ by absorption of another two photons. If the laser intensity is further increased, fragmentation pathways prefer to produce smaller fragments such as $C_3H_x^+$ and $C_2H_x^+$. In Fig.6.8 the influence of laser flux is clearly visible with the low mass fragments becoming more prominent as the laser flux increases. The large fragments such as $(M\text{-}CO_2H)^+$ and $(C_5H_3\text{+}OH)^+$ decrease dramatically. It is possible for some small fragments such as $C_3H_x^+$ and $C_2H_x^+$ to decompose into CH_x^+ , even to C^+(Boesl et. al, 1990) if the laser flux continues to increase.

However $(M\text{-}OH)^+$ fragmented by a 266nm laser decomposed through a different pathway. In the mass spectrum of Fig.6.5 it has been shown that the fragments are $(C_5H_3\text{+}OH)^+$, $C_5H_x^+$, $C_4H_x^+$, $C_3H_x^+$ and $C_2H_x^+$, but there is no $(M\text{-}CO_2H)^+$, peak. A likely explanation is that the group -OH in the molecular ion of $(M\text{-}OH)^+$ absorbs the photons at 266nm and decomposes into $(C_5H_3\text{+}OH)^+$ by loss of CO and H_2O, unlike the case using a 355nm fragmentation laser, in which the -C=O group absorbs photons. Therefore the fragmentation patterns can be controlled to some degrees by changing the

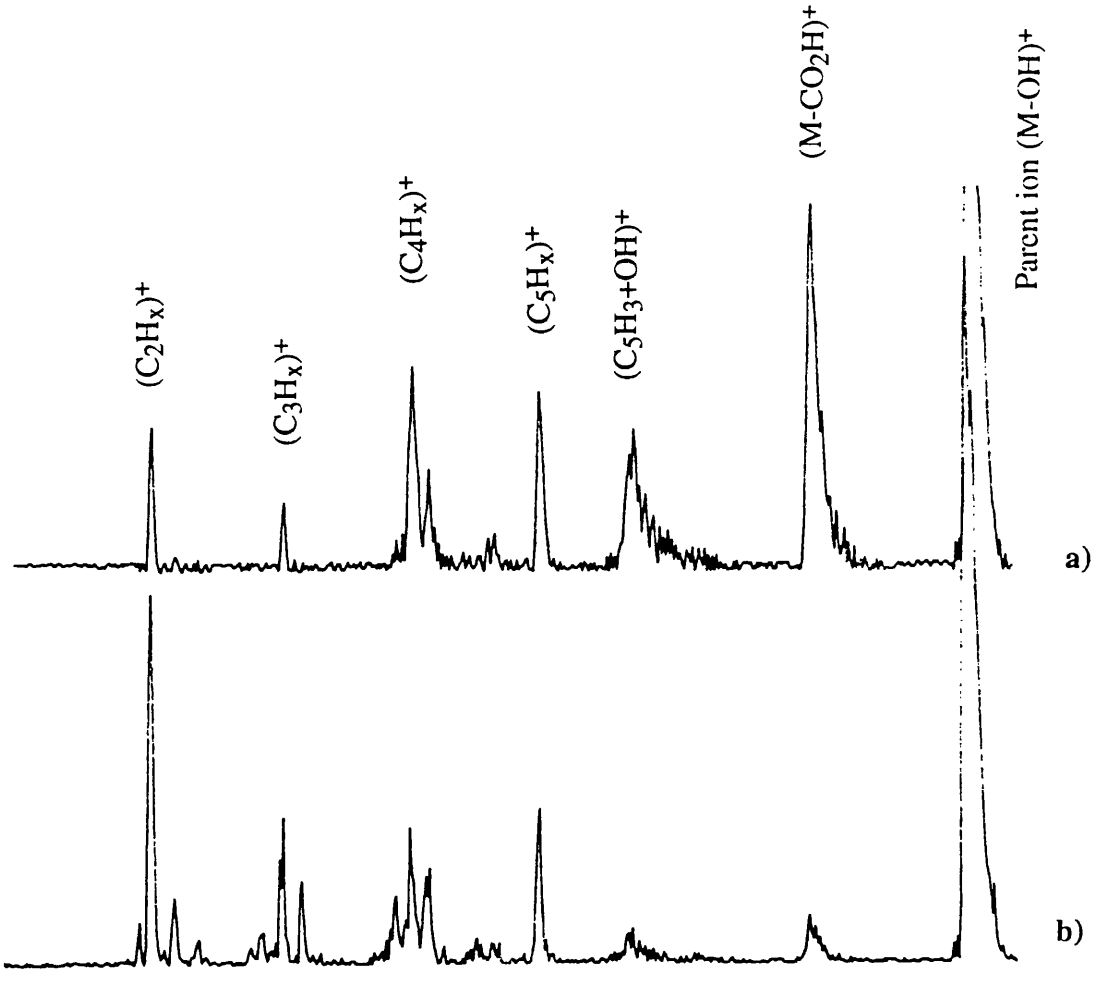

Fig.6.8 Influence of the laser flux on the fragmentation patterns. a) the fragmentation mass spectrum of $(M-OH)^+$ by an unfocused 355nm laser (laser pulse energy 60 mJ). b) the fragmentation mass spectrum of $(M-OH)^+$ by the same laser but with a focused laser beam.

wavelength of a fragmentation laser. Due to the low intensity of the 266nm fragmentation laser used in our lab, no experiments of the power dependence on ion yields have been done.

6.3 Fragmentation mass spectra of $(M)^{+\cdot}$

The parent molecular radical cation of 2,5-DHB (M) has been fragmented at the two wavelengths, 355nm and 266nm. $(M)^{+\cdot}$ shows strong photodissociation at 355nm (Fig.6.9) and the $(C_5H_3+OH)^+$ and $C_4H_x^+$ have been found in small abundance and $(M-OH)^+$ in large abundance. As mentioned above, $(M-OH)^+$ has six resonance structures which stabilise the ion. So this is the main reason why $(M-OH)^+$ ion peak is the largest among the fragments. It should be noticed that $(M)^{+\cdot}$ ion fragmented at 355nm does not lead to the product ions of $C_5H_x^+$, $C_3H_x^+$ and $C_2H_x^+$., which is significantly different from the fragmentation mass spectrum of $(M-OH)^+$ at the same wavelength.

The power dependence of the 355nm fragmentation laser on the fragments from $(M)^{+\cdot}$ has been shown in Fig.6.10. The value for the power dependence of the laser on the ion yield of $(M-OH)^+$ measured was 0.4. The value is not an integer because as the laser power increased, its decomposition into the small fragments also is increasing. The values for the power dependence of the 355nm laser on $(C_5H_3+OH)^+$ and $C_4H_x^+$ are the same (2.1). So it is possible that both $(C_5H_3+OH)^+$ and $C_4H_x^+$ are directly decomposed from $(M-OH)^+$ which is different from the fragmentation patterns of $(M-OH)^+$ in the section 6.2. According to the fragmentation pattern and power dependence values the following fragmentation pathways can be proposed(Fig.6.11):

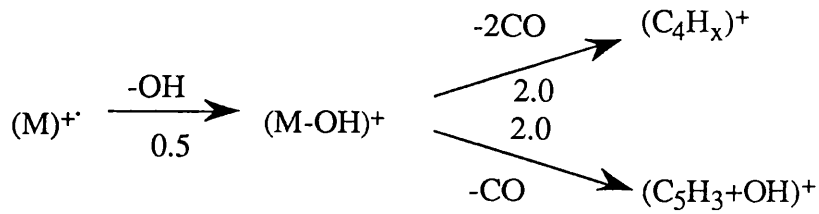

Fig. 6.11 The fragmentation pathways of the molecular radical ion of (M) and its power dependence values fragmented by a 355nm laser.

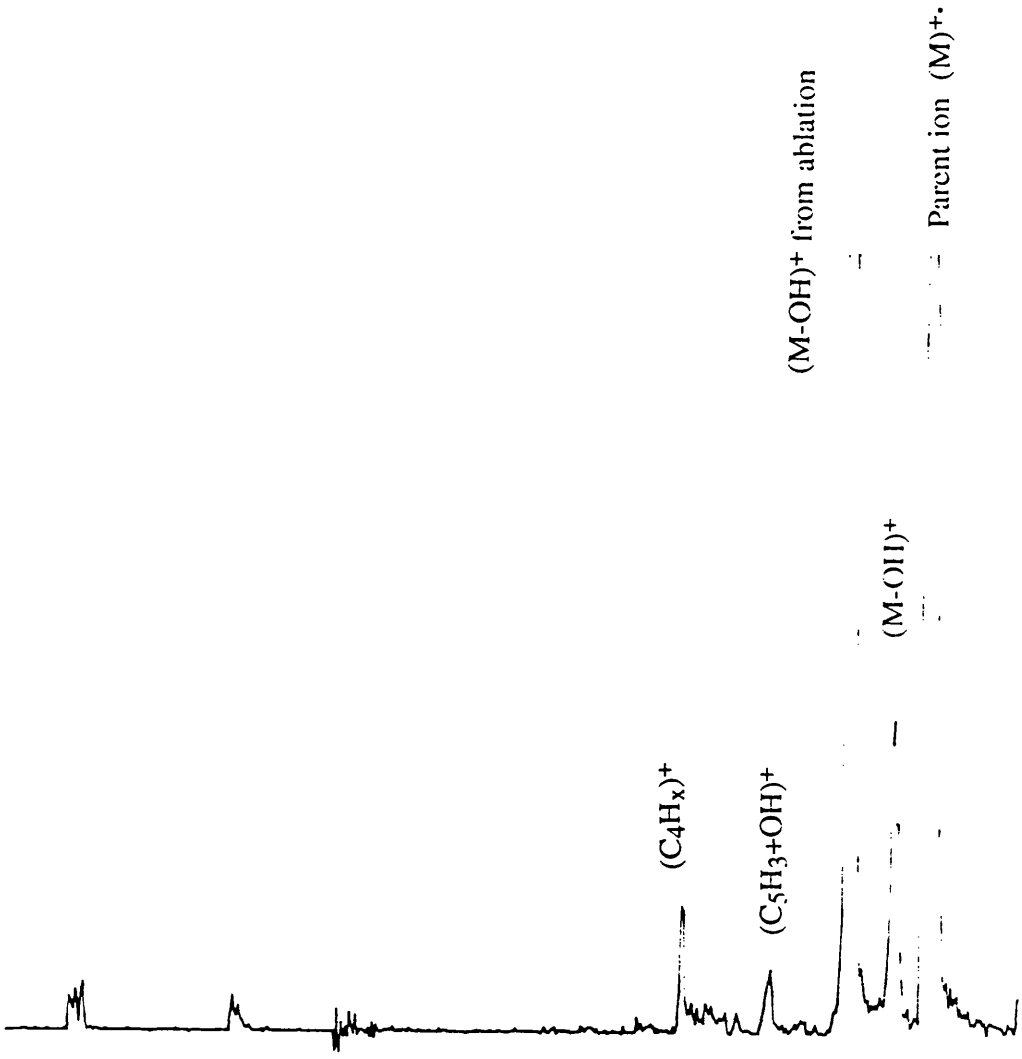

Fig.6.9 A typical fragmentation mass spectrum of $(M)^{+\cdot}$ by a 355nm photo-fragmentation laser with a pulse energy of 30mJ.

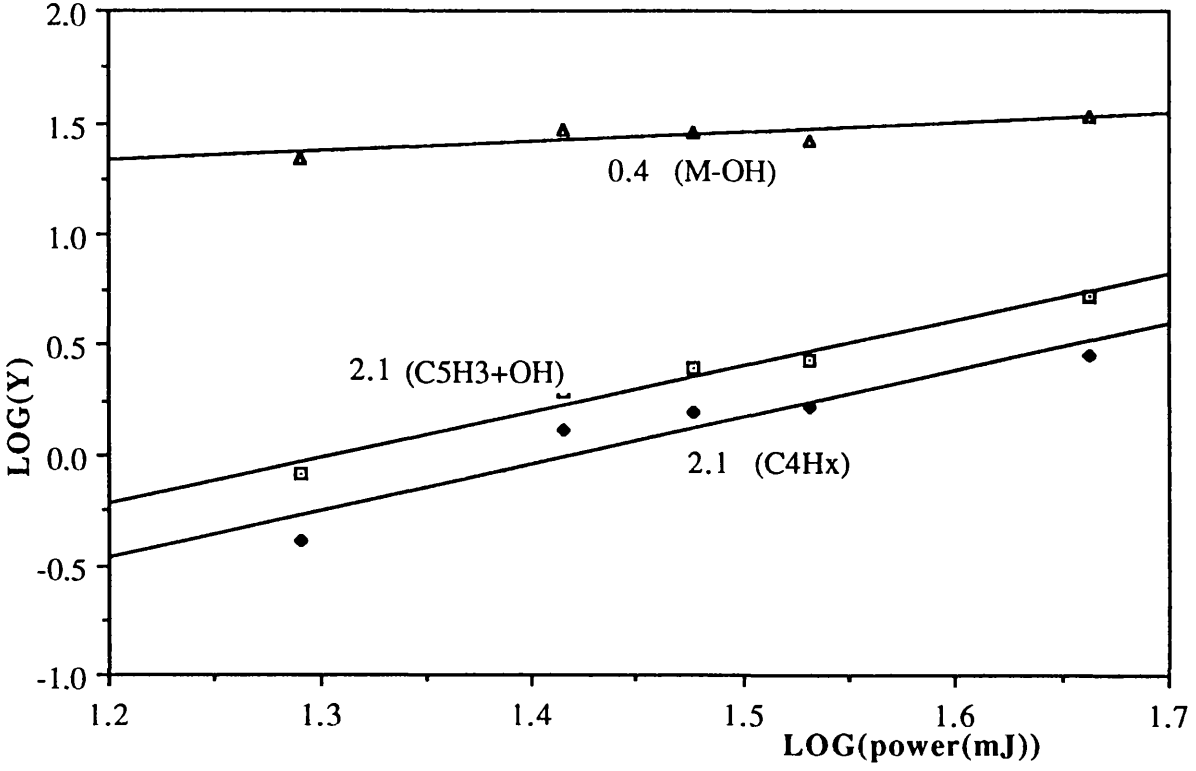

Fig. 6.10 Power depedence of a 355nm photofragmentation laser on the fragments from M+

However, no fragmentation mass peaks from $(M)^{+\cdot}$ were observed by the fragmentation laser at 266nm. Probably the power of the fragmentation laser at 266nm was not high enough or there is no strong absorption peak in $(M)^{+\cdot}$ at the wavelength of 266 nm.

6.4 Fragmentation mass spectra of $((M\text{-}OH)2\text{-}H)^+$

In the ablation mass spectrum of 2,5-DHB, the ion peak of the dimer of $(M\text{-}OH)^+$ is large compared with others(see chapter 4) except $(M\text{-}OH)^+$ and $(M)^{+\cdot}$. The dimer $((M\text{-}OH)2\text{-}H)^+$ has a very stable structure like $(M\text{-}OH)^+$. 2,5-DHB is known to form large crystals under suitable conditions (Haisa, 1983). Crystals grown from aqueous solution are produced by a hydrogen bond interaction of the carboxylic group. In addition, the dimers are linked by hydrogen bonds of OH groups forming a chain with the aromatic rings slightly tilted against each other. Moreover, hydrogen bonds of the hydroxyl group form the crystal structure by the linkage of these layers. The structure of the unit cell of 2,5-DHB crystals is shown in Fig.6.12.

$((M\text{-}OH)2\text{-}H)^+$ was formed by loss of a small stable molecule of water (H_2O) and (-OH) radical. The charge can be stabilised by (M-OH) as described before. Here there are two (M-OH), and much easier to maintain the charge. Fig.6.13 shows the structure of $((M\text{-}OH)2\text{-}H)^+$.

From the ablation mass spectrum of the pure 2,5-DHB by a 337 nm laser, it has been shown that the mass of the dimer of (M-OH) is 273 (m/z), rather than the expected 274

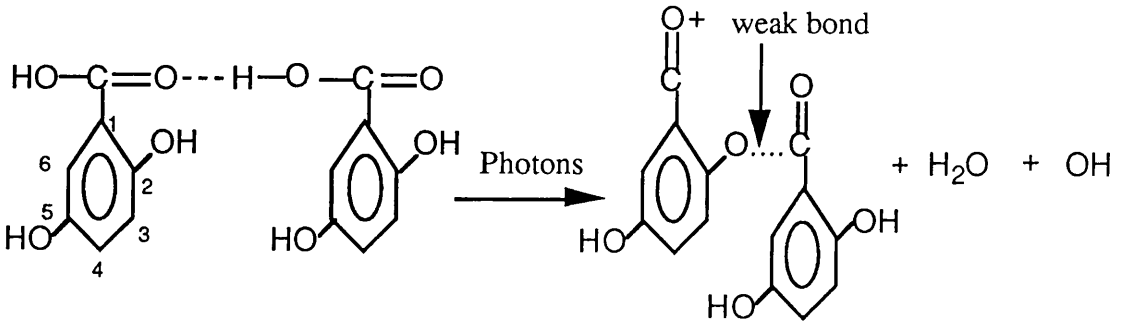

m=308, the dimer of M

(m/z 273) The dimer of (M-OH)

Fig.6.13 The fragmentation pathway and structure of 2,5-DHB dimer

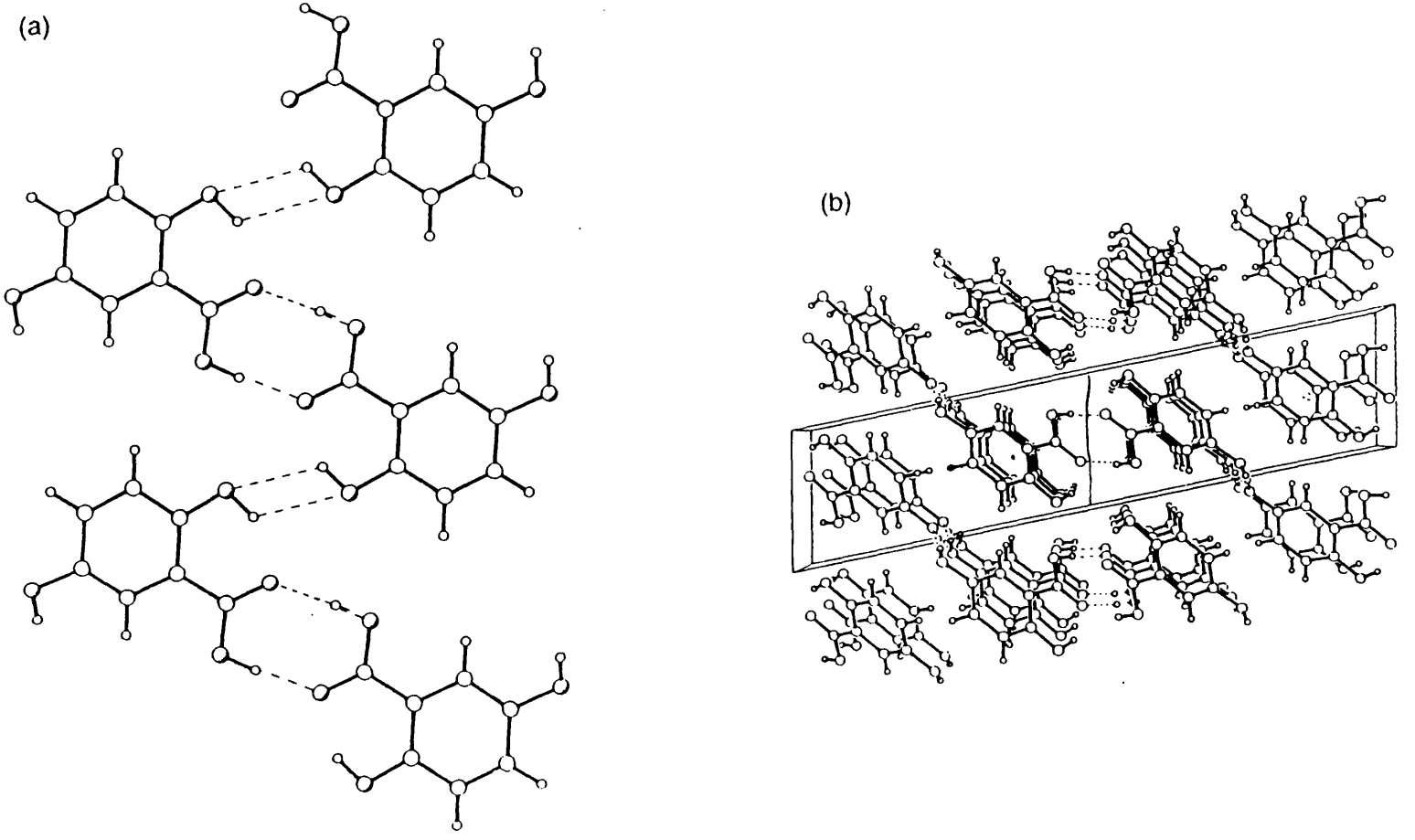

Fig.6.12 a) Dimer chain of 2,5-DHB molecules formed on crystallisation from aqueous solution. b). Unit cell of 2,5-DHB crystal lattice.

(m/z) (twice the mass (M-OH)(m/z 137)). This phenomenon occurs probably due to the oxygen in the position 2 providing more electric negative to the carbonyl group in the second (M-OH) by loss of a hydrogen to stabilising the dimer.

Fig. 6.14 presents a detailed fragmentation mass spectrum of $((M\text{-}OH)2\text{-}H)^+$. It shows that the peak of $(M\text{-}OH)^+$ is dominant among other fragments. The bond linking two (M-OH)(see Fig.6.13) is usually weak compared with the bonds forming molecules, and therefore it is easy to be fragmented by absorption of photons. In addition, the products of $((M\text{-}OH)2\text{-}H)^+$ are two $(M\text{-}OH)^+$ which is a very stable molecular ion. The other fragments are $(C_5H_3{+}OH)^+$, $C_5H_x^+$, $C_4H_x^+$, $C_3H_x^+$ and $C_2H_x^+$. These fragments are the same as those fragmented from $(M\text{-}OH)^+$. So it is reasonable to postulate that these small fragments came from further fragmentation of $(M\text{-}OH)^+$. Comparing with $(M\text{-}OH)^+$ peak, $(C_5H_3{+}OH)^+$, $C_5H_x^+$, $C_4H_x^+$, $C_3H_x^+$ and $C_2H_x^+$ are relatively small, probably the efficiency of further fragmentation is low and requires higher laser fluxes to continue its fragmentation. The power dependence of the 355nm laser on the fragment yields is shown in Fig.6.15. It can be seen that the value for $(M\text{-}OH)^+$ is small (around 0.5), and the value was 1.5 for $(M\text{-}CO_2H)^+$ and 1.9 for $(C_5H_3{+}OH)^+$. The signals of $C_5H_x^+$ $C_3H_x^+$ and $C_2H_x^+$ were very small and the power dependence could not be measured correctly, so that these values are not shown here. $C_4H_x^+$ overlapped with the ablation signal of $(M)^{+\cdot}$ and hence it could not be measured correctly as well. The fragmentation pathways of $((M\text{-}OH)2\text{-}H)^+$ are nearly as same as that of $(M\text{-}OH)^+$ as shown in Fig.6.6. The difference is that the $(M\text{-}OH)^+$ was from its dimer $((M\text{-}OH)2\text{-}H)^+$

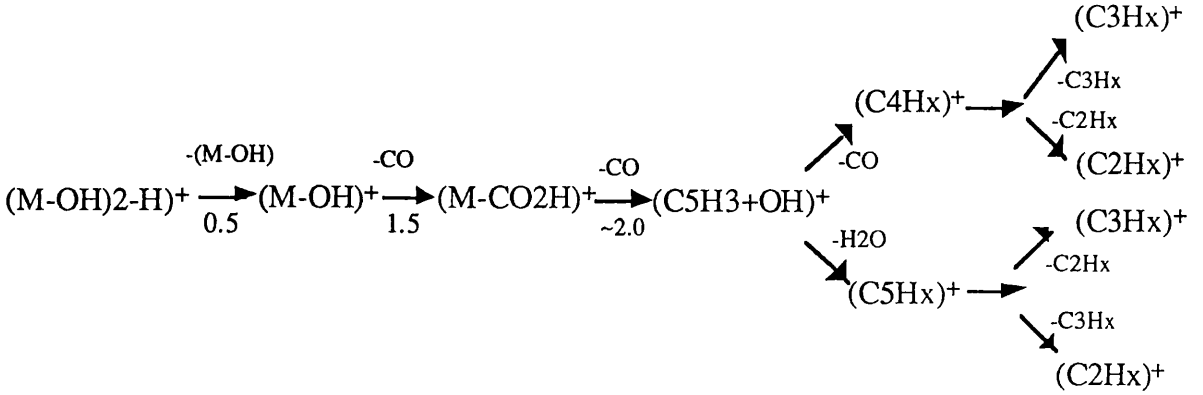

Fig. 6.16 The fragmentation pathways of the molecular ion of (2(M-OH)-H) and its power dependence values fragmented by a 355nm laser.

rather directly from 2,5-DHB. The fragmentation pathways are shown bellow (Fig.6.16)

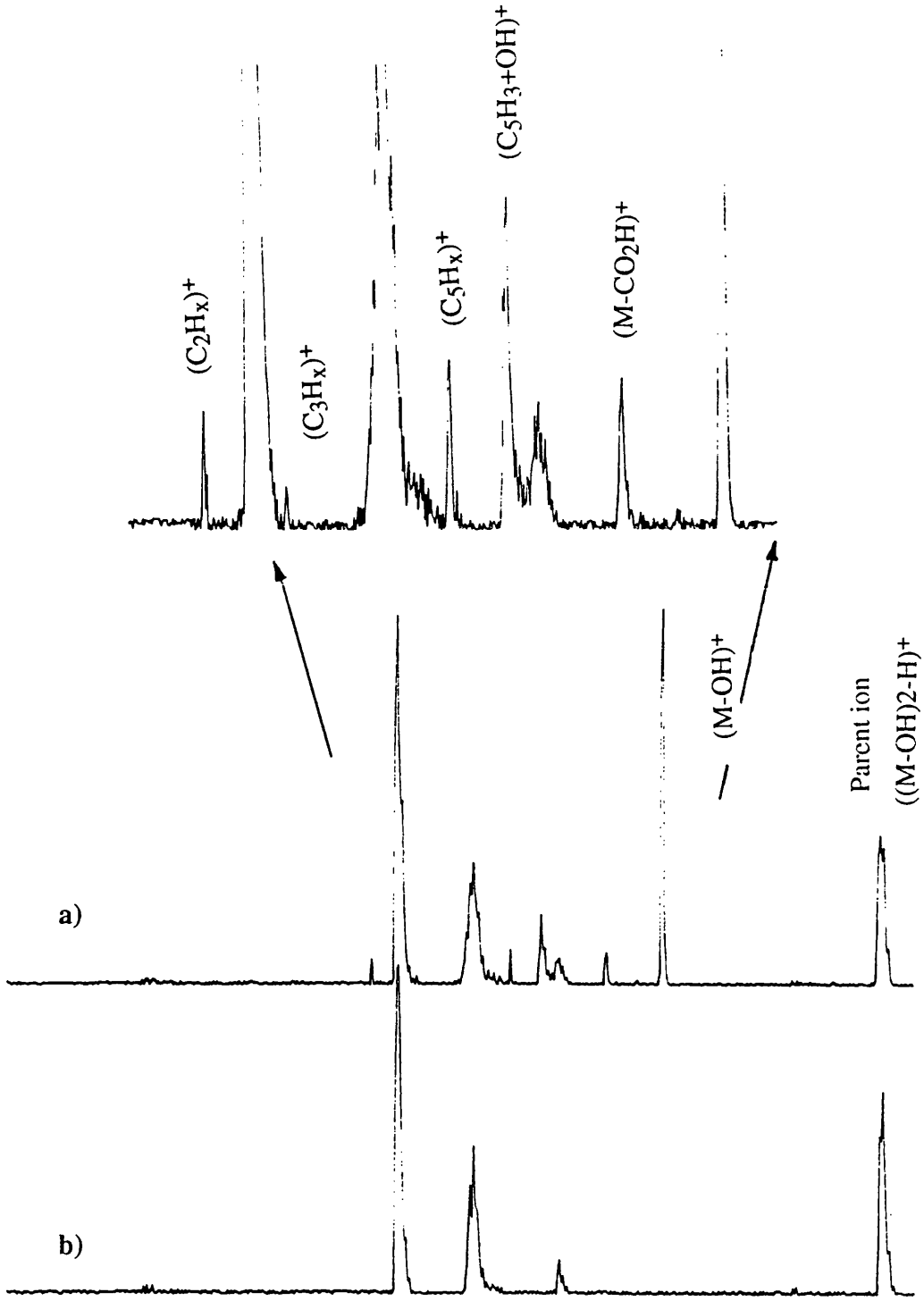

Fig.6.14 A typical fragmentation mass spectrum of $((M-OH)2-H)^+$ by a 355nm laser(30mJ). a) with the photofragmentation laser on, and b) with the photofragmentation laser off. The inset shows the detailed mass spectrum of the fragments.

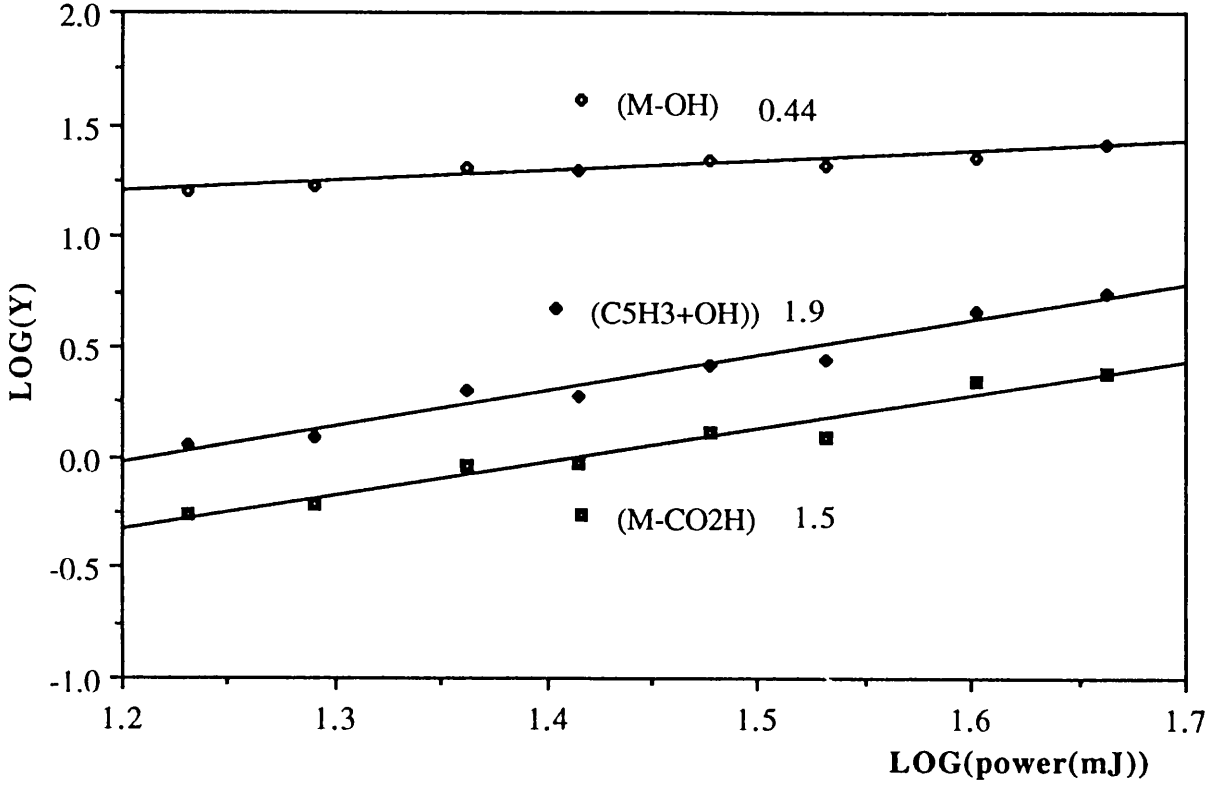

Fig.6.15 Power dependence of the 355nm photofragmentation laser on the fragments from the ion of ((M-OH)2-H)

It can also be seen that the peak of $(M\text{-}OH)^+$ is even larger than its parent ion peak ($(M\text{-}OH)_2\text{-}H)^+$. This happens due to the following two reasons: a) the X-Y deflecting plates had been optimised and some parent ions could not be detected when the fragmentation mass spectrum was taken(see Chapter 5); b) The dimer of $(M\text{-}OH)^+$ was decomposed into the ion $(M\text{-}OH)^+$ and the neutral (M-OH). The neutral fragment (M-OH) may be further ionised by the same laser pulse. Hence more $(M\text{-}OH)^+$ fragments were formed. Usually, ionisation of neutral fragments does not play any significant role (Pandolfi, et al 1982). However, in some cases, the neutrals can be further ionised by the same laser pulse if the wavelength of the laser can be strongly absorbed by the neutrals. From fragmentation of $(M\text{-}OH)^+$ by 355 nm laser it seems that there is strong absorption peak around this wavelength.

As for the fragmentation of $((M\text{-}OH)_2\text{-}H)^+$ by the fragmentation laser at a wavelength of 266nm, there is only one fragment of $(M\text{-}OH)^+$ in the mass spectrum (see Fig. 6.17) due to the low laser intensity(3mJ) which could not providing enough photons for "Ladder-switching" into smaller fragments.

6.5 The "Ladder-Switching" models of multiphoton dissociation of the molecular ions

Usually there are two methods to select a specific molecule out of a mixture of species. a) by tuning the wavelength of the ionising laser onto a resonance of this molecule; b) by setting the mass spectrometer to the mass of a specific molecular ion according to their different TOF time. In this experiment, the later method was used.

If the wavelength of the ionisation laser is tuned to a resonant intermediate state, the ionisation is enhanced considerably at a low laser intensity, resulting in the appearance of the parent ion without any subsequent ion fragmentation. This is called "soft" ionisation. A necessary condition for "soft" ionisation is that the excess energy of the ionising photons above the ionisation threshold does not exceed the lowest dissociation threshold of the ion. For non-resonant laser ionisation, much higher intensity of the ionising laser is needed. This leads to more subsequent fragmentation after the molecule was ionised. By increasing the intensity of a ionising laser, photon absorption within the molecular ions can be induced. If the absorbed energy exceeds the lowest ion dissociation

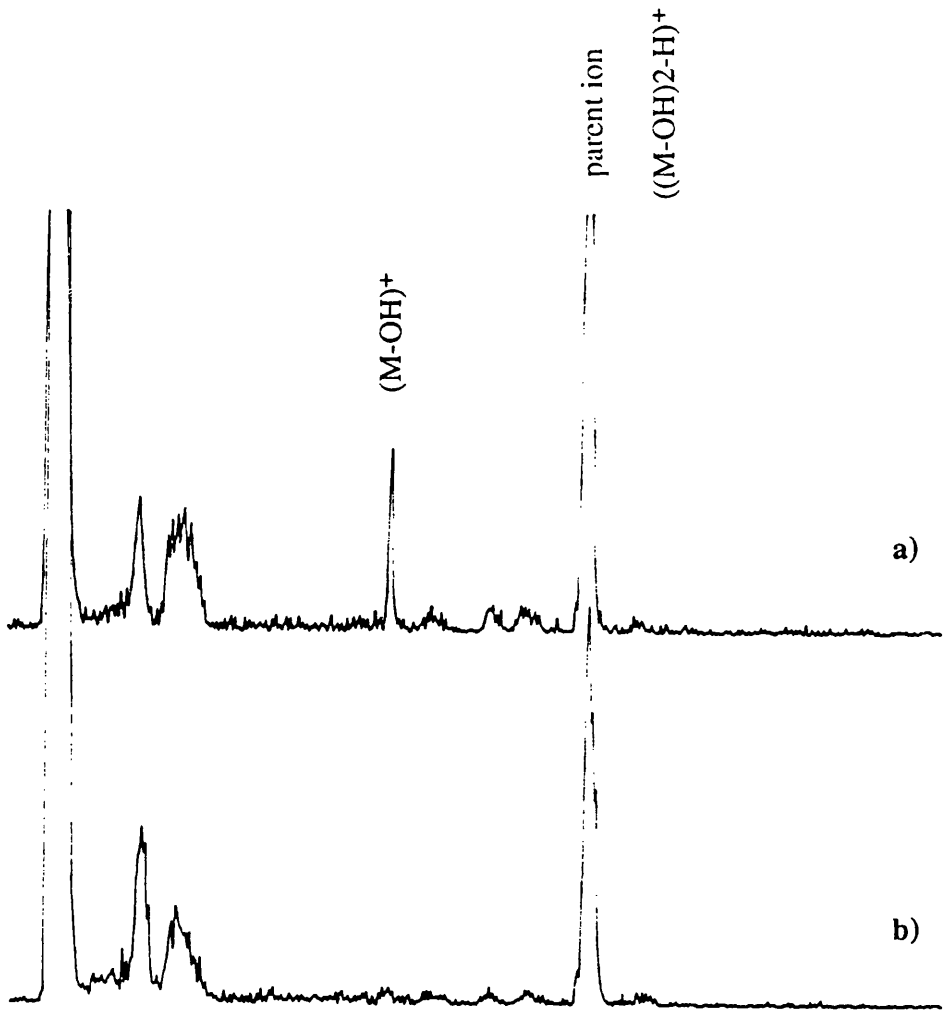

Fig.6.17 A typical fragmentation mass spectrum of ((M-OH)2-H)$^+$ by a 266nm laser(2mJ). a) with the photofragmentation laser on, and b) with the photofragmentation laser off.

threshold, fragmentation of the parent ion occurs. In most case, metastable fragments are produced if the excess energy is not very high above the thresholds. It can be seen in section 6.3 that the metastable ion of $(M\text{-}CO_2H)^+$ from $(M\text{-}OH)^+$ was produced. A further increase of the ionising laser intensity induces absorption of additional photons within the molecular ion and the dissociation rate becomes considerably faster than the photon absorption rate. Dietz (Dietz et. al, 1982) have calculated the RRKM rates against the excess energy (eV) within the molecular ions (see Fig.6.18). As a result, the fragmentation occurs first and the absorption is switched from the molecular ion to its fragment ions. and again from them to their fragment ions and so forth.

For large molecular ions, the number of dissociation threshold within a particular energy interval increase, hence more subsequent and parallel fragmentation channels exist even for absorption of one or just few photons within the molecular ions.

The ladder-switching model for the fragmentation of molecular ion $(M\text{-}OH)^+$ can be described in Fig.6.19. The $(M\text{-}OH)^+$ absorbs a photon and opens its subsequent fragmentation channel to $(M\text{-}CO_2H)^+$ by loss of CO molecule, then $(M\text{-}CO_2H)^+$ continues absorbing another photon to switch to another subsequent channel to produce $(C_5H_3\text{+}OH)^+$. $(C_5H_3\text{+}OH)^+$ absorbs more than one photons to open its parallel decay channel to form $C_4H_x^+$ and $C_5H_x^+$. Finally $C_4H_x^+$ and $C_5H_x^+$ open their further parallel channels to generate their daughter ions of $C_2H_x^+$ and $C_3H_x^+$ by absorption of two photons.

The ladder-switching models for $(M)^{+\cdot}$ and $((M\text{-}OH)_2\text{-}H)^+$ fragmented by a fragmentation laser at 355 nm are shown in Fig.6.20.

6.6 Application of TRTOF for identification of isomer ions

It has been shown in Chapter 4 that 2,5-DHB is a very good matrix in MALDI, however its isomer 2,3-DHB is not. The reasons are still uncertain, but its molecular and fragment ions ($(M)^{+\cdot}$ and $(M\text{-}OH)^+$) must play an important role in chemical ionisation of large biomolecules. Through the fragmentation patterns of these molecular ions we may gain some useful information about the underlying mechanism. Moreover many organic molecules such as chlorinated aromatics are highly toxic pollutants mainly emitted by combustion processes. New highly sensitive and selective(particularly isomer selective

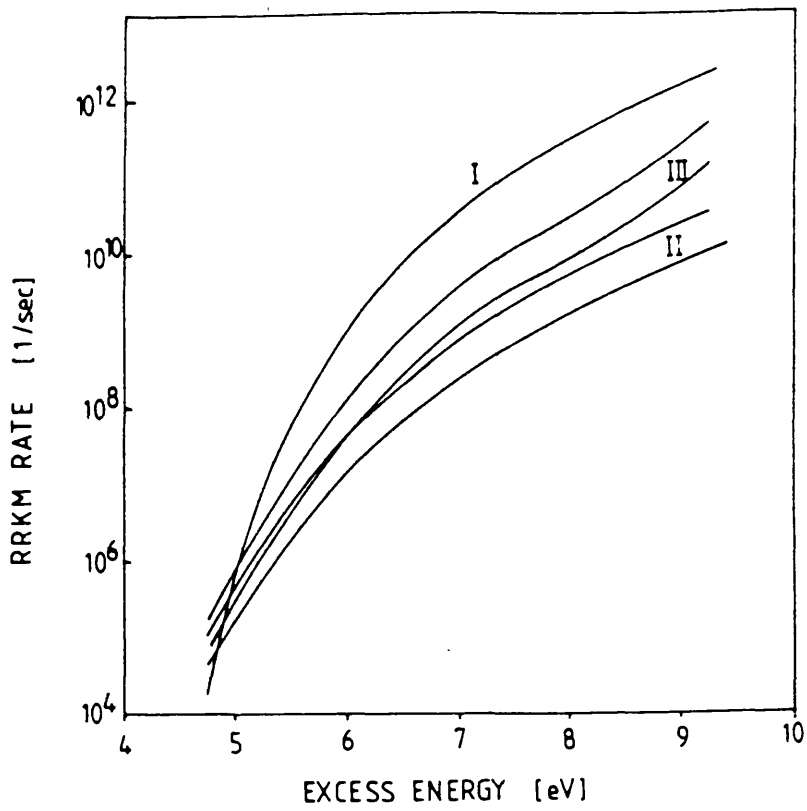

Fig.6.18 The increase of RRKM-rate curve with excess energy within molecular ions. Curve I,II,III represent the different reaction rate (calculated): I) the sum of $C_6H_6^+$ --> $C_3H_3^+ + C_3H_3$, $C_6H_6^+$ --> $C_4H_4^+ + C_2H_2$ reaction rates; II) $C_6H_6^+$ --> $C_6H_5^+ + H$ reaction rate, III) the range of total unimolecular rates. Reproduced from W.Dietz et al.(W.Dietz et at 1982).

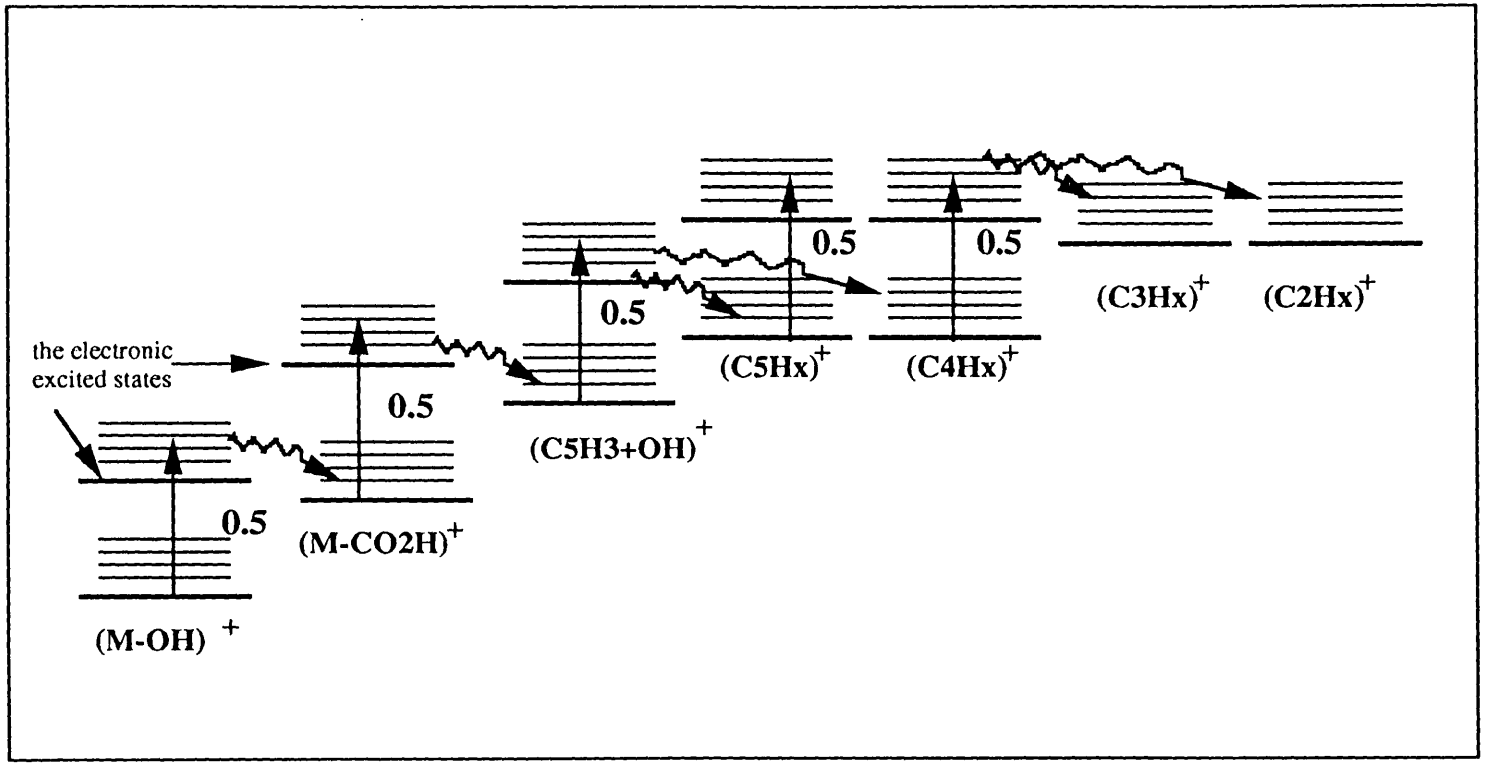

Fig.6.19 The Ladder-switching Model for the fragmentation of molecular ion $(M\text{-}OH)^+$.

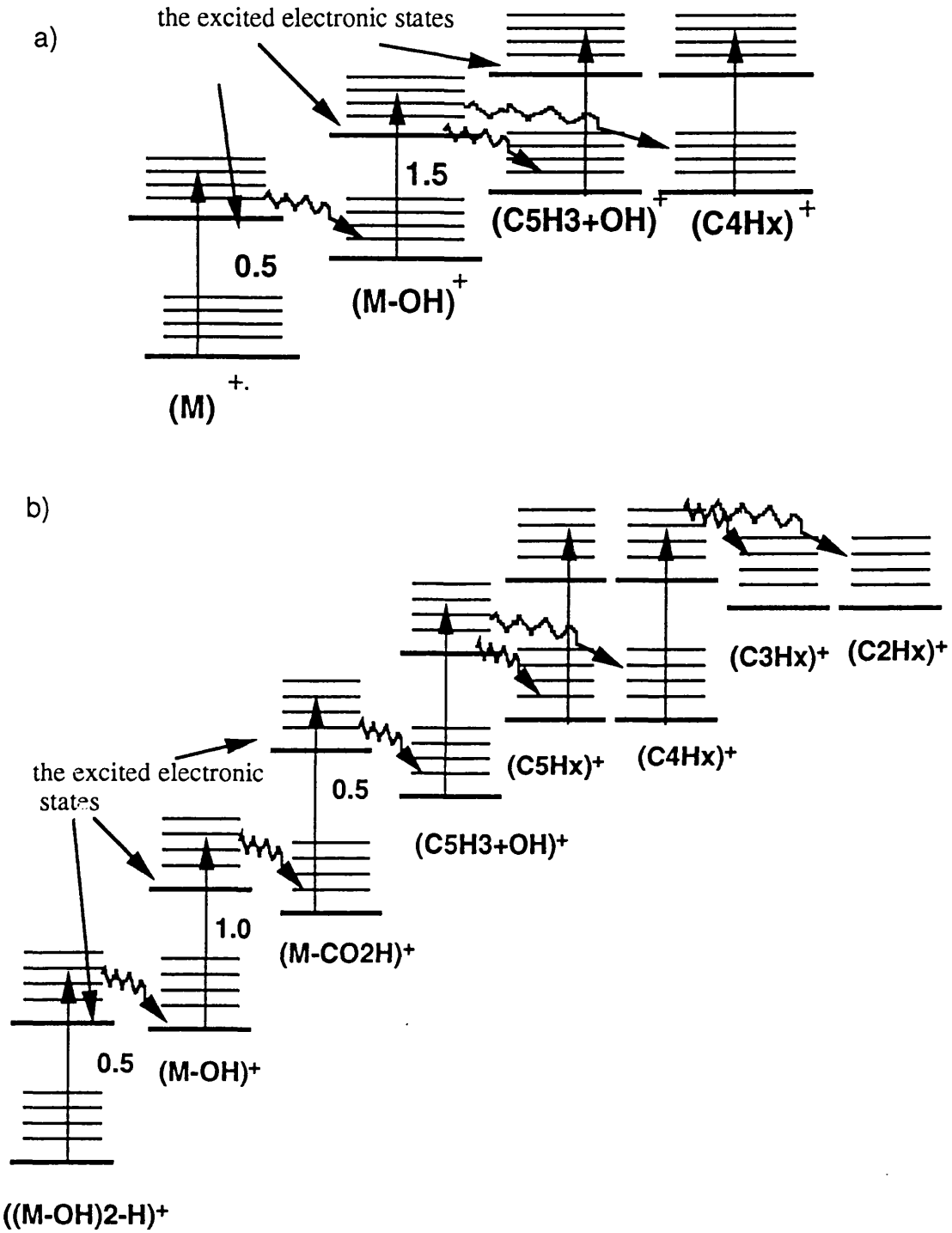

Fig.6.20 The Ladder-switching Model for the fragmentation of molecular ion a),$(M)^{+\cdot}$ and b),$((M-OH)2-H)^{+}$.

such as 1-Cl-anthrance, 2-Cl-anthrance, 9-Cl-anthrance etc.) analysis techniques are required, which give information of the isomers not within many hours or even days (as conventional gas chromatography-mass spectrometry), but within few minutes even seconds.

One of the drawbacks of electron-impact ionisation is that it is difficult to distinguish between the isomers of the molecules. Most of molecular isomers receive the energy from electrons and tend to give same mass spectra. The isomer selective resonance ionisation is an effective method of distinguishing between the isomers. However it has some preconditions to perform a successful isomer selective resonance ionisation, namely, a) the UV-spectra of the isomers must be known(usually gas phase UV-spectra of large molecules show broad absorption bands and a supersonic molecular beam is needed to cool its rotations and vibrations); b) they must exhibit sharp structure; c) multiphoton ionisation is necessary; d) a good tuneable dye laser is required.

Tandem reflectron time-of-flight mass spectrometer (TRTOF) is a new tool to distinguish between these isomers, not only molecular ion isomers but also its fragment ion isomers.

Fig.6.21 shows the fragmentation mass spectra of $(M\text{-}OH)^+$ from 2,5-DHB and 2,3-DHB by a 355nm fragmentation laser. Obviously the two fragmentation mass spectra are different. Table 6.1 lists all fragments and their masses.

Table 6.1

Names (from 2,5DHB)	MASS	Names (from 2,3DHB)	MASS
(M-CO2H)	109	(M-CO2H)	109
(C5H3+OH)	80	(C5H3+OH)	80
C5H8	68	?	62
C4H4	52	C4H4	52
C4H6	54	C4H6	54
C3H2	38	C3H2	38
C2H2	26	C2H2	26

Comparing the two fragmentation patterns it can be seen that all fragments are same except fragment C_5H_8(m/z,68) from 2,5-DHB and the mass 62(m/z) from 2,3-DHB. These fragmentation patterns act like fingerprints of the molecular ions, each differs from the others. It is powerful technique for distinguishing between the isomer ions.

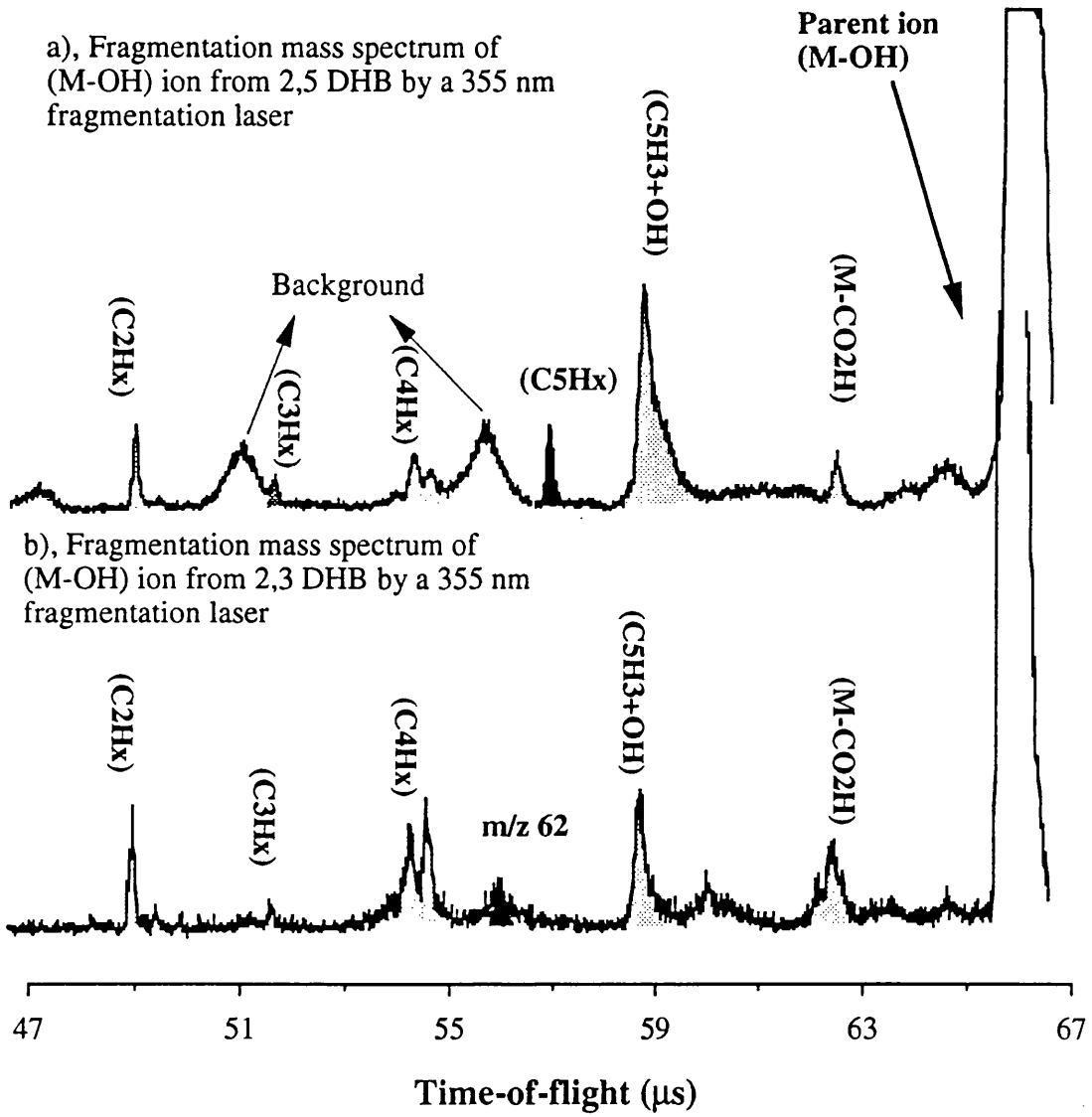

Fig.6.21 The different fragmentation patterns of the isomer ions of $(M\text{-}OH)^+$ from 2,5 DHB and 2,3 DHB by a 355 nm fragmentation laser. It shows that the isomer ions can be distiguished by this unique MS/MS technique.

The mass 62 from $(M\text{-}OH)^+$ of 2,3-DHB is not clear, probably it is $C_2H_6O_2$ because the two -OH groups link to the two neighbour carbons. The possible pathways shows in Fig.6.22:

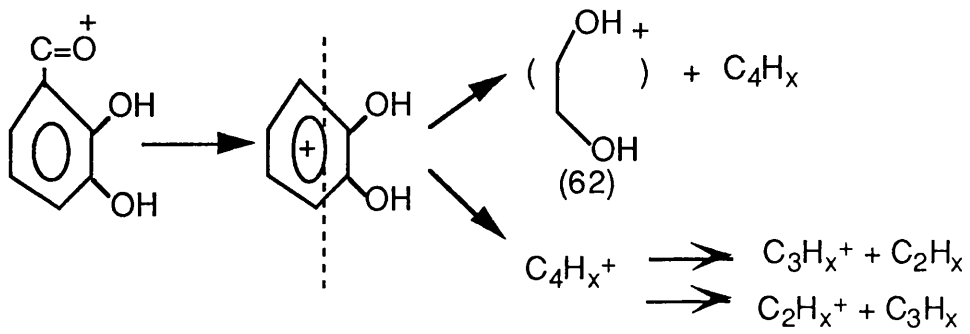

Fig. 6.22 Fragmentation pathway of (M-OH)+ from 2,3-DHB by a 355nm laser.

In addition, the fragmentation patterns of $(M\text{-}OH)^+$ from 2,5-DHB and 2,3-DHB by a 266nm fragmentation laser are also different from each other(see Fig.6.23) . Table 6.2 presents the fragments and their masses of $(M\text{-}OH)^+$ from 2,5-DHB and 2,3-DHB.

In the fragmentation mass spectrum of 2,5-DHB by a 266 nm laser there is no peak at mass 52 (m/z) assigned to C_4H_4. However in the mass spectrum of 2,3-DHB there is no ion peak of mass 68 which may be assigned to be C_5H_8. These different fragmentation

Table 6.2

Names (from 2,5DHB)	MASS	Names (from 2,3DHB)	MASS
(C5H3+OH)	80	(C5H3+OH)	80
C5H8	68		
		C4H4	52
C4H6	54	C4H6	54
C3H2	38	C3H2	38
C2H2	26	C2H2	26

patterns imply that there are different fragmentation pathways involved. Here we will not discuss these fragmentation patterns in detail because of their complexity and further experiments needed to be carried out.

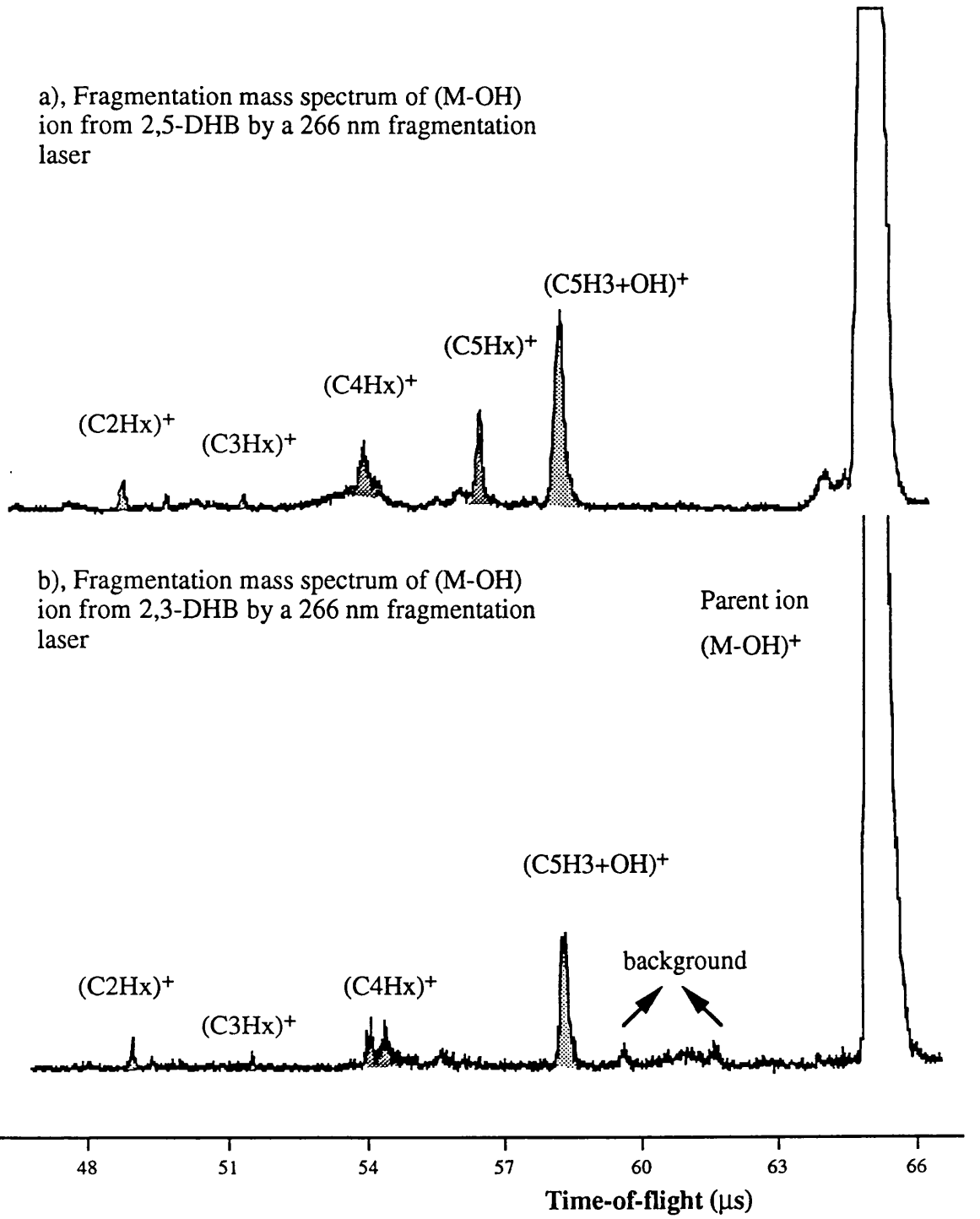

Fig.6.23 The different fragmentation patterns of the isomer ions of (M-OH)+ from 2,3-DHB and 2,5DHB by a 266nm fragmentation laser.

6.7 Conclusions

In this chapter, many details of fragmentation pathways of the ions of $(M\text{-}OH)^+$, $(M)^{+\cdot}$ and $((M\text{-}OH)_2\text{-}H)^+$ have been discussed, and most of these fragmentation patterns can be described by the "Ladder-switching" model. In addition, the distinguishing between the ion isomers in this experiment indicates another advantage of this newly developed tandem reflectron TOF mass spectrometer.

Chapter 7

Photofragmentation of Biomolecular Ions

7.1 Introduction

The sequencing and structural elucidation of peptides and proteins are essential prerequisites to understanding their biomolecular function at a molecular level. Therefore, one of the goals of analytical mass spectroscopists is the development of routine mass analysis techniques to study these molecules. Ideally, a technique should provide both the molecular weight of the intact molecule and sufficient structural information to allow the determination of the structures and sequencing of the amino acids in these biological molecules. Comparing with normal proteins and DNA sequencing methods such as gel-electrophoresis, mass spectrometric methods for biomolecular sequencing have inherently relatively high speed(seconds per residue), sensitivity and accuracy.

One of the main difficulties in using mass spectrometry in this area has been that the only small fragments of the large biomolecules can be introduced into a mass spectrometer. Recently there have been improvement in ionisation methods for peptides and proteins such as fast atom bombardment and matrix-assistant laser desorption/ionisation (MALDI)(see Chapter 4) producing intact molecular ions. In addition there have been major advances in instrumentation design with increased sensitivity and thus mass spectrometry is rapidly becoming the method of choice for tackling the structural analysis and sequencing of these biomolecules.

In this Chapter a TRTOF developed in our group was utilised for the investigation of laser photofragmentation of molecular ions of amino acids. The intact molecular ions were produced by MALDI with 2,5-DHB as a matrix, and then the intact ions were fragmented by a second laser at their turn-around points in the reflectron. The fragments were detected by duel multi-channel plate detector.

The fragmentation mass spectra of the molecular ions, PTH-tryptophan, PTH-valine, PTH-alanine, Cytosine, Guanine and Indole-2-carboxylic acid will be shown and discussed in this Chapter.

7.2 Photofragmentation of PTH-tryptophan

Photofragmentation of biomolecular ions is very important for analysis of structures and sequencing biomolecules. The newly developed TRTOF is a very useful tool for the investigation of the fragmentation patterns of a specific molecular ion. Analysis of the biologically important molecule PTH-tryptophan has been conducted in order to determine the effects of photofragmentation on biomolecular ions. PTH-tryptophan has been chosen for the following reasons: a) it is an essential amino acid in proteins. b) it has a very similar structure to L-tryptophan and so the results obtained can be used to compare with those from L-tryptophan which have been widely studied. c) the molecular weight of PTH-tryptophan (321) is greater than that of L-tryptophan (204), which eliminate the interference of the ion peaks from the matrix(154) when it is fragmented by a photofragmentation laser. Fig.7.1 shows the structural formulae of PTH-tryptophan and L-tryptophan.

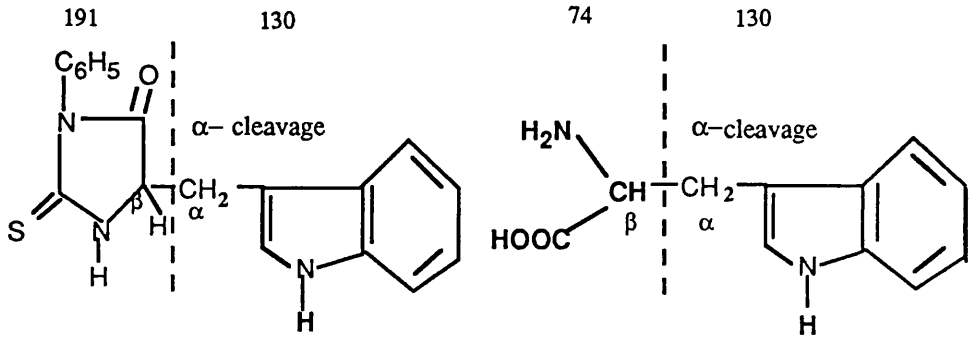

PTH-tryptophan m/z 321 **L-tryptophan m/z 204**

Fig.7.1 Structural formula of PTH-tryptophan and L-tryptophan

Static secondary ion and laser postionisation mass spectra of L-tryptophan have been reported previously. Benninghoven and Sichtermann observed very weak $(M+H)^+$ (m/z 205) signals in positive and negative static SIMS. (Benninghoven, and Sichtermann, 1978). Ervin et al. found that the overall intensity of the SIMS spectrum was more than an order of magnitude less intense than 280 nm laser postionisation mass spectrum of neutrals sputtered from a frozen, aqueous matrix(Ervin, et al. 1993). In this mass spectrum, m/z 130 $(M-74)^+$, which was produced from C_α-C_β cleavage of the amino acid component, was the base peak. In fact the mass peak m/z 130 appears in all the

published spectra recorded by following the ion-stimulated desorption of L-tryptophan, regardless of postionisation wavelength employed e.g. 193, 248, 280, or 290 nm. For the desorption of neutral L-tryptophan with a CO_2 laser followed by injection into a supersonic argon beam and photoionisation at 266nm, the m/z 130 peak is also the most intense peak in the TOF mass spectrum. (Grotemeyer; et al. 1989, 1992, 1994)). Koster and Grotemeyer(C. Koster and J.Grotemeyer 1992) also observed that the dissociation of the parent molecular ion by resonant MPI at 236 nm following the infrared laser-desorbed, jet-entrained L-tryptophan, was complete with the dominant fragment of m/z 130, regardless of photo-ionising laser power.

Ayre etc. (Ayre, et al. 1994) have investigated the mass spectral fragmentation following the desorption and postionisation of L-tryptophan in details. 7-keV Ar^+ static sputtering, 266 and 355nm pulsed laser induced desorption, and thermal desorption at 150-200 ^oC in conjunction with 118 nm, 266nm, and 355nm laser postionisation were used. The results show that the molecular fragmentation was dominated by the effect of the desorption process rather than the photoionisation method for the wavelengths studied. Fragmentation was maximal with ion-stimulated desorption, intermediate with laser-induced desorption, and minimal with thermal desorption. The base peak still appears at m/z 130 and corresponds to C_α-C_β cleavage of the amino acid side chain. No parent molecular ions were seen and only the peak m/z 130 and other small fragments were observed when a pulsed Ar^+ beam desorption is followed by 118, 266 and 355nm postionisation. In the spectrum acquired following 355nm postionisation, only the base peak at m/z 130 appears, while the recorded intensity of this peak is very weak. In order to produce ionisation, three photons must be absorbed, since the tryptophan ionisation potential is 8.43eV(Slifkin and Allison, 1967). A decreased probability of absorption of multiphoton process is apparent in the result of this low ion yield. However all the experiments have not clearly shown or are unable to show whether the fragment ions, such as the peak m/z 130, are produced from the ionisation of its neutral species or from further fragmentation of the parent molecular ions.

PTH-tryptophan is a white powder and can be easily dissolved in water. In this work PTH-tryptophan was dissolved in a saturated solution of 2,5-DHB (ratio about 1:100), and add about 3 drops of the solution on a sample stub, then dried under a warm air steam.

Fig.7.2a shows the MALDI mass spectrum of PTH-tryptophan with 2,5-DHB as a matrix. Unlike the TOF mass spectrum of L-tryptophan by a UV laser-induced desorption followed by 266nm laser postionisation in which there was a very small parent molecular ion(Ayre etc. 1994), there is the large intact parent molecular ion(m/z 322) of PTH-tryptophan in this mass spectrum. Comparing with a pure 2,5-DHB mass spectrum(Fig.5.7) it can be seen that there are two other main peaks from PTH-tryptophan, m/z 130 and m/z 191.

As we mentioned above, all of the mass spectra of desorption or postionisation of tryptophan have a base peak at m/z 130 which corresponds to the cleavage of the amino acid side chain. This base peak also appears in the MALDI mass spectrum. It has been commonly recognised that MALDI is a very "soft" ionisation technique which produces large intact molecular ions. Therefore fragments of PTH-tryptophan appearing in this spectrum can be explained since the bond of C_α-$C\beta$ is very weak and easily to be fragmented. The peak at m/z 191 is assigned to be the other part of the molecule(see Fig.7.1). However in the mass spectra of L-tryptophan obtained by other authors there was non peak at m/z 74 (L-tryptophan-130), the most possible reason is that it is not stable and will further dissociate into smaller fragments such as C_2H_x, CH_x, NH_4 etc..

The molecular ions of PTH-tryptophan were selected according to its time-of-flight in the TOF mass spectrometer(see chapter 5) and fragmented by a 266nm photofragmentation laser with a pulse width of 5ns and power energy of 2mJ. Fig.7.2b shows the fragmentation mass spectra of PTH-tryptophan. It is clearly illustrated that there are two prominent and narrow fragments appearing in the fragmentation mass spectrum comparing with its background. These two fragments are m/z131 and m/z 193((PTH-tryptophan+H)-129)$^+$, respectively.

It should be emphasised that to the author's knowledge this is a very important mass spectrum since it is the first photofragmentation mass spectrum of a biological molecular ion produced by MALDI. In the mass spectra obtained by the desorption and postionisation method, it is difficult to distinguish between the ionisation and dissociation processes of large molecular systems in the gas phase in which energy transport and charge transport may be involved. The fragmentation mass spectrum in Fig.7.2b is

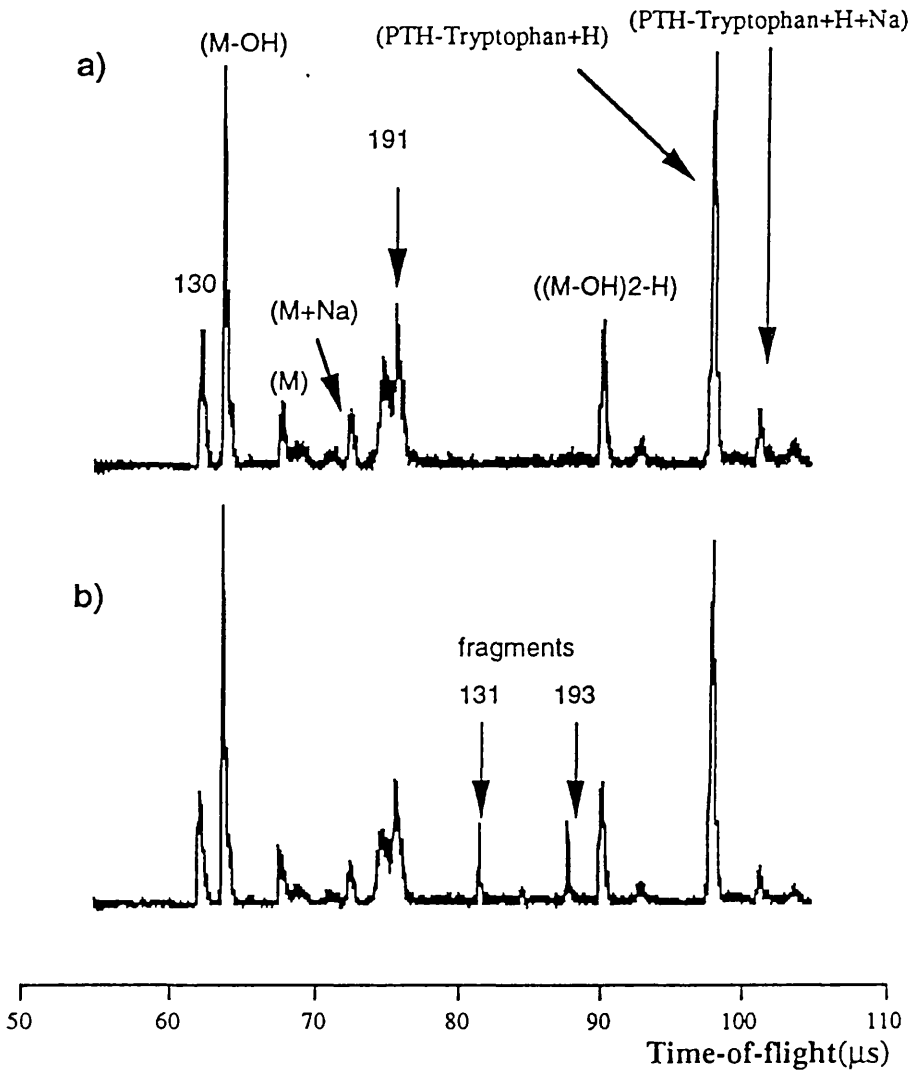

Fig.7.2 The mass spectra of PTH-tryptophan. a) The MALDI mass spectrum of PTH-tryptophan ablated by the 337nm N2 laser (70 μJ) with 2,5-DHB(M) as the matrix. b) The fragmentation mass spectrum of $(PTH\text{-}tryptophan+H)^+$ by a 266nm fragmentation laser with a pulse energy of 2 mJ. Mass of 130 and 193 in spectrum (a) are the fragments from PTH-tryptophan ablation.

obviously obtained through a dissociation process which will help us not only for the interpretation of biomolecular mass spectra, but also for the general theory of photofragmentation of molecular ions.

Usually the photofragmentation of medium to large biological molecules is very complicated. In the mass range above 300 Da of organic molecules, the number of vibrational degrees of freedom becomes very large. Fast internal vibrational energy redistribution is involved in a extremely large system and can store large amounts of internal energy in the molecule, without observing statistical fragmentation on the time observed(Schlag, and Levine, 1989). This may be one of the main reasons why the postionisation efficiency of large biomolecules decreases with the increase of the size of molecules. In order to obtain a fragmentation mass spectrum , more than 100 eV in the molecular ion (Weinkauf, et al. 1994) must be deposited. In the case of PTH-tryptophan, the power energy of the laser was not high (2mJ, unfocused). The fragmentation needs only two or three photons of 266nm, the photon energy being around 9.3-14 eV, which is far below 100 eV. This means that the parent molecular ion must contain a large amount of internal energy when it was produced by MALDI. This excited molecular cation is possibly created by its collision with the matrix molecules during the photochemical reactions in the dense desorption plume. The low mass resolution ($m/\Delta m < 200$) and slow metastable decays in MALDI indicates that the parent molecular ions are in a high internal energy levels. Therefore only a small amount of photon energy is required for the dissociation of a biomolecular ions produced by MALDI method. Another reason for the requirement of a small amount of photon energy in the photodissociation of molecular ions is that the density of electronic states in ions is much higher than that in neutrals, hence the photon absorption in ions is enhanced in comparison to neutrals. The two fragments in the fragmentation mass spectrum (Fig.7.2b) come directly from their parent ion since they always appear simultaneously whether the power of the fragmentation laser was large or small. Thus the possible fragmentation pathway can be shown in Fig.7.3. The ion peak of the mass of 131 is probably produced by proton-transfer from the β-carbon to the α-carbon while the mass of 193 generated by proton-transfer from the α-carton to the β-carbon.

The high internal excitation of the molecules or molecular ions from laser desorption can be also seen in the laser desorption and postionisation mass spectra. Ayre et al.(Ayre et

a)

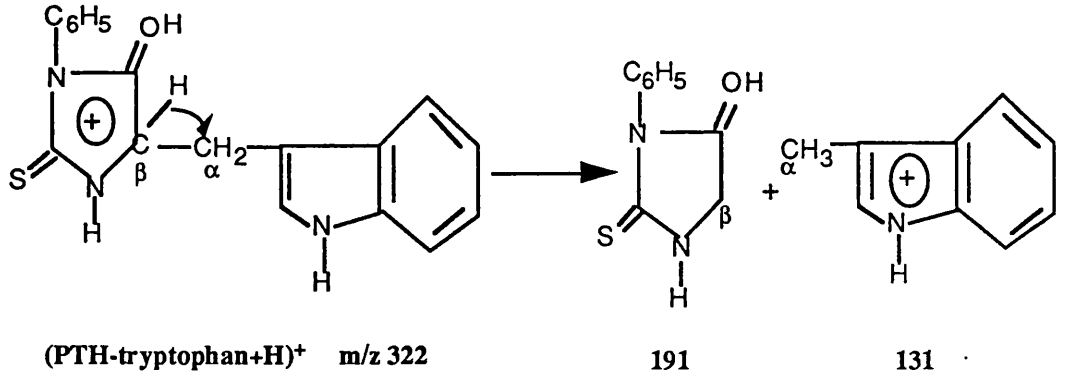

(PTH-tryptophan+H)$^+$ m/z 322 191 131

b)

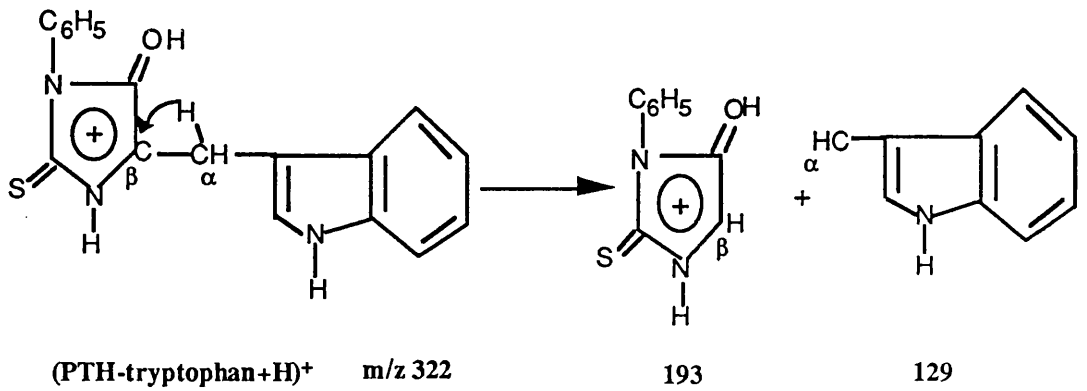

(PTH-tryptophan+H)$^+$ m/z 322 193 129

Fig.7.3 Photofragmentation of PTH-tryptophan by the 266nm laser with the pulse en ergy of 2mJ. a) f ormation of the f ragment ion at m/z131; b) formation of the fragment ion at m/z 193.

al. 1994) used 266 and 355 nm laser for desorption of L-tryptophan and 118 nm and 266 nm laser for postionisation and observed the very weak parent ion. However an intense parent ion appeared when thermal desorption of L-tryptophan was followed by either 118nm or 266nm postionisation. These results imply that the molecules or molecular ions were highly excited and easily fragmented when they were desorbed by a UV laser, but exhibited low excitation when they were desorbed by a IR laser or thermal sublimation.

The adducts of PTH-tryptophan can also be fragmented by a 266nm laser if the delay of

the photofragmentation laser is changed to the arrival of these ions at the fragmentation region. Fig.7.4 shows the fragmentation mass spectrum of (PTH-tryptophan+Na)$^+$ and (PTH-tryptophan+K)$^+$. It should be mentioned in this mass spectrum that the parent ion of PTH-tryptophan is very small because the sample layer was very close to the surface of the sample stub in order to produce a large amount of (PTH-tryptophan+Na)$^+$ and (PTH-tryptophan+K)$^+$. It is shown that there are two fragments Na^+ and K^+ coming from (PTH-tryptophan+Na)$^+$ and (PTH-tryptophan+K)$^+$, respectively. Due to the small mass difference between the two ions of (PTH-tryptophan+Na)$^+$ and (PTH-tryptophan+K)$^+$ and large energy spread, these two parent ions are overlapping in the fragmentation region and dissociated at the same time. Therefore the both fragments of Na^+ and K^+ appear in the mass spectrum at the same time. However the accurate mass of Na^+ or K^+ can be calculated according to their expected delay time of the photofragmentation laser. The bonds between molecules and adduct ions such as Na^+ and K^+ usually are very weak and can be easily fragmented. The normal fragmentation patterns are the ions of the alkali and the neutrals of the molecule.

7.3 Photofragmentation of PTH-valine

PTH-Valine is also another essential amino acid and its structure is shown in Fig.7.5 with the group of N-Phenylthiohydantoin attached to form PTH-Valine. It is similar to the structure of PTH-tryptophan which has the same group of N-Phenylthiohydantoin. However the bond of C_α-C_β is not weak as that in PTH-tryptophan because there is no stable group such as that in L-tryptophan. Therefore the fragmentation pattern may be different from that of PTH-tryptophan. Fig.7.6 shows the fragmentation mass spectra of

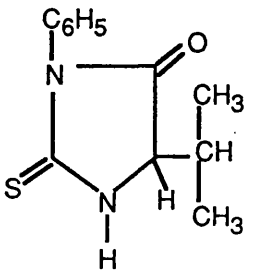

PTH-valine

(MW=234)

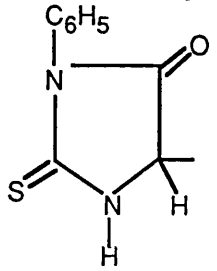

N-Phenylthiohydantoin group

(MW=191)

Fig.7.5 The structure of PTH-valine and N-Phenylthiohydantoin group.

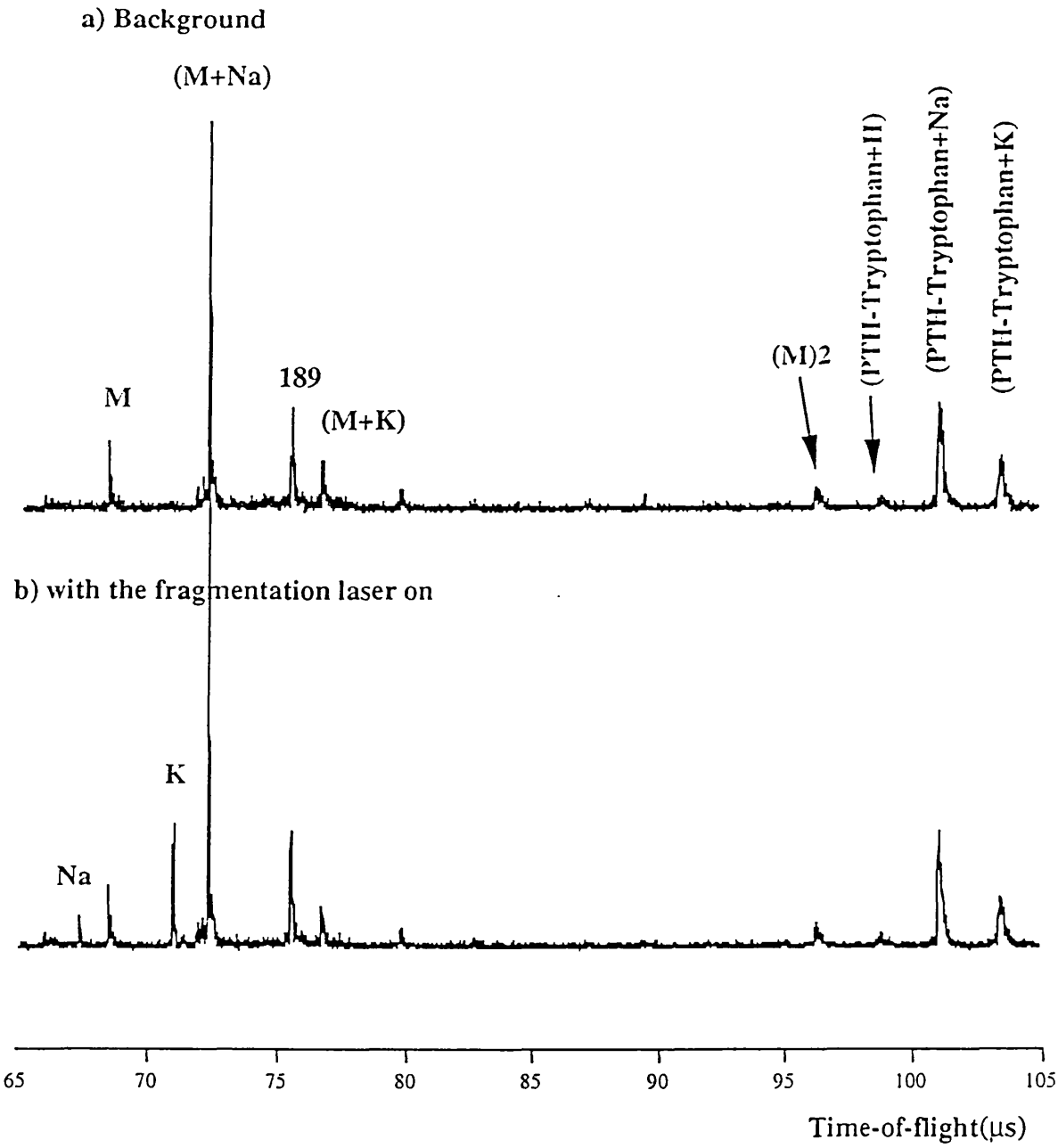

Fig.7.4 The fragmentation mass spectra of $(PTH\text{-}Try+Na)^+$ and $(PTH\text{-}Try+K)^+$. a) with the 266nm fragmentation laser off; b) with the laser on. The delay was set for the fragmentation of $(PTH\text{-}Try+K)^+$ (55.985μs with respect to the ablation laser firing time). The parent ion of (PTH-Try) was very small because the sample was nearly run out by the ablation laser and its adduct with alkali from the stub surface increased. The mass 89(m/z) is the fragment of (PTH-Try) from ablation processes. M represents the 2,5-DHB.

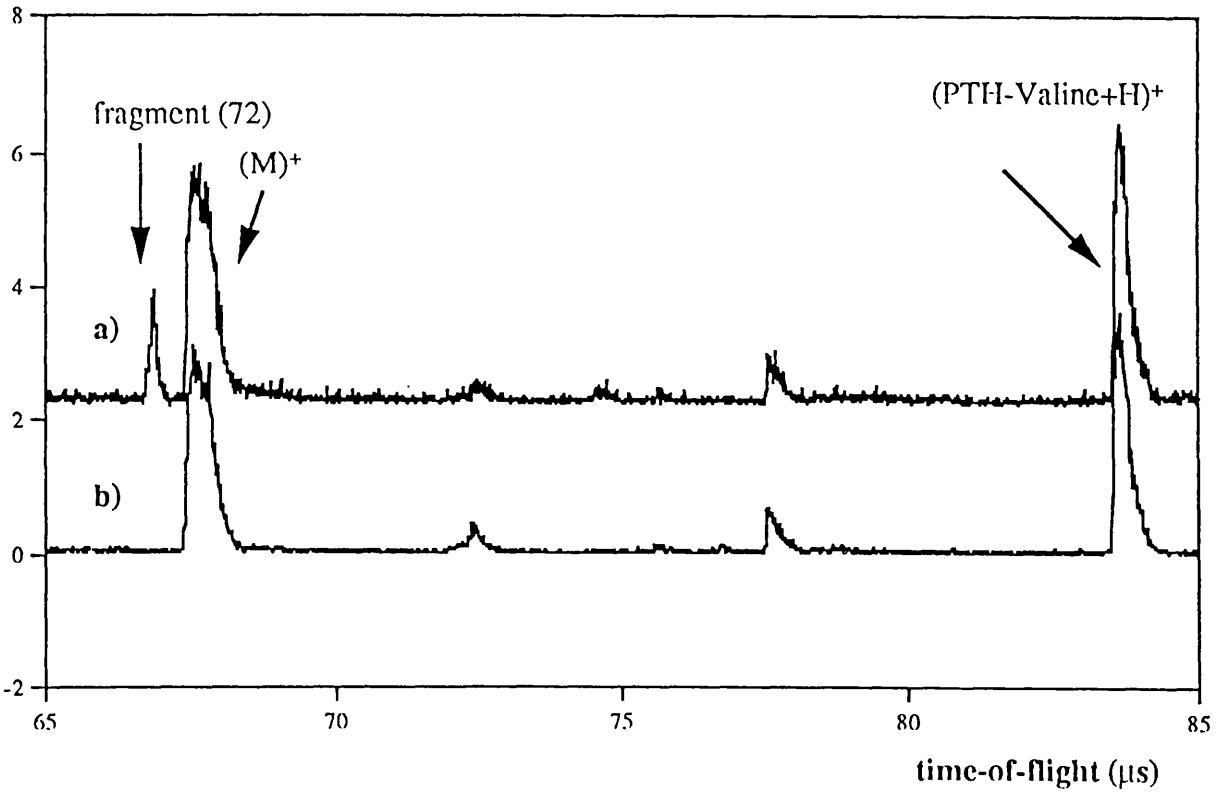

Fig. 7.6 The fragmentation mass spectra of PTH-valine with 2,5-DHB as a matrix matreial. a) with a fragmentation laser at 266nm on; b) with a fragmentation laser off

PTH-Valine desorbed by MALDI with 2,5-DHB as a matrix. $(PTH\text{-}Valine+H)^+$ was the chosen ion and was fragmented by the 266nm laser. It can be seen that there is only one fragment (m/z 72). Obviously this fragment does not come from the cleavage of C_α-C_β bond and most likely from the breaking of N-Phenylthiohydantoin ring as shows in Fig.7.5. A peptide chain normally cleaves at each CO-NH bond. Here the cleavage of the bond is CS-NH because O and S locate at the same row in the periodic table, and have similar electronic structure and chemical properties. In addition, in a normal mass spectrum of imidazole, ionised by EI, where the ring break down by the loss of HCN and the dominant peak is m/z 41(see Fig.7.7).

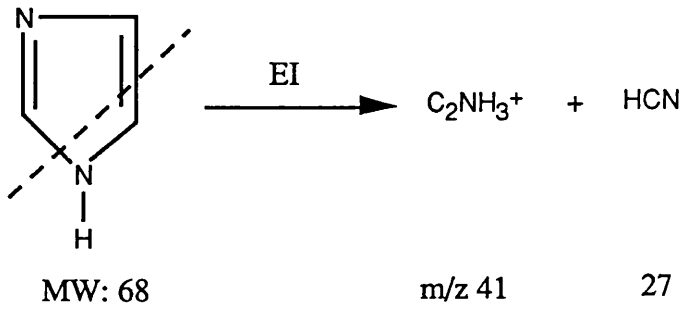

Fig.7.7 The fragmentation of imidazole by an electron-impact ionisation.

Therefore the fragmentation pathway of PTH-Valine can be written as in the following way(Fig.7.8)

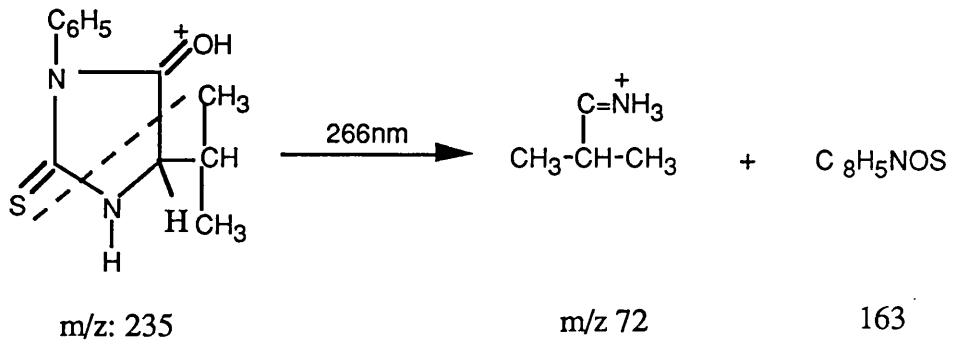

Fig.7.8 The fragmentation pathawy of $(PTH\text{-}valine+H)^+$ by a 266nm laser.

7.4 Photofragmentation of PTH-Alanine

PTH-Alanine has a very similar structure of PTH-Valine. Its molecular weight(206) is smaller than those of PTH-Valine because it has CH_3 group replacing $CH\text{-}(CH_3)_2$ (see

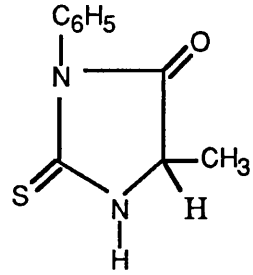

(MW=206)

Fig.7.9 The structure of PTH-alanine.

Fig.7.9). The fragmentation pattern of PTH-Alanine is expected to be similar to PTH-Valine. However the parent molecular ions can't be fragmented by a 266nm laser, possibly because the absorption cross section of PTH-Alanine at 266nm is very small. Therefore the wavelength of the fragmentation laser was changed to 355nm. Fig. 7.10 shows the fragmentation mass spectra of PTH-Alanine. Two fragments, m/z 44 and m/z 77, were obtained. The m/z 44 comes from the cleavage of C-C bond and C-N bond in the N-Phenylthiohydantoin ring which is the same rupture of PTH-Valine(see Fig.7.11 cleavage a). The fragment of m/z 77 is the benzene ring ($C_6H_5^+$) by the further fragmentation(see Fig.7.11 cleavage b). The fragment peak m/z 44 is much larger than the m/z 77, which implies that the fragmentation pattern favours the breaking of the N-Phenylthiohydantoin ring. Fig.7.11 shows the fragmentation pathway of PTH-alanine by the 355nm fragmentation laser.

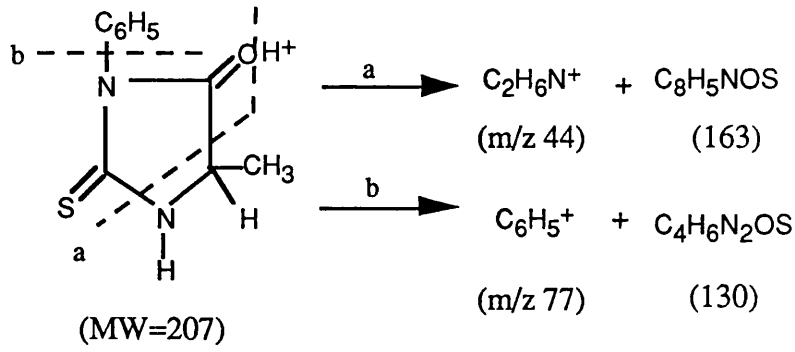

Fig.7.11 The fragmentation pathway of (PTH-alanine+H)$^+$ by the 355nm fragmentation laser.

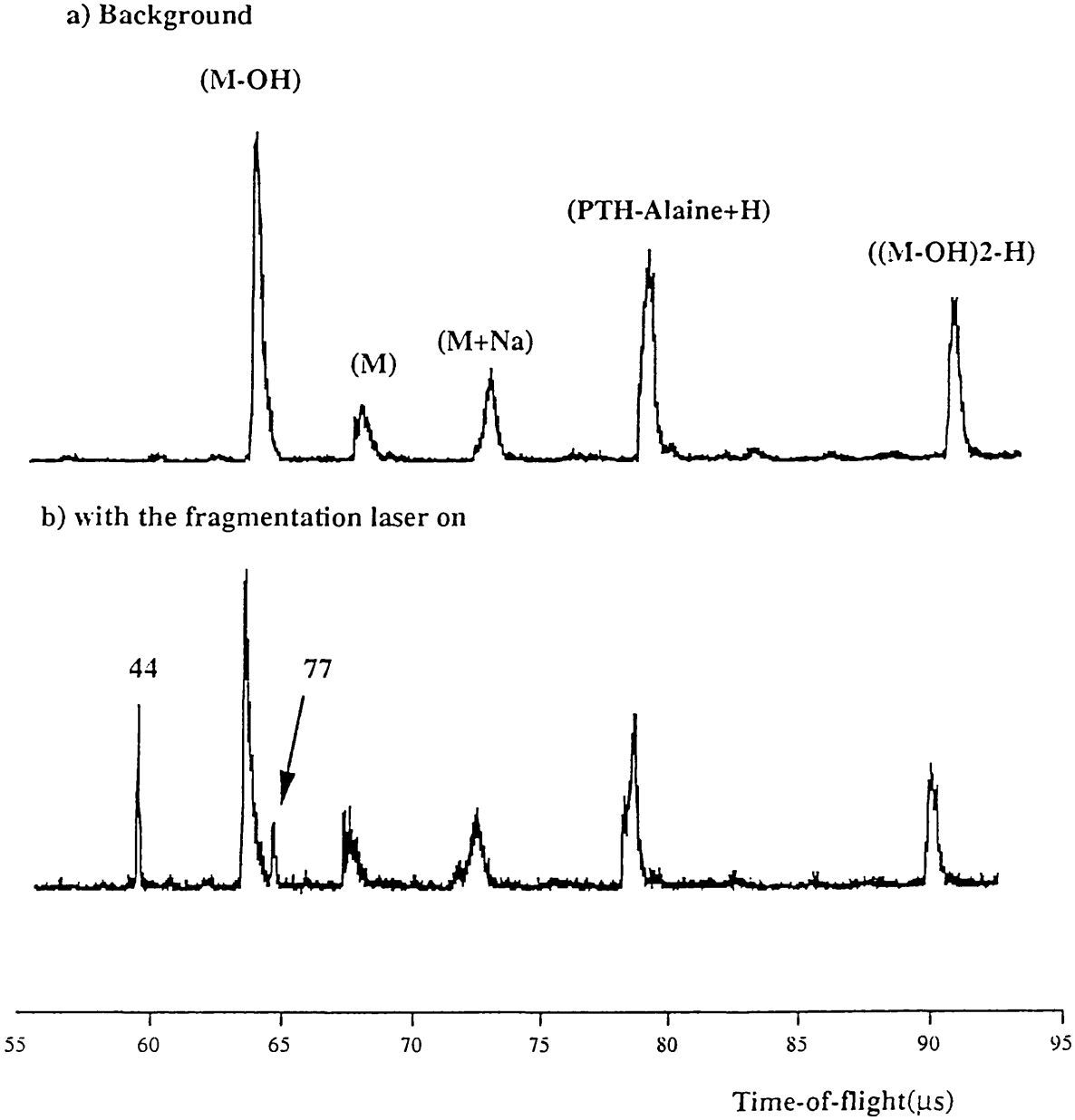

Fig. 7.10 The fragmentation mass spectra of (PTH-Alanine+H) by the 355nm fragmentation laser. a) with the fragmentation laser off; b) with the fragmentation laser on. The delay was 43.700μs. M represents 2,5-DHB.

7.5 Photofragmentation of Cytosine

The structure of Cytosine is shown in Fig.7.12. Cytosine is a basic molecular group in large biological molecules such as DNA. Therefore its photo-fragmentation pattern is of particular interest to us.

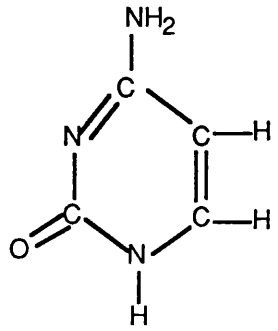

(MW: 111)

Fig.7.12 The structure of Cytosine.

Fig.7.13 presents the MALDI mass spectrum of Cytosine in which 2,5-DHB was used as a matrix. The molecular ion of $(Cytosine+H)^+$ was selected and fragmented by a 266nm fragmentation laser. Fig.7.14 shows the fragmentation mass spectra of $(Cytosine+H)^+$. Four main fragment ions m/z 18, 41, 68, 94 were obtained. The ion peak m/z 18 is NH_4^+ by cleavage of the bond NH_2-C and the other part of the fragment is $C_4H_2N_2O$ (m/z 94). The fragments of m/z 41, and 68 maybe come from rupturing the ring. Therefore the possible fragmentation patterns can be drawn in Fig.7.15.

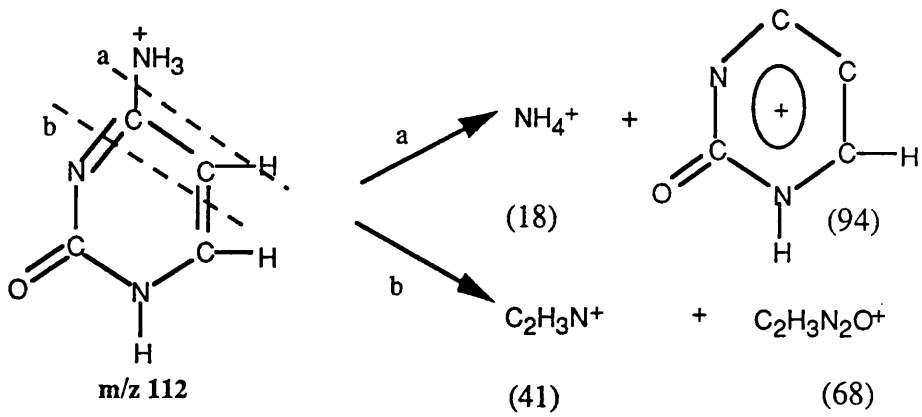

Fig.7.15 The fragmentation pathways of Cytosine by a 266nm laser.

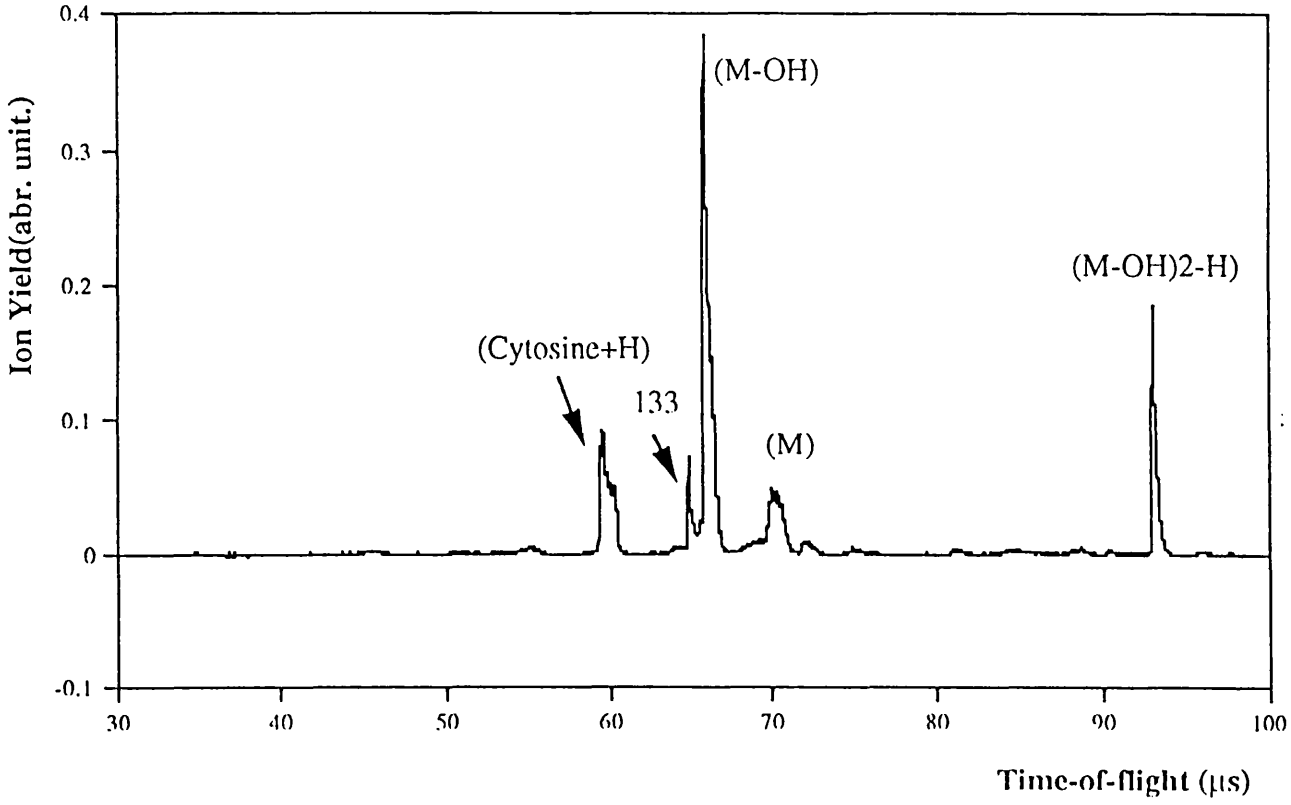

Fig.7.13 The MALDI mass spectrum of Cytosine with 2,5-DHB as a matrix generated by a 337nm N_2 Laser. The peak m/z 133 is Cs^+ used for calibration in this experiment.

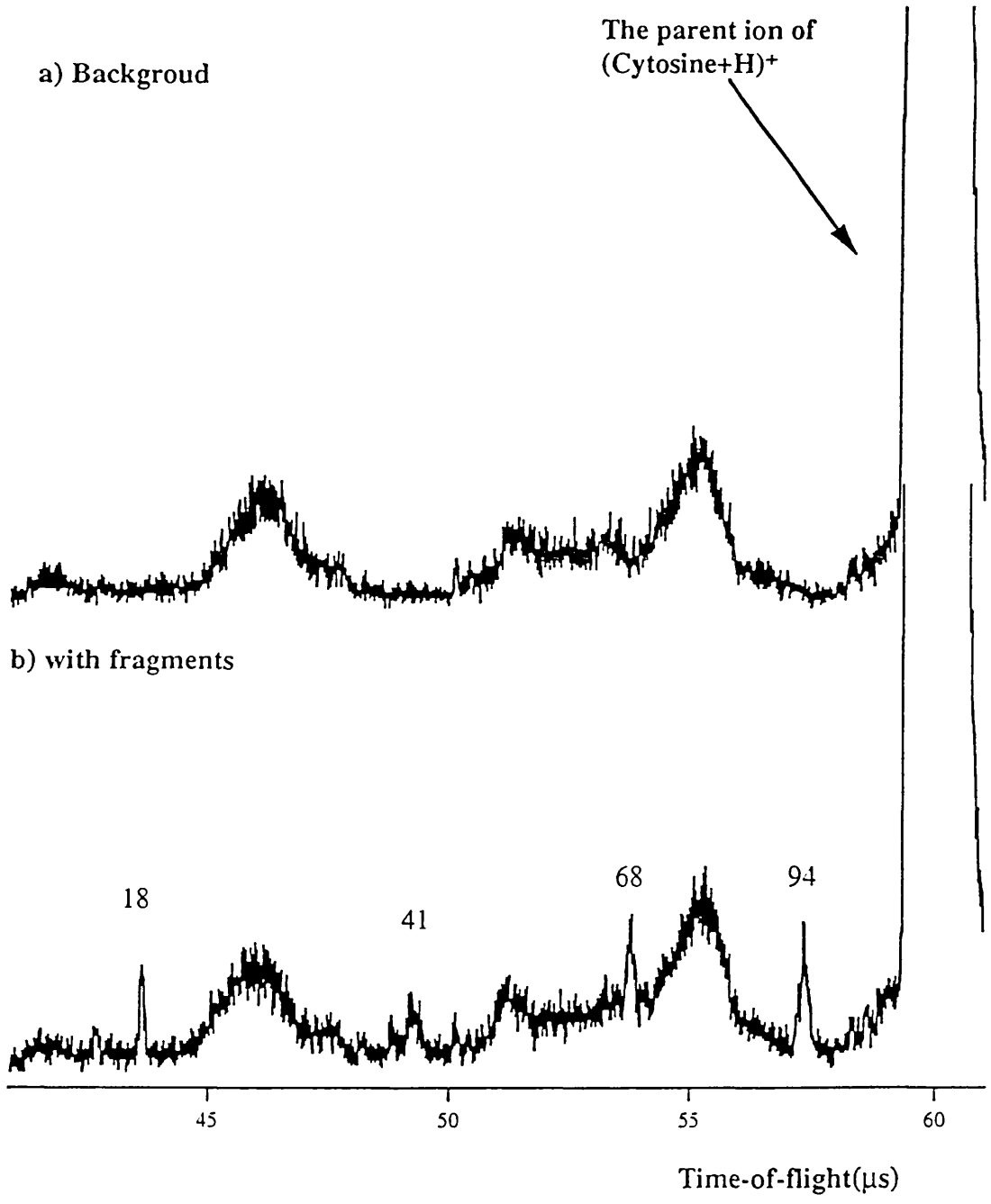

Fig.7.14 The fragmentation mass spectra of (Cytosine+H)$^+$ by a 266nm fragmentation laser with a pulse energy of 2 mJ. a) the mass spectrum with the fragmentation laser off; b) with the fragmentation laser on. The main fragments of m/z 18, 41, 68 and 94 from (Cytosine+H)$^+$ were obtained.

It should be mentioned that in Fig.7.15 the two fragment ions in each pathway are not produced simultaneously from the parent ion but rather one ion and one neutral species and vice versa.

7.6 Photofragmentation of Guanine

Guanine is also a basic molecular unit in large biomolecules. The structure of Guanine is shown in Fig.7.16.

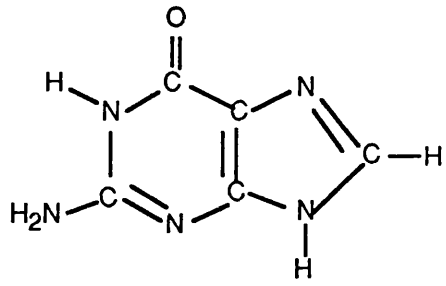

MW: 151

Fig.7.16 The structure of Guanine.

The MALDI mass spectrum of Guanine by a 337nm N_2 laser is seen in Fig.7.17. The base peak is still $(M\text{-}OH)^+$ from 2,5-DHB. The position of the parent ion peak of Guanine was very close to the peak of the parent ion of 2,5-DHB (see the inset of Fig.7.17). Fortunately the parent ion of 2,5-DHB cannot be fragmented by a 266nm laser at these conditions(see Chapter 6). Hence the fragments obtained were directly from the parent ion of Guanine.

The fragmentation mass spectra of $(Guanine+H)^+$ is shown in Fig.7.18. There are five fragment ions: m/z 28, 43, 55, 111 and 136 in this mass spectrum. The ion peaks at m/z 136 and 111 are much larger than the rest of peaks. Therefore it is reasonable to consider that the small fragments come from further fragmentation of large fragments. It is difficult to assign all these fragments, but it is easy to find out that the peak at m/z 136 is $(Guanine\text{-}NH_2)^+$ from the cleavage of H_2N-C bond (lose of mass unit of 16) and the fragment at m/z 111 from further fragmentation of 136 by loss of the small stable molecule CN. The small fragments are produced from the fragment of m/z 111 by losing

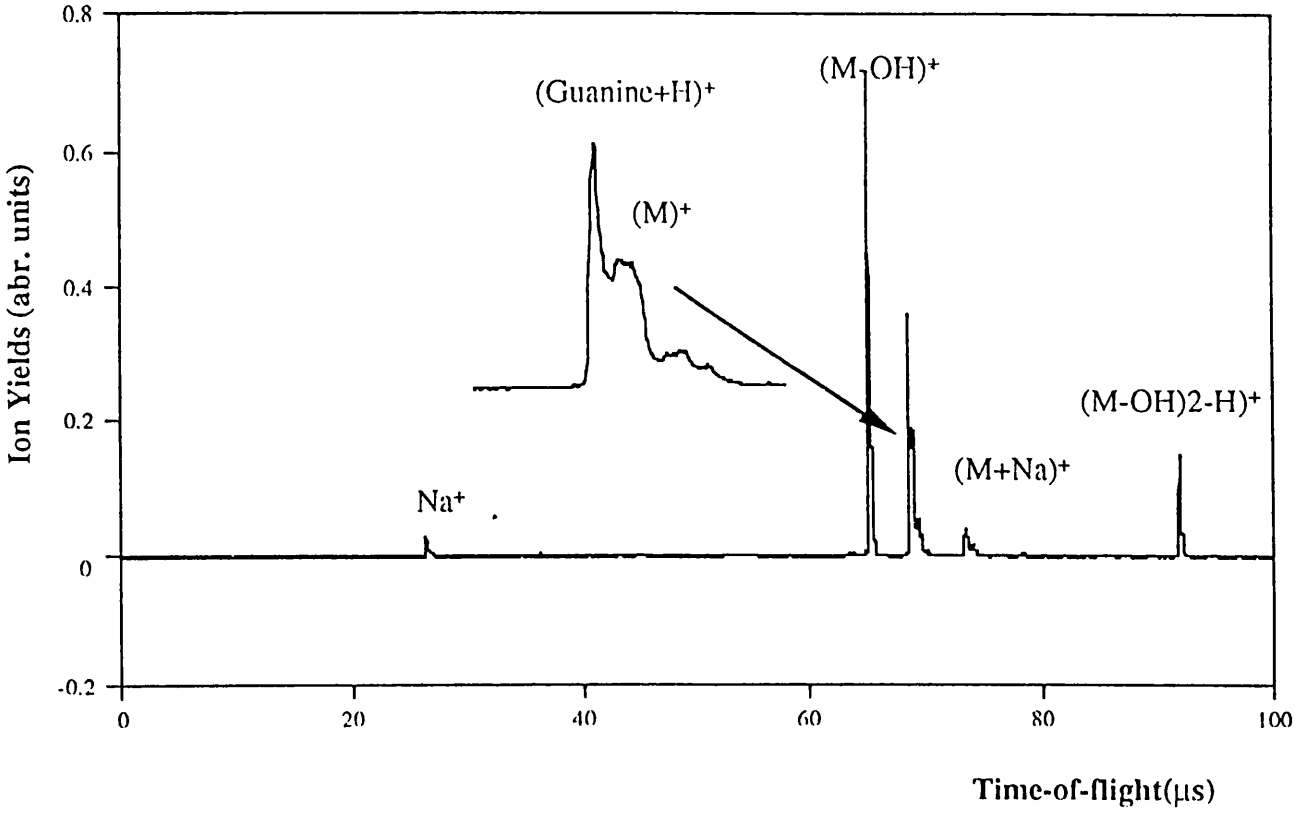

Fig. 7.17 The MALDI mass spectrum of Guanine with 2,5-DHB as a matrix(M) ablated by a N_2 laser(70 μJ). The inset shows the parent ion of Guanine.

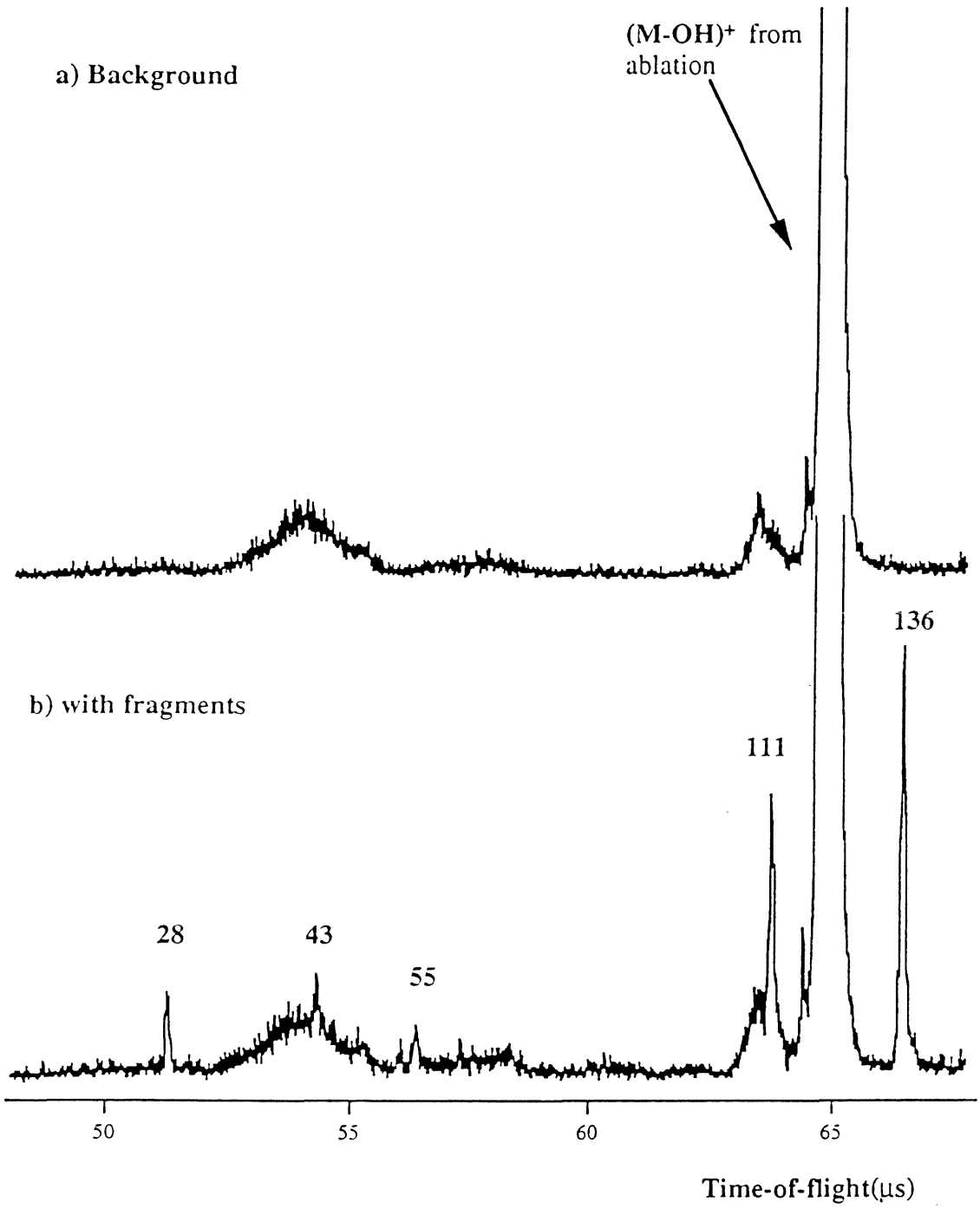

g.7.18 The fragmentation mass spectra of (Guanine+H)+ by a 266nm fragmentation laser th a pulse energy of 2 mJ. a) the mass spectrum with the fragmentation laser off; b) with e fragmentation laser on. The main fragments of m/z 28, 43, 55, 111 and 136 from the parent ns were obtained.

small neutrals such as HCN, CH_x, CO. Fig.7.19 indicates the possible fragmentation pathways of $(Guanine+H)^+$ by a 266nm laser.

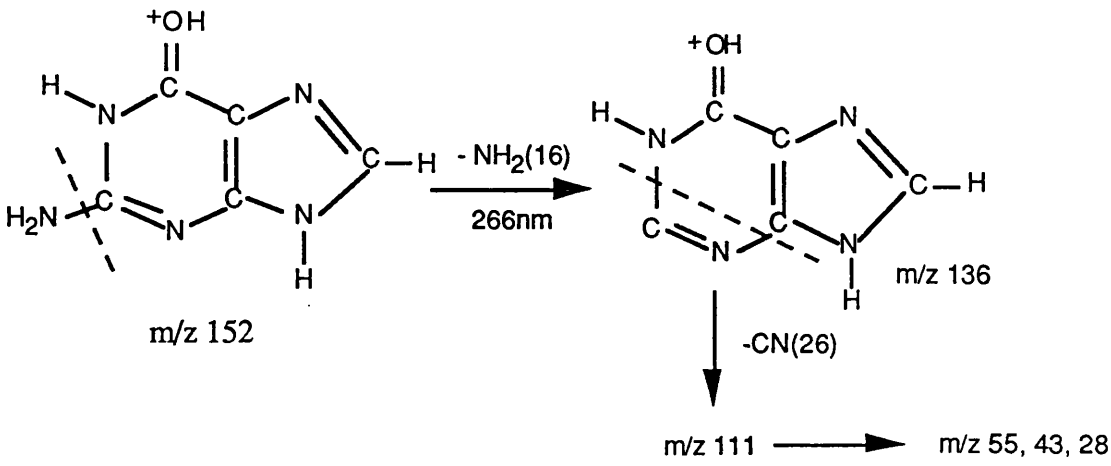

Fig.7.19 The fragmentation pathways of $(Guanine+H)^+$ by a 266nm laser.

7.7 Photofragmentation of Indole-2-carboxylic acid

Indole-2-carboxylic acid is not only an important molecule in biological chemistry, but also a matrix material in MALDI. Its fragmentation patterns are interesting to scientists working in biological mass spectrometry. Fig.7.20 shows the structure of Indole-2-carboxylic acid.

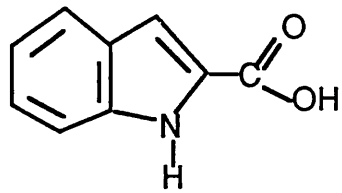

(MW=161)

Fig.7.20 The structure of Indole-2-carboxylic acid.

The ablation mass spectrum and the peak assignment of Indole-2-carboxylic acid by a 337nm N_2 laser is shown in Fig.7.21a. The main fragments of Indole-2-carboxylic acid from ablation processes are $(M-OH)^+$, $(M-CO_2H_x)^+$, $(M-C_2NO_2H_2)^+$, $C_5H_x^+$, and $(M-CO_2H_x)_2^+$. When a fragmentation laser at the wavelength of 335nm fired at the delay of 39.425μs with respect to the firing of the ablation laser, a fragmentation mass spectrum

of the parent ion Indole-2-carboxylic acid was observed (shown in Fig.7.21b). The fragments obtained were very much like those which appeared in the ablation mass spectrum. These fragments are $(M\text{-}OH)^+$(m/z 144), $(M\text{-}CO_2H)^+$(m/z 116) and $(M\text{-}C_2NO_2H_2)^+$(m/z 88). It seems that both ablation and fragmentation processes have a similar characteristic in which they tend to break weak bonds and form stable fragments. However the degree of the fragmentation and the ratios of these ion peaks are different due to the various energy of laser pulse and processes involved. In an ablation process, photo-chemical reactions and ionisation induced by collisions are dominant, thus the structure and the temperature of the sample surface, and the density of the desorbing plumes are important for the formation of an ablation mass spectrum. Especially in a high density plume, the dimers of the molecule or its fragments often appear in an ablation mass spectrum. Nevertheless, in the photofragmentation process, unimolecular dissociation and rearrangement processes are dominant, so the intensity and wavelength of a laser, and the structure of molecular ions are important in the determination of fragmentation patterns. The molecular ions always decompose into small fragments, and never form dimers in a fragmentation mass spectrum. From the intensities of fragment ions in ablation and fragmentation mass spectra (Fig.7.21), it can be seen that the largest ion peak in the ablation mass spectrum is $(M\text{-}C_2NO_2H_2)$, but the largest peak in the fragmentation mass spectrum is $(M\text{-}CO_2H)$. These facts imply that in an ablation process, the chemical ionisation is involved and carbon-carbon bonds or the bonds of carbon with other elements tend to cleave only if the products of the dissociation are particularly stable. Therefore fragmentation patterns favour the formation of stable products: the more stable the product formed is, the higher is the ion yield. In the case of the ablation mass spectrum of Indole-2-carboxylic acid, $(M\text{-}C_2NO_2H_2)^+$ is the most stable product after collisions and chemical ionisation. However in the fragmentation mass spectrum of Indole-2-carboxylic acid, $(M\text{-}CO_2H)^+$ is the most favoured product after fragmentation. One can not say that $(M\text{-}CO_2H)^+$ is more stable than $(M\text{-}C_2NO_2H_2)^+$ in the fragmentation process. The reason is that the ratios of fragment peaks depends on the intensity and wavelength of the laser involved in the photofragmentation processes.

7.8 Conclusions

For the first time, the fragmentation mass spectra of the molecular ions of PTH-tryptophan, PTH-Valine, PTH-Alanine, Cytosine and Guanine, generated by MALDI,

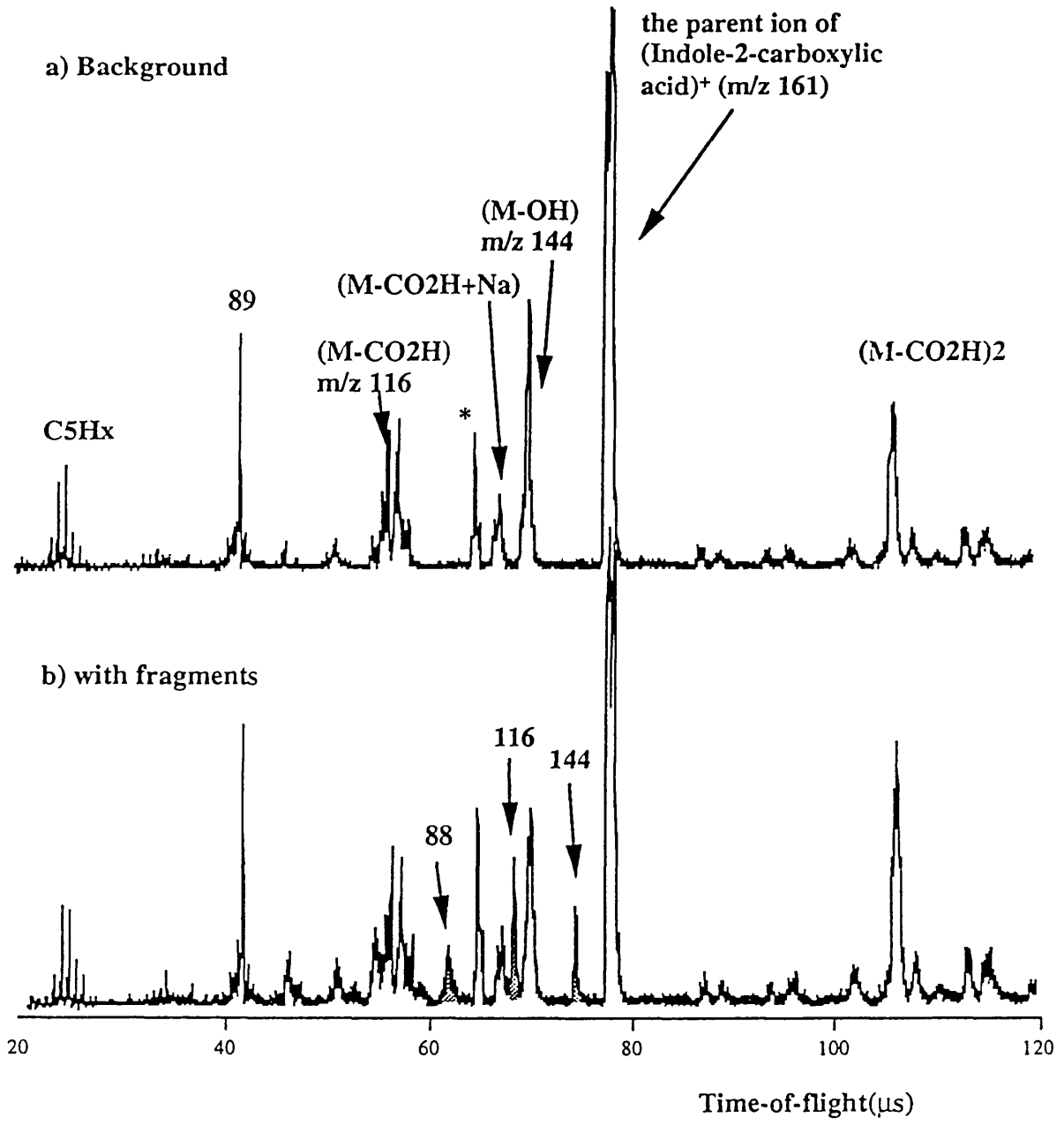

Fig.7.21 The fragmentation mass spectra of Indole-2-carboxylic acid ion by a 355nm fragmentation laser with a pulse energy of 30 mJ. a) the mass spectrum with the fragmentation laser off; b) with the fragmentation laser on. The fragments of m/z 88, 116, 144 from the parent molecular ion were observed. "*" is the Cs^+ from CsI for calibration. M represents 2,5-DHB.

.

have been successfully recorded using the newly developed TRTOF in our group and their possible fragmentation patterns have been presented. A number of possible fragmentation patterns have been discussed. These results imply a promising future for TRTOF in the photofragmentation of biomolecular ions although the necessary electronics to eliminate the detection of the bulk of the MALDI ions is still being developed..

Chapter 8

Conclusions and Future work

Conclusions

The major objective of this thesis was the development of the new tandem reflectron time-of-flight mass spectrometer and its application in the field of photofragmentation of molecular ions, particularly of biomolecular ions.

Chapter 1 described the historical development of resonance ionisation spectroscopy (RIS), matrix-assisted laser desorption ionisation(MALDI) and tandem time-of-flight mass spectrometry(MS/MS). The basic theoretical considerations were presented in Chapter 2. The instrumentation description and arrangements were shown in Chapter 3.

Chapter 4 has been dedicated to detailed experimental investigations of MALDI. The purpose of using MALDI technique in this thesis is to produce intact molecular ions which were used for the investigations of photofragmentation of molecular ions by the newly developed tandem reflectron time-of-flight mass spectrometer(TRTOF). It has been described how to choose a good matrix, how to prepare samples, and how to desorb some biomolecular ions. The mechanisms of MALDI, especially, the processes involved in ion formation have been discussed. The existence of neutral hydrogen atoms in the ablated plume was first found using RIMS technique. This finding may lead us to gain considerable insight into the underlying of photochemical reactions for ion formation in MALDI. The production of matrix ions in MALDI can be explained by an atomic hydrogen transfer reaction between the matrix radical ions. The analyte molecular ions are produced mainly by a proton-transfer reaction between the analyte molecules and the radical matrix or its fragment ions. Although MALDI is a new and evolving technique, its present development shows the high potential for the determination of the relative molecular masses of large biomolecules. One of the important features for future applications may be the fast DNA sequencing with the improvements in mass resolution, sample preparation techniques and its sensitivity.

Chapter 5 gave detailed expositions of this tandem reflectron time-of-flight mass spectrometer (TRTOF) in seven parts: fragmentation trajectories of ions in the reflectron,

mass calibration of fragmentation ions, selection of parent ions to be fragmented, fragment ion collection, reflectron field effect, fragmentation mass resolution, and influence of the fragmentation laser parameters. It has been shown that a TRTOF of considerable potential can be easily adapted from an ordinary reflectron TOF instrument to carry out tandem MS/MS experiments. The instrument has a relatively simple timing requirement for overlapping the pulsed laser and ion packets, and also has a capability of multichannel detection of the fragment ions. Furthermore, different fragmentation patterns can be obtained by changing the fragmentation laser intensity and wavelengths. This is of considerable potential for increasing our understanding of photofragmentation of molecular ions and our ability to determine the structure of large biomolecules.

In the chapter 6, TRTOF was used for fragmentation of molecular ions of 2,5-DHB(M), its fragment and dimer. Many details of fragmentation mass spectra of three different kinds of the ions: fragment$(M\text{-}OH)^+$, parent$(M)^{+\cdot}$ and dimer$((M\text{-}OH)_2\text{-}H)^+$ have been discussed. The possible fragmentation pathways of these molecular ions have been proposed. It has been found that most of these fragmentation patterns can be described by the "Ladder-switching" model. Finally, it has been observed that the fragmentation mass spectra of ion isomers can be easily distinguished due to different fragmentation patterns. Thus indicates another advantage of this newly developed tandem reflectron TOF mass spectrometer.

Chapter 7 described the applications of TRTOF in the field of photofragmentation of biomolecular ions. The fragmentation mass spectra of the molecular ions of PTH-tryptophan, PTH-Valine, PTH-alanine, Cytosine, Guanine and Indole-2-carboxylic acid were obtained and possible fragmentation pathways were discussed.

Future work

The results of this thesis imply a promising future for TRTOF in photofragmentation of biomolecular ions. However this is a preliminary model and some modifications can be made in order to get better fragmentation mass spectra. One of modifications to the system which will be implemented as soon as possible is to include a pulsed voltage on the deflecting plates which will permit only one ion to be passed through the reflectron rendering the mass spectra easier to interpret. Another modification can be carried out by adding an einzel lens after exiting the reflectron, therefore the geometric effect can be

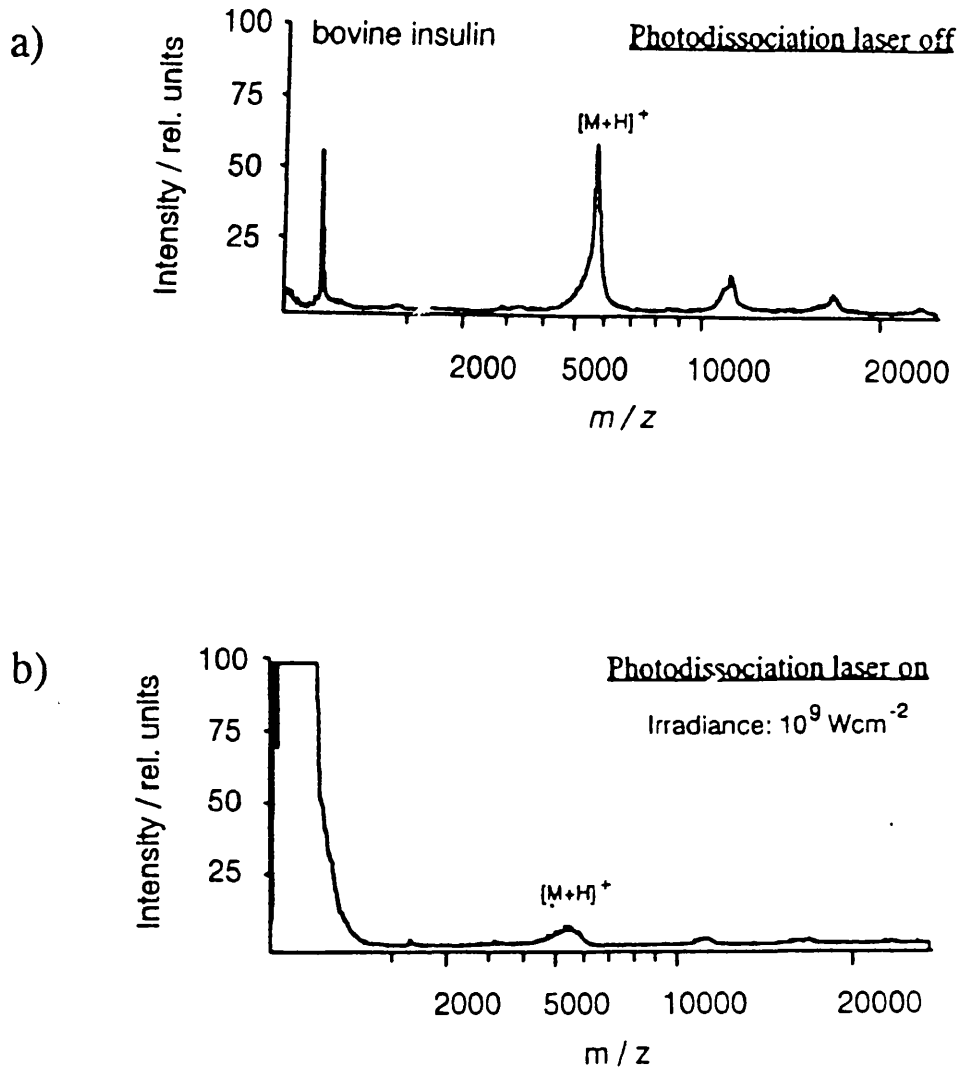

Fig.8.1 Mass spectra of insulin obtained by MALDIwithout (a) and with (b) applying a photodissociation laser. (from M.Karas et. al., 1994)

reduced and the collection efficiency of fragments will be improved.

It has been proved that there is a significant influence of the fragmentation laser parameters (wavelength, laser flux and laser pulse width) on the fragmentation mass spectra. The laser wavelength determines the photon energy and leads to changes in photofragmentation patterns. The laser flux and pulse width affects the absorption processes of molecular ions which also leads to changes in patterns of mass spectra. In this thesis only two wavelengths(266nm and 355nm) have been used for the fragmentation of the biomolecular ions. It has been found that it is difficult to fragment large biomolecular ions, especially, the molecular weight over 1000 Da(Schlag, et al., 1992), such as Substance P, by using these two wavelengths. Most absorption peaks of large biomolecules, e.g. Substance P, Bovine insulin, are below 240nm. Therefore VUV lasers should be used for photofragmentation of large biomolecular ions. Karas et al. have done some experiments using a 193nm excimer laser for photodissociation of large biomolecular ions(Karas, et. al., 1994). Fig.8.1 shows the Karas's mass spectra of bovine insulin obtained by MALDI with and without applying a photodissociation laser(193nm). It can be seen that the molecular ions of bovine insulin have been fragmented by the 193nm laser. However it is difficult for them to identify the fragments of the bovine insulin ions using the ordinary post-photofragmentation method since the fragments of the large biomolecular ion were mixed with the matrix and its fragment peaks.

Femtosecond laser pulse excitation has opened up a new door of looking at elementary chemical processes. Femtosecond excitation demonstrates high efficiency of multiphoton ionisation and large fragmentation near the photoexcited chromophores, while nanosecond excitation produces statistical energy redistribution. Oligopeptides consisting of a σ-bonded amino acid chain have several, mostly isolated, aromatic chromophores. By applying appropriate wavelengths of a femtosecond laser, nonstatistical cuts in the biomolecules will become feasible(Weinkauf, el at, 1994). Therefore, if the tunable femtosecond laser can be used for the photofragmentation of biomolecular ions in our TRTOF system, the gas-phase sequencing of oligopeptides seems to be possible.

Appendix

Diagram of Computer Program Used for the Calculation of Parameters in Photofragmentation of Molecular Ions in TRTOF

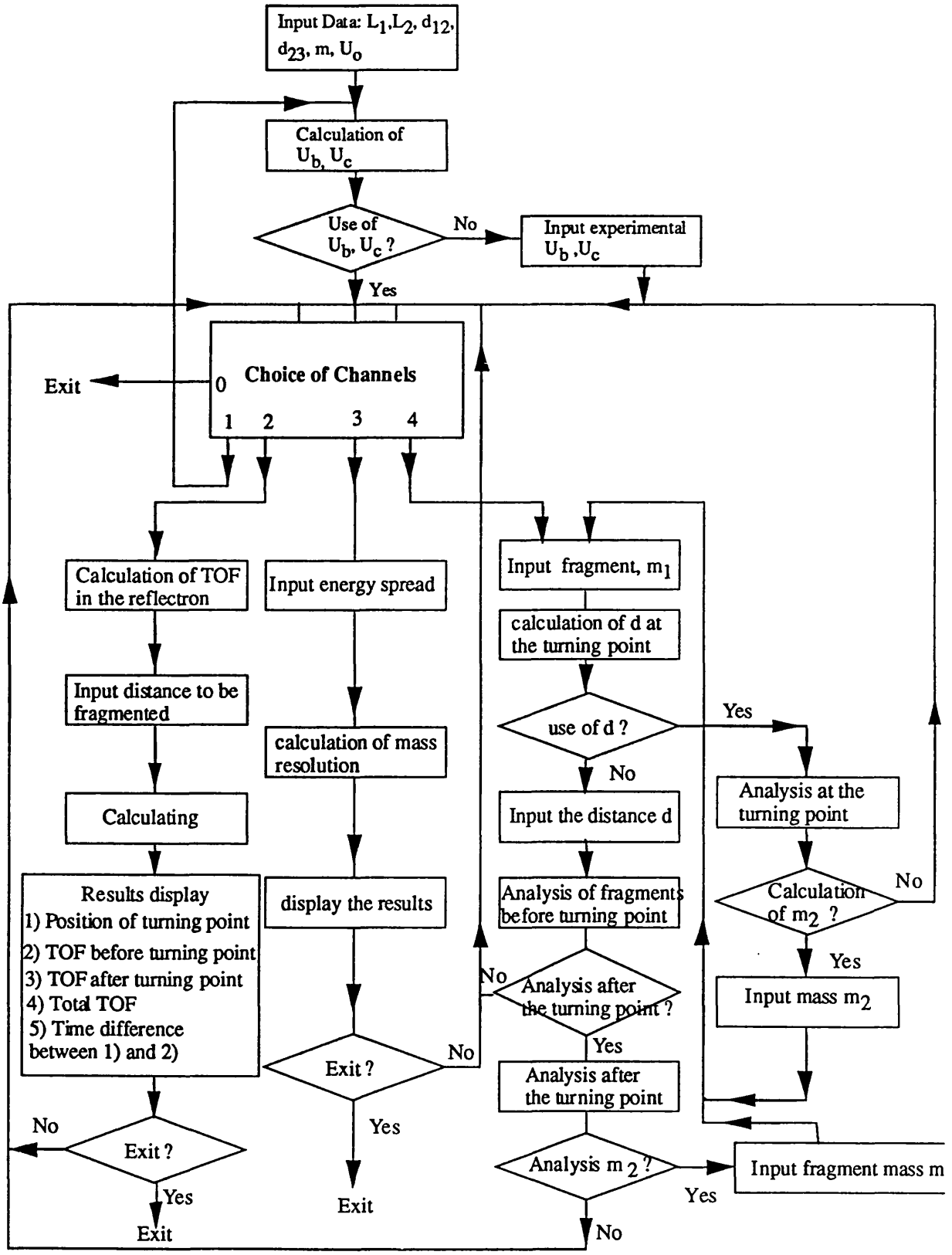

This diagram shows the principle of the computer program used for calculation of main parameters of photofragmentation of molecular ions in TRTOF. There are four main functions in this program. First of all, the best voltage settings on the retarding(U_b) and reflecting(U_c) plates in a reflectron can be calculated for the highest mass resolution of a reflectron TOF mass spectrometer. The theoretical calculation methods are shown in Chapter three. The basic input data for the calculation(see Fig. 3.5) are: the distances from a sample stub to a reflectron(L_1) and from a reflectron to a detector(L_2), the distances of a retarding region(d_{12}) and a reflecting region(d_{23}), the applied voltage on the sample stub(U_0), and the detected mass of an ion(m/z). U_b and U_c for the following calculations can be input using the theoretically calculated results of the best settings or using actually applied settings in an experiment.

Secondly, following the switch 2 in the diagram, the time-of-flight(TOF) of an ion at any position in reflectron or its total TOF moving through the system can be calculated. In addition, the position of the turn-around point of an ion in a reflectron can also be calculated. These calculations will help us to compare the theoretical calculated TOF of an molecular ion with the experimental measured TOF, and also help us to estimate the position of the turn-around point of an ion trajectory in a reflectron, which makes us possible to align another laser to fragment the ion at this position.

A general mass resolution of a reflectron time-of-flight mass spectrometer can be calculated using the third function of this program. The details of the calculation of the mass resolution can be seen in Section 5.7.

The last function of the program is used for analysis of fragmentation of ions in a tandem reflectron time-of-flight mass spectrometer (TRTOF). The analysis includes the calculations of a fragmentation TRTOF mass resolution, a position(d) and time(t) when a fragmentation takes place in a reflectron. The details of calculations can be seen in the section 3.1.3 and 5.7

References

Alexander M.L, Levinger N.E, Johnson M.A, D.Ray, W.C.Lineberger, J. Chem. Phys., 88, 6200(**1988**).

Ambartzumian R.V., Kalinin V.P., and Letokhov V.S., JETP Letters 13, 217(**1971**).

Ayre C.R, Moro L, Becker C.H; Anal.Chem., 66, 1610(**1994**).

Beavis R C and Chait B T, Rapid Commun. Mass Spectrom., 3, 12, 432(**1989**).

Beavis R C and Chait B T, Anal. Chem., 62, 1836(**1990**).

Beavis R.C., Chait B.T, Ens, W, Standing K.G., eds. NATO ASI Science Series; Plenum; New York **1990**.

Beavis R C, Organic Mass Spectrometry, 27, 653(**1992**).

Benninghoven.A, and Sichtermann.W.K., Anal Chem., 50, 1180(**1978**).

Bergmenn T, Matin T.P and Schaber H, Rev. Sci. Instrum., 60, 1(**1990**).

Boesl U, Weinkauf R, Walter K, Weickhardt C, and Schlag E.W, J.Phys.Chem. 94, 8467(**1990**).

Busch K.L, Glish G.L, McLuckey S.A, Mass Spectrometry/Mass Spectrometry: Techniques and Applications of Tandem Mass Spectrometry. VCH, New York(**1988**).

Chan T.W.D, Colburn A.W, and Derrick P.J, Org. Mass. Spectrom., 26, 342(**1991**).

Clark A, Kosmidis C, Ledingham K.W.D, Marshall A, Sander J, Singhal R.P and Campbell M,. J.Phys. B: At. Mol. Opt. Phys., 26, L665(**1993**).

Cornett D.S, LaiHing K, Cheng P.Y, Willey K.F, Duncan M.A, Rev. Sci. Instrum. 63, 2177(**1992**).

Dahl D.A, Delmore J.E., Applehans A.D., Rev. Sci. Instrum. 61, 607(**1990**).

Davis R, and Frearson M, *Mass Spectrometry*, Wiley,**1987**.

Dey M and Grotemeyer J, Eur. Mass Spectrom. 1,95(**1995**).

Dietz W, Neusser H.J, Boesl U, Schlag E.W, Chemical Physics 66, 105(**1982**).

Duncan M and Devonshire R, Optogalvanic spectroscopy in commercially available hollow cathode lamp, Inst. Phys. Conf. Ser.113, 207(**1991**).

Duong, H.T., et al., Compt. Rend. (Paris) 276B,909(**1973**)

Ehring H, Karas M and Hillenkamp F, Organic Mass Spectrometry, 27, 472(**1992**).

Ervin M.H, Wood M.C, Wingorad N, Anal.Chem., 65, 417(**1993**).

Gioumousis G, Stevenson D.P, J.Chem. Phys, 29,294(**1958**).

Grotemeyer J, Walker K, Boesl U, Schlag E.W, Int. J. Mass Spectrom. Ion Phys., 78, 69(**1987**).

Grotemeyer J and Schlag E.W, Acc, Chem. Res. 22,399(**1989**).

Haisa M, Kashino S, Hanada S.I, Tanaka K, Okazaki S and Shibagaki M, Acta Crystallogr., Sect.B 38,1480(**1983**).

Hurst G.S, Nayfeh M.H, and Young J.P, Appl. Phys. Lett. 30,229 (**1977**).

Hurst G.S and Payne M.G, Principles and Applications of Resonance Ionisition

Spectroscopy, Adam Hilger, Bristol and Philadelphia, **1988** .

Huth-Fehre.T, Becker C.H, Rapid Commun. Mass Spectrom. 5, 378(**1991**).

Jardine R, Morgan J, Alderdice D.S, and Derrick P.J, Org. Mass. Spectrom. 23, 1077(**1992**).

Juhasz P, Costello C E and Biemann K, J. Am. Soc. Mass Spectrum., 4, 399(**1993a**).

Juhasz P, Costello C E, Rapid Commun. Mass Spectrom. 7,343(**1993b**).

Kammer H.F., *In Mass Spectrometry of Large Non-Volatile Molecules for Marine Organic Chemistry*, E.R.Hilf and W.Tuszynski, eds, pp61-72,World Scientific, Singapore. (**1987**).

Karas M, Bachmann D, Bahr U, and Hillenkamp F, Int. J. Mass Spectrum. Ion Proc., 78, 53(**1987**).

Karas M and Hillenkamp F, in O.Longevialle (Ed.), *Advances in Mass Spectrometry*, Heyden & Son, London, pp.416,417(**1989**).

Karas M and Hillenkamp F, Ion Formation from Organic Solids (IFO IV), Proc. 4th Int. Conf., Munster, Germany, 1987, Wiley, Chichester, **1989**.

Karas M, Bahr U, Ingendoh A, Nordhoff E, Stahl B, Strupat K and Hillenkamp F. Anal. Chim. Acta, 241, 175(**1990**).

Karas M, Bahr U and Giebmann U, Rapid Commun. Mass Spectrom., 10, 335(**1991**).

Karas M, Dreisewerd K, Schurenberg M, Wang B, Hillenkamp F, AIP; Conference Proceedings 329, RIS'94, Bernkastel-Kues, Germany, July, **1994**.

Karataev V.I, Mamyrin B.A. and Schmikk D.V, J.Tech. Phys., 16(7), 1498(**1971**).

Kelly and Dreyfus, Surf. Sci. 198,263(**1988**).

Kinsel.G.R, Lindner J and Grotemeyer J , .Phys. Chem. 96,3157(**1992**).

Koster C, and Grotemeyer J , Org. Mass Spectrom. 27,463(**1992**).

Kratzin H.D, Wiltfang J, Karas M, Nenhoff V, Hischmann N, Anal. Biochem. 183,1(**1989**).

Ledingham K.W.D, Multiphoton ionisation and laser mass spectrometry. Summer school in laser spectroscopy. University of East Anglia, September (**1994**).

Mamyrin B.A, Russian Patent No.198034,(**1966**).

Mamyrin B.A,. Int. J. Mass Spectrom. Ion Processes, 131, 1(**1994**).

Oakey N S and MacFarlane S, Nucl. Inst. Meth., 49, 220(**1967**).

Pandolfi R.S, Gobeli D.A and EI-Sayed M.A, J. Phys. Chem., 85, 1779(**1982**).

Peugnet K, J. Appl. Phys. 48, 3206(**1977**).

Popesku D, Collins C.B, Johnson B.W, Popesku I, Phys. Rev. A9, 1182(**1974**).

Schlag E.W, Levine R.D, Chem. Phys. Lett., 163, 523(**1989**).

Schlag E.W, Grotemeyer J, Levine R.D, Chem. Phys. Lett., 190, 521(**1992**)

Slifkin M.A, Allison A.C, Nature, 215, 949(**1967**).

Strupat S, Karas M and Hillenkamp F, Int. J. Mass Spectrom. and Ion Proc. 111, 89(**1991**).

Tanaka K, Ido Y, Akita S, Yoshida T Yoshida Y, Proceedings of the Second Japan-

China Joint Symposium on Mass Spectrometry, Usaka, Japan, **1987**.

Thonnard N, Wright M.C, Davis W.A, and Willis R.D, Inst. Phys. Ser. No. 128, 27(**1992**).

Towrie M, Drysdale S L T, Jennings R, Land A P, Ledingham K W D, McCombes P T, Singhal R P, Smyth M H C and Mclean C J, Int.J of Mass Spec. and Ion Pro. 26, 309(**1990**).

Tuccio S.A, Dublin J.W, Peterson O.G, and Snavely B.B, IEEE J. Quant. Electr. QE-10, 790(**1974**).

van der Peyl G.J.Q, Isa K, Haverkamp J, and Kistemaker P.G, Nucl. Instrum. Methods, 198, 125(**1982**).

Vertes.A, Balazs.L, and Gijbels R, Rapid Commun. Mass Spectrom. 4, 263(**1990a**)

Vertes A, Gijbels R, Rapid Commun. Mass Spectrom., 4, 6, 228(**1990b**).

Vertes A, Irinyi G, Gijbels R, Anal. Chem., 65, 2389(**1993a**).

Vertes A, Gijbels R, *Laser ionisation mass analysis*; Wiley-interscience Pub.(**1993b**).

Vorm O, Roepstorff P, and Mann M, Anal. Chem., 66, 3281(**1994**).

Wang B.W, J.Am.Soc. Mass Spectrom. 4, 388(**1993**).

Weinkauf R, Aicher P, Wesley G, Grotemeyer J and Schlag E.W, J.Phys.Chem. 98, 8381(**1994**).

Wiley W.C, and McLaren I.H., Rev. Sci. Instrum., 26, 1150(**1955**).

Williams E.R, Fang L and Zare R.N, Int.J.Mass Spectrom. Ion Processes, 123, 233(**1993**).